UNIVERSITY OF LIVERPOOL

Application of few layer graphene and exfoliated graphite materials in lithium ion batteries

Thesis submitted in accordance with the requirements of the University of Liverpool for the Degree of Doctor in Philosophy

Christopher G. Sole

September 2017

Supervisor: Laurence J. Hardwick

STEPHENSON INSTITUTE FOR RENEWABLE ENERGY
Battery and Electrified Interfaces Group
UNIVERSITY OF LIVERPOOL

Abstract

Lithium ion battery technology; where energy is stored via the shuttling of Li^+ ions between two insertion type electrodes; has developed rapidly to become a common-place feature of modern life. Recently, processes to exfoliate graphite materials at scale have been developed, producing novel materials with varying degrees of purity, defect concentrations and size distributions. The high aspect ratio and conductivity of these materials has attracted interest regarding their application in lithium ion battery electrodes, which is investigated in the present study.

In the first part, the Li insertion behaviour of exfoliated graphite materials is investigated for use in in lithium ion battery negative electrodes. In Chapter 3, the mechanism of Li intercalation in a microcrystalline graphite sample is followed by *in situ* Raman spectroscopy. Then, in Chapter 4, a material produced by cathodic electrochemical exfoliation of the microcrystalline graphite sample is studied. Structural characterisation reveals a significant restacking of graphene layers has occured upon drying reulting in only subtle changes to the stacking order of the pristine graphite. The modified material displays an increased first cycle irreversible capacity and decreased reversible capacity, suggesting the process is not advantageous for the modification of graphitic negative electrode materials. *In situ* Raman spectroscopy is used to confirm the similarity in lithiation mechanism with the pristine sample, and a model is developed in order to estimate strain and doping of graphene layers from the Raman spectra of the stage 4L and 3L phases.

In Chapter 5, *in situ* Raman spectroscopy is employed to develop a fundamental understanding of how the lithium intercalation mechanism in graphitic carbons varies

with decreasing number of stacked graphene layers. Mechanical exfolation of highly crystalline natural graphite flakes is used to avoid the aforementioned problems of layer restacking, allowing investigation of flakes with accurately defined thicknesses. A similar mechanism of Li intercalation to that in bulk graphite is observed for flakes of ~ 9 layers and ~ 56 layers. However, an increase in in-plane strain is observed for the few layer graphene sample, which may be linked to the accelerated capacity fading exhibited by cells using thin graphitic flakes as negative electrode materials. Furthermore, the succesful Li intercalation of a trilayer graphene sample was accomplished, whereby Li^+ ions were observed to fill both available interlayer spaces evenly without the conventional staging effects which occur in thicker flakes.

Finally, the use of exfoliated graphite materials as conductive additives for high rate lithium ion battery electrodes is evaluated. The performance of materials produced by three different exfoliation processes are compared with carbon black and graphite additives in both $Li_4Ti_5O_{12}$ and $LiCoO_2$ composite electrodes. Variation of the conductive additives is shown to have no effect on the performance of the $Li_4Ti_5O_{12}$ due to an electronic conduction mechanism which occurs through the surfaces of lithiated active material particles. In contrast, the performance of the $LiCoO_2$ system is shown to be strongly additive dependent, whereby the exfoliated graphite additives showed inferior performance to the carbon black additive. However, the materials produced by electrochemical exfoliation did exhibit improved performance compared to the graphite and liquid exfoliated samples.

Acknowledgements

To Professor Laurence Hardwick, thank you for your scientific input, encouragement and fairly constant good humour. Thank you for filling your group with such great people and trusting us to pursue our scientific journeys. I truly appreciate what you've done for us, see you around (hopefully) and bon chance director!

To my other mentors…

Nicky Drewett - you are a legend amongst men. Mostly Spanish ones now I presume. Thank you for your patience, guidance and laughter. Laura Cabo Fernandez - you are the green, Spanish rock of the Hardwick group. Thank you for your support and wisdom. Don't mess with my strawberries. Zou Jianli – you saved my PhD! I owe you my conditioner. You are unbelievably talented, keep following your dreams, keep painting, I will see you in Zhong Guo.

To my (attractive?) assistants… Olly Rogan, Jack, David - thank you for putting a shift on when we needed to. I hope I taught you something about soil, soul and society.

To the laads – Filipee, Ebe, Tommy G, Mikey G, (Dr) FORSTER, Iain (*generation zero*) Aldous, Petar-lad, Big Jon – its been a pleasure lads.

And to friends far away - Henry!, Sid – thank you for inspiring me with your work ethic and fuelling me with your love of food.

To Rong Hao, although I'm not sure what you've contributed, you never let me down and I feel that should be acknowledged. Bloody guy.

I also want to acknowledge the people who inspired me to come down this tortuous path. Firstly, this includes Theo Tzedakis, whose electrochemistry course lives with me to this day, thank you. Secondly, to my best friend Patrice, and to the EU in general, just in case Brexit does mean Brexit – thank you, the opportunity you gave me has changed my life. Next, looking further back into the hazy past: to Madeline Woolfenden (great name), thank you for your enthusiasm and joy. Finally, slightly begrudgingly to Ms Flynn who said I would I would do a Chemistry PhD in year 9, when it was possibly the last thing I wanted to do. Thank you!

I would like to thank *everyone in the Stephenson Institute who has made this place such a special and amazing place to work.* We are blessed.

A very special thanks to *Mr Coca Clemente himself*, you are a top man and a very accommodating Spanish gentleman.

I would like to acknowledge Mr (Dr?) Ebenezer Tetsi once more. It's been an amazing experience living and learning with/from you. You are a poet, a philosopher and a right-back. Keep spreading the love.

I thank my family for their love and support, practically always. I thank Jess for her love and conversation, I appreciate you beyond typing.

I would like to dedicate this thesis to Gwen.

The author would like to thank collaborators at the University of Manchester and acknowledge the EPSRC and the University of Liverpool for funding and access to equipment.

Contents

List of Abbreviations

AFM – Atomic force microscopy

DMC – Dimethyl carbonate

EC – Ethylene carbonate

FLG – Few layer graphene

GIC – Graphite intercalation compound

LIB – Lithium ion battery

NMP – N-methyl-2-pyrolidone

OCP – Open circuit potential

OCV – Open circuit voltage

PC – Propylene carbonate

PXRD – Powder X-ray diffraction

SEM – Scanning electron microscopy

SLG – Single layer graphene

TEM – Transmission electron microscopy

XRD – X-ray diffraction

Definition of Mathematical Functions

Summation Function:

$$\Sigma_{i=1}^{n} d_i = d1 + d2 + \cdots dn$$

Product Function:

$$\Pi_{i=1}^{n} d_i = d1 \times d2 \times \ldots dn$$

1. Introduction

This chapter contains an introduction to the fundamental processes and relevant literature that shall be built upon in subsequent chapters.

"You thought, as a boy, that a mage is one who can do anything. So I thought, once. So did we all. And the truth is that as a man's real power grows and his knowledge widens, ever the way he can follow grows narrower: until at last he chooses nothing, but does only and wholly what he must do ... " — Ursula K. Le Guin, A Wizard of Earthsea

---

1.1. Demand for energy storage technologies

The global emission of climate changing gasses, particularly carbon dioxide,[1] threatens to plunge the world into unknown environmental and economic crises.[2–5] Addressing the causes and limiting the negative impacts of climate change will play a major role in the 21st century. In this context, the development of novel materials for energy storage is a worthwhile goal.[6,7] Existing energy infrastructure relies predominantly on the consumption of unsustainable fossil fuel reserves,[8] necessitating the release of large quantities of carbon dioxide. On the other hand, alternative methods of energy production such as nuclear power and the harnessing of renewable energy sources (in particular wind, solar, biomass and hydropower)[9] offer the possibility of meeting the world's projected energy consumption, with low to net-zero emissions of climate affecting gasses.[10–13] However, due to the intermittant nature of renewable technologies, improved energy storage capacity alongside improved demand side response flexibility is crucially required.[12] Significantly, in order to reduce carbon emissions related to the global transport sector there is a need for the development of cleaner and more efficient vehicles.[14] Electrochemical energy storage technologies, specifically in the form of batteries, look increasingly likely to play a leading role on both of these fronts.[15,16]

1.2. Electrochemical processes

Electrochemistry is the study of electrochemical reactions, defined as reactions where a chemical change either produces or is caused by an electric force.[17] The primary distinction between an electrochemical reaction and a chemical redox reaction are that oxidation (removal of electrons from a species) is spatially separated from reduction (gain of electrons by a species). This is achieved in an electrochemical cell whereby redox reactions occur at the surfaces of electronic conductors or semiconductors known as electrodes. Electrodes are separated by an electrolyte, a substance that permits the conduction of ions but not electrons. The circuit is completed via an external electronic conductor which contacts both electrodes.

The spatial separation of electrodes (known as the anode and cathode respectively) allows an electrochemical reaction to be described by two *half-cell* reactions. At the anode oxidation occurs:

$$Red_1 \rightarrow Ox_1 + e^- \qquad \text{Equation 1.1}$$

At the cathode reduction occurs:

$$Ox_2 + e^- \rightarrow Red_2 \qquad \text{Equation 1.2}$$

The overall reaction may thus be given as:

$$Red_1 + Ox_2 \rightarrow Ox_1 + Red_2 \qquad \text{Equation 1.3}$$

1.2.1. Thermodynamics of electrochemical cells

The spontaneous direction of an electrochemical reaction is determined by the electrochemical potentials of the species involved. If the half-cells are arbitrarily defined as left and right electrodes respectively, the energy change for a reaction is given by the change in Gibbs energy for each half-cell reaction:

$$\Delta G = (\sum_{\mathrm{i}} s_i \mu_i)_{right} - (\sum_{\mathrm{i}} s_i \mu_i)_{left} \qquad \text{Equation 1.4}$$

Where G is the Gibbs free energy, μ_i is the electrochemical potential of species i, and s_i is the stoichiometric coefficient of species i. By convention the sign of s_i is defined by writing half-cell reactions in the form:

$$\sum_{\mathrm{i}} s_i M^{z_i} \leftrightarrow ne^- \qquad \text{Equation 1.5}$$

Where M_i represents the chemical formula of species i and z the charge of any ionic species. If ΔG is negative then electrons will flow from left electrode to right electrode and vice versa. At equilibrium, when zero current flows between the two electrodes, the cell open circuit potential (U) can be measured and is related to the Gibbs free energy by:

$$\Delta G = -\mathrm{nFU} \qquad \text{Equation 1.6}$$

Where n is the number of electrons transferred and F is the Faraday constant (96485 C mol^{-1}). Furthermore, the Gibbs free energy for each half-cell reaction can be expressed in terms of product and reactant activities by:

$$\Delta G = \Delta G^{\circ} + RTlnQ \qquad \text{Equation 1.7}$$

Where ΔG° is the Gibbs energy with all reactant and products in their standard states (activities equal to one), R is the gas constant,T is temperature and Q is the reaction quotient:

$$Q = \frac{\text{activities of products}}{\text{activities of reactants}} = \prod_i a_i^{s_i} \qquad \text{Equation 1.8}$$

Where a_i is the activity and s_i the stoichiometric coefficient of species i respectively (s_i is positive for products and negative for reactants). Therefore, the open circuit potential may also be expressed in terms of the composition of the reaction mixture by the Nernst equation:

$$U = U^{\circ} - \frac{RT}{nF}\ln\left(\prod_i a_i^{s_i}\right)_{right} + \frac{RT}{nF}\ln\left(\prod_i a_i^{s_i}\right)_{left} \qquad \text{Equation 1.9}$$

Where U° is the standard cell potential. The Nernst equation is often given only in terms of one electrode, however, it should be noted that electrode potentials are always relative to another electrode and the left term only vanishes when electrode potentials are given versus a specified electrode. The use of electrodes with well-defined, reproducible potentials (known as reference electrodes) may then be used for comparison of electrode potentials . For example, electrode potentials are commonly quoted versus the standard hydrogen electrode. In the field of lithium ion batteries equilibrium electrode potentials are often quoted vs. Li^+/Li, which lies at -3.04 V versus the standard hydrogen electrode.

1.2.2. Galvanic and electrolytic cells

Electrochemical cells may be divided into two categories according to the spontaneity of the electrochemical processes that occur: galvanic cells which spontaneously produce work (ΔG is negative), and electrolytic cells which require an input of work

to drive the reaction (ΔG is positive before work is applied). The theoretical maximum work that a galvanic cell may deliver (or alternatively the minimum work required to drive an electrolytic cell) is given by the change in Gibbs free energy as defined in Equation 1.6. However, the passage of current through a cell causes the potential to change from equilibrium which is known in electrochemistry as polarisation. The magnitude of this potential drop is known as overpotential which can be separated into surface overpotential, Ohmic resistance and concentration overpotential.

1.2.3. Kinetics of electrochemical cells

1.2.3.1. Surface overpotential

At equilibrium the rate of anodic and cathodic processes is equal, hence no net current flows. A driving force is required to cause a net anodic or cathodic current which is known as the surface overpotential and given the symbol η_s. The rate of reaction in the charge transfer limited regime may be given by the Butler-Volmer equation, which has the form:

$$i = i_0 \left[\exp\left(\frac{\alpha_a F}{RT}\eta_s\right) - \exp\left(\frac{\alpha_c F}{RT}\eta_s\right)\right] \qquad \text{Equation 1.10}$$

Where i_0 is the exhange current density which determines the reversibility of the reaction. α_a and α_c are apparent transfer coefficients which relate to how application of a potential favours one direction of reaction over the other. When η_s is positive an anodic current is produced and when η_s is negative a cathodic current is produced.

1.2.3.2. Ohmic resistance

Ohmic resistance describes the resistance to the movement of charged species driven by the electric field between two electrodes. The electric field (E) is related to the gradient in potential Φ by:

$$E = -\nabla\Phi \qquad \text{Equation 1.11}$$

The flow of electrons through electronic conductors can be described by Ohm's law:

$$\mathbf{i} = -\sigma\nabla\Phi \qquad \text{Equation 1.12}$$

Where i is the current density and σ is the electronic conductivity, equal to the inverse of the resistivity. The electric field also causes an ionic current across the electrolyte. The ionic current is the net flux of charged species:

$$\mathbf{i} = \sum_i z_i F N_i \qquad \text{Equation 1.13}$$

Where N_i is the flux density of species i. However, the flux of charged species through a liquid electrolyte is a combination of the movement of ions in response to the electric field (known as migration), as well as any concentration gradients (diffusion) and bulk fluid motion (convection). In this work convection will be disregarded, therefore the flux of ions will be the result of migration and diffusion. In the absence of concentration gradients the movement of charged species may also be described by Ohm's law:

$$\mathbf{i} = -\kappa\nabla\Phi \qquad \text{Equation 1.14}$$

Where κ is the ionic conductivity of the electrolyte. However, the flow of current in most electrolytes (without convection) causes the build-up of concentration gradients.

This is due to a property known as the transference number of ions; defined as the fraction of current that is carried by that ion in a solution of uniform composition.

$$t_i = \frac{z_i F N_i}{\sum_i z_i F N_i} \qquad \text{Equation 1.15}$$

If $t_i < 1$ for the reacting species then a concentration gradient develops. The presence of a gradient in concentration of species i (∇c_i) will also cause a flux of ions, which is proportional to the diffusion coefficient of species i (D_i) by Fick's first law:

$$\boldsymbol{N}_{i,diffusion} = -D_i \nabla c_i \qquad \text{Equation 1.16}$$

hence the migration flux should not be considered independently from diffusion. The unified treatment of migration and diffusion is known as concentrated-solution theory, however, a thorough explanation of this theory is beyond the scope of this work and may be found elsewhere.[18]

1.2.3.3. Concentration overpotential

As the Nernst equation (Equation 1.9) shows the potential of an electrode is shifted by changes in concentration, so the presence of concentration gradients in a cell creates another source of overpotential. This is best explained through consideration of a concentration cell such as that depicted in Figure 1. In this example, a solution of 0.1 M $CuSO_4$ is connected to a solution of 0.05 M $CuSO_4$ via a porous glass disk which prevents rapid mixing but allows the flow of current and slow diffusion between the solutions. If identical Cu electrodes are placed into each solution there is a potential difference between the electrodes which may be approximated by:

$$\eta_c = (1 - t_+)\frac{RT}{F} ln \frac{c_I}{c_{II}} \qquad \text{Equation 1.17}$$

Where c_I and c_{II} represent the concentrations in compartments I and II respectively. Equation 1.17 may be used to used to calculate the potential difference between any two points in a solution with a concentration gradient across it, known as the concentration overpotential.

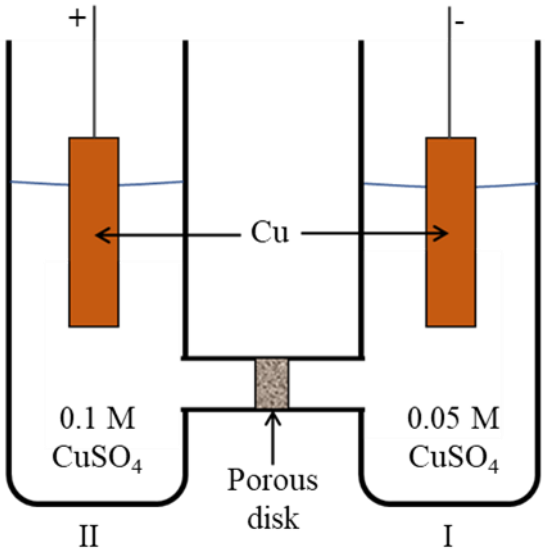

Figure 1: Example of a concentration cell

1.2.4. Overall cell voltage

The overall cell voltage (V) during current flow will depend on:

- the open circuit potential (U)
- the surface overpotentials at each electrode ($\eta_{s(\text{cathode})}$ and $\eta_{s(\text{anode})}$)
- the ohmic potential drop ($\Delta\,\Phi_{\text{ohmic}}$)
- the concentration overpotential at each electrode ($\eta_{c(\text{cathode})}$ and $\eta_{c(\text{anode})}$).

For a galvanic cell:

$$V = U - \eta_{s(\text{anode})} - \eta_{c(\text{anode})} + \eta_{s(\text{cathode})} + \eta_{c(\text{cathode})} - \Delta\Phi_{\text{ohmic}}$$

Figure 2 shows that as current is increased the various sources of overpotential cause a drop in the operating voltage of a galvanostatic cell. As discussed above, the opposite effect will occur within an electrolytic cell.

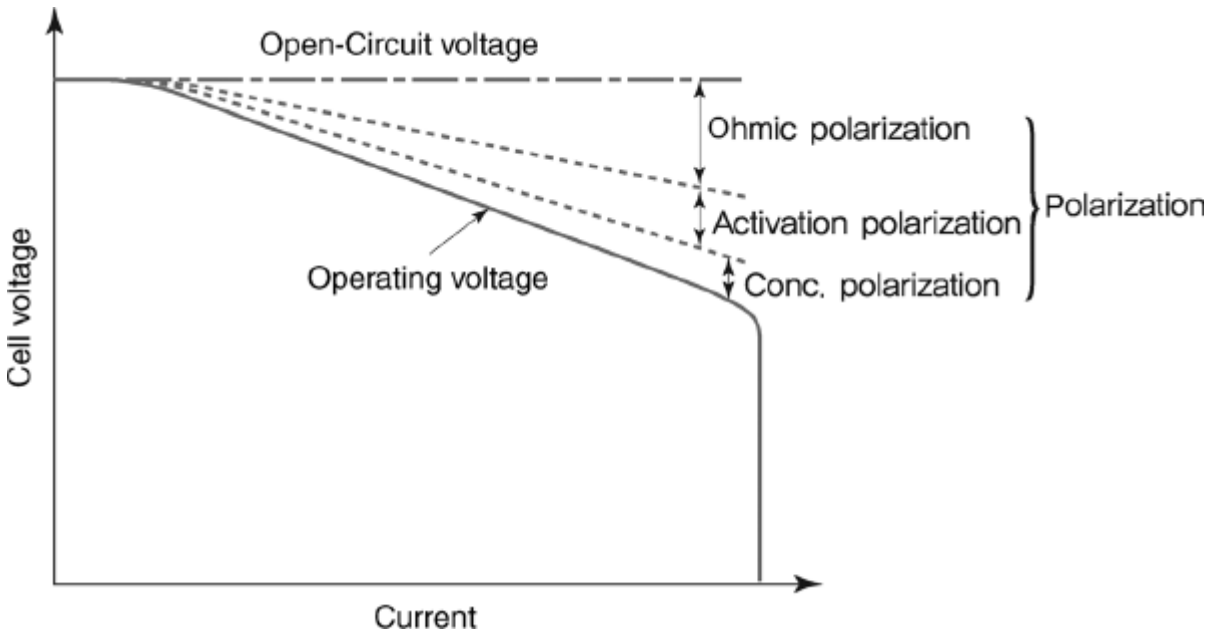

Figure 2: Effect of increasing current on the operating voltage of a galvanostatic cell (from [19]). Activation polarization refers to surface overpotential.

The net work delivered by a galvanic cell or required by an electrolytic cell when a current I flows for time t is given by:

$$w_{net} = \int IV\, dt \qquad \text{Equation 1.18}$$

Therefore polarisation causes less energy to be delivered by galvanostatic cells and means electrolytic cells require more energy to drive the electrochemical reaction.

1.2.5. Batteries

Batteries are made up of two or more cells connected in either parallel or series and can be separated into primary and secondary batteries. Primary batteries are non-rechargeable due to the irreversible nature of the electrochemical reaction that occur within them. Secondary batteries make use of reversible electrochemical reactions thus allowing multiple charge/ discharge cycles. During charging a secondary battery acts as multiple electrolytic cells, converting electricity to chemical energy, and on discharge the battery acts as mutiple galvanic cells whereby an electric direct current is generated.

1.2.6. Characteristics of electrochemical cells for energy storage

Charge capacity

The charge capacity or capacity, Q (Ah), is the the total amount of charge that flows through a cell:

$$Q = \int_{t_1}^{t_2} I(t)dt \qquad \text{Equation 1.19}$$

Theoretical specific capacity

The theoretical specfic capacity, q_{th} (Ah kg^{-1}), defines the charge capacity per kg of reactants, m_i, which may be calculated from the stoichiometric cell reaction:

$$q_{th} = \frac{nF}{\sum_i m_i} \qquad \text{Equation 1.20}$$

For energy storage applications it is often desirable to maximise the energy within a given mass or volume. Throughout this work the terms specific energy (Wh kg^{-1}) and energy density (Wh dm^{-3}) will be collectively described as energy metrics:

Theoretical specific energy

$$w_{th} = \frac{nF\Delta U}{\sum_i m_i} \qquad \text{Equation 1.21}$$

Theoretical energy density

$$w_{V,th} = \frac{nF\Delta U}{\sum_i V_i} \qquad \text{Equation 1.22}$$

Furthermore, power refers to the rate at which that energy can be released or converted (to chemical energy). The terms specific power (W kg^{-1}) and power density (W dm^{-3}) will be collectively described as power metrics:

Specific power

$$p = \frac{I\Delta U}{\sum_i m_i} \qquad \text{Equation 1.23}$$

Power density

$$p_V = \frac{I\Delta U}{\sum_i V_i} \qquad \text{Equation 1.24}$$

The charge/discharge current (C rate)

The term *C rate* (*C/Δt*) is commonly used by battery scientists to describe the rate of charge/discharge of an electrochemical cell, where *C* denotes either the theoretical or nominal charge capacity (Ah) and *Δt* is usually in hours. In this work the *C rate* will be used to describe the current rate at which the theoretical charge capacity of a cell

(Ah) is fully reached, where 1C is the current required to fully charge/discharge in one hour. For example, C/37 means a current theoretically allowing full charge or discharge in 37 hours.

Irreversible capacity

The irreversible capacity (%) defines how much charge capacity is lost after each cycle:

$$\text{irreversible capacity} = 100\% \times \frac{Q_{Charge} - Q_{Discharge}}{Q_{Charge}} \qquad \text{Equation 1.25}$$

1.3. Lithium ion batteries

Lithium is the lightest (6.94 g mol^{-1}) and most electropositive metal (-3.04 V vs. standard hydrogen electrode) and thus represents a highly desirable negative electrode material for battery applications. However, the use of lithium metal electrodes in rechargeable batteries (with liquid electrolytes) is limited due to serious safety issues during cell charging. As lithium is deposited at the negative electrode, the formation and growth of dendritic structures can lead to short circuits and associated cell failure, thermal runaway and explosion hazards.[15]

This has led to the development of the inherently safer lithium ion battery (LIB) technology, where lithium is stored in the ionic state in both negative and positive electrodes.[15,20–23] The first commercial LIB was released by Sony in 1991,[24] preceded by several separate inventions[25] that included the work of Goodenough,[26] Yazami[27] and Whittingham.[28] Figure 3 shows the operating mechanism of a Li ion battery. On charging, electrons flow from the positive electrode to the negative electrode through an external circuit, accompanied by the extraction of Li^+ ions from the positive electrode and insertion into the negative electrode via a lithium ion conducting electrolyte. On discharge, the opposite process occurs, releasing stored energy. The open circuit potential of such a cell is equal to the difference of electrochemical potentials of Li in the two electrodes when in mutual contact with an electrolyte:

$$U = -\frac{(\mu_{Li}^{+ve} - \mu_{Li}^{-ve})}{nF} \qquad \text{Equation 1.26}$$

where U is the open circuit potential of the cell, μ_{Li}^{+ve} and μ_{Li}^{-ve} the electrochemical potentials of Li in the positive electrode and negative electrode respectively, n = 1 (since one e^- is transferred per lithium) and F is Faraday's constant.

Using $w_{th} = \frac{nF\Delta U}{\sum_i m_i}$ Equation 1.21 1.21 and $w_{V,th} = \frac{nF\Delta U}{\sum_i V_i}$

Equation 1.22 1.22, the energy metrics of these systems are maximised by selection of electrode materials able to reversibly insert lithium ions with a large gravimetric capacity and at low and high electrochemical potentials (for the positive and negative electrode material respectively).

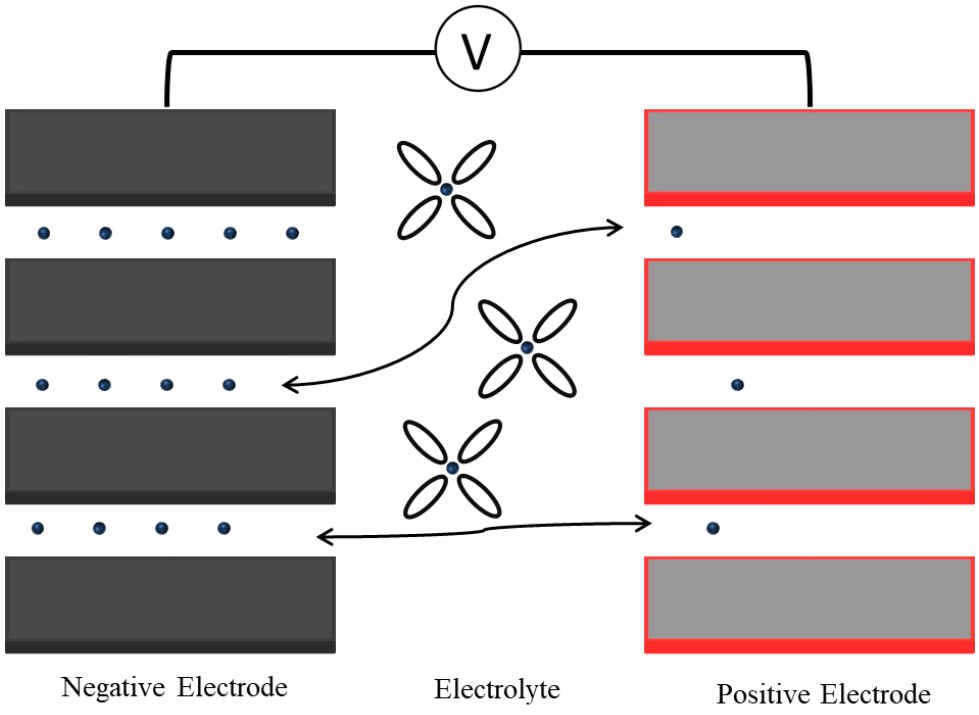

Figure 3: Schematic of working mechanism of lithium ion batteries. Li+ ions are represented by blue spheres.

LIBs have become the most popular portable energy storage technology accounting for over 60% of total portable battery sales.[29] LIB costs have been driven down[30] by a rapid increase in production which has extended the viability of LIBs for various applications - for example, they are currently being deployed in various large scale grid storage applications.[16] Tarascon and Armand showed in 2001[15] that LIBs outcompete all conventional rechargeable battery technologies (excluding Li metal batteries) in terms of gravimetric and volumetric energy density.[15] Between then and

now further progress has been achieved with state of the art commercial cells being reported with specific energy ~240 Wh kg^{-1} and volumetric energy density ~670 Wh L^{-1}.[31]

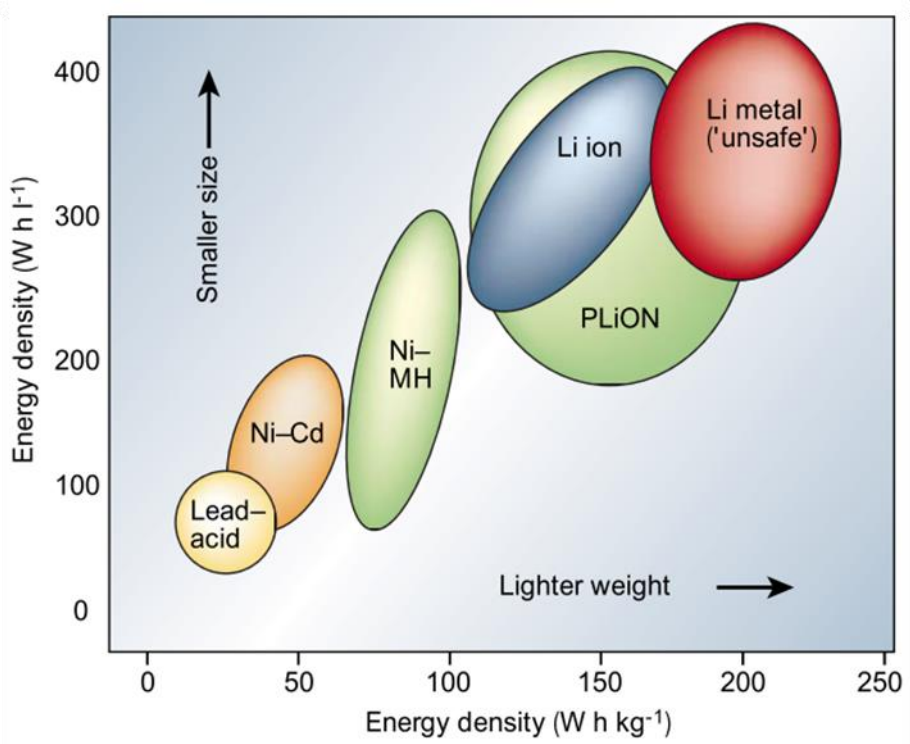

Figure 4: Comparison of gravimetric and volumetric specific energy of various electrochemical energy storage technologies, PLiON represents plastic Li ion technology. Adapted from Tarascon et al.[15]

1.3.1. Materials for lithium ion batteries

Figure 5 shows the equilibrium potential vs. Li^+/Li and theoretical capacity of common materials used in LIBs. Primarily, commercial cells have been based around the use of graphite as negative electrode and a high potential metal oxide material as positive electrode. The first commercial cells employed a $LiCoO_2$ positive electrode but more recently the partial substitution of Co with Mn, Ni and Al has been used to increase energy and power metrics, improve cycling and safety measures and reduce

costs.[20,24,32] The use of lower potential positive electrode materials such as $LiFePO_4$ or $Li_{1-x}Mn_2O_4$ is also prevalent due to lower cost and improved cycling performance.[20]

As discussed, the role of the electrolyte in LIBs is to transport Li^+ ions between electrodes during cycling. An ideal electrolyte will have low Ohmic resistance to current flow, alongside a large transference number (ideally 1) to avoid the build-up of concentration gradients at large current densities and associated concentration polarisation. Most commercial systems use liquid electrolytes for this role, however, the large operating voltage of conventional systems poses severe limitations to the choice of electrolyte, particularly during charging when the low potential at the negative electrode surface causes reductive decomposition of electrolyte species and consumption of Li^+ ions.[33] To ensure reversible electrochemical cycling the formation of a stable surface film, known as the solid electrolyte interphase (SEI), must occur. The SEI permits conduction of Li^+ ions but prevents e^- conduction thus limiting electrolyte decomposition beyond the first few cycles.[33] Conventional electrolytes thus consist of a liquid solvent (generally a mixture of carbonates), a lithium salt and additives with optimised properties for stable electrochemical cycling.[34] Some common electrolyte solvents and salts are shown in Table 1.1. Furthermore, the development of solid electrolytes and polymer gel systems for both increased safety and energy metrics is at an advanced stage.[35,36]

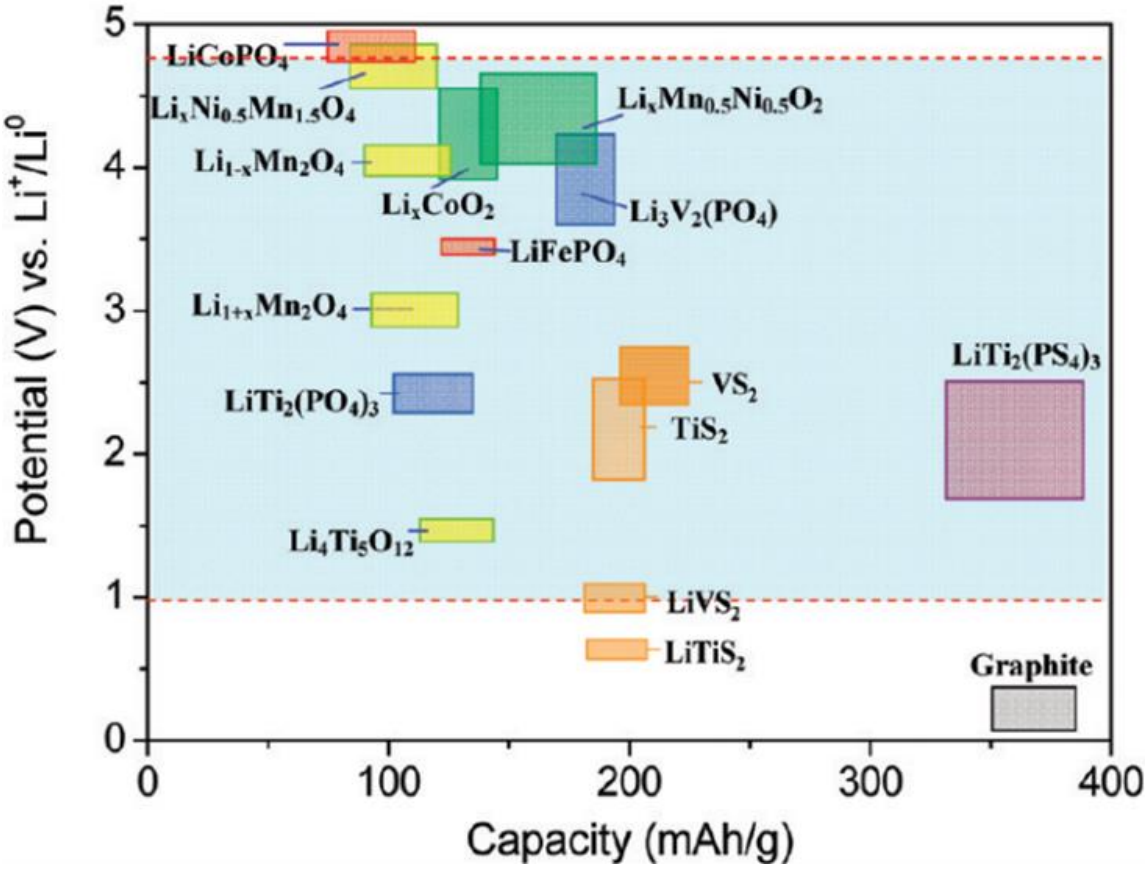

Figure 5: Potential (V) vs. Li^+/Li and reversible capacity (mAh g^{-1}) of various electrode materials used in LIBs (adapted from [37]). The blue region represents the electrochemical stability window of common carbonate based electrolytes used in LIBs.

Table 1.1: Conductivity of 1M electrolytes of various solvents and salts (mS cm^{-1})[38–40]

Solvent	**$LiPF_6$**	**$LiClO_4$**	**$LiBF_4$**	**$LiAsF_6$**	**LiTFSI**
PC	5.8	5.6	3.4	5.7	5.1
DMC	3.0	3.0	1.5	-	-
EC:DMC (1:1)	10.7	8.4	4.9	11.1	9
EC:PC (1:1)	6.6	14	4.3	-	-

1.4. Graphite

The structure of graphite consists of stacked layers of sp^2 hybridised carbon, known individually as 'graphene' layers. Graphene layers are weakly held together by van der Waals interactions, allowing easy exfoliation of layers and slipping of sheets over each other, making graphite useful as a solid lubricant.[41]

The weak inter-sheet bonding in graphite also allows the intercalation of molecules and ions between graphene layers, thus forming graphite intercalation compounds (GICs). In particular, graphite displays the ability to reversibly intercalate Li at a low electrode potential of between 0.005 – 0.2 V versus Li^+/Li, via the reaction:

$$C_6 + Li^+ + e^- \leftrightarrow LiC_6 \qquad \text{Equation 1.27}$$

Using Equation 1.20 this affords a theoretical capacity of 372 mAh g^{-1}. The combination of relatively large theoretical capacity and low intercalation potential makes graphite highly suitable as a negative electrode material. For this reason, graphite remains the most commonly used negative electrode material in LIBs.

1.4.1. Crystalline structure of graphite

Figure 6**Error! Reference source not found.**(a) shows the crystalline structure of graphite in its most common form, known as hexagonal (2H) graphite, with ABA stacking order of graphene layers and corresponding to the $P6_3/mmc$ (D_{6h}^4) space group.[42] It displays interlayer spacing of 3.35 Å and in-plane C-C bond distances of ~ 1.42 Å. The hexagonal unit cell is defined by lattice parameters $a_1 = a_2 = 2.46$ Å and c = 6.71 Å. There are 4 atoms per unit cell: atoms labelled A and A' out-of-plane

neighbours at 3.35 Å distances, whilst atoms B and B' have no out-of-plane neighbours. Figure 6(b) shows the first Brillouin zone of graphite displaying the labelling of high symmetry points and reciprocal lattice vectors in reciprocal space.

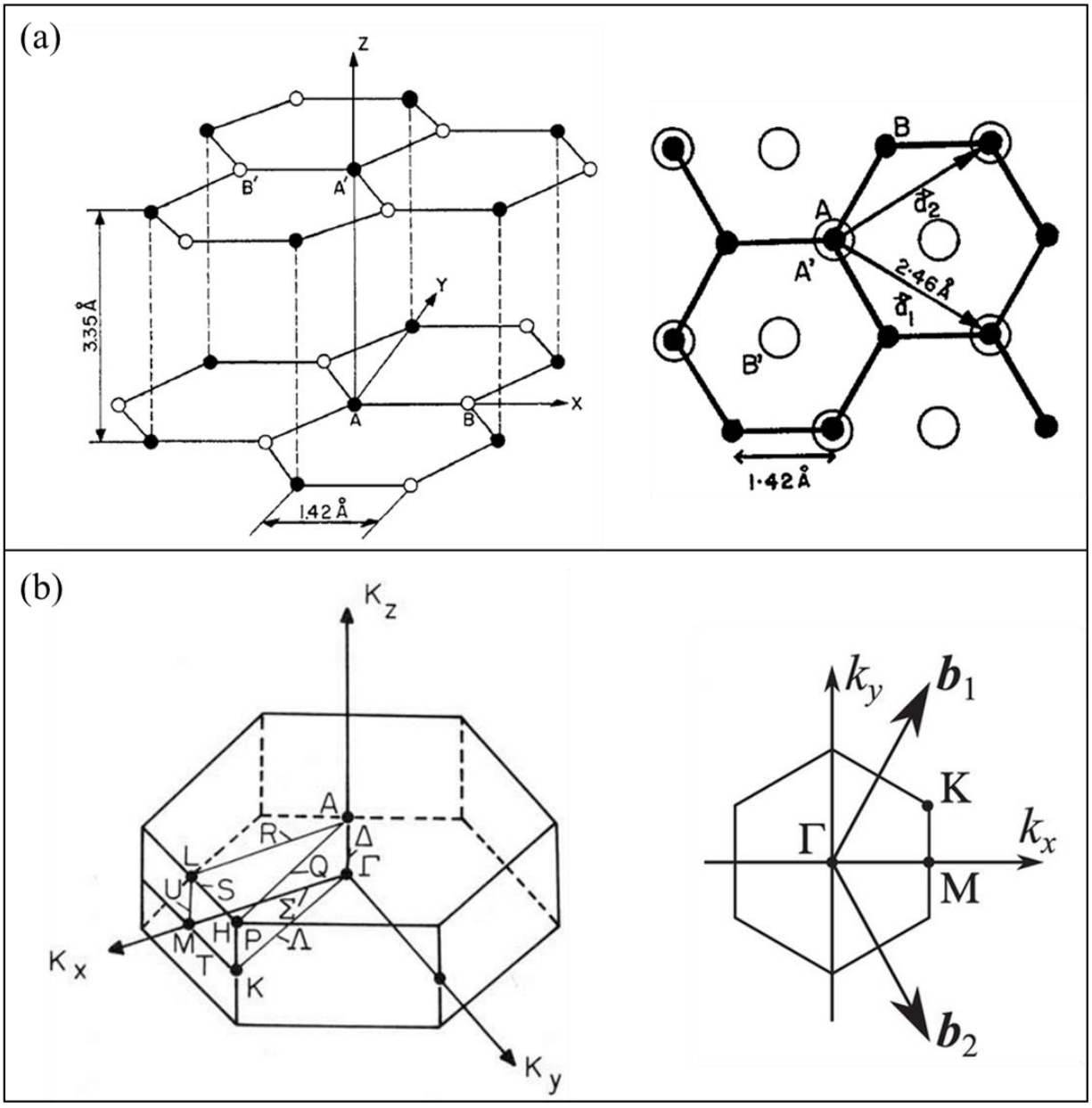

Figure 6: (a) Crystalline structure of hexagonal graphite and view perpendicular to graphene sheets. (b) First three-dimensional Brillouin zone (BZ) of graphite with conventional labelling of high symmetry points, and simplified two-dimensional BZ derived from $k_z = 0$ plane of the full BZ. Adapted from [42–44].

An alternative though less prevalent ABCABC stacking sequence of graphene layers is also possible which results in rhombohedral (3R) graphite.[42] Furthermore, stacking disorder may exist within graphite structures resulting in either a mixture of 2H and 3R structures or rotational disorder whereby there is no stacking order between layers.[45] Graphitic structures which exhibit no stacking order are known as turbostratic graphite.

1.4.2. Limitations of Graphite in LIBs

1.4.2.1. Solid electrolyte interphase formation

At potentials below ~ 1.0 V vs. Li^+/Li conventional carbonate electrolytes used in LIBs decompose at the negative electrode surface due to irreversible reduction reactions.[46] As discussed, this produces an SEI layer that is an electronic insulator (thus preventing further electrolyte decomposition), yet allowing Li^+ ion conduction. Therefore, the formation of a stable SEI layer is essential for facilitating the efficient electrochemical cycling of graphite electrodes at the potentials required for lithiation.

Furthermore, due to the low potential of lithiation (approaching 0 V vs. Li^+/Li), safety precautions must be employed on charging to avoid the plating of lithium metal and associated risks described earlier. For example, this inherently limits the charging rate that may be used due to the increased polarisation that occurs at high current densities. Furthermore, the risk of Li plating in commercial LIBs is commonly reduced by intentionally increasing the capacity of graphite electrodes compared to the positive electrode during cell assembly in a process known as cell balancing. The use of excess graphite mass within negative electrodes reduces the practical energy and power metrics for LIBs. Moreover the lithium plating phenomena may be further exacerbated

by the inherent inhomogeneity of the SEI layer which causes an inhomogeneous current distribution at the electrode surface.[33,47,48]

Additionally, although still not fully understood graphite electrodes are likely to be responsible for at least part of the capacity fading that occurs during extended cycling of LIBs.[49] Due to structural changes of materials that occur during electrochemical cycling, cracking/degradation of both particles and the SEI layer may occur, exposing fresh electrode surfaces to the electrolyte and causing continual reformation of the SEI layer. This process gradually reduces the amount of Li^+ ions available and leads to a reduction in cell capacity.[50]

1.4.2.2. Alternative negative electrode materials

The development of alternative negative electrodes is an ongoing process. The use of lithium titanate anodes offer improved rate capability and cyclability due to the zero-strain lithium insertion which occurs at potentials ~1.55 V vs Li^+/Li.[51] However, a low theoretical capacity (175 mAh g^{-1}) coupled with the higher insertion potential leads to cells with lower energy density.[51] In contrast, the use of high capacity Si anodes (3572 mAh g^{-1})[52] is prevented by large volume expansion/contraction of ~300% during lithiation/delithiation, which limits cycle life due to repeated SEI breakage and reformation.

1.5. Graphene: Discovery, Properties and Production

Graphene is defined by the International Union of Pure and Applied Chemistry (IUPAC) as a single carbon layer of the graphite structure, whose nature can be described by analogy to a polycyclic aromatic hydrocarbon of quasi infinite size. Despite prior knowledge of the relative ease of graphite exfoliation[53] and the observation of single layers of molybdenum sulphide as long ago as 1986,[54] the isolation and characterisation of crystalline, atomically-thin graphene sheets was first reported in 2004 by Novoselov et al.[55] This discovery precipitated a surge of research activity in the field of two dimensional materials,[56–58] and led to the award of the 2010 Nobel Prize in Physics. Single layer graphene was found to have remarkable physical properties including near ballistic electron transport,[59] unusual magnetic properties[60] and quasi-relativistic behaviour.[61] Furthermore, the excitement surrounding its conductivity and optical/mechanical properties have led to investigations into its suitability for nanoelectronics, thin-film transistors, (opto)electronics, energy storage and photonics applications.[58]

Furthermore, the interest in graphene has attracted interest in the properties and applications of few layer graphene (defined by Raccichini et al.[62] as between 2 to 10 stacked graphene layers). The electronic structure of 2 and 3 stacked graphene layers, known as bilayer and trilayer graphene respectively, have been shown to vary considerably from both SLG and bulk graphite.[63] Furthermore, bilayer graphene studies allow investigation of the effect of rotational stacking order on the electronic structure.[64] Similar methods have also allowed the isolation of other novel 2D materials showing exotic properties.[65]

1.5.1. Production of graphene and exfoliated graphite materials

The production of high quality graphene at commercial scales has proved non-trivial.[62] The main methods of graphene production are summarised in Figure 7 with regards to the resultant graphene quality, cost aspect, scalability, purity and yield.

Mechanical exfoliation was the method used to first isolate graphene and produces very high quality and purity graphene sheets at low cost. This method involves the separation of graphene sheets by purely mechanical forces without the aid of solvents. Typical examples involve the application of a normal force with commercial 'scotch tape' to achieve micromechanical cleavage. However, the yield is low and the technique is inherently unscalable so is likely to remain of use for fundamental studies only. Similarly, chemical vapour deposition (CVD),[66] bottom-up synthesis and synthesis on SiC produce high quality graphene, with comparable purity to the mechanical route. Although these routes are more scalable than mechanical exfoliation (especially CVD which is used in the industrial semiconductor industry to produce thin films) the low yield and high cost of graphene production by these methods would prevent the use of graphene in many applications.

In contrast, the chemical exfoliation of graphite using strong oxidizing agents[67] and sonication or stirring, followed by reduction of graphene oxide,[68] yields a large quantity of single layer flakes and due to scalability and relatively low cost has allowed numerous reduced graphene oxide (rGO) products to reach the market.[69] However, rGO often displays low purity and a large quantity of defects and oxygen containing groups, which increases the chemical reactivity and decreases the conductivity.[69–71]

Meanwhile, in liquid phase exfoliation pristine or expanded graphite is dispersed in a solvent (to reduce the strength of Van der Waals attraction between layers), then exfoliated by application of an electrochemical or mechanical driving force. Mechanical methods include sonication or shear mixing, whilst electrochemical exfoliation relies on the application of an electric field. Both methods produce high purity and quality graphene with relatively low costs, however, the physical methods generally reduce lateral flake size to sub-micron dimensions.[72,73] Alternatively, the electrochemical exfoliation of graphite represents a scalable approach with the possibility of maintaining the high conductivity of low defect concentration single and few layer graphene sheets with large lateral flake dimensions.[74–77]

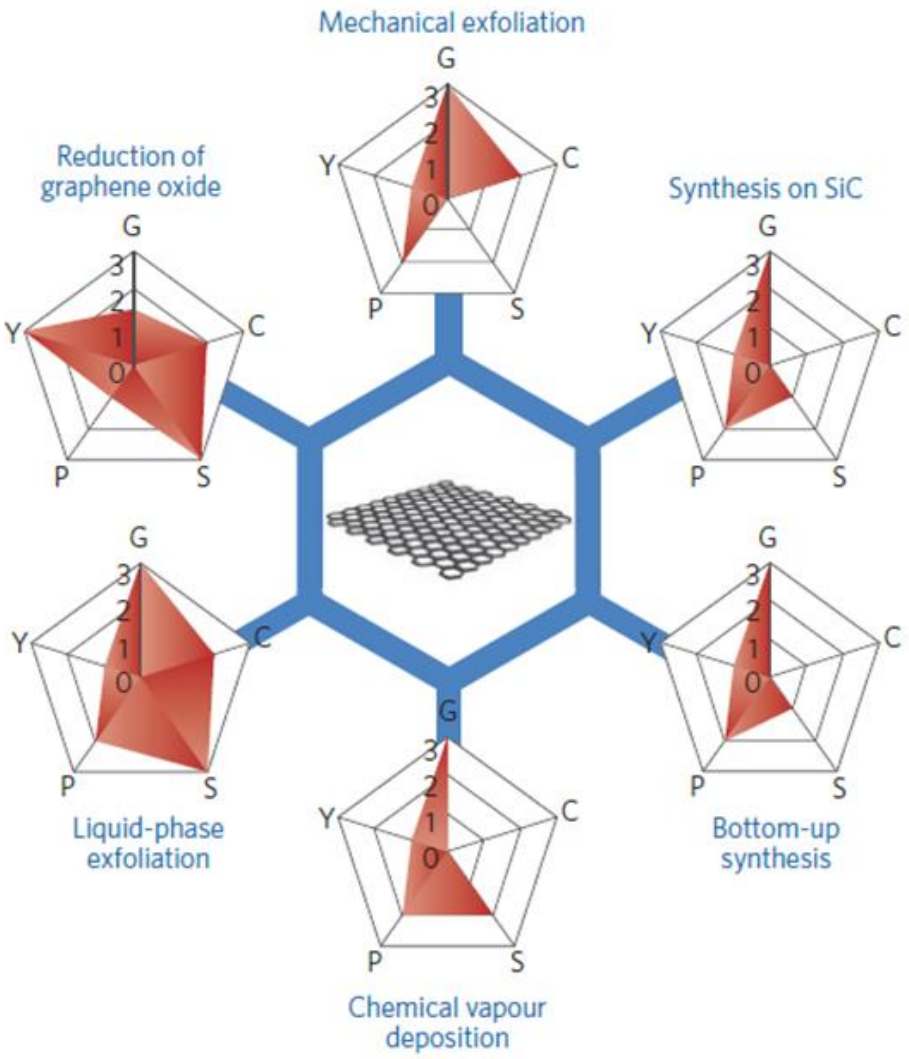

Figure 7: Schematic of the most common methods of graphene production. The overall production process of each method has been evaluated in terms of graphene quality (G), cost aspect (C), scalaility (S), purity (P) and yield (Y) where 0 = none or not applicable, 1 = low, 2 = average and 3 = high. A low value for the cost aspect relates to a high cost of production. Adapted from Raccichini et al.[62]

1.5.2. Graphenic and exfoliated graphite materials as alternative negative electrode materials

It is known that the dimensions of graphite particles have a strong effect on their electrochemical properties for lithium intercalation.[78] Therefore, following the success

in developing methods for single and few layer graphene production, many research groups determined to test these materials as negative electrode materials for LIBs. The primary drive for this research was the prediction of SLG's theoretical lithium storage capacity being double that of graphite, i.e. if two layers of Li^+ ions adsorbed to each sheet Li_2C_6 could be formed rather than LiC_6 and the capacity would increase from 372 mAh g^{-1} to 744 mAh g^{-1}. This was suggested after earlier observations of increased lithiation capacities for hard carbons which have been described as graphene sheets with a randomly oriented, 'house of cards' structure.[79–81]

A comprehensive review of published electrochemical performances of graphene materials as negative electrodes (between 2008 and early 2017) has been reported elsewhere,[82] which concluded that such materials have not lived up to their promised expectations in the LIB field, with no clear applications apparent. The vast majority of initial reports focussed on rGO materials.[83–88] Large lithiation capacities for the first cycle were observed, however this was found to be highly irreversible and correlated directly to the specific surface area and thus assigned to irreversible surface passivation reactions. Furthermore, a large proportion of inserted Li capacity occurred above 0.5 V vs. Li^+/Li as observed for hard carbons,[23] whilst a large hysteresis was observed on delithiation with most capacity between 1 - 3.5 V resembling behaviour in hydrogen rich carbons.[23,89] The final drawback was rapid capacity fading during cycling. Similar behaviour was observed in graphene synthesised by CVD and by the unzipping of carbon nanotubes.[90,91]

In 2010 an important mechanistic study was reported where the Li^+ storage mechanism of SLG and FLG were investigated.[92] The FLG electrode showed intercalation behaviour comparable to graphite. Significantly, the SLG electrode displayed radically

different behaviour, with a much lower capacity of Li^+ storage by adsorption. This was supported by several modelling studies that suggested strong coulombic repulsion lowers the binding energy for Li^+ adsorption on SLG and hence leads to lower surface coverage compared to the LiC_6 conformation obtainable in graphite.[93–95] Low reversible capacities were also observed in further experimental studies.[96,97]

However, numerous studies have shown that reversible capacities larger than 372 mAh g^{-1} are achievable, in particular by assembly of hierarchical[98–100] or 'holey' structures,[101] chemical activation[102] or edge functionalisation.[103] These increased capacities are likely explained by enhanced lithium storage in defects, cavities and nanopores and display rapid capacity fading during cycling.[81] Additionally, large reversible capacities with improved cycling stability have been achieved by the doping of graphene sheets with heteroatoms (N, B, S, etc.),[104–112] as had been suggested by density functional theory simulations.[95] However, information required for the practical comparison of these systems with state of the art electrodes are often missing, such as volumetric capacity values or electrode mass loadings. Notable exceptions are the high volumetric capacities reported by Xu et al.[100] and Ji et al.,[112] using a hierarchical, solvated network and a compressed composite-foam electrode respectively. Nevertheless, these results still showed large voltage hysteresis on delithiation making them impractical for commercial battery applications. Moreover, examination of the effect of heteroatom doping is beyond the scope of this work.

Improved performance in terms of first cycle irreversibility, capacity retention and delithiation voltage have also been observed in liquid exfoliated graphene electrodes, although with reduced reversible capacities.[113–116] This may be linked to reduced defect content as described earlier. Furthermore, studies have been conducted in full

cell configuration (vs. lithium iron phosphate) allowing direct comparison of energy and power metrics with graphite electrodes.[117] Although values are not that impressive, it should be highlighted that liquid phase processes generally produce a wide distribution of thickness and lateral dimensions of exfoliated flakes. To gain more insight into the structure-property relationship a systematic study by Sun et al.[118] used a sedimentation-based separation to correlate the lithiation behaviour with flake dimensions. This study showed conclusively that as the lateral dimensions and thickness of flakes decreases the first cycle irreversible capacity and capacity fading increases, whilst reversible capacity decreases. Furthermore, increased voltage hysteresis on delithiation was linked directly to increased lithium surface adsorption, compared to intercalation in thicker flakes.

However, despite these unattractive properties of FLG for practical electrode applications, experimental and modelling studies have suggested there may be subtle differences in Li intercalation mechanism depending on layer number.[119,120] In fact, the conventional staging process during Li intercalation of bulk graphite will be inherently limited by the number of available interlayer spaces. Furthermore, as will be discussed in Chapter 4 there may be some benefits in terms of reduced solid state diffusion limitations for thinner particles. These factors may go some way to explaining the improved low temperature performance that has been observed in various graphene or exfoliated graphite samples.[111,116] For these reasons further study of the mechanistic differences during Li intercalation into FLG and thin graphitic samples is worthwhile.

1.6. Raman spectroscopy

Raman spectroscopy is a form of vibrational spectroscopy used to investigate molecular and crystalline structures by the inelastic scattering of electromagnetic radiation. Figure 8 shows the scattering processes of light with matter. Electrons are excited by the fast-changing electric field of an incoming photon into a 'virtual' excited state. The electron relaxes back to the ground electronic state emitting a photon which is said to be scattered. Elastic scattering occurs when the photon is scattered with the same energy (and frequency) as the incoming photon:

$$E_L = E_{Sc} \qquad \text{Equation 1.28}$$

Where E_L and E_{Sc} are the energy of the incoming and scattered photon respectively. This process is commonly known as Rayleigh scattering and will produce an intense peak on a detector with an appropriate diffraction grating. Inelastic scattering may occur, with less probability, when the energy (and frequency) of the scattered light is different from that of the incoming laser. This can occur as the stokes process, whereby the electron returns to an excited vibrational state so that:

$$E_{Sc} = E_L - h\nu \qquad \text{Equation 1.29}$$

Where ν is the frequency of an excited vibrational state and h is planck's constant. The Stokes scattering process may occur if the excited electron was occupying an excited vibrational state prior to excitation by the photon. It may then relax to a lower vibrational state such that:

$$E_{Sc} = E_L + h\nu \qquad \text{Equation 1.30}$$

Raman spectra are usually collected from Stokes Raman processes due to their larger intensity compared to anti-Stokes. This is due to a low occupation of vibrational states above the ground state making Stokes processes much more likely to occur.

Furthermore, the intensity of each of these process can be increased if the excitation is selected to match a specific energy level or stationary state within the probed structure.[121] This is known as resonant Raman scattering.

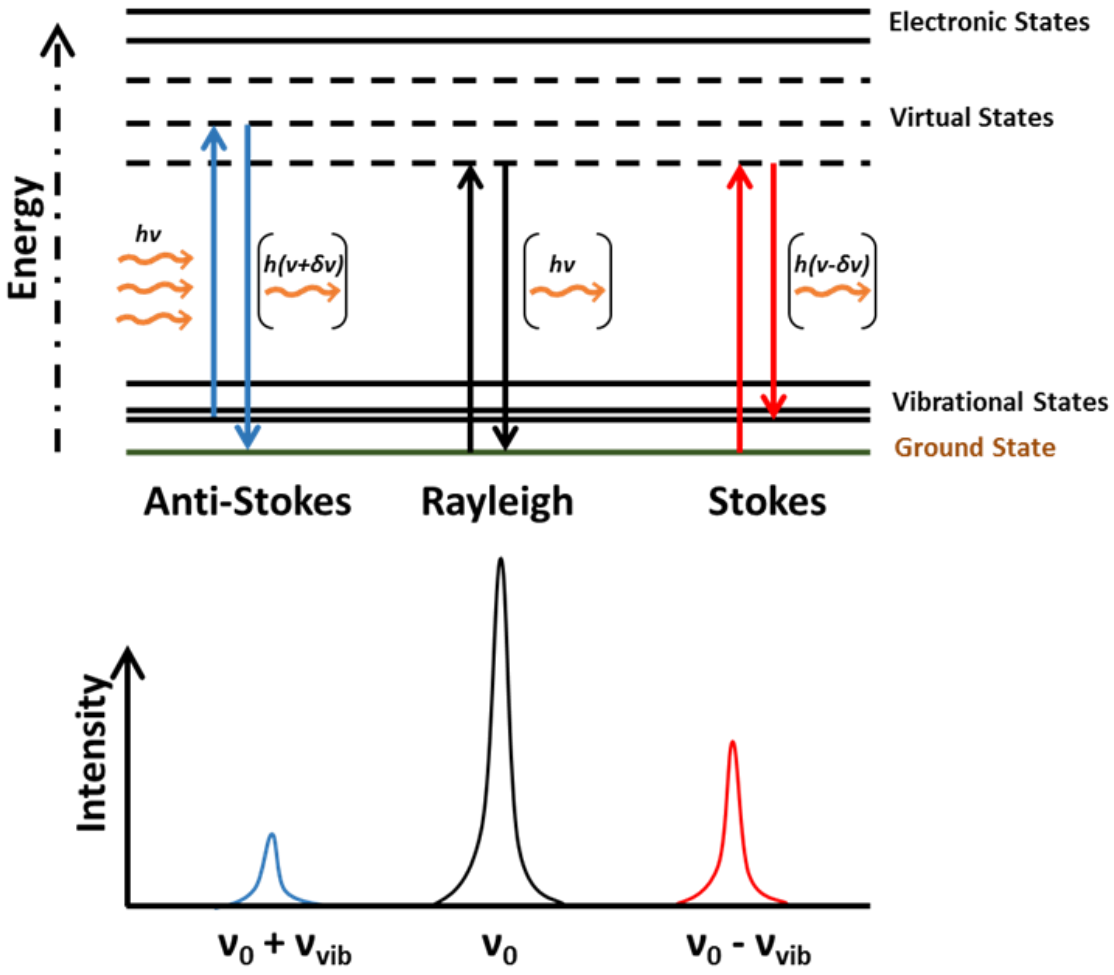

Figure 8: Scattering processes of light (inelastic anti-Stokes Raman, elastic Rayleigh and inelastic Stokes Raman) and positions on the frequency spectrum.

1.6.1. Vibrations in crystalline solids (phonons)

In a molecule with N atoms there are 3N - 6 normal modes of vibration. This arises due to the subtraction of 3 modes for translation (which have no restoring force) and 3 modes for rotation (which have a very low frequency) from the 3N degreess of freedom. In a crystalline solid with N_Ω unit cells and N atoms per unit cell there are $3N_\Omega$ N vibrational modes which due to periodicity may be described as a continuum of quantised quasiparticles, known as phonons. Phonons may be divided into 3N branches where the difference between phonons within a branch is given by the associated wavevector (q), where:

$$q = \frac{2\pi}{\lambda} \qquad \text{Equation 1.31}$$

and

$$E = \hbar\omega_q \qquad \text{Equation 1.32}$$

$\hbar$ is planck's constant divided by 2π, ω_q is the angular frequency and λ is the wavelength of the vibration which describes the change in phase from one unit cell to the next. A plot of ω_q vs. q is known as the phonon dispersion.

There are 3 acoustic branches which contain phonons associated with pure translation of the unit cell; however, acoustic phonons with q = 0 represent translation of the entire crystalline lattice and therefore have zero energy. The remaining 3N - 3 branches have non-zero energy at q = 0 and are known as optical branches. Representative vibrations of a 1D crystal with two atoms per unit cell can be observed in Figure 9. Since the lattice is periodic with lattice constant a, all possible vibrations may be described within the first Brillouin zone, i.e. $-\frac{\pi}{a} \leq \lambda \leq \frac{\pi}{a}$.

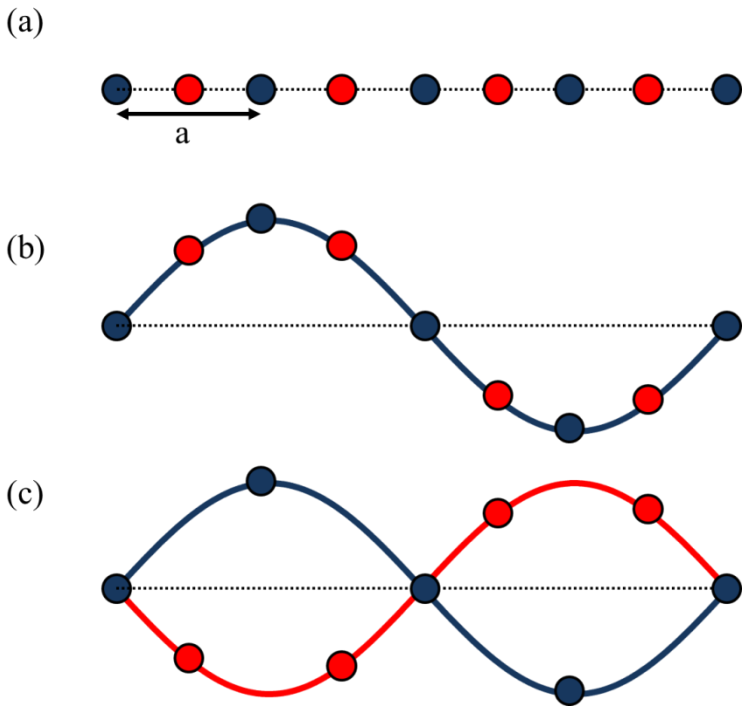

Figure 9: (a) equilibrium position of atoms in theoretical 1D crystal with 2 types of atoms. Effect on atomic positions of transverse acoustic (b) and optical (c) phonons with $\lambda = 4a$.

1.6.1.1. Selection rules for Raman active modes in crystalline solids

When scattering of electromagnetic radiation occurs there must be conservation of energy and momentum, therefore:

$\omega_L = \omega_{Sc} \pm \omega_q$ Equation 1.33

$k_L = k_{S_C} \pm q$ Equation 1.34

Where ω_L, ω_{Sc} and ω_q are the angular frequency of the incoming laser, scattered light and phonon respectively. k_L, k_{S_C} and q are the wavevectors of incoming laser, scattered light and phonon respectively.

Typical Raman experiments are conducted in the (UV to IR) 1064 – 229 nm range (corresponding to 1.2 – 5.4 eV).[63] The lattice parameter, a, is generally on the order of several angstroms (Å) so k_L, $k_{Sc} \ll \pi/a$. This leads to the the fundamental Raman selection rule for first order scattering due to conservation of momentum - only phonons near the Γ point ($q \approx 0$) are measured. However, optical modes are only Raman active if the vibration causes changes to the polarisability of the crystalline structure, which is known as the gross Raman selection rule.

1.7. Raman spectroscopy of graphitic carbons

1.7.1. Electronic band structure of graphite

The electronic band structure of graphite is shown in Figure 10, where the dashed line represents the Fermi level (E_F): the maximum energy of occupied electronic states at absolute zero temperature.

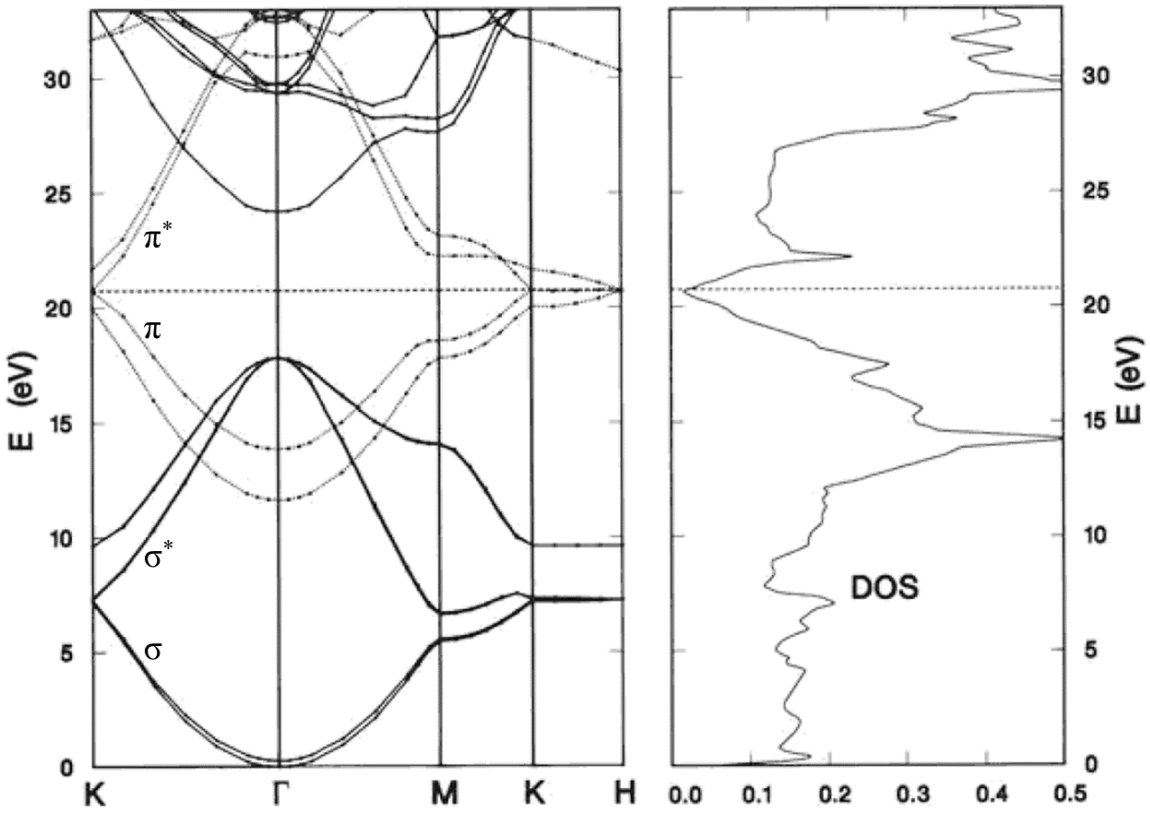

Figure 10: Calculated electronic band structure (left panel) and corresponding density of states (DOS) (right panel) of hexagonal graphite adapted from [122]. The dashed line represents the Fermi Level and zero energy is defined as the bottom of the lowest valence band. The units of DOS are states per eV per C atom.

Figure 10 shows that graphite is a semimetal due to a non zero density of states at the Fermi level, caused by a meeting of π and π^* bands at the K and H points; thus graphite

displays a large concentration of carriers at ambient temperature or with an applied voltage. Significantly, the lack of a band gap also means the Raman process in graphite may be resonant, hence Raman spectroscopy can be used to changes to the electronic structure.

1.7.2. Vibrational modes and phonon dispersion in graphite

The optical zone centre modes of graphite are given in Figure 11 and may be decomposed into:

$$\Gamma = A_{2u} + 2B_{2g} + E_{1u} + 2E_{2g} \qquad \text{Equation 1.35}$$

The A_{2u} and E_{1u} modes are IR active, whilst the E_{2g} modes are Raman active. The acoustic modes are decomposed into $\Gamma = A_{2u} + E_{1u}$. Given the anisotropic nature of graphite with strong in-plane bonding and weak Van der Waals' interactions out-of-plane, the phonon dispersion of graphite closely resembles that of graphene,[123] which is given in Figure 13. Notably, in graphite the acoustic modes of single layer graphene are split into one acoustic and one optical mode close to the Γ point (which is the source of the low frequency Raman active E_{2g1} mode). However, these modes are not investigated in the current study, thus the phonon dispersion of graphene is suitable for the discussion of Raman active optical modes in graphite.

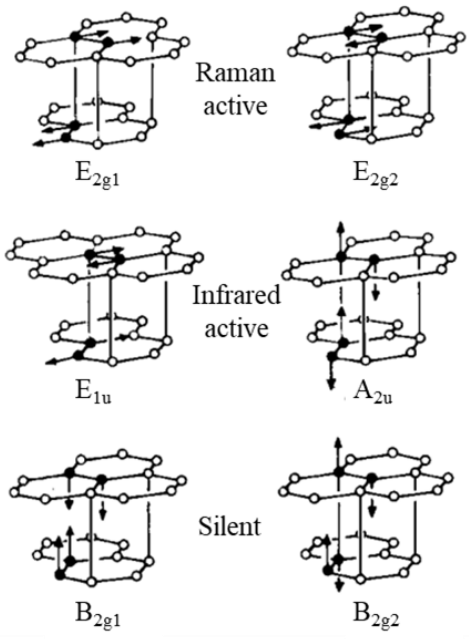

Figure 12: Γ point optical vibrational modes in hexagonal graphite showing atomic displacements and symmetries (adapted from [124]).

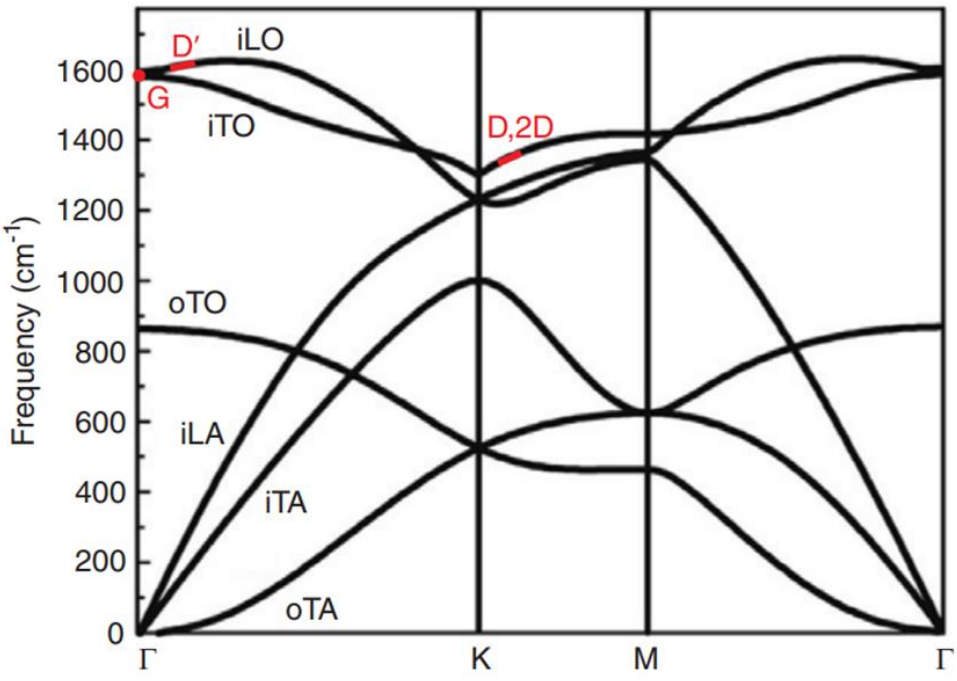

Figure 13: Calculated phonon dispersion of graphene adapted from Beams et al.[125], where the labels i and o indicate in-plane or out of plane vibrations respectively, T and L represent transverse or longitudinal vibrations, A and O indicates acoustic or optical vibrations. Positions of the Raman active phonons are indicated.

In the phonon dispersion of graphite an anomalous softening of phonons has been observed at the Γ and K points,[123] which is explained by a behaviour known as Kohn anomaly and related to the anomalous screening of particular vibrations by electronic states.[126] Kohn anomalies may only occur for wavevectors (q) where there are two electronic states k_1 and k_2 lying on the Fermi surface (states where $E = E_F$), such that:

$$k_2 = k_1 + q \qquad \text{Equation 1.36}$$

Therefore, Kohn anomalies occur at q = Γ and q = K. The Fermi level may be increased or decreased by the addition of extra charge carriers (electrons or holes), in a process commonly known as doping. Therefore doping of graphene moves the position of the Kohn anomaly and affects the frequency of atomic vibrations at the Γ and K points.[127]

1.7.3. Raman spectra of graphite

Figure 14 shows the most prominent Raman peaks in the region 1200 - 3000 cm^{-1} using a 633 nm excitation laser. At ~ 1580 cm^{-1} the G band corresponds to the high-frequency E_{2g2} phonon at the Γ point (q = 0). The process occurs via resonant (whereby the excited electronic state coincides with an unoccupied state in the electronic dispersion) and non-resonant pathways as shown in Figure 16(a).

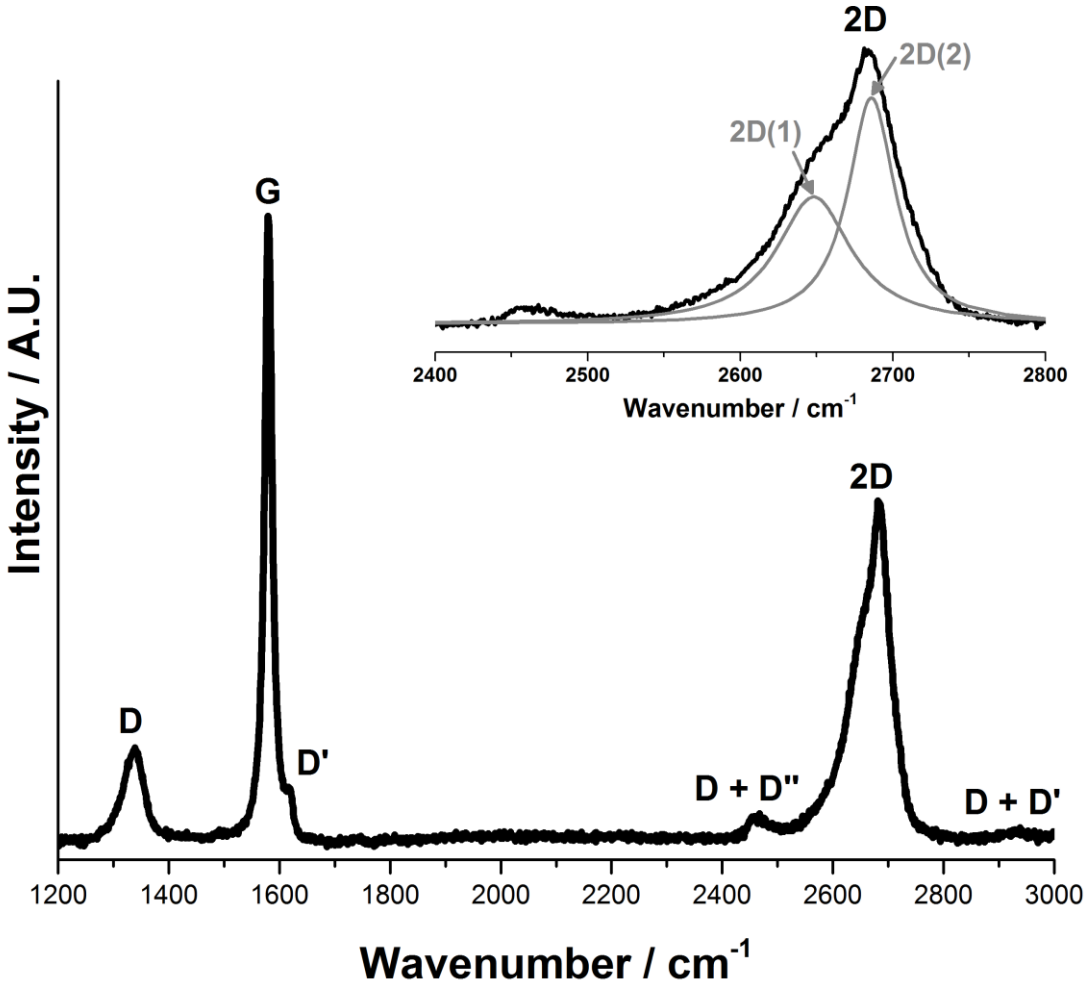

Figure 15: Raman spectrum of pristine microcrystalline graphite powder showing labelled bands. In set shows expanded 2D band with fitted 2D(1) and 2D(2) peaks.

All forms of graphitic carbons (except for low defect concentration single crystal graphite), with also produce a second feature at ~ 1330 cm^{-1} known as the D peak. The D peak is produced by the breathing modes of six atom rings as shown in Figure 16(b), arising from the in-plane transverse optical phonon close to the K point. It is the intervalley process (between K and K$^{'}$ points in reciprocal space) as shown in Figure 16(c) and must be activated by the presence of defects to conserve momentum due to the non-zero phonon wavevector. Furthermore, it is active by double resonance so is strongly dispersive with excitation energy due to the phonon dispersion around the K point.[128,129]

The 2D band ~ 2600 – 2700 cm^{-1} (sometimes referred to as the G' band within the literature) is the overtone of the D band. It is always present because momentum is conserved by two phonons with opposite wave vectors as shown in Figure 16(d). The Raman process may be either doubly or triply resonant and therefore is sensitive to the electronic structure, which varies with the number and orientation of layers. For example, single layer graphene displays a single Lorentzian peak,[130] whilst bilayer graphene may be fitted by four peaks corresponding to the four different resonant processes that may occur.[131] Meanwhile, above ~ 4-5 layers the 2D band is indistinguishable from that of bulk graphite where in general the band may be fit by two peaks as shown in Figure 15, and labelled 2D(1) and 2D(2) throughout this work.

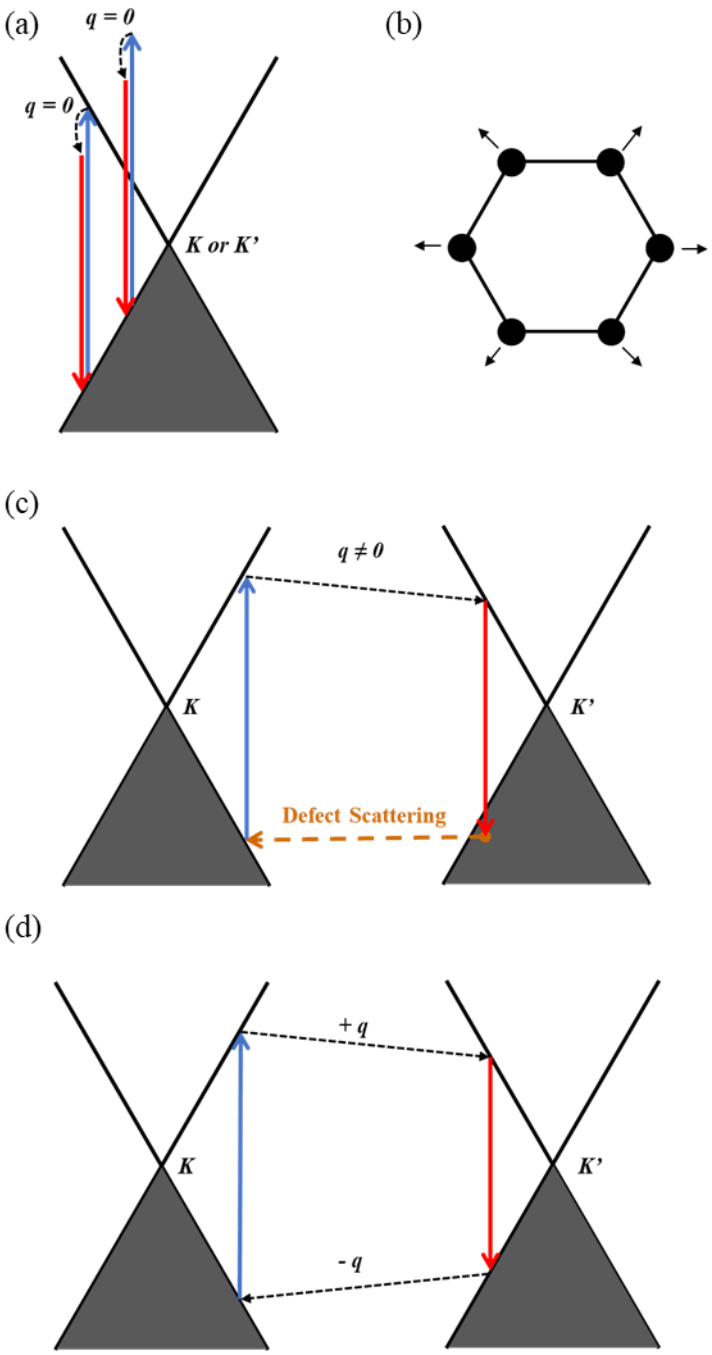

Figure 16: Raman processes responsible for (a) G band, (c) D band and (d) 2D band. Solid black lines represent the electron dispersion and occupied states are shaded. Photon absorption and emission are blue and red arrows respectively. Dashed black arrows represent creation of a phonon is and dashed orange arrows represent scattering on a defect. (b) Atomic displacements of the A_{1g} mode at the K point, responsible for the D peak.

Further bands are observable in the Raman spectrum and have been well explained elsewhere.[63] A Raman peak at ~ 42 cm^{-1}, commonly known as the C peak, is present due to the E_{2g1} phonon at the Γ point (corresponding to shear motion of rigid graphene sheets) and is also highly sensitive to layer number.[63] However, this peak is difficult to detect as its low frequency is below the filter cut-off of many spectrometers and has not been investigated in this work. Furthermore, the doubly resonant, defect activated D' peak and several overtones (D + D', D + D", 2D', etc.) are also present but at intensities which are challenging to observe due to low signal to noise ratio during *in situ* experiments.

1.8. References

(1) Hansen, J.; Johnson, D.; Lacis, A.; Lebedeff, S.; Lee, P.; Rind, D.; Russell, G. Climate Impact of Increasing Atmospheric Carbon Dioxide. *Science* **1981**, *213* (4511), 957–966.

(2) Stern, N. H. (Nicholas H.; Great Britain. Treasury. *The Economics of Climate Change : The Stern Review*; Cambridge University Press, 2007.

(3) McNutt, M. Climate Change Impacts. *Science* **2013**, *341* (6145).

(4) IPCC. *2014: Climate Change 2014: Synthesis Report. Contribution of Working Groups I, II and III to the Fifth Assessment Report of the Intergovernmental Panel on Climate Change*; Geneva, 2014.

(5) Campbell, K. M.; Gulledge, J.; Mcneill, J. R.; Podesta, J.; Ogden, P.; Fuerth, L.; Woolsey, R. J.; Lennon, A. T. J.; Smith, J.; Weitz, R.; et al. *The Age of Consequences: The Foreign Policy and National Security Implications of Global Climate Change*; 2007.

(6) Strbac, G.; Aunedi, M.; Konstantelos, I.; Moreira, R.; Teng, F.; Moreno, R.; Pudjianto, D.; Laguna, A.; Papadopoulos, P. Opportunities for Energy Storage: Assessing Whole-System Economic Benefits of Energy Storage in Future Electricity Systems. *IEEE Power Energy Mag.* **2017**, *15* (5), 32–41.

(7) Electric Power Research Institute. *Electricity Energy Storage Technology Options: A White Paper on Applications, Costs and Benefits*; Palo Alto, CA, 2010.

(8) International Energy Agency. *World Outlook Energy*; 2015.

(9) Mitchell, C. Momentum Is Increasing towards a Flexible Electricity System Based on Renewables. *Nat. Energy* **2016**, *1*, 15030.

(10) Clack, C. T. M.; Qvist, S. A.; Apt, J.; Bazilian, M.; Brandt, A. R.; Caldeira, K.; Davis, S. J.; Diakov, V.; Handschy, M. A.; Hines, P. D. H.; et al. Evaluation of a Proposal for Reliable Low-Cost Grid Power with 100% Wind, Water, and Solar. *Proc. Natl. Acad. Sci.* **2017**, *114* (26), 6722–6727.

(11) MacDonald, A. E.; Clack, C. T. M.; Alexander, A.; Dunbar, A.; Wilczak, J.; Xie, Y. Future Cost-Competitive Electricity Systems and Their Impact on US CO_2 Emissions. *Nat. Clim. Chang.* **2016**, *6* (5), 526–531.

(12) Mileva, A.; Johnston, J.; Nelson, J. H.; Kammen, D. M. Power System Balancing for Deep Decarbonization of the Electricity Sector. *Appl. Energy* **2016**, *162*, 1001–1009.

(13) Mai, T.; Sandor, D.; Wiser, R.; Schneider, T. *Renewable Electricity Futures Study: Executive Summary*; Golden, CO, 2012.

(14) King, J. *The King Review of Low-Carbon Cars Part I: The Potential for CO_2 Reduction*; 2007.

(15) Tarascon, J. M.; Armand, M. Issues and Challenges Facing Rechargeable Lithium Batteries. *Nature* **2001**, *414* (6861), 359–367.

(16) Dunn, B.; Kamath, H.; Tarascon, J.-M. Electrical Energy Storage for the Grid: A Battery of Choices. *Science* **2011**, *334* (6058).

(17) Pletcher, D. *A First Course in Electrode Processes*, 2nd ed.; RSC Publishing .

(18) Newman, J.; Thomas-Alyea, Karen, E. *Electrochemical Systems*, 3rd ed.; John Wiley & Sons, Ltd., 2004.

(19) Park, J.-K. *Principles and Applications of Lithium Secondary Batteries*; Wiley-VCH, 2012.

(20) Armand, M.; Tarascon, J.-M. Building Better Batteries. *Nature* **2008**, *451* (7179), 652–657.

(21) Bruce, P. G.; Scrosati, B.; Tarascon, J.-M. Nanomaterials for Rechargeable Lithium Batteries. *Angew. Chem. Int. Ed. Engl.* **2008**, *47* (16), 2930–2946.

(22) Bruce, P. G. Solid-State Chemistry of Lithium Power Sources. *Chem. Commun.* **1997**, No. 19, 1817.

(23) Winter, M.; Besenhard, J. O.; Spahr, M. E.; Novák, P. Insertion Electrode Materials for Rechargeable Lithium Batteries. *Adv. Mater.* **1998**, *10* (10), 725–763.

(24) Ozawa, K. Lithium-Ion Rechargeable Batteries with $LiCoO_2$ and Carbon Electrodes: The $LiCoO_2$/C System. *Solid State Ionics* **1994**, *69* (3–4), 212–221.

(25) Nagaura, T.; Tozawa, K. Lithium Ion Rechargeable Battery. *Prog. Batter. Sol. Cells* **1990**, *9*, 209–217.

(26) Goodenough, J. B.; Mizuchima, K. Electrochemical Cell with New Fast Ion Conductors. US4302518A, 1981.

(27) Yazami, R.; Touzain, P. A Reversible Graphite-Lithium Negative Electrode for Electrochemical Generators. *J. Power Sources* **1983**, *9* (3), 365–371.

(28) Whittingham, M. Electrical Energy Storage and Intercalataion Chemistry. *Science* **1976**, *192* (March), 1126.

(29) Gratz, E.; Sa, Q.; Apelian, D.; Wang, Y. A Closed Loop Process for Recycling Spent Lithium Ion Batteries. *J. Power Sources* **2014**, *262* (0), 255–262.

(30) Nykvist, B.; Nilsson, M. Rapidly Falling Costs of Battery Packs for Electric Vehicles. *Nat. Clim. Chang.* **2015**, *5*, 329–332.

(31) Hagen, M.; Hanselmann, D.; Ahlbrecht, K.; Maça, R.; Gerber, D.; Tübke, J. Lithium-Sulfur Cells: The Gap between the State-of-the-Art and the Requirements for High Energy Battery Cells. *Adv. Energy Mater.* **2015**, *5* (16), 1401986.

(32) Yabuuchi, N.; Ohzuku, T. Novel Lithium Insertion Material of $LiCo_{1/3}Ni_{1/3}Mn_{1/3}O_2$ for Advanced Lithium-Ion Batteries. *J. Power Sources* **2003**, *119–121*, 171–174.

(33) Aurbach, D. Review of Selected Electrode–solution Interactions Which Determine the Performance of Li and Li Ion Batteries. *J. Power Sources* **2000**, *89* (2), 206–218.

(34) Li, Q.; Chen, J.; Fan, L.; Kong, X.; Lu, Y. Progress in Electrolytes for Rechargeable Li-Based Batteries and beyond. *Green Energy Environ.* **2016**, *1* (1), 18–42.

(35) Stephan, A. M. Review on Gel Polymer Electrolytes for Lithium Batteries. *Eur. Polym. J.* **2006**, *42* (1), 21–42.

(36) Goodenough, J. B.; Singh, P. Review—Solid Electrolytes in Rechargeable Electrochemical Cells. *J. Electrochem. Soc.* **2015**, *162* (14), A2387–A2392.

(37) Goodenough, J. B.; Kim, Y. Challenges for Rechargeable Li Batteries. *Chem. Mater.* **2010**, *22* (3), 587–603.

(38) Gabano, J. P. *Lithium Batteries*; Academic Press: London, 1983.

(39) Xu, K. Nonaqueous Liquid Electrolytes for Lithium-Based Rechargeable Batteries. **2004**.

(40) Linden, D.; Reddy, T. B. *Handbook of Batteries*; McGraw-Hill: New York, 2002.

(41) Feneberger, K. Graphite: Solid Lubricant. *Ind. Lubr. Tribol.* **1973**, *25* (5), 176–178.

(42) Chung, D. D. L. Review: Graphite. *J. Mater. Sci.* **2002**, *37*, 1475–1489.

(43) Pisanty, A. The Electronic Structure of Graphite: A Chemist's Introduction to Band Theory. *J. Chem. Educ.* **1991**, *68* (10), 804–808.

(44) Yakovlev, V. S.; Stockman, M. I.; Krausz, F.; Baum, P. Atomic-Scale Diffractive Imaging of Sub-Cycle Electron Dynamics in Condensed Matter. **2015**, *5*, 14581.

(45) Shi, H. Structure and Lithium Intercalation Properties of Synthetic and Natural Graphite. *J. Electrochem. Soc.* **1996**, *143* (11), 3466.

(46) Peled, E. The Electrochemical Behavior of Alkali and Alkaline Earth Metals in Nonaqueous Battery Systems—The Solid Electrolyte Interphase Model. *J. Electrochem. Soc.* **1979**, *126* (12), 2047–2051.

(47) Aurbach, D.; Talyosef, Y.; Markovsky, B.; Markevich, E.; Zinigrad, E.; Asraf, L.; Gnanaraj, J. S.; Kim, H.-J. Design of Electrolyte Solutions for Li and Li-Ion Batteries: A Review. *Electrochim. Acta* **2004**, *50* (2–3), 247–254.

(48) Aurbach, D.; Zinigrad, E.; Cohen, Y.; Teller, H. A Short Review of Failure Mechanisms of Lithium Metal and Lithiated Graphite Anodes in Liquid Electrolyte Solutions. **2002**, *148*, 405–416.

(49) Palacín, M. R.; de Guibert, A. Why Do Batteries Fail? *Science* **2016**, *351* (6273).

(50) Agubra, V.; Fergus, J. Lithium Ion Battery Anode Aging Mechanisms. *Materials (Basel).* **2013**, *6* (4), 1310–1325.

(51) Ohzuku, T.; Ueda, A.; Yamamoto, N. Zero-Strain Insertion Material of Li $[Li_{1/3}Ti_{5/3}]O_4$ for Rechargeable Lithium Cells. *J. Electrochem. Soc.* **1995**, *142* (5), 1431–1435.

(52) Key, B.; Morcrette, M.; Tarascon, J.-M.; Grey, C. P. Pair Distribution Function Analysis and Solid State NMR Studies of Silicon Electrodes for Lithium Ion Batteries: Understanding the (De)lithiation Mechanisms. *J. Am. Chem. Soc.* **2011**, *133* (3), 503–512.

(53) D. D. L. Chung. Review: Exfoliation of Graphite. *J. Mater. Sci.* **1987**, *22*.

(54) Joensen, P.; Frindt, R. F.; Morrison, S. R. Single Layer MoS2. *Mater. Res. Bull.* **1986**, *21*, 457–461.

(55) Novoselov, K. S. Electric Field Effect in Atomically Thin Carbon Films. *Science* **2004**, *306* (5696), 666–669.

(56) Charlier, J.; Zhu, P. C.; Eklund, J.; Ferrari, A. C. Electron and Phonon Properties of Graphene : Their Relationship with Carbon Nanotubes. *709* (2008), 673–709.

(57) Novoselov, K. S.; Geim, a K.; Morozov, S. V; Jiang, D.; Katsnelson, M. I.; Grigorieva, I. V; Dubonos, S. V; Firsov, a a. Two-Dimensional Gas of Massless Dirac Fermions in Graphene. *Nature* **2005**, *438* (7065), 197–200.

(58) Geim, A. K.; Novoselov, K. S. The Rise of Graphene. *Nat. Mater.* **2007**, *6* (3), 183–191.

(59) Berger, C.; Song, Z.; Li, X.; Wu, X.; Brown, N.; Naud, C.; Mayou, D.; Li, T.; Hass, J.; Marchenkov, A. N.; et al. Electronic Confinement and Coherence in Patterned Epitaxial Graphene. *Science* **2006**, *312* (5777), 1191–1196.

(60) Guo, Y.; Zhang, F.; Yang, J.; Wang, F.; NuLi, Y.; Hirano, S. Boron-Based Electrolyte Solutions with Wide Electrochemical Windows for Rechargeable Magnesium Batteries. *Energy Environ. Sci.* **2012**, *5* (10), 9100.

(61) Novoselov, K. S.; Jiang, Z.; Zhang, Y.; Morozov, S. V.; Stormer, H. L.; Zeitler, U.; Maan, J. C.; Boebinger, G. S.; Kim, P.; Geim, A. K. Room-Temperature Quantum Hall Effect in Graphene. *Science* **2007**, *315* (5817), 1379–1379.

(62) Raccichini, R.; Varzi, A.; Passerini, S.; Scrosati, B. The Role of Graphene for Electrochemical Energy Storage. *Nat. Publ. Gr.* **2014**, *14* (December 2014), 271–279.

(63) Ferrari, A. C.; Basko, D. M. Raman Spectroscopy as a Versatile Tool for Studying the Properties of Graphene. *Nat. Nanotechnol.* **2013**, *8* (4), 235–246.

(64) Dai, S.; Xiang, Y.; Srolovitz, D. J. Twisted Bilayer Graphene: Moiré with a Twist. *Nano Lett.* **2016**, *16* (9), 5923–5927.

(65) Coleman, J. N.; Lotya, M.; O'Neill, A.; Bergin, S. D.; King, P. J.; Khan, U.; Young, K.; Gaucher, A.; De, S.; Smith, R. J.; et al. Two-Dimensional Nanosheets Produced by Liquid Exfoliation of Layered Materials. *Science* **2011**, *331* (6017), 568–571.

(66) Gao, L.; Ni, G.-X.; Liu, Y.; Liu, B.; Castro Neto, A. H.; Loh, K. P. Face-to-Face Transfer of Wafer-Scale Graphene Films. *Nature* **2014**, *505* (7482), 190–194.

(67) Hummers, W. S.; Offeman, R. E. Preparation of Graphitic Oxide. *J. Am. Chem. Soc.* **1958**, *80* (6), 1339–1339.

(68) Li, D.; Müller, M. B.; Gilje, S.; Kaner, R. B.; Wallace, G. G. Processable Aqueous Dispersions of Graphene Nanosheets. *Nat. Nanotechnol.* **2008**, *3* (2), 101–105.

(69) Park, S.; Ruoff, R. S. Chemical Methods for the Production of Graphenes. *Nat. Nanotechnol.* **2009**, *4* (4), 217–224.

(70) Stankovich, S.; Dikin, D.; Piner, R. D.; Kohlhaas, K.; Kleinhammes, A.; Jia, Y.; Wu, Y.; Nguyen, S. T.; Ruoff, R. S. Synthesis of Graphene-Based Nanosheets via Chemical

Reduction of Exfoliated Graphite Oxide. *Carbon* **2007**, *45*, 1558–1565.

(71) Dreyer, D. R.; Park, S.; Bielawski, C. W.; Ruoff, R. S. The Chemistry of Graphene Oxide. *Chem. Soc. Rev.* **2010**, *39* (1), 228–240.

(72) Paton, K. R.; Varrla, E.; Backes, C.; Smith, R. J.; Khan, U.; O'Neill, A.; Boland, C.; Lotya, M.; Istrate, O. M.; King, P.; et al. Scalable Production of Large Quantities of Defect-Free Few-Layer Graphene by Shear Exfoliation in Liquids. *Nat. Mater.* **2014**, *13* (June), 624–630.

(73) Hernandez, Y.; Nicolosi, V.; Lotya, M.; Blighe, F. M.; Sun, Z.; De, S.; McGovern, I. T.; Holland, B.; Byrne, M.; Gun'Ko, Y. K.; et al. High-Yield Production of Graphene by Liquid-Phase Exfoliation of Graphite. *Nat. Nanotechnol.* **2008**, *3*, 563–568.

(74) Zhou, M.; Tang, J.; Cheng, Q.; Xu, G.; Cui, P.; Qin, L. Few-Layer Graphene Obtained by Electrochemical Exfoliation of Graphite Cathode. *Chem. Phys. Lett.* **2013**, *572*, 61–65.

(75) Abdelkader, A. M.; Cooper, A. J.; Dryfe, R. A. W.; Kinloch, I. A. How to Get between the Sheets: A Review of Recent Works on the Electrochemical Exfoliation of Graphene Materials from Bulk Graphite. *Nanoscale* **2015**, 6944–6956.

(76) Parvez, K.; Wu, Z. S.; Li, R.; Liu, X.; Graf, R.; Feng, X.; Müllen, K. Exfoliation of Graphite into Graphene in Aqueous Solutions of Inorganic Salts. *J. Am. Chem. Soc.* **2014**, *136*, 6083–6091.

(77) Cooper, A. J.; Wilson, N. R.; Kinloch, I. A.; Dryfe, R. A. W. Single Stage Electrochemical Exfoliation Method for the Production of Few-Layer Graphene via Intercalation of Tetraalkylammonium Cations. *Carbon* **2014**, *66*, 340–350.

(78) Buqa, H.; Goers, D.; Holzapfel, M.; Spahr, M. E.; Novák, P. High Rate Capability of Graphite Negative Electrodes for Lithium-Ion Batteries. *J. Electrochem. Soc.* **2005**, *152* (2), A474–A481.

(79) Sato, K.; Noguchi, M.; Demachi, A.; Oki, N.; Endo, M. A Mechanism of Lithium Storage in Disordered Carbons. *Science* **1994**, *264* (5158), 556–558.

(80) Dahn, J. R.; Zheng, T.; Liu, Y.; Xue, J. S. Mechanisms for Lithium Insertion in Carbonaceous Materials. *Science* **1995**, *270*, 590–593.

(81) Kaskhedikar, N. A.; Maier, J. Lithium Storage in Carbon Nanostructures. *Adv. Mater.* **2009**, *21* (25–26), 2664–2680.

(82) Raccichini, R.; Varzi, A.; Wei, D.; Passerini, S. Critical Insight into the Relentless Progression Toward Graphene and Graphene-Containing Materials for Lithium-Ion Battery Anodes. *Adv. Mater.* **2017**, *29* (11), 1603421.

(83) Yoo, E.; Kim, J.; Hosono, E.; Zhou, H.; Kudo, T.; Honma, I. Large Reversible Li Storage of Graphene Nanosheet Families for Use in Rechargeable Lithium Ion Batteries. *Nano Lett.* **2008**, *8* (8), 2277–2282.

(84) Wang, G.; Shen, X.; Yao, J.; Park, J. Graphene Nanosheets for Enhanced Lithium Storage in Lithium Ion Batteries. *Carbon* **2009**, *47* (8), 2049–2053.

(85) Pan, D.; Wang, S.; Zhao, B.; Wu, M.; Zhang, H.; Wang, Y.; Jiao, Z. Li Storage

Properties of Disordered Graphene Nanosheets. *Chem. Mater.* **2009**, *21* (14), 3136–3142.

(86) Wang, C.; Li, D.; Too, C. O.; Wallace, G. G. Electrochemical Properties of Graphene Paper Electrodes Used in Lithium Batteries. *Chem. Mater.* **2009**, *21* (13), 2604–2606.

(87) Guo, P.; Song, H.; Chen, X. Electrochemical Performance of Graphene Nanosheets as Anode Material for Lithium-Ion Batteries. *Electrochem. commun.* **2009**, *11* (6), 1320–1324.

(88) Abouimrane, A.; Compton, O. C.; Amine, K.; Nguyen, S. T. Non-Annealed Graphene Paper as a Binder-Free Anode for Lithium-Ion Batteries. *J. Phys. Chem. C* **2010**, *114* (29), 12800–12804.

(89) Liu, Y.; Xue, J. S.; Zheng, T.; Dahn, J. R. Mechanism of Lithium Insertion in Hard Carbons Prepared by Pyrolysis of Epoxy Resins. *Carbon* **1996**, *34* (2), 193–200.

(90) Reddy, A. L. M.; Srivastava, A.; Gowda, S. R.; Gullapalli, H.; Dubey, M.; Ajayan, P. M. Synthesis Of Nitrogen-Doped Graphene Films For Lithium Battery Application. *ACS Nano* **2010**, *4* (11), 6337–6342.

(91) Bhardwaj, T.; Antic, A.; Pavan, B.; Barone, V.; Fahlman, B. D. Enhanced Electrochemical Lithium Storage by Graphene Nanoribbons. *J. Am. Chem. Soc.* **2010**, *132* (36), 12556–12558.

(92) Pollak, E.; Geng, B.; Jeon, K.-J.; Lucas, I. T.; Richardson, T. J.; Wang, F.; Kostecki, R. The Interaction of Li with Single-Layer and Few-Layer Graphene. *Nano Lett.* **2010**, *10* (9), 3386–3388.

(93) Ferre-Vilaplana, A. Storage of Hydrogen Adsorbed on Alkali Metal Doped Single-Layer All-Carbon Materials. *J. Phys. Chem. C* **2008**, *112* (10), 3998–4004.

(94) Ataca, C.; Akturk, E.; Ciraci, S.; Ustunel, H. High-Capacity Hydrogen Storage by Metallized Graphene. **2009**.

(95) Liu, Y.; Artyukhov, V. I.; Liu, M.; Harutyunyan, A. R.; Yakobson, B. I. Feasibility of Lithium Storage on Graphene and Its Derivatives. *J. Phys. Chem. Lett.* **2013**, *4* (10), 1737–1742.

(96) Mukherjee, R.; Thomas, A. V.; Krishnamurthy, A.; Koratkar, N. Photothermally Reduced Graphene as High-Power Anodes for Lithium-Ion Batteries. *ACS Nano* **2012**, *6* (9), 7867–7878.

(97) Liang, M.; Zhi, L. Graphene-Based Electrode Materials for Rechargeable Lithium Batteries. *J. Mater. Chem.* **2009**, *19* (33), 5871.

(98) Yin, S.; Zhang, Y.; Kong, J.; Zou, C.; Li, C. M.; Lu, X.; Ma, J.; Boey, F. Y. C.; Chen, X. Assembly of Graphene Sheets into Hierarchical Structures for High-Performance Energy Storage. *ACS Nano* **2011**, *5* (5), 3831–3838.

(99) Hu, C.; Lv, L.; Xue, J.; Ye, M.; Wang, L.; Qu, L. Branched Graphene Nanocapsules for Anode Material of Lithium-Ion Batteries. *Chem. Mater.* **2015**, *27* (15), 5253–5260.

(100) Xu, Y.; Lin, Z.; Zhong, X.; Papandrea, B.; Huang, Y.; Duan, X. Solvated Graphene Frameworks as High-Performance Anodes for Lithium-Ion Batteries. *Angew. Chemie*

Int. Ed. **2015**, *54* (18), 5345–5350.

(101) Zhao, X.; Hayner, C. M.; Kung, M. C.; Kung, H. H. Flexible Holey Graphene Paper Electrodes with Enhanced Rate Capability for Energy Storage Applications. *ACS Nano* **2011**, *5* (11), 8739–8749.

(102) Compton, O. C.; Jain, B.; Dikin, D. A.; Abouimrane, A.; Amine, K.; Nguyen, S. T. Chemically Active Reduced Graphene Oxide with Tunable C/O Ratios. *ACS Nano* **2011**, *5* (6), 4380–4391.

(103) Xu, J.; Jeon, I.-Y.; Seo, J.-M.; Dou, S.; Dai, L.; Baek, J.-B. Edge-Selectively Halogenated Graphene Nanoplatelets (XGnPs, X = Cl, Br, or I) Prepared by Ball-Milling and Used as Anode Materials for Lithium-Ion Batteries. *Adv. Mater.* **2014**, *26* (43), 7317–7323.

(104) Wu, Z.-S.; Ren, W.; Xu, L.; Li, F.; Cheng, H.-M. Doped Graphene Sheets as Anode Materials with Superhigh Rate and Large Capacity for Lithium Ion Batteries. *ACS Nano* **2011**, *5* (7), 5463–5471.

(105) Wang, H.; Zhang, C.; Liu, Z.; Wang, L.; Han, P.; Xu, H.; Zhang, K.; Dong, S.; Yao, J.; Cui, G.; et al. Nitrogen-Doped Graphene Nanosheets with Excellent Lithium Storage Properties. *J. Mater. Chem.* **2011**, *21* (14), 5430.

(106) Wang, H.; Wang, Y.; Li, Y.; Wan, Y.; Duan, Q. Exceptional Electrochemical Performance of Nitrogen-Doped Porous Carbon for Lithium Storage. *Carbon* **2015**, *82*, 116–123.

(107) Liu, X.; Wu, Y.; Yang, Z.; Pan, F.; Zhong, X.; Wang, J.; Gu, L.; Yu, Y. Nitrogen-Doped 3D Macroporous Graphene Frameworks as Anode for High Performance Lithium-Ion Batteries. *J. Power Sources* **2015**, *293*, 799–805.

(108) Zhou, Y.; Zeng, Y.; Xu, D.; Li, P.; Wang, H.; Li, X.; Li, Y.; Wang, Y. Nitrogen and Sulfur Dual-Doped Graphene Sheets as Anode Materials with Superior Cycling Stability for Lithium-Ion Batteries. *Electrochim. Acta* **2015**, *184*, 24–31.

(109) Huang, S.; Li, Y.; Feng, Y.; An, H.; Long, P.; Qin, C.; Feng, W.; Wang, G.; Wei, F.; Lee, J.; et al. Nitrogen and Fluorine Co-Doped Graphene as a High-Performance Anode Material for Lithium-Ion Batteries. *J. Mater. Chem. A* **2015**, *3* (46), 23095–23105.

(110) Sun, J.; Wang, L.; Song, R.; Yang, S.; Liu, Y. T.; Qu, L.; Qu, L.; Wang, G. L.; Wei, F.; Karnik, R. Nitrogen-Doped Holey Graphene Foams for High-Performance Lithium Storage. *RSC Adv.* **2015**, *5* (111), 91114–91119.

(111) Wang, Z.-L.; Xu, D.; Wang, H.-G.; Wu, Z.; Zhang, X.-B. *In Situ* Fabrication of Porous Graphene Electrodes for High-Performance Energy Storage. *ACS Nano* **2013**, *7* (3), 2422–2430.

(112) Ji, J.; Liu, J.; Lai, L.; Zhao, X.; Zhen, Y.; Lin, J.; Zhu, Y.; Ji, H.; Zhang, L. L.; Ruoff, R. S. In Situ Activation of Nitrogen-Doped Graphene Anchored on Graphite Foam for a High-Capacity Anode. *ACS Nano* **2015**, *9* (8), 8609–8616.

(113) Shanmugharaj, A. M.; Choi, W. S.; Lee, C. W.; Ryu, S. H. Electrochemical Performances of Graphene Nanosheets Prepared through Microwave Radiation. *J. Power Sources* **2011**, *196* (23), 10249–10253.

(114) Jang, J.-H.; Rangappa, D.; Kwon, Y.-U.; Honma, I.; Matthews, M. J.; Brown, S. D. M.; Dresselhaus, M. S.; Choi, J. Y.; Lee, Y. H.; Ferrari, A. C.; et al. Direct Preparation of 1-PSA Modified Graphenenanosheets by Supercritical Fluidic Exfoliation and Its Electrochemical Properties. *J. Mater. Chem.* **2011**, *21* (10), 3462–3466.

(115) Sun, H.; Del Rio Castillo, A. E.; Monaco, S.; Capasso, A.; Ansaldo, A.; Prato, M.; Dinh, D. A.; Pellegrini, V.; Scrosati, B.; Manna, L.; et al. Binder-Free Graphene as an Advanced Anode for Lithium Batteries. *J. Mater. Chem. A* **2016**, *4* (18), 6886–6895.

(116) Raccichini, R.; Varzi, A.; Chakravadhanula, V. S. K.; Kübel, C.; Balducci, A.; Passerini, S. Enhanced Low-Temperature Lithium Storage Performance of Multilayer Graphene Made through an Improved Ionic Liquid-Assisted Synthesis. *J. Power Sources* **2015**, *281*, 318–325.

(117) Hassoun, J.; Bonaccorso, F.; Agostini, M.; Angelucci, M.; Betti, M. G.; Cingolani, R.; Gemmi, M.; Mariani, C.; Panero, S.; Pellegrini, V.; et al. An Advanced Lithium-Ion Battery Based on a Graphene Anode and a Lithium Iron Phosphate Cathode. *Nano Lett.* **2014**.

(118) Sun, H.; Varzi, A.; Pellegrini, V.; Dinh, D. A.; Raccichini, R.; Del Rio-Castillo, A. E.; Prato, M.; Colombo, M.; Cingolani, R.; Scrosati, B.; et al. How Much Does Size Really Matter? Exploring the Limits of Graphene as Li Ion Battery Anode Material. *Solid State Commun.* **2017**, *251*, 88–93.

(119) Lee, E.; Persson, K. A. Li Absorption and Intercalation in Single Layer Graphene and Few Layer Graphene by First Principles. *Nano Lett.* **2012**, *12* (9), 4624–4628.

(120) Hui, J.; Burgess, M.; Zhang, J.; Rodriguez-Lopez, J. Layer Number Dependence of Li^+ Intercalation on Few-Layer Graphene and Electrochemical Imaging of Its Solid-Electrolyte Interphase Evolution. *ACS Nano* **2016**, *10* (4), 4248–4257.

(121) Yu, P. Y.; Cardona, M. *Fundamentals of Semiconductors*; Graduate Texts in Physics; Springer Berlin Heidelberg: Berlin, Heidelberg, 2010.

(122) Holzwarth, N. A. W. Electronic Band Structure of Graphite Intercalation Compounds. In *Graphite Intercalation Compounds II : Transport and Electronic Properties*; Zabel, H., Solin, S. A., Eds.; Springer Berlin Heidelberg, 1992; pp 7–48.

(123) Mohr, M.; Maultzsch, J.; Dobardžić, E.; Reich, S.; Milošević, I.; Damnjanović, M.; Bosak, A.; Krisch, M.; Thomsen, C. Phonon Dispersion of Graphite by Inelastic X-Ray Scattering. *Phys. Rev. B - Condens. Matter Mater. Phys.* **2007**, *76* (3).

(124) Dresselhaus, M. .; Dresselhaus, G.; Eklund, P. .; Chung, D. D. . Lattice Vibrations in Graphite and Intercalation Compounds of Graphite. *Mater. Sci. Eng.* **1977**, *31*, 141–152.

(125) Beams, R.; Gustavo Cançado, L.; Novotny, L. Raman Characterization of Defects and Dopants in Graphene. *J. Phys. Condens. Matter* **2015**, *27* (8), 83002.

(126) Kohn, W. Image of the Fermi Surface in the Vibration Spectrum of a Metal. *Phys. Rev. Lett.* **1959**, *2* (9), 393–394.

(127) Piscanec, S.; Lazzeri, M.; Mauri, F.; Ferrari, A. C.; Robertson, J. Kohn Anomalies and Electron-Phonon Interactions in Graphite. *Phys. Rev. Lett.* **2004**, *93*, 185503.

(128) Thomsen, C.; Reich, S. Double Resonant Raman Scattering in Graphite. *Phys. Rev. Lett.* **2000**, *85* (24), 5214–5217.

(129) Vidano, R. P.; Fischbach, D. B.; Willis, L. J.; Loehr, T. M. Observation of Raman Band Shifting with Excitation Wavelength for Carbons and Graphites. *Solid State Commun.* **1981**, *39* (2), 341–344.

(130) Ferrari, A. C.; Meyer, J. C.; Scardaci, V.; Casiraghi, C.; Lazzeri, M.; Mauri, F.; Piscanec, S.; Jiang, D.; Novoselov, K. S.; Roth, S.; et al. Raman Spectrum of Graphene and Graphene Layers. *Phys. Rev. Lett.* **2006**, *97* (18), 187401.

(131) Cançado, L.; Reina, a.; Kong, J.; Dresselhaus, M. Geometrical Approach for the Study of G′ Band in the Raman Spectrum of Monolayer Graphene, Bilayer Graphene, and Bulk Graphite. *Phys. Rev. B* **2008**, *77* (24), 245408.

2. Experimental

2.1. Electrochemical methods

Electrochemical experiments generally study the process occurring at one electrode known as the working electrode. However, an electrochemical cell always contains a second electrode known as the counter electrode to complete the circuit. Experiments are carried out by controlling the cell potential or the current that passes through the cell. Additionally, three electrode experiments may also be performed whereby a reference electrode is added to the circuit. No current flows through the reference electrode allowing the potential of both the working and counter electrodes to be measured (or controlled) with respect to the reference electrode potential. Electrochemical methods used in this thesis may be separated into galvanostatic, potentiostatic and linear sweep voltammetry techniques.

2.1.1.1. Galvanostatic and potentiostatic measurements

In galvanostatic measurements a constant current is applied between the working and counter electrodes, and the change in potential is measured. By convention, negative and positive currents cause reduction and oxidation of the working electrode respectively. The applied current may be set to change after a certain time limit (as shown in Figure 17(a)) or when the cell potential reaches set upper and lower limits (referred to as cut-off voltages in Chapter 6). This method has the advantage that it reproduces practical battery discharge conditions. In potentiostatic measurements a constant potential is applied and the resultant change in current is measured. An

example of this technique is shown in Figure 17(b), where the potential is changed after a set time limit in a step-wise fashion.

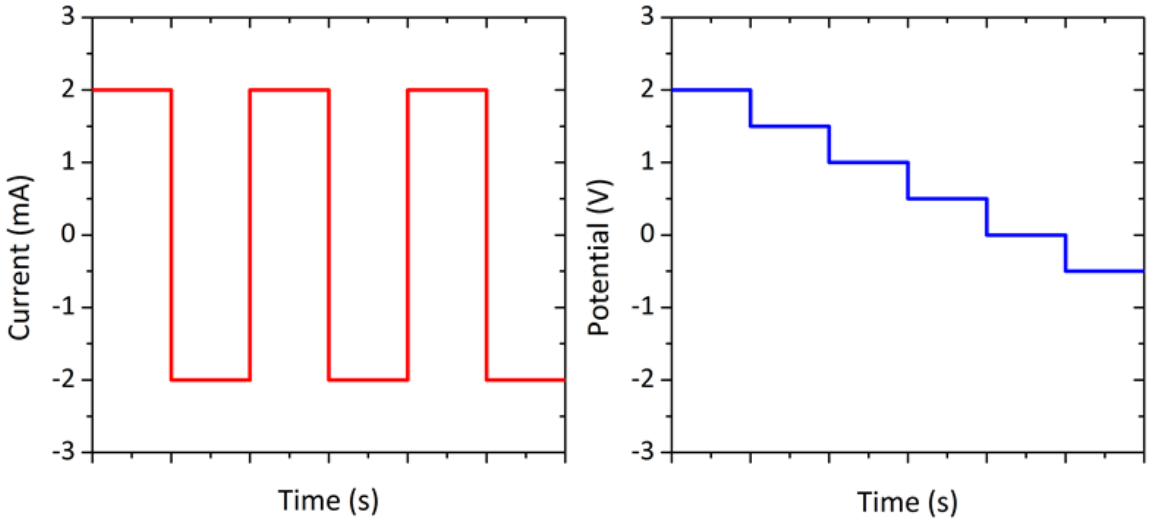

Figure 17: (a) Example of galvanostatic measurement, with current changing after set time limit, (b) example of potentiostatic step measurement.

2.1.1.2. Battery cycling procedures

Battery cycling procedures used herein are summarised in Figure 18. Cycles consist of alternate charging and discharging steps which may be either constant-current (CC)) type or constant-current-constant-voltage (CCCV) type. The CC method employs galvanostatic conditions described above until a cut-off voltage (E_{min} or E_{max} below) is reached. The CCCV method employs an additional constant voltage step, usually held at the cut-off voltage until the current drops to a minimum level (labelled I_{Cutoff} below).

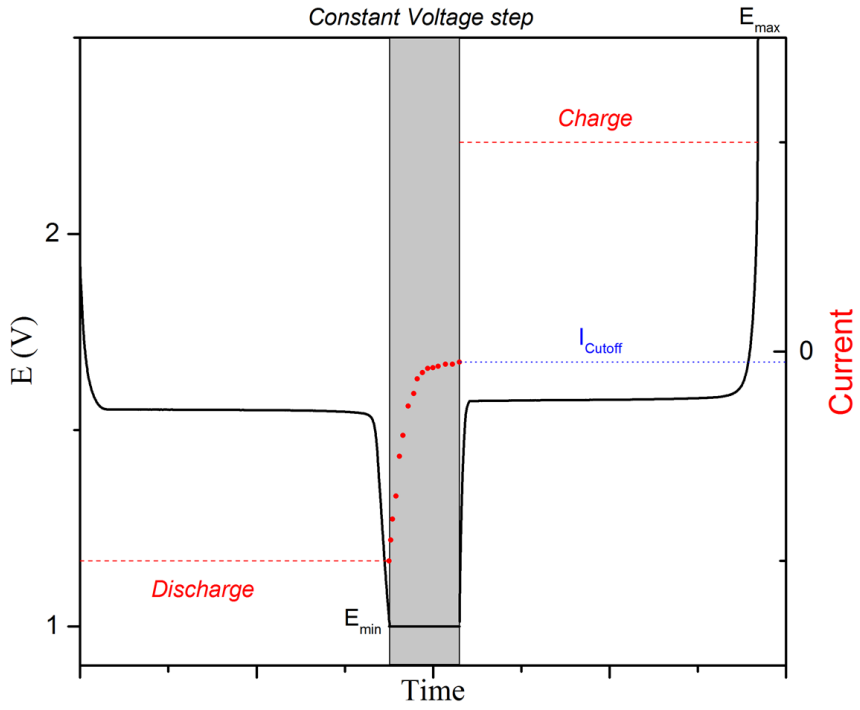

Figure 18: Example of a discharge/charge cycle for a lithium titanate electrode employing a CCCV method on the discharge and a CC (galvanostatic) method on the charge cycle.

2.1.1.3. Linear sweep Voltammetry

In linear sweep voltammetry the potential of the working electrode is changed with a constant rate between set potential limits, whilst the change in current is measured. The change in potential as a function of time is known as the *scan rate* (V s^{-1}). An extension of this technique is known as cyclic voltammetry whereby a positive scan is followed by a negative scan in cyclic fashion; however, this thesis only involves the linear technique.

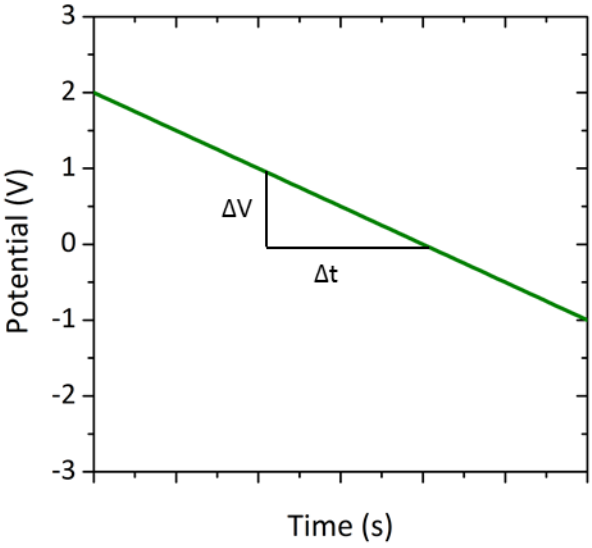

Figure 19: Example of linear sweep voltammetry technique where the *scan rate* may be calculated from the gradient indicated (= $\Delta V/\Delta t$).

2.2. Characterisation methods

2.2.1. Scanning electron microscopy (SEM)

Scanning electron microscopy (SEM) is used primarily to characterise the surface morphology of samples on the nanometre to micrometre scale. The sample is bombarded with a scanning beam of electrons generated by an electron gun with energy in the range 0.1 - 30 keV. The electron beam interacts with the sample to a depth of ~ 1 μm. Images may be produced from the amplified signals of backscattered or secondary electrons produced by elastic or inelastic scattering processes with the sample respectively. Elastic scattering is highly sensitive to elemental composition, whilst the inelastic process occurs via interaction between the energetic electron beam and weakly bound electrons in the conduction band of metals or the outer shell valence band of semiconductors and insulators. A JEOL 6610 scanning electron microscope was used operating at accelerating voltages of 3.0, 10.0 and 20.0 keV.

2.2.2. Transmission electron microscopy (TEM)

Transmission electron microscopy (TEM) operates via transmission of a beam of high energy electrons (accelerating voltage in the 100 to 1000 kV range) through an ultrathin sample. The interaction between the sample and electrons allows imaging at a significantly higher resolution than SEM due to the smaller de-Broglie wavelength of electrons. Electrons transmitted through the sample are magnified and focussed by objective lens to form an image on the imaging screen. Measurements were conducted by Dr. Laura Cabo Fernandez and Dr. Jianyun Cao.

2.2.3. Nitrogen adsorption/ desorption isotherms (BET)

Brunauer–Emmett–Teller (BET) theory is widely used to calculate the surface area of solid materials from the physical adsorption of gas molecules onto solid surfaces. The theory can be applied to systems with multilayer adsorption and adsorption/ desorption isotherms are usually carried out with non-reactive gases, most commonly nitrogen. The theory applies through the following assumptions: that gas molecules physically adsorb on a solid in layers up to infinite dimensions, there is no interaction between the adsorbed layers and that the Langmuir theory (generally applied to monolayer adsorption) applies to each individual layer. Adsorption/ desorption isotherms are generally measured at the probe gas boiling point e.g. 77K for N_2. Measurements were conducted by Jet Lee of the University of Liverpool.

2.2.4. Powder X-ray diffraction (PXRD)

Powder X-ray diffraction (PXRD) is a non-destructive technique that can be used to study the crystallographic structure and chemical composition of materials. The technique relies on the constructive interference of monochromatic X-rays with the periodic structure of a crystalline lattice. X-rays are produced by the irradiation of an anode material (e.g. Cu, Mo, Mg, Al) with high-energy electrons (produced by a hot tungsten filament cathode) causing the emission of a continuous spectrum of X-rays. A monochromator is used to supress X-rays other than the desired wavelength which is characteristic of the anode material used, then the monochromatic X-rays are directed onto the sample whereby a diffracted beam is produced only when constructive interference occurs, that is when the scattering angle satisfies Bragg's law:

$n\lambda = 2d_{hkl} \sin\theta$ Equation 2.1

where n is any integer, λ is the characteristic wavelength used, θ is the diffraction angle and d_{hkl} is the distance between lattice planes as shown in Figure 20 (for reflection geometry). (*h*,*k*,*l*) values represent the miller indices used to define planes of atoms, whereby (h,k,l) are the reciprocal of the plane's intercepts on the x-, y-, and z-axes in terms of lattice constants a, b, and c.

In this work powder X-ray diffraction (PXRD) was used whereby an average diffraction pattern of powder samples is collected. Data in Chapter 4 was collected on a Bruker D8 Advance operating in transmission mode with a Cu source (λ = 1.5418 Å). Data in Chapter 6 was collected on a Rigaku SmartLab X-ray Diffractometer with Cu source in reflection mode

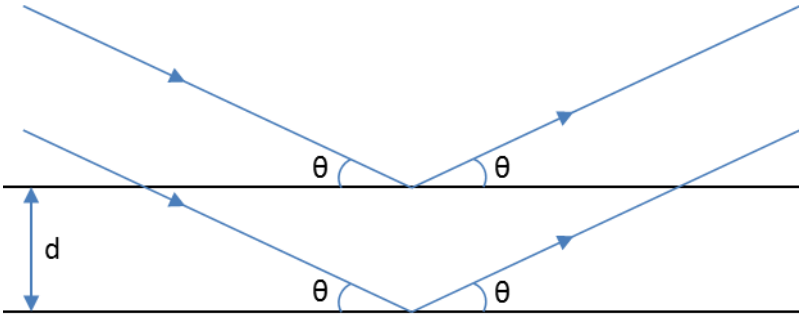

Figure 20: Scattering of X-rays by crystalline lattice planes according to Bragg, where d is the distance separating lattice planes and θ the angle of reflection.

2.2.5. Raman Spectroscopy

The theory underpinning Raman spectroscopy is outlined in Chapter 1. Raman spectra were collected at room temperature (ca. 23 °C) using a Renishaw *inVia* spectrometer, with 632.8 nm (He–Ne laser) or 532 nm (green diode) focused through a microscope

via a 50× objective lens (Leica). Suitable filters were used to minimise the laser power at the surface to < 0.5 MW cm^{-2}. Higher laser powers should be avoided so as to prevent both heating of the sample area and laser degradation of the surrounding electrolyte (which produces fluorescing species such as LiF). Peak fitting was performed using Lorentzian functions and the Peak analyser on Origin software (Chapters 3 and 5) or with a mixed Lorentzian and Gaussian function using WiRE Version 4 software (Chapters 4 and 6).

2.3. *In situ* Raman experiments

The development of suitable electrode configurations and electrochemical testing techniques for conducting *in situ* Raman experiments evolved throughout this work as summarised in Figure 21. The preparation and study of free-standing electrodes and contacted single flakes is described below.

Figure 21: Summary/process diagram of *in situ* Raman method development and suggestions for future studies in this area.

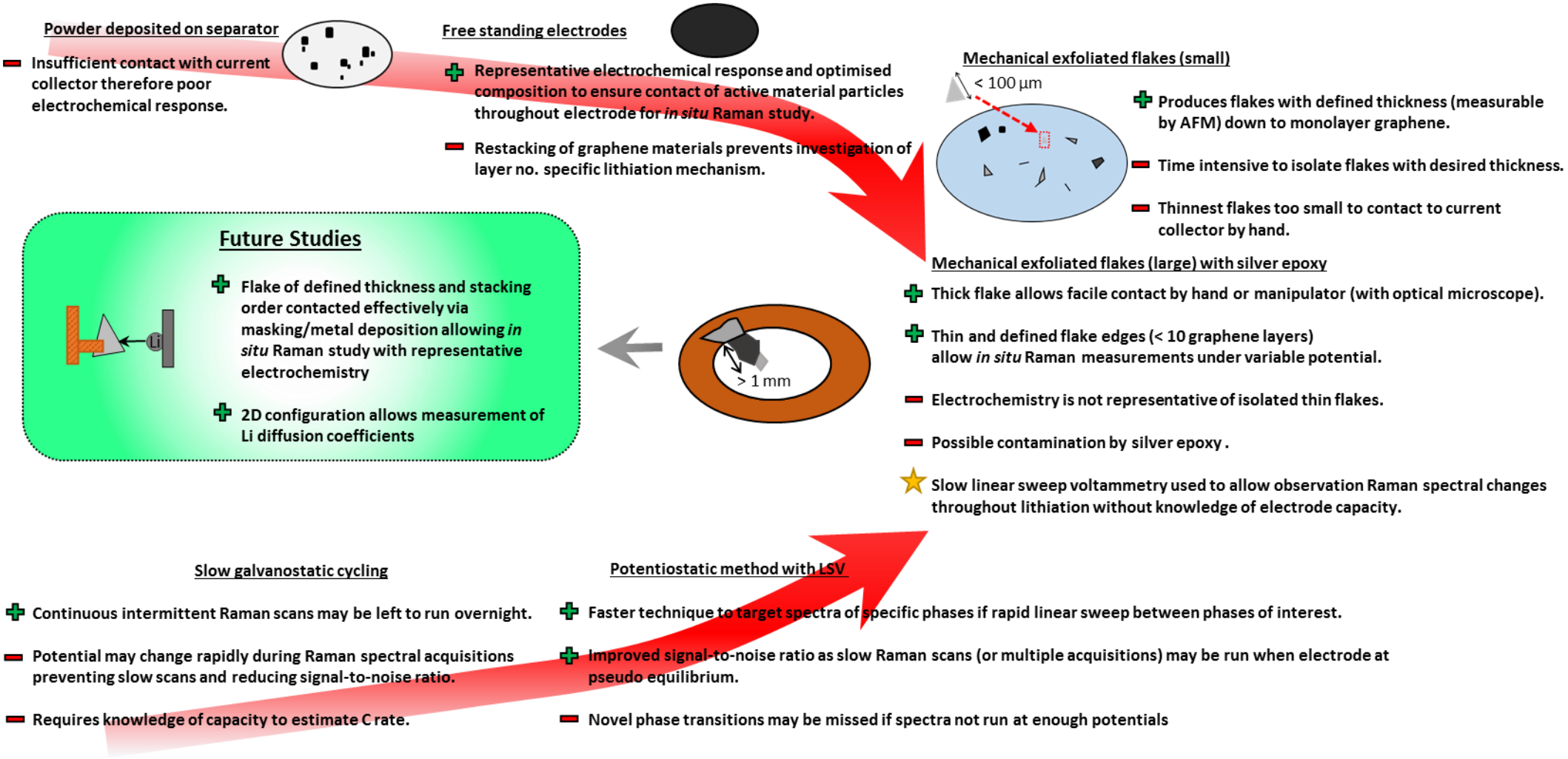

2.3.1. Free-standing electrode configuration

2.3.1.1. Free-standing electrode preparation

Free-standing electrodes were prepared by solvent extraction method as follows: graphite (50 wt%), Poly(vinylidene fluoride-hexafluoropropylene) co-polymeric binder (Kynar-flex, Arkema) (20 wt%) and dibutyl phthalate (Aldrich) (30 wt%) were dispersed in acetone. The slurry was cast onto a glass plate and removed as a free-standing film once dry. The dibutyl phthalate plasticiser was then extracted by soaking in diethyl ether, leaving a porous film ~ 50 µm thick. This was cut into 6 mm diameter electrodes (Figure 22(a)), which had a porous structure due to the solvent extraction method (Figure 22(b). The loadings of the electrodes were ~ 5 mg cm^{-2}, with a typical electrode mass being ~ 1.5 mg. Electrodes were dried under vacuum at 90 °C, then transferred to an argon filled glovebox (O_2, H_2O < 1ppm) for Raman cell assembly.

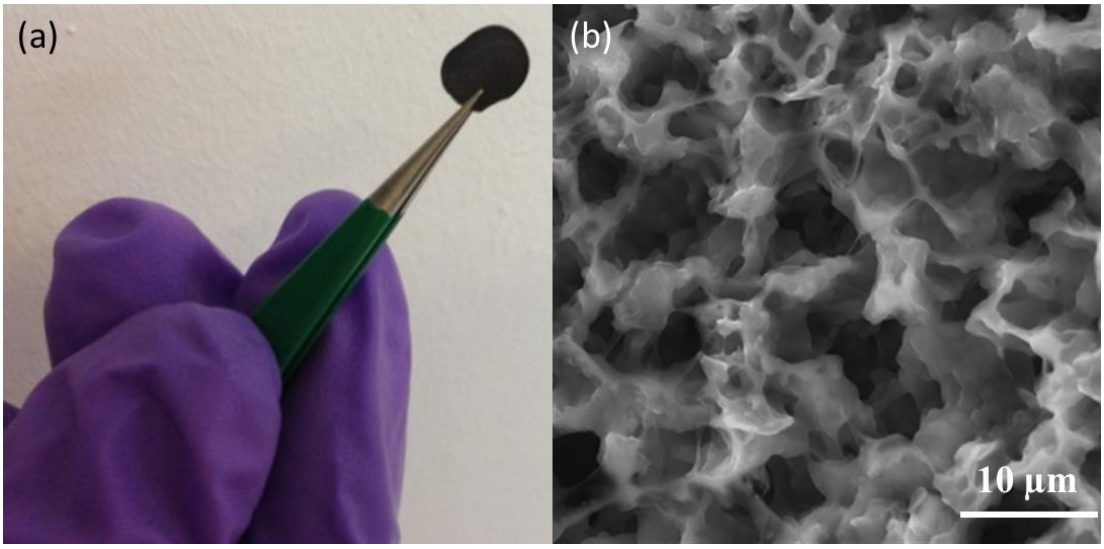

Figure 22: Photograph (a) and SEM image (b) of microcrystalline graphite free standing electrode showing porosity created by solvent extraction method.

2.3.1.2. *In situ* Raman cell setup for free-standing electrode experiments

Experiments used an *in situ* Raman cell (ECC Opto-Std, El-Cell), configured as shown in Figure 23(a). The cell is hermetically sealed to atmosphere, enabling air-sensitive electrochemical processes to be investigated *in situ*. The aperture allows a Raman laser to be focussed upon the back surface of a free-standing electrode, so that Raman spectra may be obtained during electrochemical cycling. The 3 electrode configuration was employed whereby a small piece of Li metal was inserted at the tip of the reference electrode contact pin. Once sealed, the cell was impregnated with 1 M $LiPF_6$ in EC-DMC electrolyte (BASF) by application/release of a negative pressure with an electrolyte-filled syringe. The Raman cell was then positioned atop the Raman microscope stage and connected to a potentiostat (Biologic) as shown in Figure 23(b).

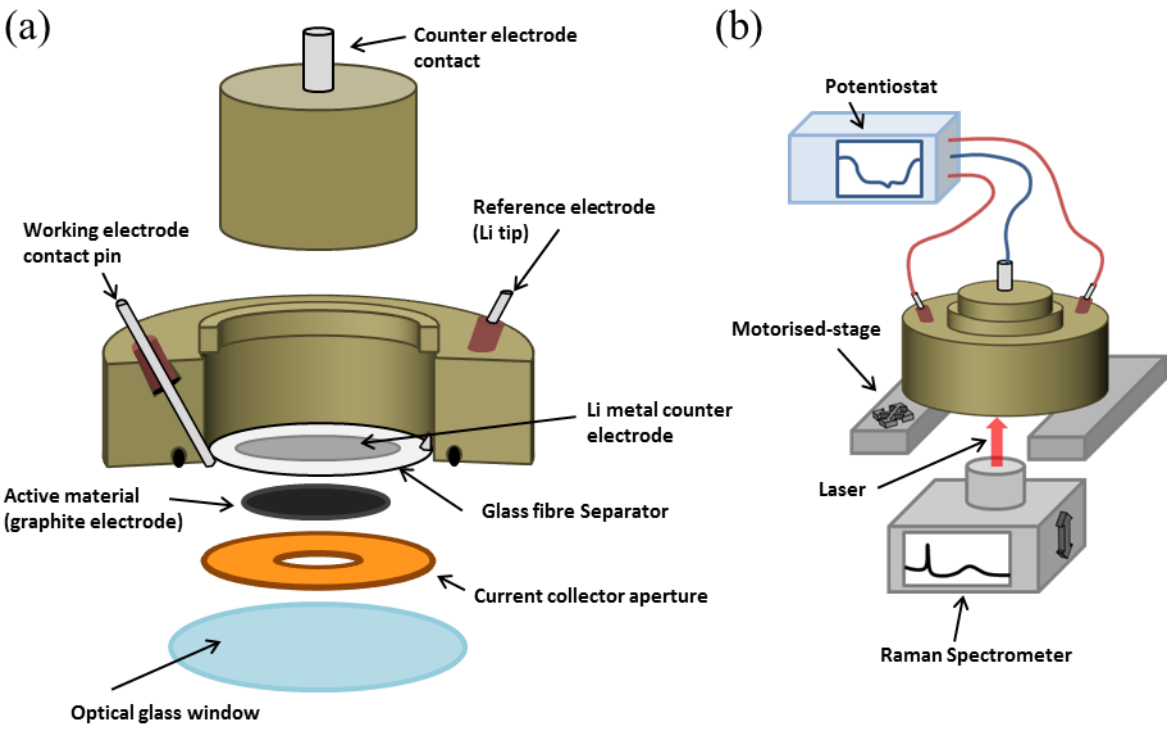

Figure 23: (a) *In Situ* Raman cell setup for free standing electrode experiments and (b) positioning of cell during *in situ* measurement

2.3.2. Mechanically-exfoliated single graphite flake experiments

The same cell was adapted for the single flake measurements in Chapter 5. Mechanical exfoliation of highly crystalline natural graphite flakes (NGS Naturgraphit GmbH) was performed via the 'scotch tape method'[1,2] onto borosilicate glass cover slides. This method produced a distribution of flakes on the slide as shown in Figure 24. Flakes were carefully screened via Raman spectroscopy and selected according to the following requirements: ideal flakes should possess a thin, flat region of several square micrometres area to be investigated by Raman spectroscopy; meanwhile the lateral dimensions of the flake should be larger than a few hundred micrometres and thick enough (> 500 nm) at one edge to facilitate electronic connection using silver epoxy. Selected flakes were isolated (still adhered to the glass substrate) using a diamond glass cutter and the thickness of the region to be investigated was determined by atomic force microscopy (AFM). An electronic connection between the graphitic flake and the copper current collector was made with silver epoxy, leaving the area of interest pristine. The position of the flake was aligned to coincide with the small aperture (ca. 1 mm diameter) in the center of the copper current collector (see Figure 24a) to allow optical observation and spectroscopy. To minimize electrolyte contamination the silver epoxy contact was positioned facing the glass window. The contacted single flake electrode was assembled as the working electrode in the *in situ* Raman cell (ECC Opto-Std, El-Cell) (Figure 24b) in 2 electrode configuration, with Li metal counter electrode and an electrolyte impregnated glass fibre separator (1 M $LiPF_6$ in EC-DMC electrolyte (BASF)).

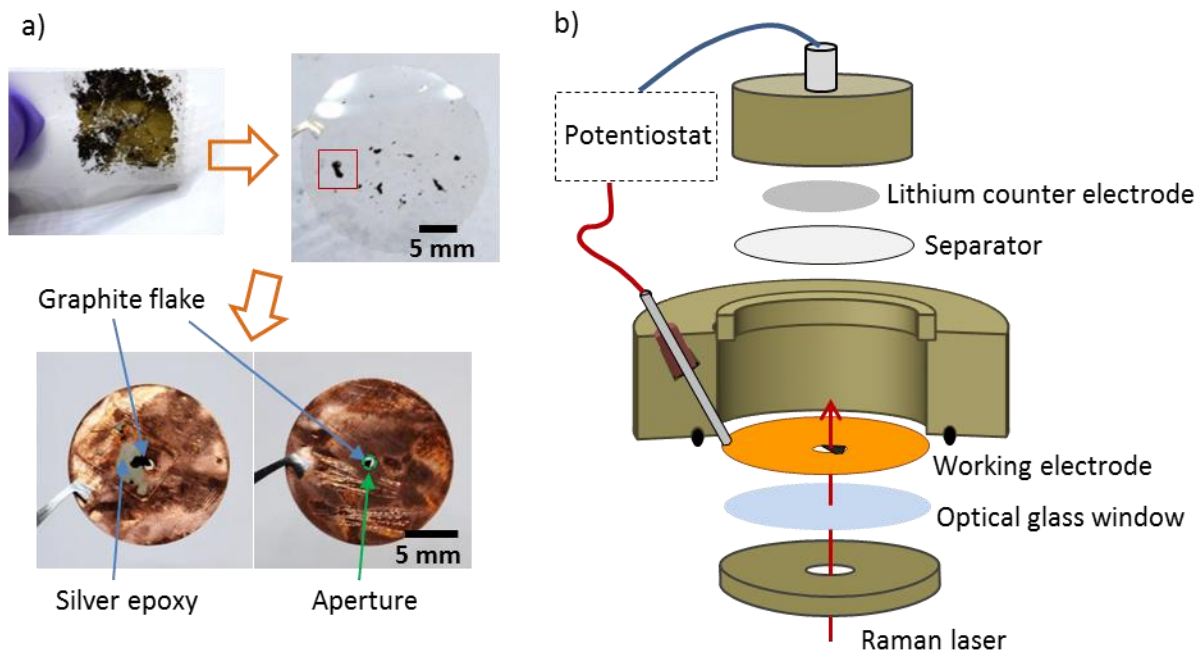

Figure 24: Schematic illustration of the assembly the *in situ* Raman cell with single flake electrodes. a) Graphite flakes were mechanically exfoliated onto a borosilicate glass cover slide. One graphite flake was selected and connected to a copper current collector using silver epoxy, ensuring that the area of interest was aligned with the aperture in the center for direct observation. b) The graphite flake was assembled in the *in situ* Raman cell (ECC Opto-Std, El-Cell).

2.4. Coin cell tests

2.4.1. Production of composite electrodes: slurry formulation and electrode casting

In general, electrodes used in LIBs are composites composed of active materials, conductive additives and binder, the roles of which will be discussed in Chapter 6. Electrodes were produced for coin cell experiments by a tape-casting method.[3] Firstly, electrode slurries were prepared by dispersion of electrode materials in N-methylpyrrolidone (NMP). Dispersion was achieved by a combination of mixing techniques (stirrer bars, Vortex-Genie 1 Touch Mixer (Scientific Industries) and Intelli-Mixer RM-2 (LTF Labortechnik)).

In general, the following order of dispersion was followed:

1) Poly(vinylidene fluoride-co-hexafluoropropylene) co-polymeric binder (PVdF-HFP) (Kynarflex, Arkema) was dissolved in NMP.
2) Conductive additives were added and dispersed.
3) Active material was added and dispersed.

Following dispersion electrode slurries were cast onto metallic current collectors (Figure 25) using a doctor blade and paint applicator (K paint applicator with vacuum bed, RK PrintCoat Instruments). Cu foil was used for graphite electrodes (Chapter 4) and Al foil for lithium titanate and lithium cobalt oxide electrodes (Chapter 6). Casts were dried under an IR lamp and then transferred to a vacuum oven (~ 110 °C).

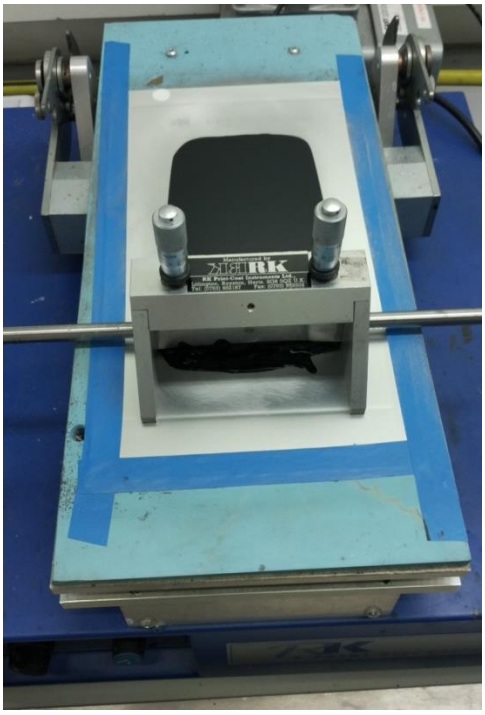

Figure 25: Casting procedure for composite electrodes.

2.4.1.1. Dispersion process for exfoliated graphite conductive additives

When exfoliated graphite samples were used as conductive additives the process was altered to encourage exfoliation of partially restacked graphene sheets. The following procedure was followed:

1) Exfoliated graphte conductive additives were added and dispersed in NMP via 20 minutes ultrasonication (50% power, 37 kHz, Fisherbrand FB11205 ultrasonic cleaner)
2) Poly(vinylidene fluoride-co-hexafluoropropylene) co-polymeric binder was added and dissolved.
3) Any additional conductive co-additives were added and dispersed.
4) Active material was added and dispersed.

2.4.1.2. Calendering to desired porosity

Electrodes in Chapter 6 were calendered at room temperature using a cylinder press (MSK-HRP-01, MTI). Porosities were controlled by variation of the calender gap until the desired electrode thickness was achieved. The porosity of each electrode tested was calculated according to:

$$\text{Porosity} = \frac{V_{actual}\text{-}V_{predicted}}{V_{actual}} \times 100 \qquad \text{Equation 2.2}$$

Where V_{actual} is the measured electrode volume (area multiplied by thickness) and $V_{predicted}$ is the predicted volume, calculated according to:

$$V_{actual} = \frac{m_{electrode}}{\rho_{average}} \qquad \text{Equation 2.3}$$

Where $m_{electrode}$ is the electrode mass and $\rho_{average}$ is the average electrode density, calculated according to:

$$\rho_{average} = \sum \frac{W_i}{100} \rho_i \qquad \text{Equation 2.4}$$

Where ρ_i is the density of each constituent and W_i the wt. % of constituent i in the electrode.

In general, electrodes were calendered to achieve a porosity of ~ 30 %. However, in most cases V_{actual} was measured with a precision of ± 5 µm due to the limitations of the thickness gauge (Mitutoyo Thickness Gauge 547-320S), i.e. thickness was measured in 10 µm steps (10 µm, 20 µm, 30 µm and so on). Figure 26 shows the effect of the uncertainty associated with the calculated porosity for electrodes with measured thickness between 20 - 60 µm, considering this measurement to be the only source of

error. As expected, the uncertainty in the calculated porosity increases as electrode thickness decreases. This uncertainty should be considered in the context of the composite electrode evaluation in Chapter 6, although all measurements in Chapter 6 investigate trends and therefore the conclusions of the chapter are valid regardless of these considerations. However, a more precise thickness gauge (Mitutoyo Thickness Gauge 547-401) with a precision of ± 0.5 µm was used for experiments where the effect of porosity was specifically investigated.

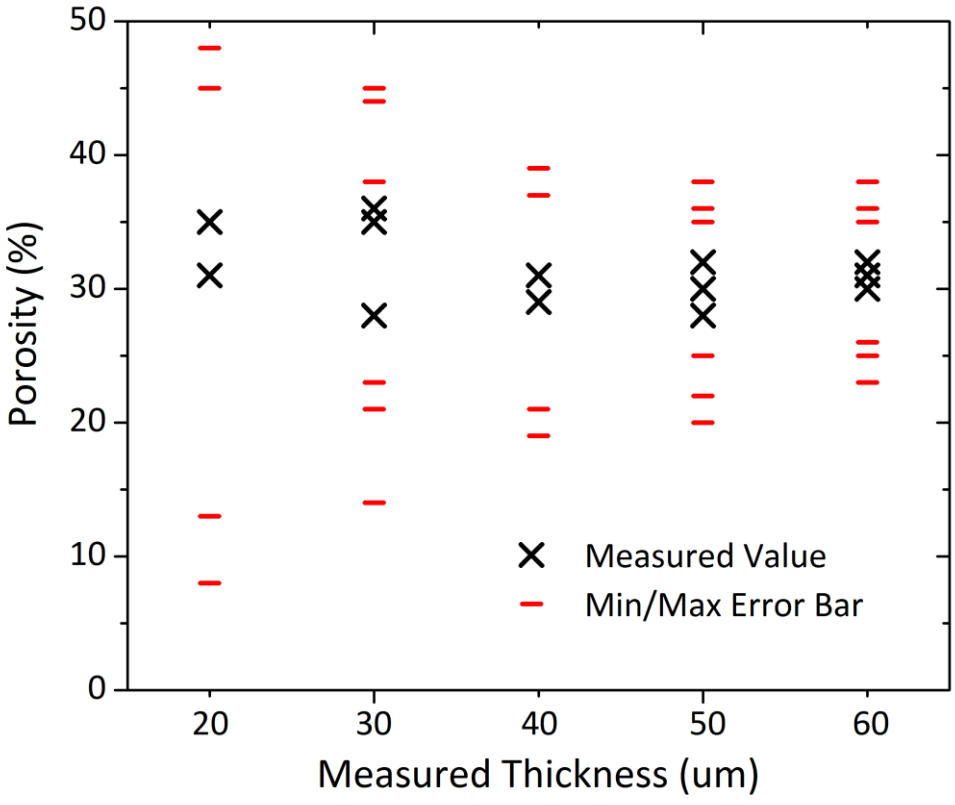

Figure 26: Calculated porosity, showing associated error bars from the uncertainty in the thickness measurement (± 5 µm).

2.4.2. Coin cell assembly

2025 type coin cells were assembled in an Argon filled glove box (O_2, H_2O < 1ppm) in the configuration shown in Figure 27. A Li metal counter electrode (0.75 mm thickness x 16 mm diameter, Sigma) was used. The polypropylene O-ring gasket ensures hermetic sealing. Separators used were either 2 x borosilicate glass fibre (Whatman, Grade GF/C) or 1 x polypropylene membrane (Cellguard 2500 Microporous Monolayer Membrane). The number of stainless steel spacers (0.5 mm thick) used was adjusted depending on the separator: 1 x spacer was used with the glass fibre separators and 2 x spacers with the polypropylene membrane. 1M $LiPF_6$ in EC-DMC (BASF) was used as electrolyte, and separators were impregnated with excess volume.

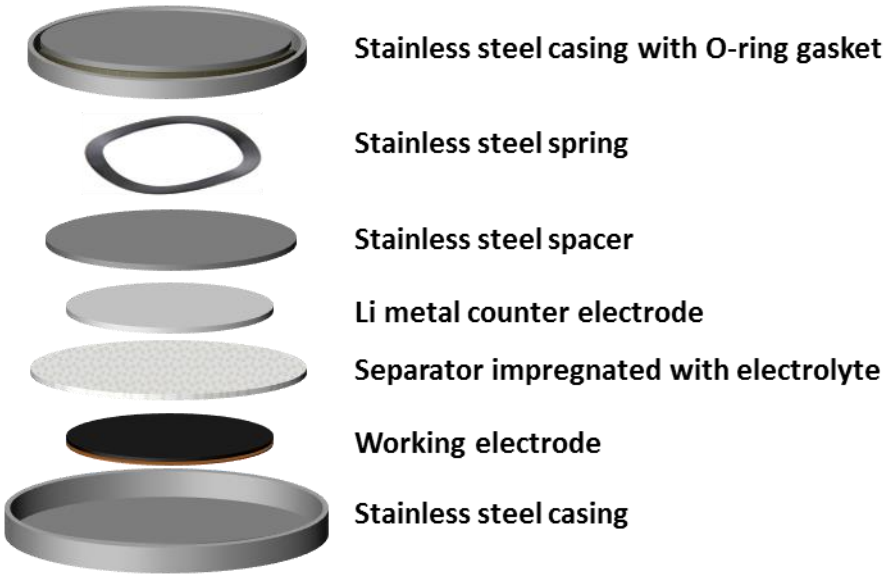

Figure 27: Schematic of coin cell configuration

2.4.3. Coin cell electrochemical testing procedures

Electrochemical charge/discharge measurements were carried out at 30 °C on a battery cycler (Maccor Series 4000). The cycling procedures and currents were varied depending on the active material tested and are described in subsequent results chapters. Tests were performed with at least three electrodes to confirm reproducibility of results. Reported results are either the average of these tests (with standard deviation plotted as error bars), or the best performing electrodes, which are plotted for clarity of presentation and only when described trends were valid across all measurements.

2.5. Cathodic electrochemical exfoliation of graphite

Materials tested in Chapter 4 and Chapter 6 were produced by a cathodic electrochemical exfoliation process, developed by the University of Manchester.[4,5] As illustrated in Figure 28, a two electrode system is used, whereby a pressed pellet of graphitic carbon acts as the cathode and a graphite rod as the anode. The electrolyte is composed of dimethyl sulfoxide (DMSO) saturated with lithium chloride (LiCl) and triethylammonium hydrochloride (Et_3NHCl). A negative voltage of -10 V is applied between the two electrodes for 8 hours, which causes exfoliation of the graphitic pellet cathode due to the intercalation of solvated Li^+ and Et_3NH^+ ions (exfoliated flakes are dispersed in the electrolyte). The exfoliated product is dispersed in water, then collected by vacuum filtration and washed repeatedly with water to remove residual ions. Finally, the obtained powder is dried at 80 °C for 5 hours.

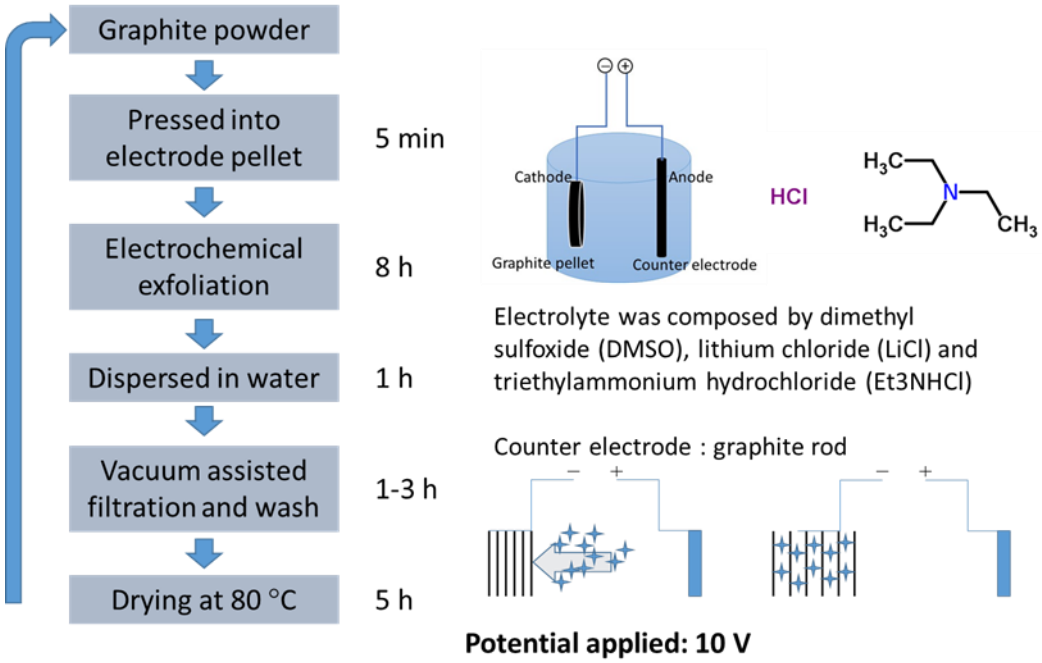

Figure 28: Cathodic electrochemical exfoliation process developed by the University of Manchester.[5]

This method was used to produce materials used in Chapter 4 and Chapter 6, whereby the precursor graphite material (for the pressed cathode) in Chapter 4 was SFG 6 microcrystalline graphite (TIMCAL TIMREX®) and in Chapter 6 was not disclosed.

2.6. References

(1) Novoselov, K. S. Electric Field Effect in Atomically Thin Carbon Films. *Science* **2004**, *306* (5696), 666–669.

(2) Novoselov, K. S.; Jiang, D.; Schedin, F.; Booth, T. J.; Khotkevich, V. V; Morozov, S. V; Geim, A. K. Two-Dimensional Atomic Crystals. *Proc. Natl. Acad. Sci. U. S. A.* **2005**, *102* (30), 10451–10453.

(3) Marks, T.; Trussler, S.; Smith, A. J.; Xiong, D.; Dahn, J. R. A Guide to Li-Ion Coin-Cell Electrode Making for Academic Researchers. *J. Electrochem. Soc.* **2011**, *158* (1), A51.

(4) Abdelkader, A. M.; Kinloch, I. A.; Dryfe, R. A. W. Continuous Electrochemical Exfoliation of Micrometer-Sized Graphene Using Synergistic Ion Intercalations and Organic Solvents. *ACS Appl. Mater. Interfaces* **2014**, *6* (3), 1632–1639.

(5) Sole, C.; Drewett, N. E.; Liu, F.; Abdelkader, A. M.; Kinloch, I. A.; Hardwick, L. J. The Role of Re-Aggregation on the Performance of Electrochemically Exfoliated Many-Layer Graphene for Li-Ion Batteries. *J. Electroanal. Chem.* **2015**, *753*, 35–41.

3. *In situ* Raman spectroscopy of Li intercalation into microcrystalline graphite

3.1. Overview of chapter

Prior to the investigation of thickness related effects, the behaviour of a microcrystalline graphite sample during electrochemical Li intercalation was investigated. In general, particles of microcrystalline graphite are composed of graphitic crystallites with in-and out-of-plane dimensions in the range of tens to hundreds of nanometres. Characterisation of these dimensions will be discussed further in Chapter 4. Microcrystalline graphite is commonly used in Li ion batteries (LIBs) due to low cost and good electrochemical performance arising due to relatively short diffusion distances and low first cycle irreversibility.

This chapter begins with an introduction to the graphite intercalation compounds (GICs) which are formed during the room temperature Li intercalation of graphite. This includes a review of the structural data of phases that have been observed in the literature. This precedes the discussion of an *in situ* Raman study of the electrochemical lithiation and delithiation of a microcrystalline graphite sample under galvanostatic conditions. This experiment revealed a large red-shift in 2D band frequency, accompanying the previously reported Raman response of the G band, suggesting significant strain and/or doping of the graphene sheets during lithiation.

3.2. Insertion mechanisms in lithium ion battery materials: solid solution and two-phase reactions

Li insertion into LIB active materials may occur either by formation of a solid solution or via a two-phase reaction, depending on the miscibility of Li between the initial phase and the phase with increased Li concentration, following insertion.[1] If there is a miscibility gap between the two phases, as in the lithium titanate system for example, where $Li_4Ti_5O_{12}$ undergoes Li insertion to become $Li_7Ti_5O_{12}$,[2] then a two-phase reaction occurs as Li concentrations between the two phases are thermodynamically unstable. Lithiation proceeds by a change in the ratio of $Li_4Ti_5O_{12}$:$Li_7Ti_5O_{12}$ by movement of a distinct phase boundary through particles. A two-phase reaction process can be observed under low rate galvanostatic conditions as a plateau in the voltage profile (vs. Li^+/Li) as indicated in Figure 29(a) for a theoretical insertion reaction, $MA + Li^+ + e^- \rightarrow LiMA$. In accordance with Equation 1.26, cell potential is proportional to the difference in electrochemical potential between negative and positive electrodes. Under open circuit conditions and intermediate Li concentrations ($0.2 < x < 0.8$), the two phases are in equilibrium where there is no change in electrochemical potential ($\Delta G = 0$), resulting in a constant potential observable as a voltage plateau.

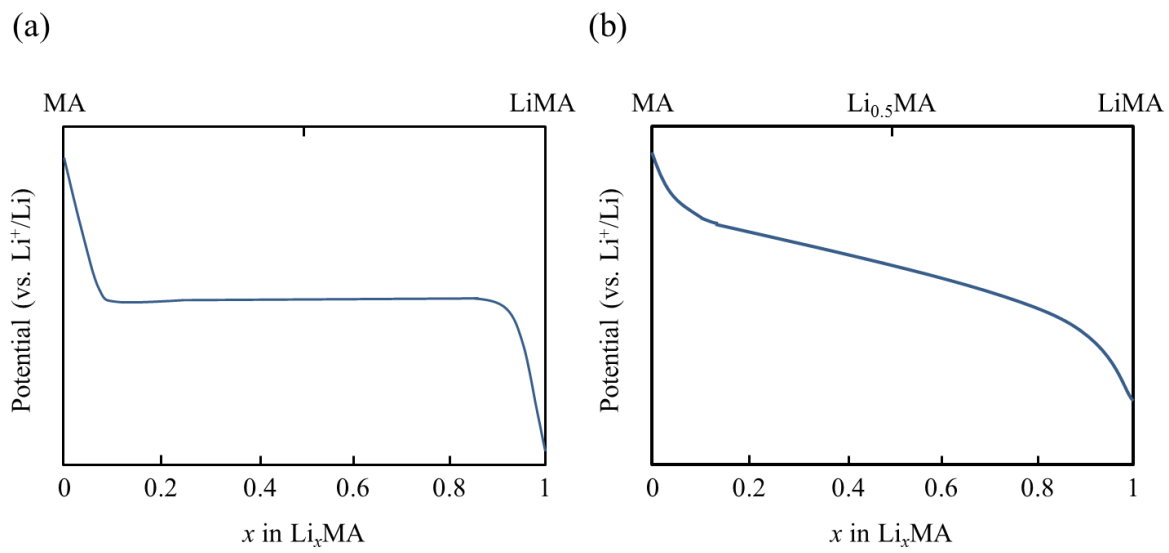

Figure 29: Open circuit potential behaviour of theoretical compound MA, undergoing lithiation to LiMA via (a) a two-phase reaction mechanism or (b) a solid solution mechanism.

In contrast, in systems where no miscibility gap exists, (for example, during delithiation of $LiNi_{1/3}Mn_{1/3}Co_{1/3}$)[3] a solid solution exists between the Li poor and Li rich phase, i.e. all values of x are possible in Li_xMA, where $0 \leq x \leq 1$. Under low rate galvanostatic conditions such a solid-solution mechanism results in a sloping voltage profile (vs. Li^+/Li) as shown in Figure 29(b). This is because the electrochemical potential of Li in the insertion material increases with increasing Li concentration (x in Li_xMA). Such insertion mechanisms are generally considered useful for high rate materials due to avoiding the rate limitations of phase transformations and Li diffusion across phase boundaries.[4] However, recent studies suggest that by nano-sizing electrode materials which thermodynamically operate via two-phase mechanisms, such materials may be encouraged to operate via a metastable solid solution mechanism at high current rates.[4,5]

3.3. Graphite intercalation compounds

GICs may be characterised as donor or acceptor types dependent on their interaction with the electronic structure of graphite during chemical intercalation. A basic model for the electronic structure of graphene and graphite is shown in Figure 30 - the difference being graphene has a non-zero density of states at the Fermi level. Upon intercalation, the electronic structure of graphite begins to resemble that of single layer graphene due to decoupling of the graphene sheets. In donor GICs (such as Li) the highest occupied molecular orbital (HOMO) of the intercalant species lies above the Fermi level and thus charge transfer occurs whereby electron density is transferred from the intercalant HOMO to the π^* band of the graphene sheet and the Fermi level increases. In acceptor GICs the lowest unoccupied molecular orbital (LUMO) of the intercalant species lies below the Fermi level and thus electron density is transferred to the intercalant LUMO from the π band of the graphene sheet, decreasing the Fermi level. Alternatively, if GICs are formed by electrochemical methods the intercalation of ionic species occurs accompanied by the transfer of electrons either to or from the external circuit (for acceptor and donor type respectively), however, the resultant electronic structure is identical to the chemical process.

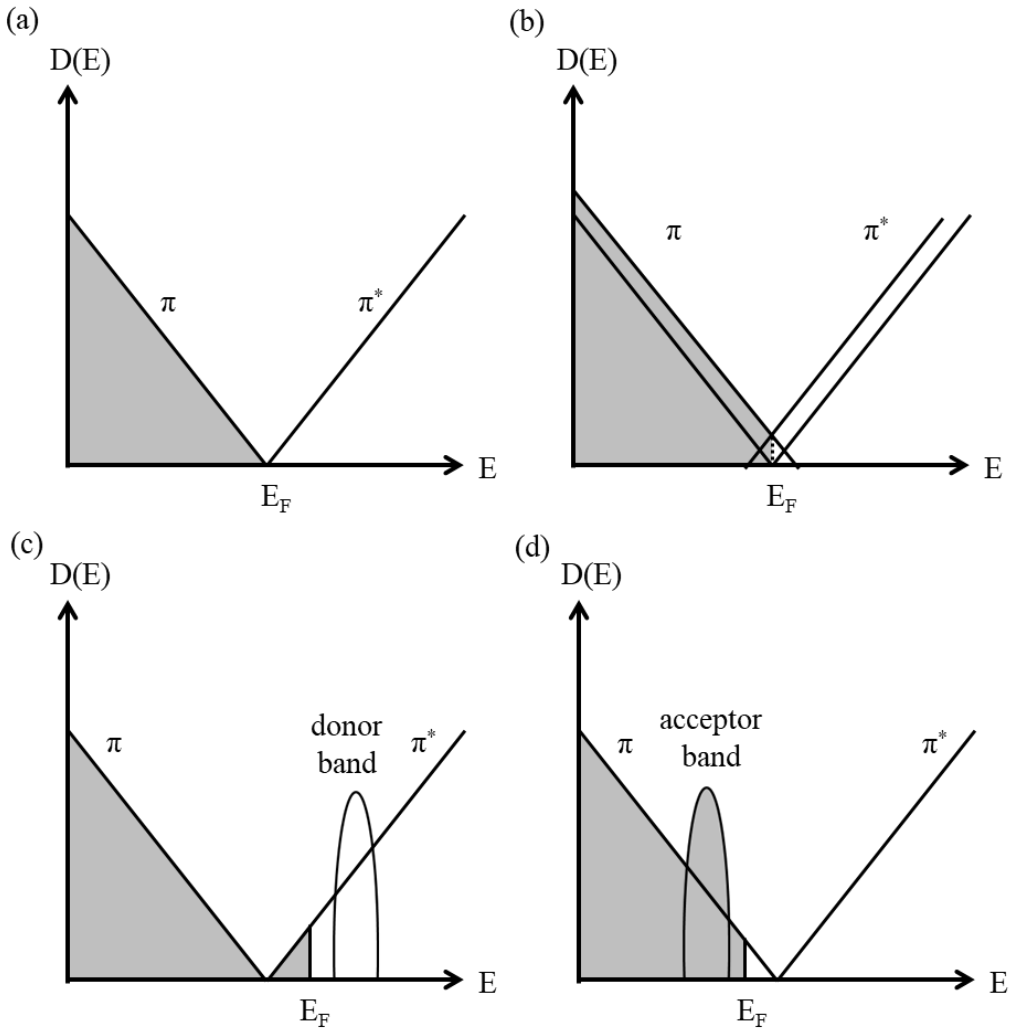

Figure 30: Schematic of electronic structures of (a) graphene, (b) graphite, (c) donor GICs, (d) acceptor GICs, where D(E) is the density of states and E_F is the Fermi energy, redrawn from [6].

3.4. Thermodynamic stage transitions in lithium-graphite intercalation compounds

At atmospheric pressure and ~300 K the formation of graphite intercalation compounds (GICs) with Li is known to occur by the sequential process shown in Figure 31.[7] Intercalation proceeds via formation of staged GICs, classified by a stage index, n, which represents the number of graphene layers separating layers of intercalated ions.

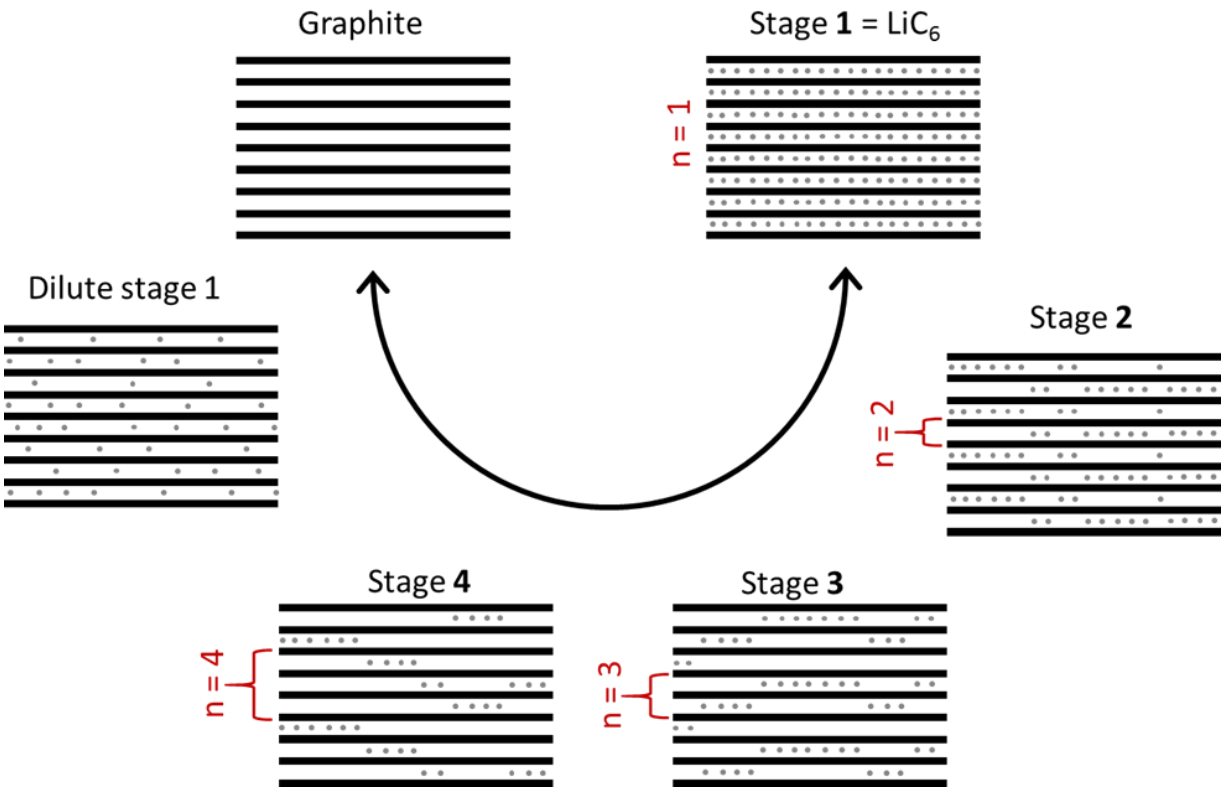

Figure 31: Thermodynamic stage transitions during lithium intercalation into graphite. Grey spheres correspond to Li^+ ions.

The structural transformations during electrochemical intercalation ~ 300 K have been well studied and are summarised in Figure 32. The voltage profile (plotted in blue,

upper window) clearly shows the appearance of phase transitions and solid solution regions as plateaus and sloping regions respectively. The letter L next to the stage number (n) is used to describe a phase which displays no in-plane ordering of Li^+ ions.

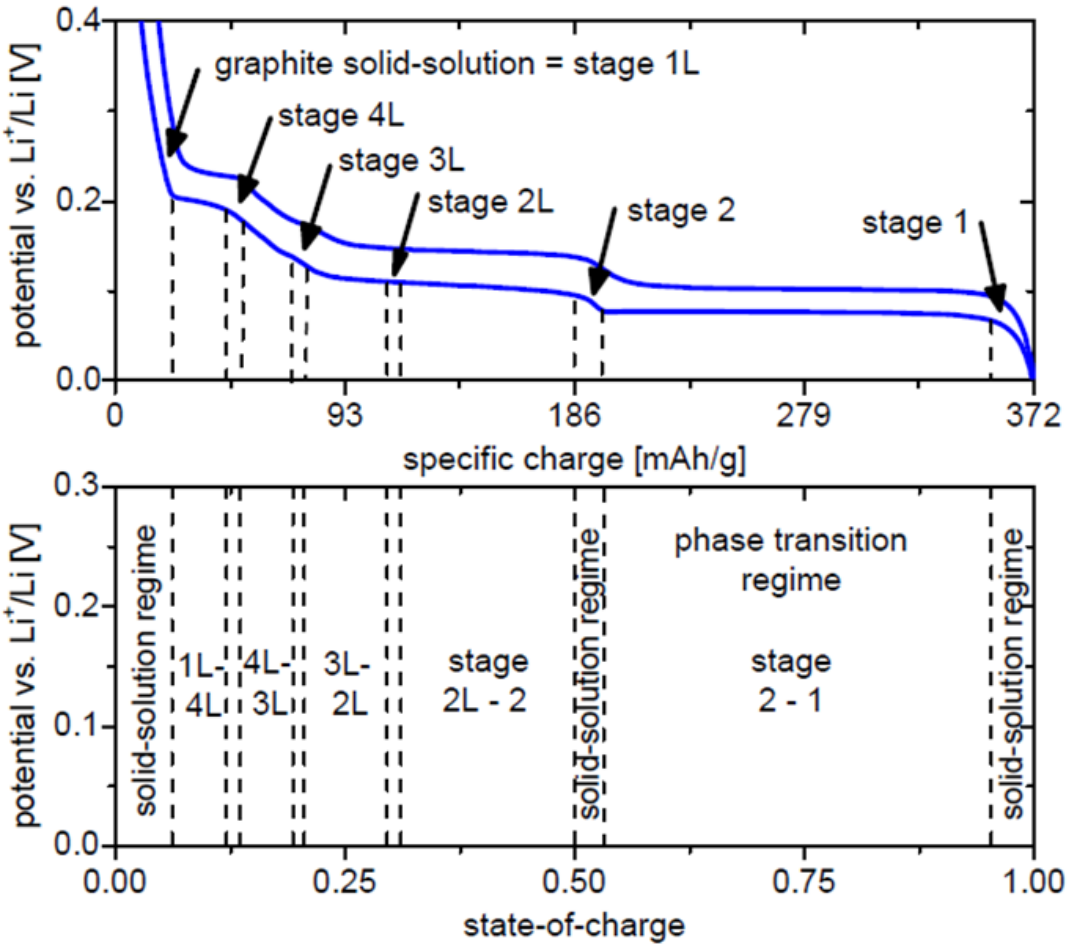

Figure 32: Thermodynamic stage transitions during electrochemical lithium intercalation. Adapted from [8], originally derived from phase diagrams ~300K.[7,9] Dashed lines indicate solid-solution regimes between pure phases.

The reported structural parameters during the intercalation process are given in

Table 3.1. Graphite commonly exists in the hexagonal $P6_3/mmc$ (D_{6h}^4) space group whereby graphite layers are stacked with an ABAB stacking sequence.[10] The initial intercalation occurs into every gallery (interlayer space) without any in plane ordering of Li^+ ions, forming a solid solution (1L) commonly referred to as dilute stage 1. This is not the formation of a new phase but occurs due to the miscibility of Li in graphite at ~ 300 K.[9]

The stage 4L GIC is formed ~ 0.2 V whereby the coexistence of the two phases is indicated by the plateau in the voltage profile. Below this a sloping voltage profile indicates the stage 4L to 3L phase transition, followed by the 3L to 2L phase transition. The precise nature of this region (4L to 2L) in terms of phase transitions and the stacking order of graphene sheets is still under debate. Numerous studies have observed the continuous shift of the c-axis parameter in this region by *in situ* powder X-ray diffraction (PXRD), which has been explained by a solid-solution phase transition mechanism.[7,11,12] Stacking order of the graphene sheets for stage 2L has been determined as [AB|BA],[11,13] whilst stage 3L has been estimated as either [ABA|ACA] or [ABA|ABA].[12] No stacking order has been suggested for stage 4L although c lattice parameters have been suggested on oxidation and reduction.[14]

Table 3.1: Summary of crystallographic data for room temperature Li graphite intercalation compounds. The subscripts ox and red refer to lattice parameters observed on the oxidation and reduction cycle respectively. Adapted from Heß et al.[15]

Phase	**Space Group**	**Lattice Parameter**		**Reference**
		a (Å)	c (Å)	
Graphite (2H)	P63/mmc	a = 2.461 ± 0.0001	-	16
		a = 2.460	c = 6.704	17
		a = 2.464 ± 0.002	c = 6.711 ± 0.004	18
Stage 4L			c_{ox} = 13.76, c_{red} = 13.9	14
Stage 3L		a = 2.4684	c = 10.408 (c = 2 x 3.33 + 3.748)	12
Stage 3L			c_{ox} = 10.401, c_{red} = 10.473	14
Stage 2L		a = 2.4725	c = 7.065	11
Stage 2L			c = 7.055 ± 0.005	13
Stage 2	P6/mmm	a = 4.2867	c = 7.025	11
Stage 2			c_{ox} = 7.043, c_{red} = 7.072	14
Stage 2	P6/mmm		c = 7.024 ± 0.005	13
Stage 2	P6/mmm	a = 4.288 ± 0.002	c = 7.065 ± 0.01	19
Stage 2	P6/mmm	a = 4.290	c = 7.047	20
Stage 1		a = 4.316	c = 3.703	14
Stage 1	P6/mmm	a = 4.305 ± 0.002	c = 3.706 ± 0.01	19
Stage 1	P6/mmm	a = 4.305	c = 3.706	11
Stage 1	P6/mmm	a = 4.0307	c = 3.680	20

Another phase transition to form the dense stage 2 GIC occurs ~ 0.10 V. This phase has similar occupation of galleries perpendicular to the graphene sheets as stage 2L, however, it displays in-plane ordering of Li^+ ions as shown in Figure 33(a). Li^+ ions occupy one in every three C_6 rings with regular 4.3 Å spacing and an [AAα] stacking sequence is observed.

Finally, ~ 0.08 V the stage 1 phase forms whereby all galleries become filled with similar in-plane ordering to the dense stage 2 phase (Figure 33(a)) and an [Aα] stacking sequence is observed as in Figure 33(b).

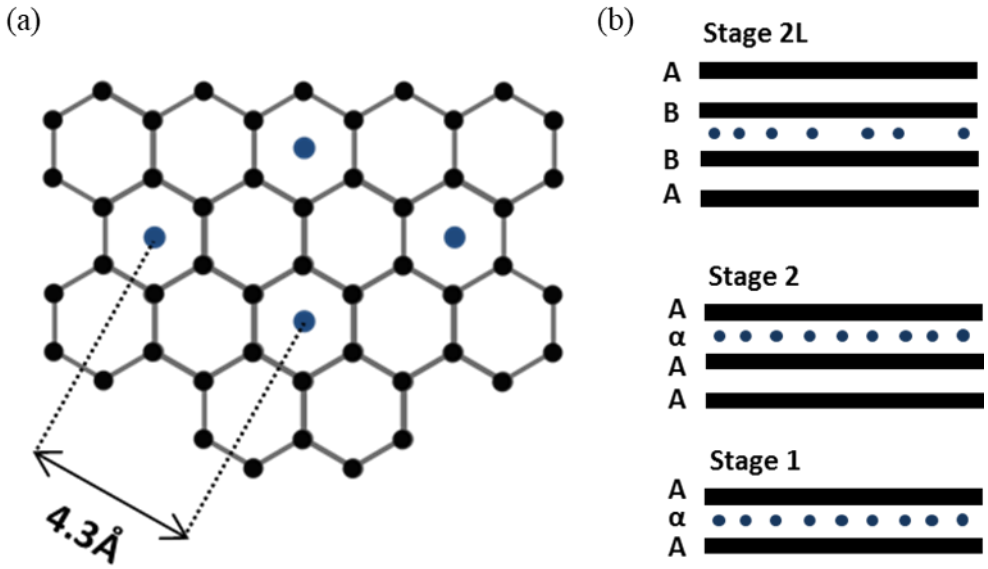

Figure 33: (a) In-plane ordering of filled galleries of dense stage 1 and stage 2 phases. (b) Stacking order of stages 1, 2 and 2L – order of stages 3L and 4L are not defined.

3.4.1. Kinetics of stage transitions and Daumas-Hérold domains

To permit the transition from one stage to another without the emptying of entire galleries Daumas and Hérold[21] suggested the formation of intercalate islands or so called Daumas-Hérold domains as shown in Figure 34. This domain structure has been supported by several theoretical studies[22–24] and even observed experimentally by transmission electron microscopy.[25] The observed phase transitions must therefore be accounted for by the rearrangement of domains and associated redistribution of Li^+

ions within galleries. Furthermore, minor shifts of the graphene sheets are required to account for the observed changes in stacking order. The existence of such a mechanism implies a distortion of graphene sheets at the domain boundaries due to the difference in interlayer spacing between filled and non-filled galleries, as can be observed in Figure 34.

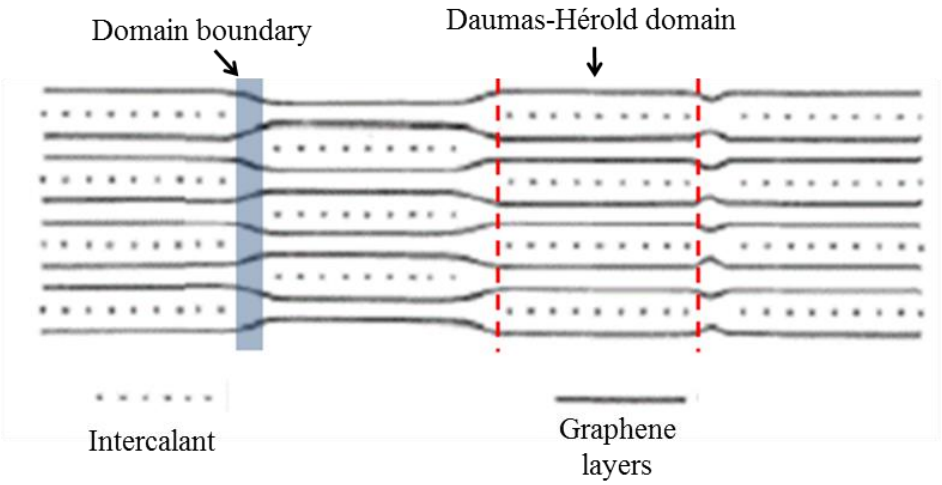

Figure 34: Example of a stage 2 graphite intercalation compound showing intercalate islands known as Daumas-Hérold domains and distortion of graphene layers at domain boundaries (adapted from [26]).

3.5. Previous *in situ* Raman spectroscopy studies of lithium intercalation into graphitic carbons

The first use of *in situ* Raman spectroscopy to observe the intercalation of lithium into carbon in a typical LIB electrolyte was reported by Inaba et al.[27] The use of *in situ* Raman microscopy to study battery materials has since become widespread, as discussed in two recent review aticles.[28,29] *In situ* Raman spectroscopy has highlighted the inhomogeneous nature of lithium intercalation (even in single graphite particles).[30,31] Furthermore, the combination of *in situ* Raman and optical microscopy has provided strong experimental evidence for the Daumus-Hérold theory of intercalation by allowing direct observation of stage transitions.[32] Other studies have analysed the use of graphite-exfoliating electrolyte mixtures[33] and the intercalation of ionic liquid anions at high potentials.[34] However, although previous studies have reported the 2D band behaviour for chemically intercalated alkali metal GICs,[35,36] the *in situ* behaviour during electrochemical Li intercalation in a typical LIB electrolyte have not been reported.

3.6. *In situ* Raman spectroscopy of lithium intercalation into microcrystalline graphite

The experiment was performed using a free-standing electrode where the active material was a synthetic, microcrystalline graphite (SFG6, TIMCAL, TIMREX®), physical properties of which are reported in Table 3.2. The *in situ* cell had an open circuit potential ca. 3.0 V (vs. Li^+/Li) and was galvanostatically cycled at 20 mA g^{-1} carbon (equivalent to a C-rate, as defined in Chapter 1, of C/19) between 5 mV and 1.5 V.

Table 3.2: Physical properties of SFG6 microcrystalline graphite.[37] The d90 value represents the particle size that 90 % (by mass) of the powder is smaller than. The L_c value will be discussed further in Chapter 4.

Particle size (d90)	**BET surface area**	**Out-of-plane crystallite size (L_c)**
5.5 – 7.5 µm	17 ^{2}/g	> 100 nm

Figure 35 shows the load curve for the first lithiation/delithiation cycle. The lithiation capacity of the first cycle exceeds the theoretical maximum of 372 mAh g^{-1} due to the partial reduction of electrolyte during the formation of the SEI. Raman spectra were collected at each numbered point on Figure 35; the corresponding Raman spectra are shown in Figure 36 alongside the potential (V vs. Li^+/Li) at which each spectrum was collected. All the spectra are base-line corrected and stacked arbitrarily up the y axis to allow for clear visualisation.

Raman spectra were collected from the same region of an individual graphite particle (see Chapter 2). At OCP (ca. 3.0 V vs. Li^+/Li) the D band (ca. 1330 cm^{-1}) was not apparent suggesting the selected region has a low defect density. Regardless, the D

band has been previously reported to lose signal intensity during the early stages of lithiation.[31] For this reason, the study has focussed on the most significant bands of the graphite sample, namely the G band at 1580 cm^{-1} and 2D band at ~2670 cm^{-1}. The constituent peak positions of these bands throughout electrochemical cycling are given alongside their full width half maximum (FWHM) in Table 3.2.

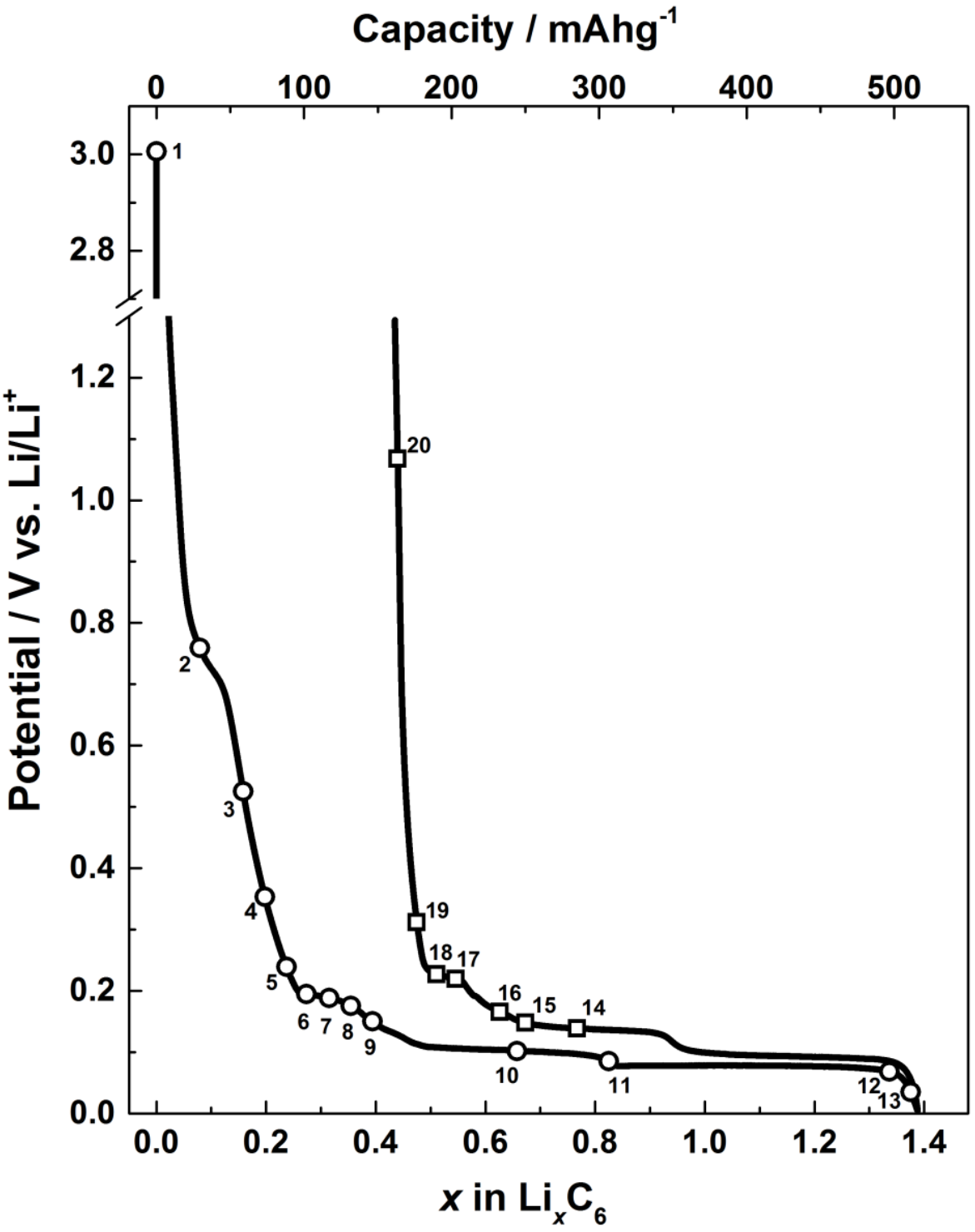

Figure 35: Potential vs. Capacity for the first lithiation/delithiation of SFG6 microcrystalline graphite with Raman spectra acquisition events marked (numbers correspond to Figure 36).

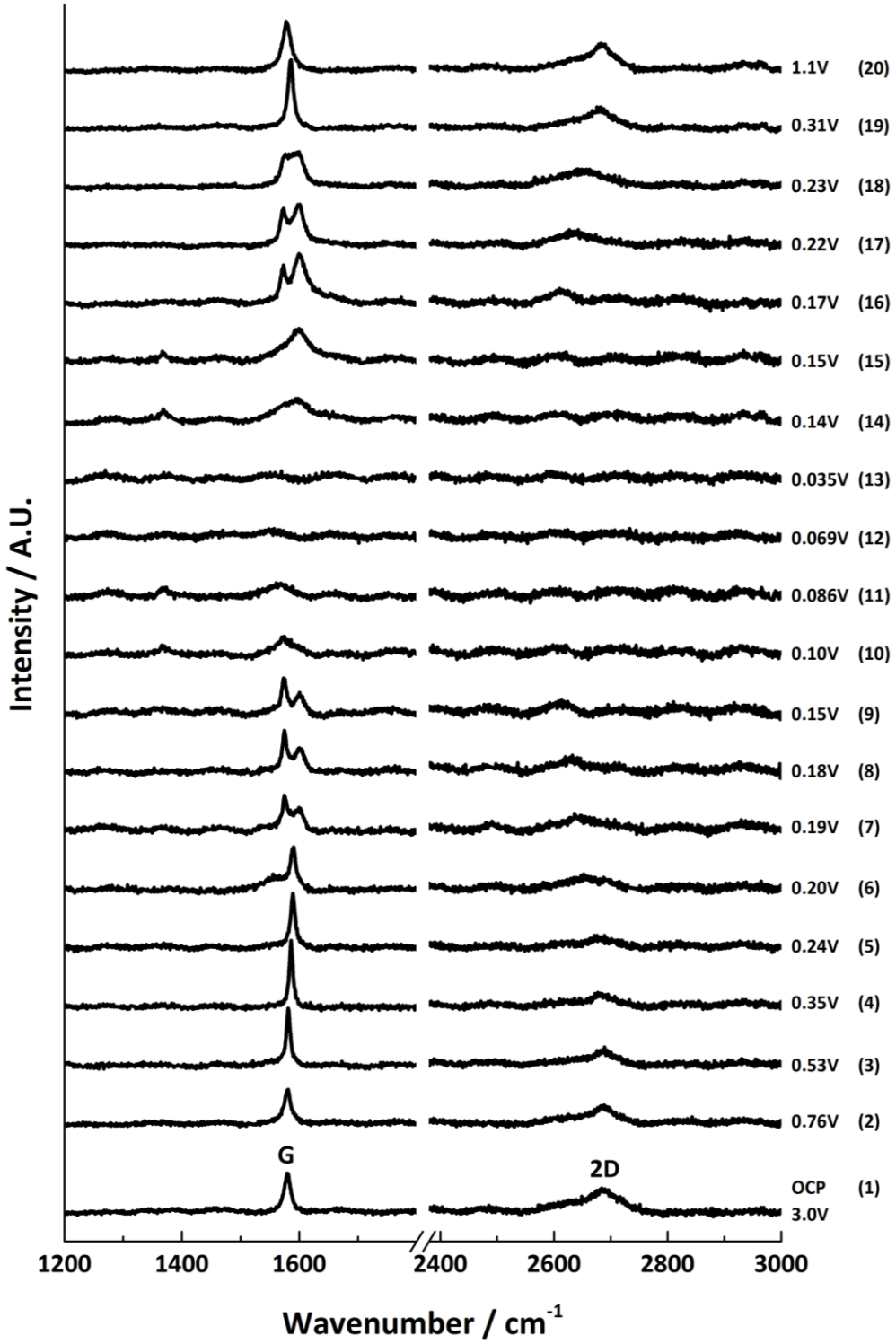

Figure 36: *In situ* Raman data showing the G and 2D band as a function of potential during the first lithiation/delithiation cycle of SFG6 microcrystalline graphite (numbers correspond to Figure 35).

Table 3.3: Wavenumber (cm^{-1}) and full-width-half-maxima (FWHM) of G and 2D bands recorded during the first lithiation/delithiation cycle of SFG6 microcrystalline graphite.

E(V)	G		E2g2(i)		E2g2(b)		2D(1)		2D(2)	
	ω (cm^{-1})	FWHM (cm^{-1})	ω (cm^{-1})	FWHM (cm^{-1})	ω (cm^{-1})	FWHM (cm^{-1})	ω (cm^{-1})	FWHM (cm^{-1})	ω (cm^{-1})	FWHM (cm^{-1})
3.00	1580	12	-	-	-	-	2625	61	2688	53
0.76	1580	14	-	-	-	-	2625	57	2687	50
0.53	1581	9	-	-	-	-	2632	68	2687	36
0.35	1586	7	-	-	-	-	2622	30	2683	35
0.24	1589	9	-	-	-	-	2615	27	2681	45
0.20	1590	11	-	-	-	-	-	-	2656	75
0.19	-	-	1576	12	1599	15	-	-	2646	73
0.18	-	-	1575	9	1600	15	-	-	2629	59
0.15	-	-	1574	11	1601	15	-	-	2611	31
0.10	-	-	-	-	1550	-	-	-	-	-
0.086	-	-	-	-	1540	-	-	-	-	-
0.069	-	-	-	-	-	-	-	-	-	-
0.035	-	-	-	-	-	-	-	-	-	-
0.14	-	-	-	-	1592	57	-	-	-	-
0.15	-	-	-	-	1598	44	-	-	-	-
0.17	-	-	1573	8	1601	30	-	-	2614	51
0.22	-	-	1573	11	1598	22	-	-	2636	73
0.23	-	-	1577	16	1597	23	-	-	2649	90
0.31	1586	11	-	-	-	-	2630	48	2682	45
1.10	1579	15	-	-	-	-	2635	60	2685	39

3.6.1. Lithiation cycle

In brief, the following was observed during lithiation:

- ca. 0.60 - 0.20 V - blue-shifting of the G band from 1580 cm^{-1} to 1590 cm^{-1}, accompanied by the gradual weakening (and eventual disappearance) of the 2D(1) band intensity.
- ca. 0.20 - 0.15 V - the formation of a doublet G band (E_{2g2}(i) and E_{2g2}(b) at 1575 cm^{-1} and 1601 cm^{-1} respectively), alongside a large red-shift of the 2D(2) band.
- ca. 0.10 – 0.07 V - loss of 2D band intensity alongside formation of a broad, red-shifted G band (~1550 cm^{-1}) and a weak peak around 1370 cm^{-1}.
- below 0.07 V - loss of all distinct Raman peak signals.

The *in situ* Raman spectra measured are discussed in detail below, with respect to the expected thermodynamic phase transitions.

3.6.2. Formation of solid electrolyte interphase and dilute stage 1 (ca. 1.0 – 0.20 V)

3.6.2.1. Shift and sharpening of G Band

There is no significant effect on the G band position of the SEI formation, which begins blow ca. 1.0 V (Figure 36, spectrum (2)).[38] However, ca. 0.6 - 0.2 V an upshift of the G band from 1580 cm^{-1} to 1590 cm^{-1} is observed (Figure 36, spectra (3 - 6)), which coincides with the beginning of lithium insertion between graphene sheets, which occurs ~ 0.55 V.[39] This can be observed on the load curve (Figure 35) as a sloping potential vs. capacity profile, indicating dilute stage 1 formation. The upshift of the G band position can be attributed to electronic doping of the graphene sheets as has been well studied in electrostatic doping experiments on single layer graphene.[40,41] As discussed in Chapter 1, electron doping of graphene sheets raises the Fermi level and causes the Kohn anomaly to move away from the Γ point in the phonon dispersion – resulting in a stiffening of the E_{2g2} vibrational mode. The magnitude of this shift has been previously explained at low levels of doping by a breakdown of the adiabatic Born-Oppenheimer (ABO) approximation.[40] The high frequency of the E_{2g2} mode at the Γ point is associated with atomic displacements of period ~ 3 fs,[40] which is faster than the typical electron-momentum relaxation times in graphite of a few hundred femtoseconds.[42,43] Therefore, electrons are prevented from relaxing their momenta to the instantaneous adiabatic ground state during the atomic displacement and phonon renormalisation must be explained by non-adiabatic electron-phonon coupling.[40]

The G band was observed to shift linearly with a potential slope of -28 ± 1 cm^{-1} V^{-1} as shown in Figure 37, which is similar to the value of -29 cm^{-1} V^{-1} determined by Shi et

al.[44] for a microcrystalline graphite material. The full width at half maximum (FWHM) initially narrows before broadening over this potential range. The narrowing of the G band has also been observed in doping experiments on graphene.[40,41,45] As the potential falls below ~ 0.24 V the FWHM increases which can be explained by the emerging signals of the doublet peaks associated with the stage 4L formation described below.

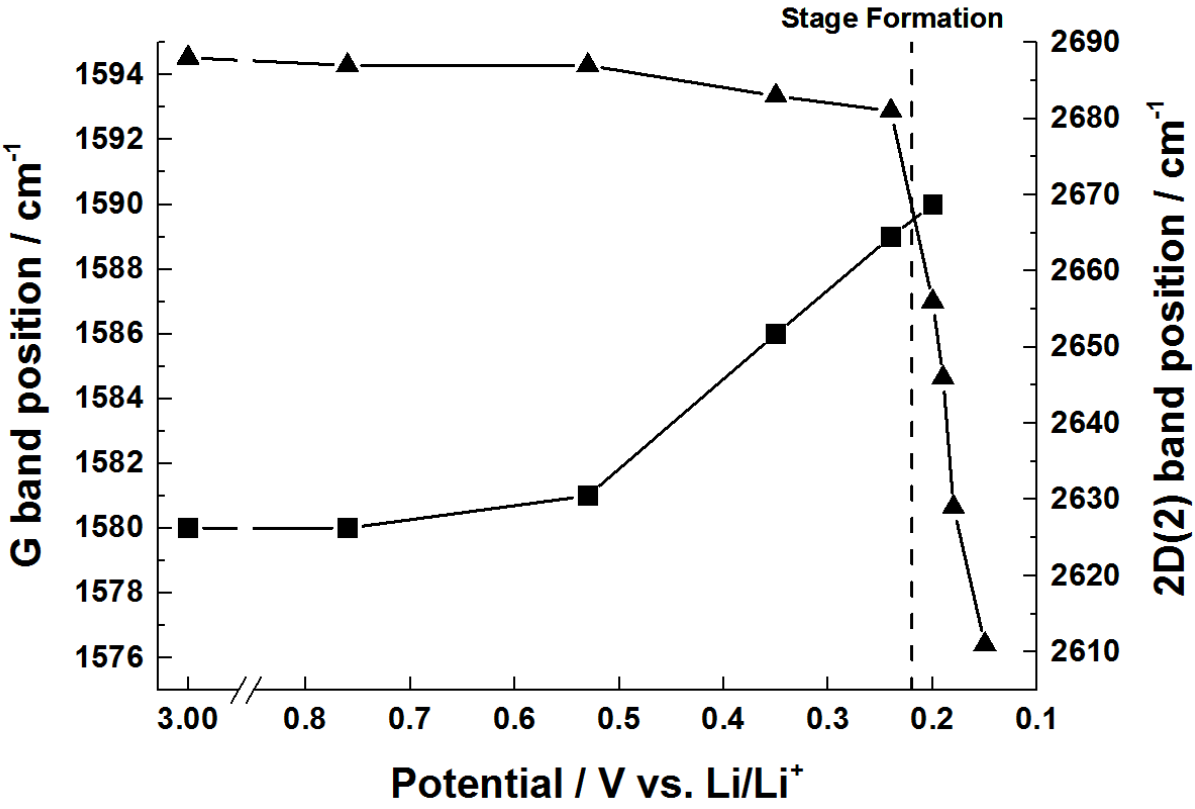

Figure 37: G band and 2D(2) band positions as a function of potential during first lithiation cycle of the SFG6 microcrystalline graphite electrode. The dashed line indicates the initiation of stage 4L formation.

3.6.2.2. 2D band red-shift

The 2D band position has been fitted by two peaks labelled 2D(1) and 2D(2) as described in Chapter 1. No significant change in band position was observed between

1.0 - 0.53 V; the region where SEI formation is expected to begin. This is in contrast to the behaviour of the D band which has been observed in previous studies to rapidly lose intensity over the same potential range.[46] However, no defects are required for activation of the 2D band and so it may be proposed that the weakening and eventual disappearance of the D band is linked to the surface passivation and lithiation of defects during the early stages of lithiation.

During dilute stage 1 formation (0.53 - 0.24 V) there is an apparent change in the shape of the 2D band and a gradual red-shift (softening) of the band position. The shape of the 2D peak is sensitive to the electronic coupling between graphene layers which is disrupted by the increasing concentration of intercalant species.[47,48] For peak fitting purposes the shape change has been explained by a reduction in 2D(1) peak intensity relative to the 2D(2) peak. Softening of both peak positions is observed. The 2D(2) peak position is shown in Figure 37 and displays a linear shift of ~ 21 ± 1 cm^{-1} V^{-1}.

3.6.3. Stage 4L and 3L formation (ca. 0.20 - 0.11 V)

3.6.3.1. G band doublet formation

The formation of the stage 4L GIC from the dilute stage 1 begins ca. 0.20 V, the existence of two distinct phases in equilibrium during the phase transition is indicated by the plateau in the voltage profile (Figure 35). This is followed by the formation of stage 3L ca. 0.19 - 0.15 V, whereby the extended slope in potential suggests a solid solution phase transition mechanism as previously proposed.[7,11,12]

It is well known that GICs with stage $n > 2$ exhibit a doublet G band in their Raman spectra. Therefore, the splitting of the singlet G peak into a distinct doublet between 0.19 - 0.11 V (Figure 38) confirms the presence of stage 4L and/or 3L phases. The splitting has been quantitatively explained by the phonon dispersion calculations of Al-Jishi and Dresselhaus,[49] but can be qualitatively understood by the nearest-layer model of Nemanich and Solin.[50]

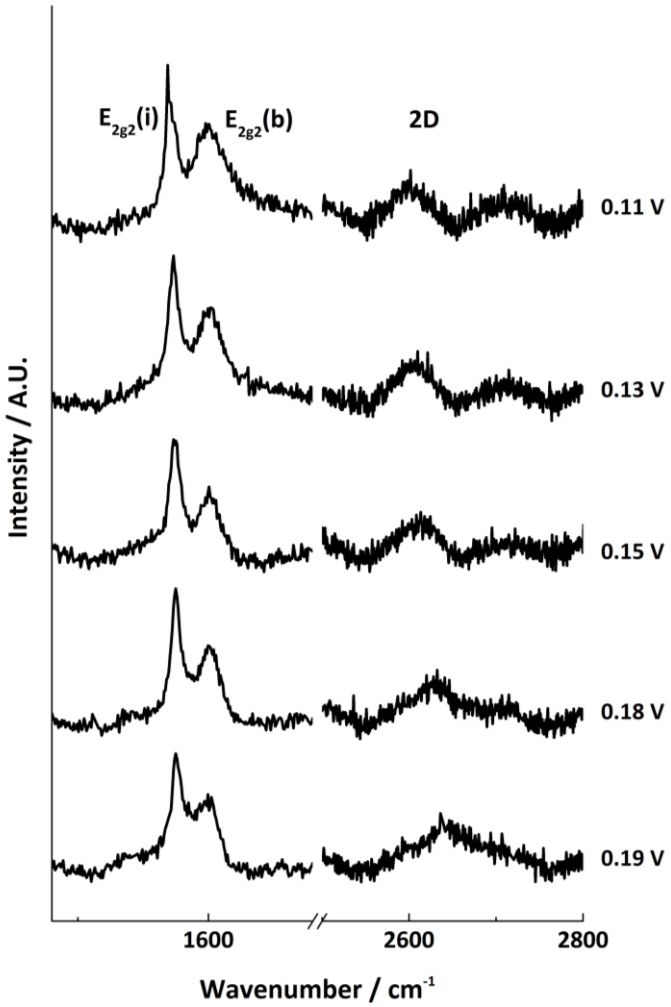

Figure 38: *In situ* Raman spectra between 0.19 – 0. 11 V, showing splitting of the G band into E_{2g2}(i) and E_{2g2}(b) modes, and red-shift of the 2D.

The nearest-layer model describes GICs by considering the different nearest-layer environments of graphene layers in the structure. Graphene layers may be defined as either bounding or interior layers depending on whether they are adjacent to (bounding) or non-adjacent to (interior) an intercalant layer as shown in Figure 39. By consideration of the Daumus-Hérold domains discussed earlier it is clear that each graphene layer consists of regions of bounding character and interior character. However, the size of these domains is large enough to cause distinct G band signals

for each environment. Therefore, the peaks are labelled E_{2g2}(i) and E_{2g2}(b) for the lower frequency interior and higher frequency bounding layer mode respectively.

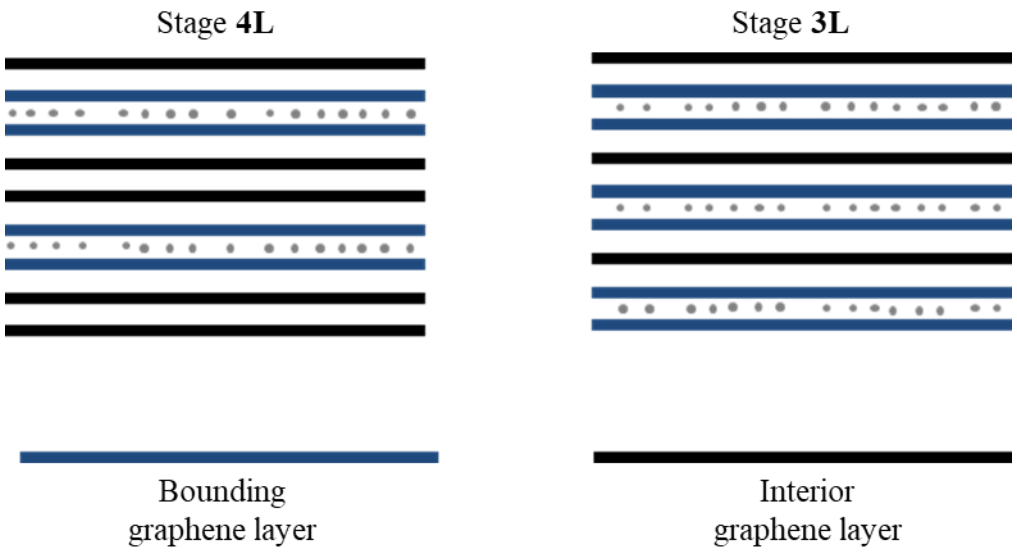

Figure 39: Definition of interior and bounding layers in stage 4L and 3L Li GICs. Grey spheres correspond to Li^+ ions.

The higher frequency of the E_{2g2}(b) mode corresponds to the increased electronic doping of bounding layers relative to interior layers. The inequivalent doping of graphene layers in higher stage (n > 2) GICs has been explained by numerous electronic band structure calculations and summarised elsewhere.[51,52] A simple model to describe the electronic structure of the inequivalent graphite layers was presented by Holzwarth:[51]

- The charge on each layer is assumed to be evenly distributed such that bounding and interior layers can be described as uniform sheets with charge per unit area of σ_b and σ_i respectively. Within this model the intercalant ions create no net fields due to symmetry and therefore do not need to be explicitly considered.

- Charge transfer to the bounding layers is assumed to be larger than to interior layers i.e. $\sigma_b > \sigma_i$, as predicted by electronic band structure calculations.[52,53] Therefore, a larger electric field will exist between the intercalant layer and the bounding graphene layers than the interior layers.
- The electrostatic potential of the bounding layers will hence be reduced relative to the interior layers. This is represented in Figure 40 by a realignment of the two-dimensional π bands according to the electrostatic potential of each layer. The energy of the bounding layer π bands is effectively reduced. Thus, for any given Fermi level there is a higher occupation of bounding layers, demonstrating that the assumption $\sigma_b > \sigma_i$ is self-consistent. Although this model ignores the interactions between graphite layers, the electrostatic energy shifts discussed are energetically comparable and in qualitative agreement with more realistic calculations.[52,54,55]

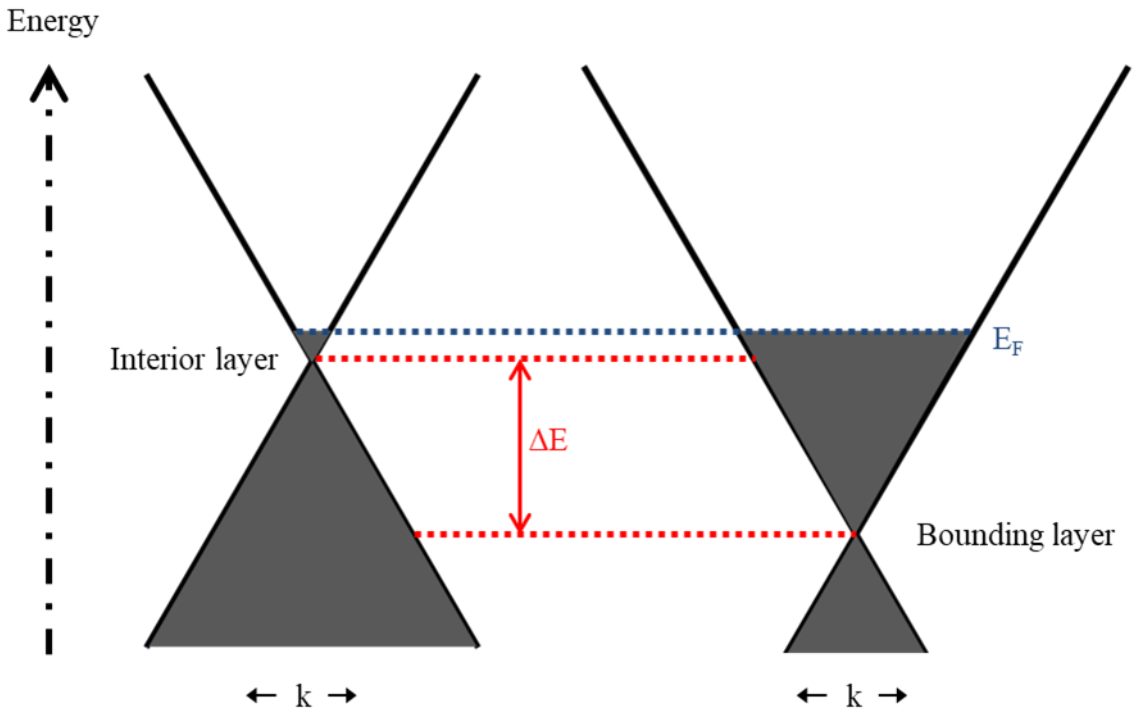

Figure 40: Schematic of π energy bands near the Fermi level for a stage 3 graphite intercalation compound, where ΔE represents the difference in electronic energy caused by inequivalent electrostatic potential (redrawn from [51]). Shaded regions indicate occupied states, E_F represents the Fermi level.

Raman spectroscopy has previously been used to estimate the intercalation stage index, *n* from the relative intensities of the G band doublet, *R*, using the following equation:[50]

$$R = \frac{I_i}{I_b} = \frac{\sigma_i}{\sigma_b}\,\frac{n-2}{2} \qquad (n > 2) \qquad \text{Equation 3.1}$$

Where I_i and I_b represent the intensities of the interior E_{2g2}(i) and bounding E_{2g2}(b) layer modes respectively, and σ_i / σ_b is a stage independent constant indicating the ratio of the Raman cross section for the E_{2g2}(i) and E_{2g2}(b) modes. Previous studies

have assumed σ_i / σ_b to be 1, thus using Equation 3.1 at 0.19 V gives an *R* value of ca. 1.0 which signifies the presence of stage 4L.

However, the value of *R* has been demonstrated to be highly dependent on laser wavelength for potassium GICs, suggesting σ_i / σ_b may also vary with wavelength.[56] Furthermore, caution should be taken when comparing intensity ratios across the literature – for example, using a 514.5 nm laser for stage 4 values of *R* ranging from ca. 0.8[27] to ca. 0.1[56] have been reported for alkali metal GICs, suggesting additional deviations due to the use of area or height for peak intensity calculations may be widespread. Regardless, the doublet G band is observable down to 0.11 V.

3.6.3.2. Shift and shape change of the 2D band

In contrast to the observed splitting of the G band, below 0.24 V the 2D band appears to resemble a single Lorentzian peak. This analysis assumes the 2D(1) peak is no longer discernible continuing the loss in intensity observed above and the peak position has been assigned to the red-shifted 2D(2) peak. The presence of a single peak suggests electronic decoupling of layers such as occurs in single layer graphene or turbostratic graphite.[57] Chacón-Torres et al.[56] have recently suggested that stage 4 donor GICs should display a similar electronic structure to bilayer graphene and hence display a complex 2D band shape. However, Raman spectra of stage 4 $SbCl_5$-GIC and Rb-GIC reported by Eklund et al.[36] strongly suggest the presence of a single peak. Furthermore, as the 2D band is highly sensitive to electronic structure, the inequivalent electronic doping of interior and bounding layers should also lead to a complex 2D band line-shape. However, the resonant process responsible for the 2D band is known to be forbidden due to Pauli blocking in highly charged graphene layers.[48] In this case it will

occur when the laser energy (E_L) < 2($\Delta E + E_F$), as shown in Figure 41 (where ΔE is the decrease of the bounding layer energy relative to the interior layers). Therefore, it is thought that the 2D band is present only for the interior layers and forbidden for bounding layers as previously predicted.[56,58]

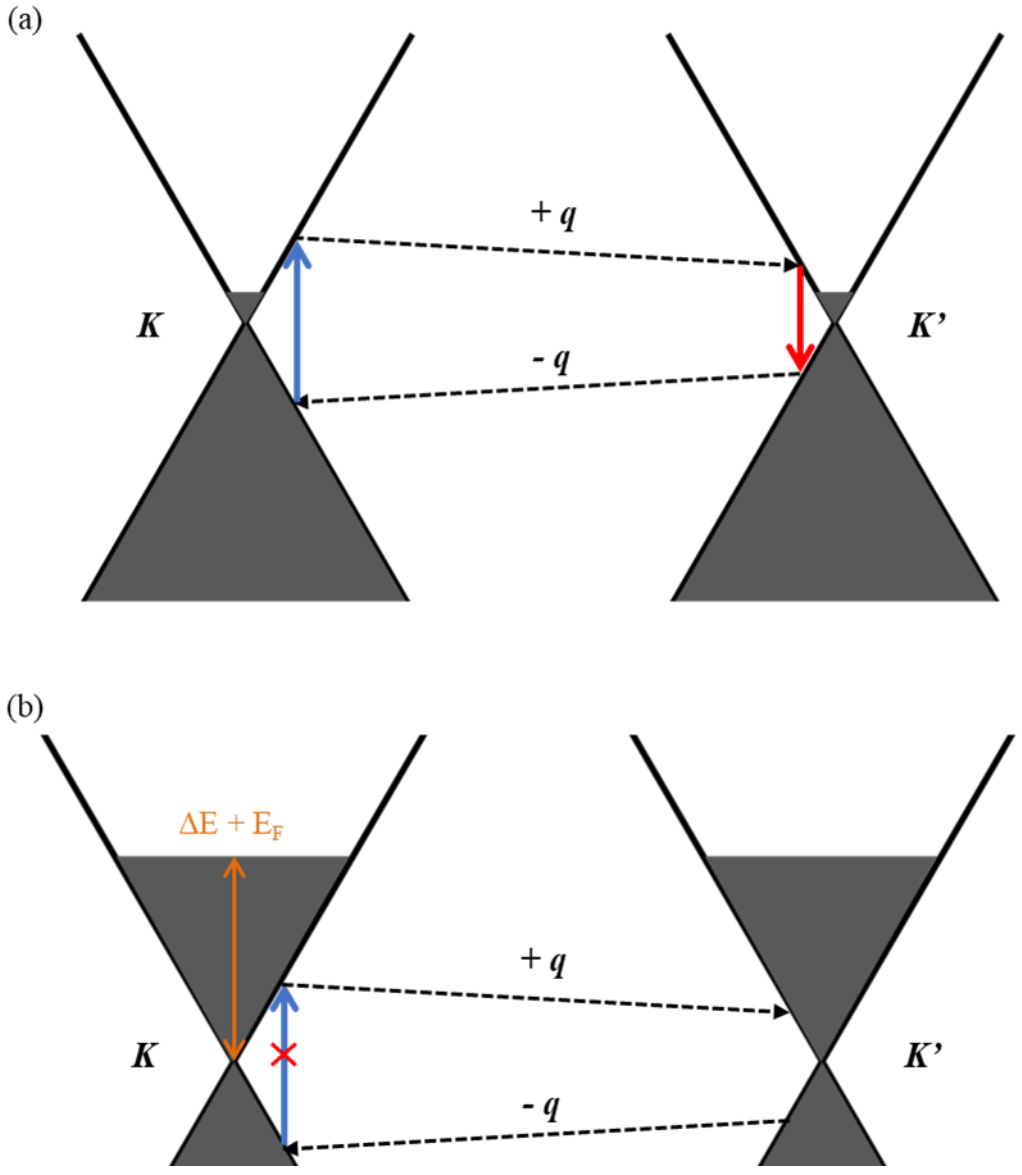

Figure 41: Resonant Raman process for 2D band in (a) interior layer and (b) bounding layer. The electronic excitation is forbidden for the bounding layer when laser energy (E_L) < 2($\Delta E + E_F$) due to occupation of the available excited states (known as Pauli blocking).

Figure 37 shows that below 0.20 V, accompanying the onset of stage 4L formation, the red-shift of the 2D(2) peak significantly increases to a rate of 802 ± 87 cm^{-1} V^{-1}. Whereas the G band was observed to blue-shift with electron doping, the 2D band is known to red-shift.[35,56] Li intercalation causes occupation of the π^* anti-bonding band, which produces a weakening and elongation of the intra-layer C-C bonds within the graphene sheets.[16,59,60] Figure 42 shows that with increasing reciprocal stage number ($1/n$), the C-C bond length has been shown to increase by XRD. Significantly, although there is a larger electronic doping of the bounding than the interior layers, XRD data suggests similar in-plane expansion of all layers suggesting the mismatch of lattice parameters in adjacent layers is energetically disfavourable.[58] Furthermore, Pietronero and Strässler[60] have used this behaviour to estimate the charge concentration on graphene sheets directly from the measured C-C bond length.

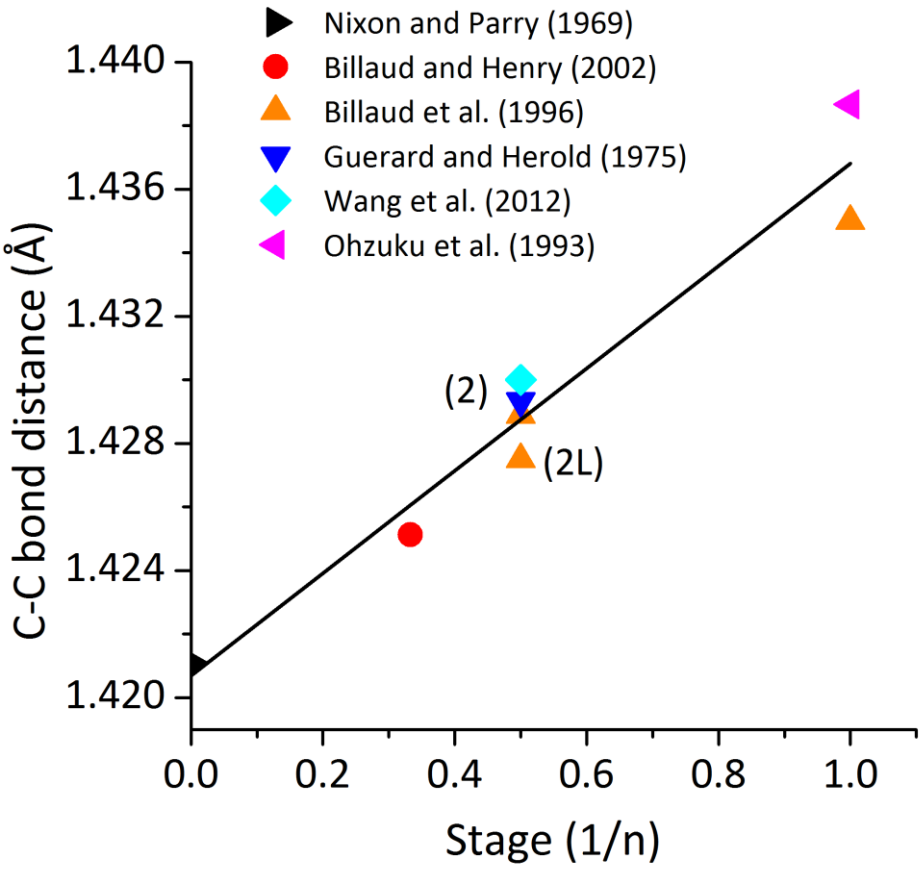

Figure 42: C-C bond length (Å) versus inverse stage (1/n) from crystallographic data.[11,12,14,16,19,20] Trend line is plotted in black, numbers in brackets distinguish lattice parameters reported for stage 2L and stage 2 phases.

Significantly, the continuous nature of the 2D band red-shift between 0.24 - 0.15 V suggests there is a continuous increase in electronic doping during the stage 4L to 3L phase transition. This provides further evidence for the solid solution phase transition mechanism suggested by *in situ* XRD measurements, where a continuous increase in Li^+ concentration occurs rather than a separation into two distinct phases.[7,11,12]

Finally, as mentioned above, the Daumus-Hérold model of intercalation suggests there may be an additional source of strain due to the distortion of graphene sheets at domain boundaries. However, this would suggest larger intercalants would produce more

structural strain and hence larger 2D band red-shifts, which has not been observed in the literature.[34,36,56]

3.6.4. Stage 2 and 1 formation (0.10 – 0.005 V)

3.6.4.1. G band behaviour

Between 0.10 V and 0.069 V the doublet G band is no longer clearly discernible (which suggests the presence of a stage 2 compound where no interior layers exist. Spectrum 10 (at 0.10 V) lies within a large plateau in the voltage profile (Figure 35) supporting the phase transition of stage 2L to stage 2 by a two phase reaction. A band ca. 1601 cm^{-1} has been reported for chemically intercalated stage 2 Li GIC,[58] however, in contrast Figure 36 displays a broad asymmetric band ca. 1550 cm^{-1} which is assigned to the red-shifted E_{2g2}(b) mode. This broad band is last observed at ca. 1540 cm^{-1} in spectrum 11 (0.086 V) before disappearing into the noise.

The red-shift of this band may also be explained by the increase in C-C bond lengths as discussed above. A similar red-shifted G band position was observed by Zabel et al. when graphene sheets were subjected to biaxial strain (C-C bond length expansion) by the application of ca. 1 bar of pressure.[61] Such an effect has also been observed for the intercalation of donor species into less ordered carbon materials.[62–64] The asymmetric band ca. 1550 cm^{-1} may therefore be assigned to a stage 2 liquid phase whilst the redshifted mode at ca. 1540 cm^{-1} is assigned to the dense stage 2 phase. It should be noted that the appearance of a weak peak ca. 1370 cm^{-1} has also been observed during this region. This peak has previously been observed in low-stage alkali metal GICs and assigned to the A_{1g} vibration, corresponding to the D band.[65] However, no explanation for the unexpected reappearance of this mode has been proposed.

During the final plateau in the voltage profile ca. 0.08 V, a phase transition from the dense stage 2 to stage 1 phases is expected. Raman signals of stage 1 LiC_6 compounds

are reported in the literature with a distinct asymmetric feature due to electron-phonon coupling effects.[65] However, Figure 36 (spectra 12 – 13) shows that no Raman bands are visible during this region. This may explained by a decrease in Raman scattering intensity of the heavily doped stage 1 compounds, due to a reduction in optical skin depth,[27] which results in an insufficient signal-to-noise ratio in the *in situ* cell.

3.6.4.2. 2D band disappearance

The 2D band is no longer observable below 0.10 V upon the formation of the stage 2 and stage 1 compounds (Figure 36, spectra 10 – 13). As discussed, there are no interior layers in the low stage GICs and therefore the disappearance of the 2D band is linked to Pauli blocking of the resonant Raman process in bounding layers as shown in Figure 41(b).

3.6.5. Delithiation cycle

During the delithiation cycle the reverse processes occur, although at slightly higher potential due to polarisation (Figure 35 and Figure 36). At 0.14 V, the reappearance of the unassigned peak at 1370 cm^{-1} occurs, in addition to the E_{2g2}(b) mode of stage 2L at 1592 cm^{-1} (spectrum 14). The E_{2g2}(b) mode upshifts to 1601 cm^{-1} and increases in intensity as the potential is increased to 0.15 V (spectrum 15). The increased frequency indicates a shorter C-C bond length and hence a lower in-plane Li^+ density, which can be inferred from the position of the spectral acquisitions on the voltage profile.

At 0.17 V, the lower frequency E_{2g2}(i) mode emerges at 1373 cm^{-1} accompanied by the reappearance of the 2D(2) peak at 2614 cm^{-1}, indicating the formation of stage 3L. As the potential is increased the phase transition from stage 3L to 4L occurs, inducing a change in the value of *R* (defined by Equation 3.1) and a blue-shift of the 2D(2) peak. By 0.31 V (spectrum 19), the doublet G band has returned to the single upshifted E_{2g2} mode of the dilute stage 1 compound at 1586 cm^{-1}. This accompanies the reformation of the double peak line-shape of the 2D band, suggesting renewal of electronic coupling between graphene layers.

Finally, between 0.31 – 1.1 V both the G and 2D bands shift back to their OCP positions (prior to lithiation) with only minor deviations in wavenumber (Figure 9). Furthermore, no increase in the intensity of the D band relative to the G band was observed, which indicates that there was no significant increase in structural disorder of the graphite particle measured.[66]

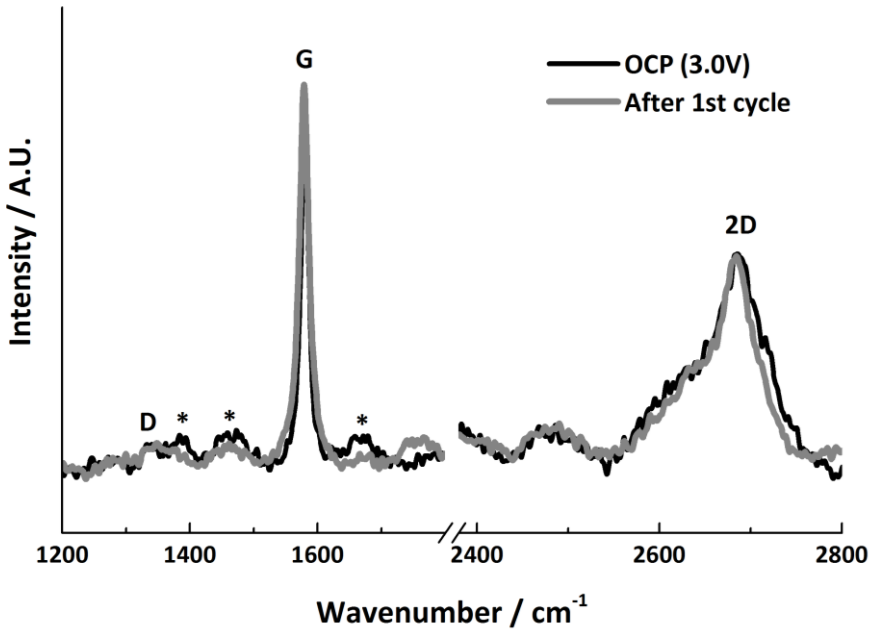

Figure 43: *In situ* Raman spectra before and after lithiation, * indicates signal from electrolyte bands.

3.7. Conclusions

In summary, *in situ* Raman spectra were collected throughout the first lithiation/delithiation cycle of a microcrystalline graphite electrode in 1M $LiPF_6$ in EC-DMC electrolyte. Reversible cycling was demonstrated without significant structural changes to the particle investigated. Spectral changes of the G band were observed in agreement with previous studies, including the characteristic band splitting during the stage 4L to 3L region and a broadened, red-shifted G band during the stage 2 region (accompanied by a new band ca. 1370 cm^{-1}). However, no Raman bands were observed during the stage 1 region, which was linked to a reduced signal-to-noise ratio for this compound. Significantly, the 2D band behaviour has also been reported. A large red-shift of the 2D band was observed during the stage 4L to 3L phase transition which has been linked to the increase in C-C bond lengths; whilst the continuous nature of the band-shift supports previous empirical evidence for the presence of a solid solution mechanism. The disappearance of the 2D band for stage ≤ 2 phases has been linked to Pauli blocking of the resonant Raman process.

3.8. References

(1) Gao, J.; Shi, S.-Q.; Li, H. Brief Overview of Electrochemical Potential in Lithium Ion Batteries. *Chinese Phys. B* **2016**, *25* (1), 18210.

(2) Li, D.; Zhou, H. Two-Phase Transition of Li-Intercalation Compounds in Li-Ion Batteries. *Mater. Today* **2014**, *17* (9), 451–463.

(3) Yabuuchi, N.; Ohzuku, T. Novel Lithium Insertion Material of $LiCo_{1/3}Ni_{1/3}Mn_{1/3}O_2$ for Advanced Lithium-Ion Batteries. *J. Power Sources* **2003**, *119–121*, 171–174.

(4) Owen, J.; Hector, A. Phase-Transforming Electrodes. *Science* **2014**, *344* (6191), 1451–1452.

(5) Liu, H.; Strobridge, F. C.; Borkiewicz, O. J.; Wiaderek, K. M.; Chapman, K. W.; Chupas, P. J.; Grey, C. P. Capturing Metastable Structures during High-Rate Cycling of $LiFePO_4$ Nanoparticle Electrodes. *Science* **2014**, *344* (6191), 1252817–1252817.

(6) Enoki, T.; Suzuki, M.; Endo, M. *Graphite Intercalation Compounds and Applications*; Oxford University Press: New York, 2003.

(7) Dahn, J. R. Phase Diagram of Li_xC_6. *Phys. Rev. B* **1991**, *44* (17), 9170–9177.

(8) Heß, M.; Novak, P. Shrinking Annuli Mechanism and Stage-Dependent Rate Capability of Thin-Layer Graphite Electrodes for Lithium-Ion Batteries. *Electrochim. Acta* **2013**, *106*, 149–158.

(9) Woo, K. C.; Mertwoy, H.; Fischer, J. E.; Kamitakahara, W. A.; Robinson, D. S. Experimental Phase Diagram of Lithium-Intercalated Graphite. *Phys. Rev. B* **1983**, *27* (12), 7831–7834.

(10) Chung, D. D. L. Review: Graphite. *J. Mater. Sci.* **2002**, *37*, 1475–1489.

(11) Billaud, D.; Henry, F. X.; Lelaurain, M.; Willmann, P. Revisited Structures of Dense and Dilute Stage II Lithium-Graphite Intercalation Compounds. *J. Phys. Chem. Solids* **1996**, *57* (6–8), 775–781.

(12) Billaud, D.; Henry, F. X. Structural Studies of the Stage III Lithium-Graphite Intercalation Compound. *Solid State Commun.* **2002**, *124* (8), 299–304.

(13) Woo, K. C.; Kamitakahara, W. A.; DiVincenzo, D. P.; Robinson, D. S.; Mertwoy, H.; Milliken, J. W.; Fischer, J. E. Effect of In-Plane Density on the Structural and Elastic Properties of Graphite Intercalation Compounds. *Phys. Rev. Lett.* **1983**, *50* (3), 182–185.

(14) Ohzuku, T.; Iwakoshi, Y.; Sawai, K. Formation of Lithium-Graphite Intercalation Compounds in Nonaqueous Electrolytes and Their Application as a Negative Electrode for a Lithium Ion (Shuttlecock) Cell. *J. Electrochem. Soc.* **1993**, *140* (9), 2490.

(15) Heß, M. Kinetics and Stage Transitions of Graphite for Lithium-Ion Batteries, PhD thesis. ETH / PSI, 2013.

(16) Nixon, D. E.; Parry, G. S. The Expansion of the Carbon-Carbon Bond Length in Potassium Graphites. *J. Phys. C Solid State Phys.* **1969**, *2* (10), 1732–1741.

(17) Hofmann, U.; Wilm, D. Über Die Kristallstruktur Von Kohlenstoff. *Berichte der Bunsengesellschaft für Phys. Chemie* **1936**, *42* (7B), 504–522.

(18) Trucano, P.; Chen, R. Structure of Graphite by Neutron Diffraction. *Nature* **1975**, *258* (5531), 136–137.

(19) Guerard, D.; Herold, A. Intercalation of Lithium into Graphite and Other Carbons. *Carbon* **1975**, *13* (4), 337–345.

(20) Wang, X.-L.; An, K.; Cai, L.; Feng, Z.; Nagler, S. E.; Daniel, C.; Rhodes, K. J.; Stoica, A. D.; Skorpenske, H. D.; Liang, C.; et al. Visualizing the Chemistry and Structure Dynamics in Lithium-Ion Batteries by in-Situ Neutron Diffraction. *Sci. Rep.* **2012**, *2* (747).

(21) Daumas, N.; Herold, A. Untitled. *C. R. Seances Acad. Sci. Ser. C* **1969**, *268*, 373–375.

(22) Krishnan, S.; Brenet, G.; Machado-Charry, E.; Caliste, D.; Genovese, L.; Deutsch, T.; Pochet, P. Revisiting the Domain Model for Lithium Intercalated Graphite. *Appl. Phys. Lett.* **2013**, *103* (25), 251904.

(23) Ulloa, Sergio E.; Kirczenow, G. Nonlinear Theory of Domain Walls and the Anomalies of Intercalation Kinetics. *Phys. Rev. Lett.* **1985**, *55* (2), 4–7.

(24) Anderson Axdal, S. H.; Chung, D. D. L. A Theory for the Kinetics of Intercalation of Graphite. *Carbon* **1987**, *25* (3), 377–389.

(25) Wang, F.; Graetz, J.; Moreno, M. S.; Ma, C.; Wu, L.; Volkov, V.; Zhu, Y. Chemical Distribution and Bonding of Lithium in Intercalated Graphite: Identification with Optimized Electron Energy Loss Spectroscopy. *ACS Nano* **2011**, *5* (2), 1190–1197.

(26) Kirczenow, G. Interference Phenomena in the Theory of Daumas-Hérold Domain Walls. *Phys. Rev. Lett.* **1982**, *49* (25), 1853–1856.

(27) Inaba, M.; Yoshida, H.; Ogumi, Z.; Abe, T.; Mizutani, Y.; Asano, M. In Situ Raman Study on Electrochemical Li Intercalation into Graphite. *J. Electrochem. Soc.* **1995**, *142* (1), 20–26.

(28) Stancovski, V.; Badilescu, S. In Situ Raman Spectroscopic-Electrochemical Studies of Lithium-Ion Battery Materials: A Historical Overview. *J. Appl. Electrochem.* **2014**, *44* (1), 23–43.

(29) Baddour-Hadjean, R.; Pereira-Ramos, J.-P. Raman Microspectrometry Applied to the Study of Electrode Materials for Lithium Batteries. *Chem. Rev.* **2010**, *110* (3), 1278–1319.

(30) Migge, S.; Sandmann, G.; Rahner, D.; Dietz, H.; Plieth, W. Studying Lithium Intercalation into Graphite Particles via in Situ Raman Spectroscopy and Confocal Microscopy. *J. Solid State Electrochem.* **2004**, *9* (3), 132–137.

(31) Hardwick, L. J.; Buqa, H.; Novák, P. Graphite Surface Disorder Detection Using in Situ Raman Microscopy. *Solid State Ionics* **2006**, *177*, 2801–2806.

(32) Dimiev, A. M.; Ceriotti, G.; Behabtu, N.; Zakhidov, D.; Pasquali, M.; Saito, R.; Tour, J. M. Direct Real-Time Monitoring of Stage Transitions in Graphite Intercalation Compounds. *ACS Nano* **2013**, *7* (3), 2773–2780.

(33) Hardwick, L. J.; Buqa, H.; Holzapfel, M.; Scheifele, W.; Krumeich, F.; Novak, P. Behaviour of Highly Crystalline Graphitic Materials in Lithium-Ion Cells with Propylene Carbonate Containing Electrolytes: An in Situ Raman and SEM Study. *Electrochim. Acta* **2007**, *52* (15), 4884–4891.

(34) Hardwick, L. J.; Hahn, M.; Ruch, P.; Holzapfel, M.; Scheifele, W.; Buqa, H.; Krumeich, F.; Novák, P.; Kötz, R. An in Situ Raman Study of the Intercalation of Supercapacitor-Type Electrolyte into Microcrystalline Graphite. *Electrochim. Acta* **2006**, *52* (2), 675–680.

(35) Parret, R.; Paillet, M.; Huntzinger, J.-R.; Nakabayashi, D.; Michel, T.; Tiberj, A.; Sauvajol, J.-L.; Zahab, A. A. In Situ Raman Probing of Graphene over a Broad Doping Range upon Rubidium Vapor Exposure. *ACS Nano* **2013**, *7* (1), 165–173.

(36) Eklund, P. C.; Giergiel, J.; Boolchand, P. *Physics of Intercalation Compounds : Proceedings of an International Conference Trieste, Italy, July 6-10, 1981*; Pietronero, L., Tosatti, E., Eds.; Springer Berlin Heidelberg, 1981.

(37) TIMCAL TIMREX® SFG6 Primary Synthetic Graphite (material property data sheet) http://www.matweb.com/search/datasheet.aspx?matguid=7ccdb40c6318412eb847b97a27876491&ckck=1 (accessed Sep 18, 2017).

(38) Aurbach, D. Review of Selected Electrode–solution Interactions Which Determine the Performance of Li and Li Ion Batteries. *J. Power Sources* **2000**, *89* (2), 206–218.

(39) Huang, W.; Frech, R. In Situ Raman Studies of Graphite Surface Structures during Lithium Electrochemical Intercalation. *J. Electrochem. Soc.* **1998**, *145* (3), 765–770.

(40) Pisana, S.; Lazzeri, M.; Casiraghi, C.; Novoselov, K. S.; Geim, A. K.; Ferrari, A. C.; Mauri, F. Breakdown of the Adiabatic Born-Oppenheimer Approximation in Graphene. *Nat. Mater.* **2007**, *6* (3), 198–201.

(41) Yan, J.; Zhang, Y.; Kim, P.; Pinczuk, A. Electric Field Effect Tuning of Electron-Phonon Coupling in Graphene. *Phys. Rev. Lett.* **2007**, *98* (16), 166802.

(42) Kampfrath, T.; Perfetti, L.; Schapper, F.; Frischkorn, C.; Wolf, M. Strongly Coupled Optical Phonons in the Ultrafast Dynamics of the Electronic Energy and Current Relaxation in Graphite. *Phys. Rev. Lett.* **2005**, *95* (18), 187403.

(43) Moos, G.; Gahl, C.; Fasel, R.; Wolf, M.; Hertel, T. Anisotropy of Quasiparticle Lifetimes and the Role of Disorder in Graphite from Ultrafast Time-Resolved Photoemission Spectroscopy. *Phys. Rev. Lett.* **2001**, *87* (26), 267402.

(44) Shi, Q.; Dokko, K.; Scherson, D. A. In Situ Raman Microscopy of a Single Graphite Microflake Electrode in a Li^+-Containing Electrolyte. *J. Phys. Chem. B* **2004**, *108*, 4789–4793.

(45) Das, A.; Pisana, S.; Piscanec, S.; Chakraborty, B.; Saha, S. K.; Waghmare, U. V.; Yiang, R.; Krishnamurhthy, H. R.; Geim, A. K.; Ferrari, A. C.; et al. Electrochemically Top Gated Graphene: Monitoring Dopants by Raman Scattering. *Nat. Nanotechnol.*

2007, *3* (4), 210–215.

(46) Hardwick, L. J.; Buqa, H.; Novak, P. Graphite Surface Disorder Detection Using in Situ Raman Microscopy. *Solid State Ionics* **2006**, *177* (26–32), 2801–2806.

(47) Zhao, W.; Tan, P. H.; Liu, J.; Ferrari, A. C. Intercalation of Few-Layer Graphite Flakes with $FeCl_3$: Raman Determination of Fermi Level, Layer by Layer Decoupling, and Stability. *J. Am. Chem. Soc.* **2011**, *133*, 5941–5946.

(48) Ferrari, A. C.; Basko, D. M. Raman Spectroscopy as a Versatile Tool for Studying the Properties of Graphene. *Nat. Nanotechnol.* **2013**, *8* (4), 235–246.

(49) Al-Jishi, R.; Dresselhaus, G. Lattice-Dynamical Model for Alkali-Metal-Graphite Intercalation Compounds. *Phys. Rev. B* **1982**, *26* (8), 4523–4538.

(50) Solin, S. A. *Graphite Intercalation Compounds*; Zabal, H., Solin, S. A., Eds.; Springer-Verlag: Berlin, 1990; Vol. I.

(51) Holzwarth, N. A. W. Electronic Band Structure of Graphite Intercalation Compounds. In *Graphite Intercalation Compounds II : Transport and Electronic Properties*; Zabel, H., Solin, S. A., Eds.; Springer Berlin Heidelberg, 1992; pp 7–48.

(52) Chacón-Torres, J. C.; Wirtz, L.; Pichler, T. Raman Spectroscopy of Graphite Intercalation Compounds: Charge Transfer, Strain, and Electron-Phonon Coupling in Graphene Layers. *Phys. Status Solidi* **2014**, *251* (12), 2337–2355.

(53) Holzwarth, N. A. W.; Louie, S. G.; Rabii, S. Lithium-Intercalated Graphite: Self-Consistent Electronic Structure for Stages One, Two, and Three. *Phys. Rev. B* **1983**, *28* (2), 1013–1025.

(54) Leung, S. Y.; Dresselhaus, G. Dispersion Relations in Graphite Intercalation Compounds: Electronic Energy Bands. *Phys. Rev. B* **1981**, *24* (6), 3490–3504.

(55) Holzwarth, N. A. W. Graphite Intercalation Compounds: A Simple Model of Fermi Surface and Transport Properties. *Phys. Rev. B* **1980**, *21* (8), 3665–3674.

(56) Chacón-Torres, J. C.; Wirtz, L.; Pichler, T. Manifestation of Charged and Strained Graphene Layers in the Raman Response of Graphite Intercalation Compounds. *ACS Nano* **2013**, *7* (10), 9249–9259.

(57) Malard, L. M.; Pimenta, M. A.; Dresselhaus, G.; Dresselhaus, M. S. Raman Spectroscopy in Graphene. *Phys. Rep.* **2009**, *473* (5–6), 51–87.

(58) Dresselhaus, M. S.; Dresselhaus, G. Intercalation Compounds of Graphite. *Adv. Phys.* **2002**, *51* (1), 1–186.

(59) Kertesz, M. Changes of Lattice Geometries Upon Charge Transferle. *Mol. Cryst. Liq. Cryst.* **1985**, *126* (1), 103–110.

(60) Pietronero, L.; Strassler, S. Bond-Length Change as a Tool to Determine Charge Transfer and Electron Phonon Coupling in Graphite Intercalation Compounds. *Phys. Rev. Lett.* **1981**, *47*, 593–596.

(61) Zabel, J.; Nair, R. R.; Ott, A.; Georgiou, T.; Geim, A. K.; Novoselov, K. S.; Casiraghi,

C. Raman Spectroscopy of Graphene and Bilayer under Biaxial Strain: Bubbles and Balloons. *Nano Lett.* **2012**, *12* (2), 617–621.

(62) Inaba, M.; Yoshida, H.; Ogumi, Z. In Situ Raman Study of Electrochemical Lithium Insertion into Mesocarbon Microbeads Heat-Treated at Various Temperature. *J. Electrochem. Soc.* **1996**, *143* (8), 2572–2578.

(63) Endo, M.; Kim, C.; Karaki, T.; Fujino, T.; Matthews, M. J.; Brown, S. D. M.; Dresselhaus, M. S. In Situ Raman Study of PPP-Based Disordered Carbon as an Anode in a Li Ion Battery. *Synth. Met.* **1998**, *98* (1), 17–24.

(64) Wang, Z. X.; Huang, X. J.; Xue, R. J.; Chen, L. Q. A New Possible Mechanism of Lithium Insertion and Extraction in Low-Temperature Pyrolytic Carbon Electrode. *Carbon* **1999**, *37* (4), 685–692.

(65) Pichler, T.; Ganin, A. Y.; Rosseinsky, M. J. Raman Response of Stage-1 Graphite Intercalation Compounds Revisited. *Phys. Rev. B* **2012**, *86* (75406), 1–6.

(66) Ferrari, A. C.; Robertson, J. Interpretation of Raman Spectra of Disordered and Amorphous Carbon. *Phys. Rev. B* **2000**, *61* (20), 14095–14107.

4. The role of re-aggregation on the Li intercalation behaviour of electrochemically exfoliated microcrystalline graphite

4.1. Overview of chapter

This chapter examines the Li intercalation behaviour of an electrochemically exfoliated microcrystalline graphite material with a focus on the role of re-aggregation. Structural characterisation of a sample modified by a cathodic electrochemical exfoliation process is presented, which reveals significant restacking of the exfoliated flakes and only subtle differences with the pristine microcrystalline graphite. A comparison of the Li intercalation behaviour is then presented through electrochemical charge/discharge cycling and *in situ* Raman spectroscopy. The Raman spectra are analysed with respect to the shift and shape change of the 2D band and a preliminary model for the estimation of C-C bond lengths and explanation of the E_{2g2}(i) and E_{2g2}(b) mode frequencies (for the stage 4L and 3L phases) is presented.

4.2. Solid state diffusion limitations in graphitic negative electrodes for lithium ion batteries

Microcrystalline graphite particles are composed of partially oriented crystallites as shown in Figure 44(a), defined by average structural parameters L_a and L_c: the in-plane and out of plane crystallite size respectively. The rate of (de)intercalation of Li in graphite is limited by solid state diffusion also described by Fick's first law (Equation 1.16). Anisometric Li diffusion has been observed in graphite whereby Li diffusion parallel to graphene sheets is several orders of magnitude faster (~ 10^{-7} cm^2 s^{-1}) than diffusion perpendicular to sheets (along crystallite grain boundaries) (~ 10^{-11} cm^2 s^{-1}), as indicated shown in Figure 44(a).[1]

(a)

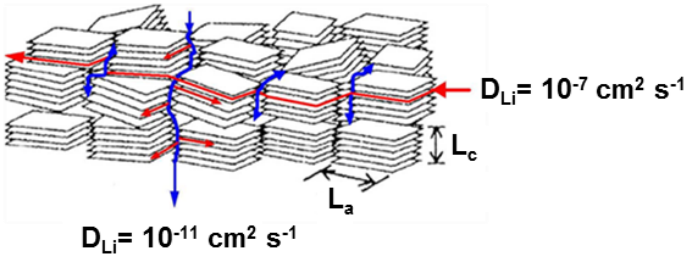

(b)

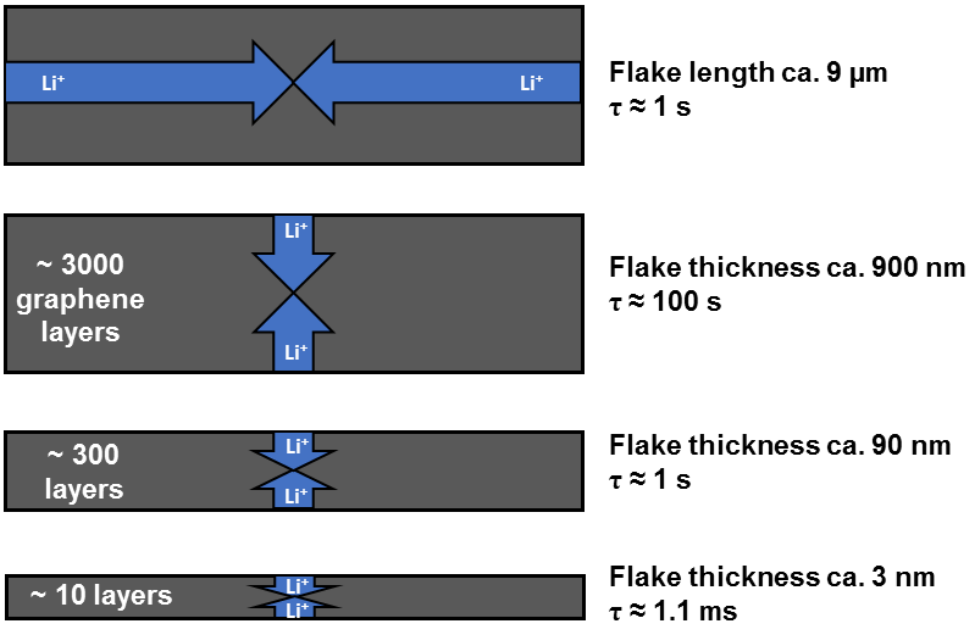

Figure 44: (a) Schematic of Li^+ ion diffusion through microcrystalline graphite particles. Individual particles are composed of crystallites defined by parameters L_a and L_c. Possible diffusion pathways of Li^+ ions perpendicular (blue) and parallel (red) to graphene sheets are indicated.[2] (b) Design principle and diffusion times for increasing rate performance of graphitic negative electrodes through reducing particle thickness.

It has been proposed that the design of graphite particles with increased aspect ratio (length:thickness) may reduce solid state diffusion limitations and lead to increased rate capability for LIB negative electrodes.[2] Figure 44(b) shows the effect of particle dimensions on the Li diffusion time (τ):

$\tau = L^2/2D_{Li}$ Equation 4.1

Where D_{Li} is the diffusion coefficient of Li and L is the diffusion length (= particle size / 2). Thus, for a particle of length 9 μm and thickness 900 nm (aspect ratio 10:1) the Li diffusion time along grain boundaries is 100 times slower than between graphene sheets. By decreasing the particle thickness, the limitation of grain boundary diffusion is reduced; for example, in graphite particles of 90 nm thickness (~ 300 graphene layers) there is parity of diffusion times, whilst for 10 graphene layers the grain boundary diffusion time is ~ 900 times less than for in-plane Li^+ diffusion.

A reductive electrochemical exfoliation process has been developed by the University of Manchester and demonstrated to be an effective method for generating single and multilayer graphene sheets with diameters greater than one micron.[3,4] The reductive nature of the method results in flakes with low oxygen content and the scalability of the process has attracted interest for LIB electrode applications. Meanwhile, although it is acknowledged that graphenic material re-aggregates if allowed to dry out; the nature of this re-aggregation process must be understood in order to overcome the obstacles this represents to material storage, transportation and processing. Furthermore, an understanding of the significance of these structural changes to the electrochemical Li intercalation behaviour is desirable to direct the development of scalable processes to produce graphitic materials with high rate capability for LIB applications.

4.2.1. Structural characterisation of modified graphite

The microcrystalline graphite sample investigated in Chapter 3 (SFG6, TIMCAL, TIMREX®), was modified by collaborators at the University of Manchester using the electrochemical exfoliation process developed by Abdeljader et al.[2,3] (described in Chapter 2). The exfoliated product was collected by vacuum filtration and dried at 80 °C prior to delivery and structural characterisation – this sample will be referred to as the 'modified graphite' sample below. Figure 45 shows PXRD patterns for the pristine and modified graphite samples. The modified graphite displays highly similar structural characteristics to the pristine graphite, indicating that significant restacking of exfoliated graphene sheets had occurred.

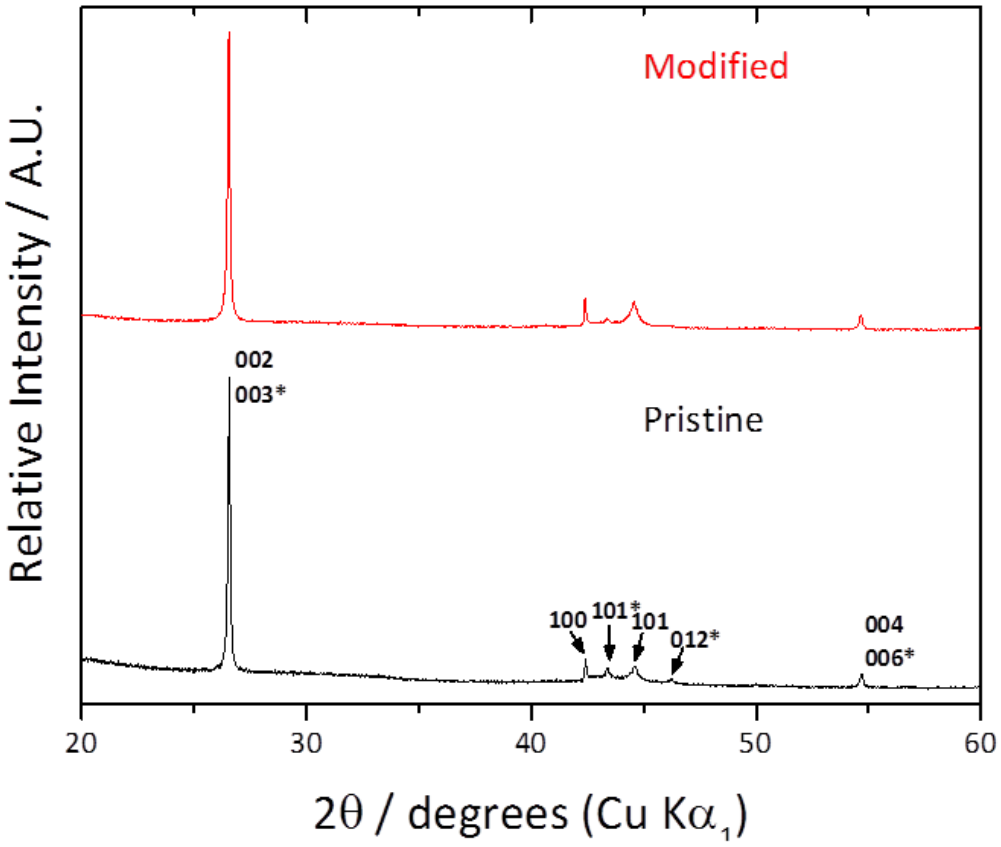

Figure 45: PXRD of pristine and modified microcrystalline graphite, * indicates rhombohedral phase.

The (100) and (002) peaks were analysed using the Scherrer equation:

$$L = \frac{K\lambda}{\beta\cos\theta}$$ Equation 4.2

where L is the average crystallite size along the analysed plane, λ is the wavelength of the X-rays, θ is the Bragg diffraction angle of the analysed plane, β is the full width at half-maximum (FWHM) of the analysed peak and K is a constant known as the dimensionless shape factor which in this case is equal to 0.9. Results are shown in Table 4.1 and indicate a slight decrease in crystallite size of ca. 10 – 15 % in L_a and L_c following the modification process. Furthermore, the rhombohedral fraction (3R phase) was determined for each sample by comparison of the intensity ratio of the

(101) hexagonal and rhombohedral diffraction peaks. A significant decrease from 41 % to 14 % was observed indicating that restacking of flakes occurred preferentially to the hexagonal (ABAB) stacking order, rather than the rhombohedral (ABCABC) arrangement.

Table 4.1: Structural bulk parameters, surface properties and 1st cycle irreversible capacity of pristine and modified graphite samples.

	BET ($m^2 g^{-1}$)	**L_a (Å)**	**L_c (Å)**	**Rhombohedral 3R-phase (%)**	**First cycle irreversible capacity (%)**
Pristine graphite[5]	17.1	622	303	37	20
Pristine graphite (this work)	22	817	797	41	22
Modified graphite	21	764	685	14	28

Finally, the structural similarity of the modified material with the pristine graphite was confirmed by BET surface area analysis. The surface area of the modified sample was found to be ca. 21 $m^2 g^{-1}$, which is almost identical to the value for the pristine sample of ca. 22 $m^2 g^{-1}$ (Table 4.1).

4.2.2. Lithium ion battery tests

The performance of the modified sample was compared to the pristine graphite as a negative electrode for LIBs. An assymetric electrochemical cycling procedure was developed whereby an initial galvanostatic discharge at 10 mA g^{-1} (C/37) down to 0.005 V (vs. Li^+/Li) is followed by a potentiostatic step at this potential, until the current dropped below 5 mA g^{-1}. This slow rate and potentiostatic step promotes the formation of a stable solid electrolyte interphase (SEI) during the first Li insertion cycle. On delithiation, the cell was charged up to 1.5 V vs. at C/37. On subsequent cycles the galvanostatic current on delithiation was varied to compare rate performance. Current rates used and approximate C rate are shown in Table 4.2. During lithiation cycles 2 - 32 a constant current rate of C/5 was used to avoid lithium plating.

Table 4.2: Galvanostatic current and approximate C rate for delithiation cycles in asymmetric cycling procedure.

Cycle number	1	2 - 4	5 - 9	10 - 14	15 - 19	20 - 24	25 - 29	30 - 32
Current rate /mA g^{-1}	10	74.4	374	1870	3740	5610	7480	74.4
C Rate	C/37	C/5	C	5C	10C	15C	20C	C/5

The voltage profile during the first lithiation/delithiation cycle (at C/37 rate) is shown in Figure 46. As discussed in Chapter 1, the delithiation of highly exfoliated few layer graphene samples is expected to occur at higher potentials vs. Li^+/Li due to a larger proportion of surface adsorption compared to intercalation. Therefore, the agreement between the electrochemical responses further confirms the structural similarity of the materials and hence the restacking of graphene sheets. Both samples display first cycle lithiation capacities of ~ 450 mAh g^{-1}, suggesting the surface area and defect

concentrations of the samples are comparable in agreement with the BET analysis. However, the modified sample shows a reduction delithiation capacity, being ~ 320 mAh g^{-1} vs. ~ 360 mAh g^{-1} for the pristine graphite. Previous reports have suggested that the interlayer space between turbostratically stacked graphene sheets are not able to reversibly intercalate Li due to locking together by defects.[6,7] Therefore, it is proposed that the restacking process results in samples with an increased turbostratic disorder of ca. 10 %.

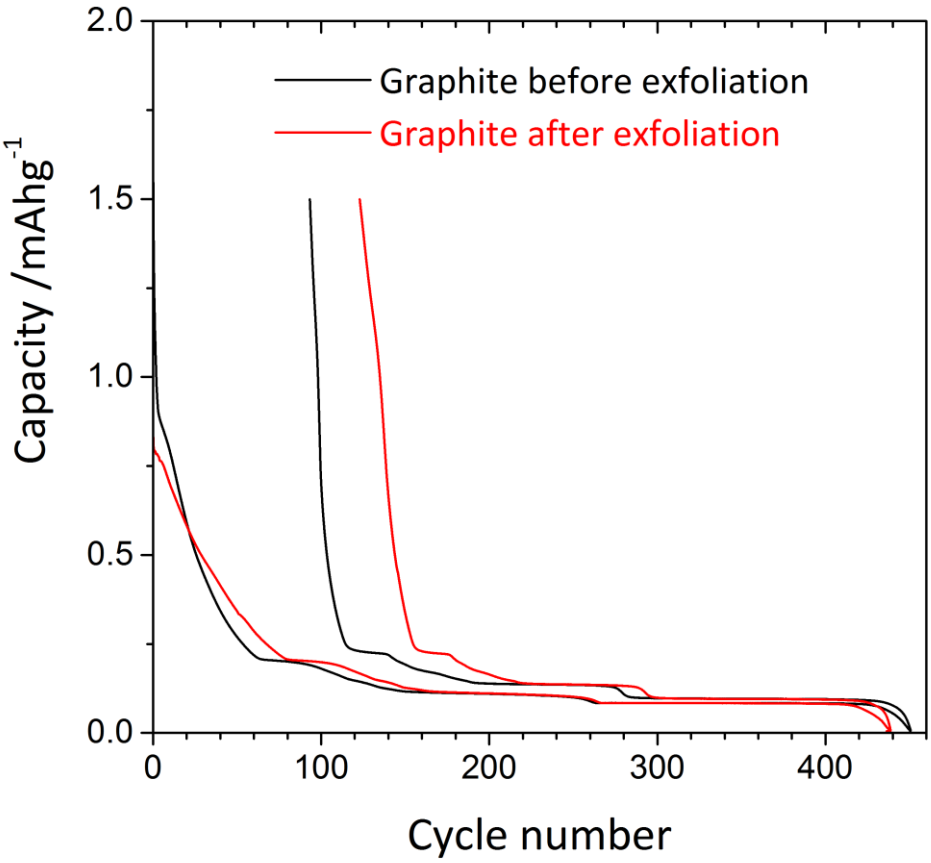

Figure 46: Voltage vs. capacity curves for first lithiation/delithiation cycle of SFG6 microcrystalline graphite and the modified sample.

Figure 47 shows the results of an asymmetric cycling procedure whereby the rate performance of the two materials on delithiation was compared at varying rates up to 20C. At high rates the modified material appears to display improved capacity

retention. However, the active mass loading of the electrodes was slightly less for the modified material (2.3 mg cm^{-2}) compared to the pristine graphite (2.8 mg cm^{-2}). Furthermore, the thickness and porosity of these electrodes was not carefully controlled. In Chapter 6 the effect of electrode thickness, porosity and mass loading will be shown to be critical to the rate performance of composite electrodes, therefore further experiments are required before firm conclusions regarding rate capability may be drawn. Therefore conducting further experiments with increased electrode loading is suggested to minimise the significance of minor deviations in loading, thickness and porosity. Furthermore, as discussed later, differences in electrode performance are more clearly visualised by testing electrodes at similar current densities rather than C rates. This would also enable the influence of electrolyte transport limitations due to the separator to be identified if present.

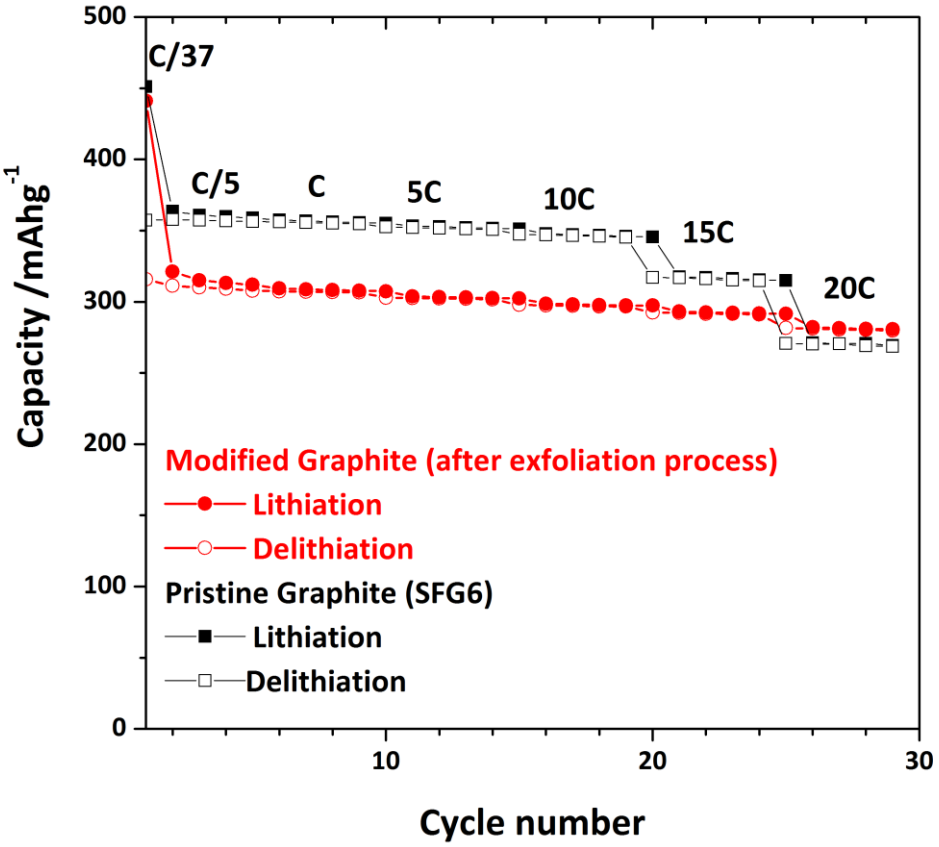

Figure 47: Rate performance of pristine graphite (SFG6) and the modified graphite sample. The labelled C rates describe the current on delithiation cycle only. The full procedure is described in Chapter 2.

4.2.3. *In situ* Raman spectra during the first lithiation cycle

4.2.3.1. Characterisation of disorder in regions of the electrode surface

In situ Raman spectra of the modified graphite were collected to compare with the pristine graphite. Spectra were collected from three regions of the composite electrode which displayed varying degrees of structural disorder. Raman spectra of the three regions at open circuit potential (OCP) are displayed in Figure 48. The three regions exhibit varying ratios of D band intensity (I_D) to G band intensity (I_G), commonly referred to as I_D/I_G ratio.

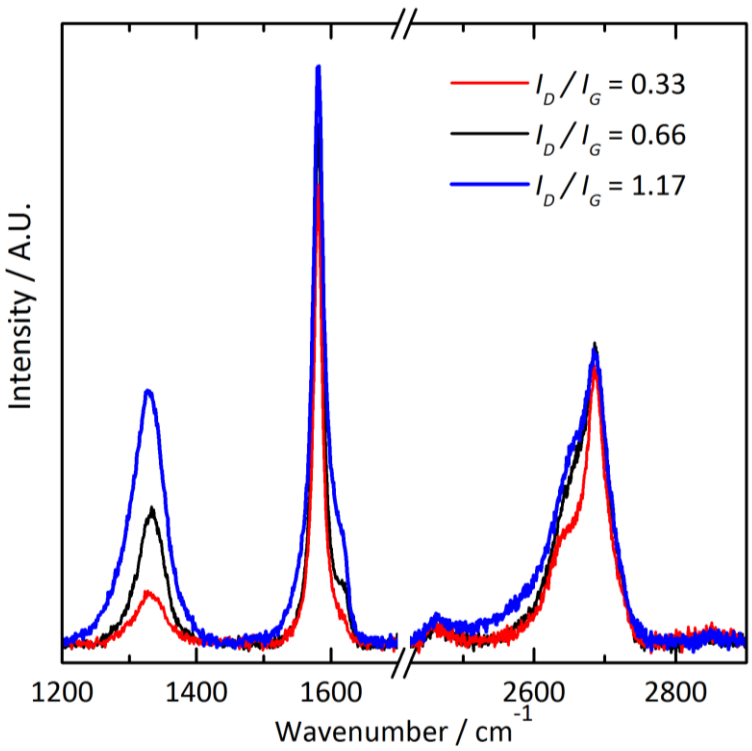

Figure 48: Raman spectra at OCP of selected regions on the modified graphite electrode with varying I_D/I_G ratio.

The I_D/I_G ratio was shown by Tuinstra and Koenig to be proportional to $1/L_a$ in disordered graphite materials.[8] Cançado et al.[9] studied this relationship and found the proportionality to be highly laser wavelength dependent, suggesting the relationship:

$$L_a(\text{nm}) = \left(2.4 \times 10^{-10}\right)\lambda_{\text{laser}}^4 \left(\frac{I_D}{I_G}\right)^{-1} \qquad \text{Equation 4.3}$$

There is some controversy in the literature over whether the use of peak height or area should be used for accurate estimations of disorder from the I_D/I_G ratio. Several authors have argued that for disordered graphite materials, no significant difference is produced in the values of L_a calculated depending on the use of either peak height or area.[10,11] However, the use of peak height is preferred to reduce deviations due to the fitting method.[10] Table 4.3 compares L_a values calculated using Equation 4.3 for the three regions of the modified graphite electrode using both peak area and height. In addition, the mean average value of ten randomly selected regions is shown.

Table 4.3: I_D/I_G ratios and calculated L_a values using both peak area and peak height for the modified graphite sample.

	Peak Area		**Peak Height**	
	I_D/I_G	L_a **(nm)**	I_D/I_G	L_a **(nm)**
Spot 1	0.33	117	0.11	350
Spot 2	0.66	58	0.26	148
Spot 3	1.17	33	0.45	86
Average of 10 spots	0.78	50	0.29	134

A L_a value of ~ 76 nm was derived by application of the Scherrer formula to PXRD data of the modified graphite sample (Table 4.1). This value should be compared with the average values in Table 4.3, which suggests the average crystallite size may be underestimated by the peak area method and overestimated by peak height method. However, since Raman spectroscopy is a surface region analysis technique whilst

XRD investigates the bulk, Raman could be expected to produce smaller values of L_a because the concentration of structural defects are likely to be increased at particle surfaces.

4.2.3.2. *In situ* Raman spectra of lithium insertion into the modified graphite sample under potentiostatic conditions

Potentiostatic conditions were used for the *in situ* Raman experiment which allowed spectra to be collected with longer acquisition times and increased signal-to-noise ratio. The cell was held at each potential for 20 minutes or until the current dropped by over 95 % from the peak current, before the collection of Raman spectra.

Results for spot 2 are shown in Figure 49 with peak positions and FWHM given in Table 4.4. Potentials below 0.05 V, where stage 1 compounds are expected to occur, were not investigated as these spectra were of little interest to the mechanistic study. Similar behaviour to the pristine graphite is observed which further confirms the structural similarity between the two samples. Significantly, the shape of the 2D peak could be clearly distinguished and supports the conclusions of Chapter 3. The following band behaviour was observed:

- At 0.4 V the G peak exhibits blue-shifting and narrowing of the FWHM, confirming the formation of dilute stage 1. The D peak loses intensity, whilst there is a minor downshift in the 2D peak position.
- At 0.2 V the G peak begins to broaden accompanying the formation of the doublet bands of stage 4L. The 2D band resembles a single broad Lorentzian peak.

- Between 0.18 V to 0.11 V the G band is clearly split into a doublet band representative of the stage 4L and 3L structures. The 2D band shape remains a single peak and downshifts with decreasing potential.
- At 0.08 V the 2D peak is no longer visible. The G band has broadened and downshifted to 1571 cm^{-1} whilst the reappearance of the unassigned peak at 1371 cm^{-1} is also observed.

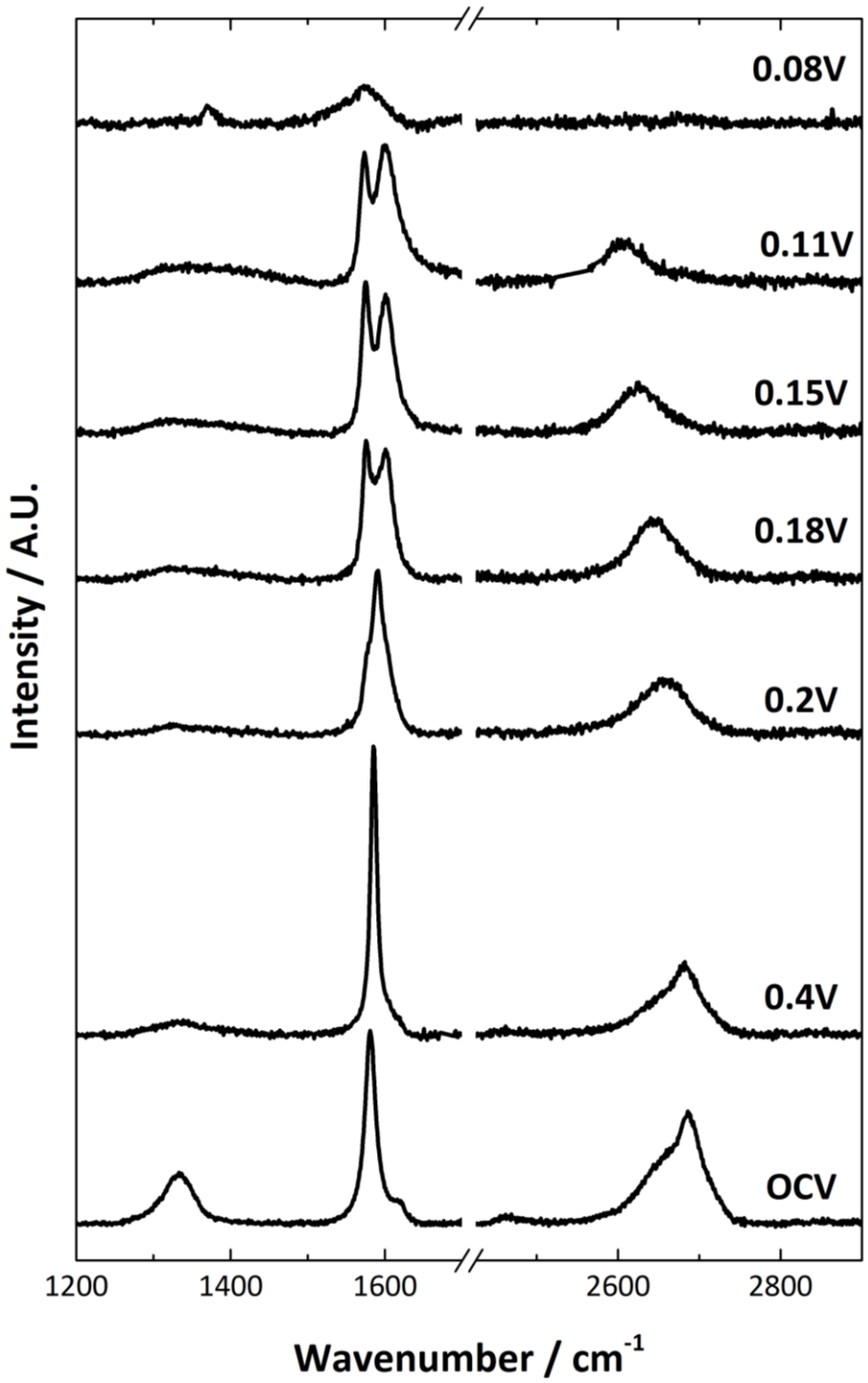

Figure 49: Representative *in situ* Raman spectra of first cycle lithium intercalation into modified graphite sample. The potential (V) at which each spectrum was collected is displayed. All the spectra are base-line corrected and stacked arbitrarily up the y-axis to allow for clear visualisation.

Table 4.4: Peak positions and FWHM during first lithiation cycle of the modified graphite sample.

E(V)	G		E2g2(i)		E2g2(b)		2D(1)		2D(2)	
	ω (cm-1)	**FWHM (cm-1)**	**ω (cm-1)**	**FWHM (cm-1)**	**ω (cm-1)**	**FWHM (cm-1)**	**ω (cm-1)**	**FWHM (cm-1)**	**ω (cm-1)**	**FWHM (cm-1)**
3.0	1581	17	-	-	-	-	2647	62	2688	42
0.40	1585	10	-	-	-	-	2639	57	2683	48
0.20	1591	28	-	-	-	-	-	-	2655	76
0.18	-	-	1576	13	1600	27	-	-	2644	66
0.15	-	-	1575	13	1601	28	-	-	2626	68
0.11	-	-	1573	12	1601	40	-	-	2607	66
0.08	1571	61	-	-	-	-	-	-	-	-

4.2.3.3. Comparison of spectra for regions of varying disorder

Spot 1 and 3 showed similar behaviour to that exhibited by spot 2 (Figure 49). In particular, the shift in the 2D(2) peak position was compared as shown in Figure 50. The similarity of the shift indicates that local graphitic disorder (structural defects and crystallite size) does not affect the behaviour of the 2D band during lithium insertion. This suggests that the increase in C-C bond length (which causes the red-shift of the 2D band) is inherently linked to the increasing occupation of the π^* band during Li intercalation, as suggested by Pietronero and Strassler.[12]

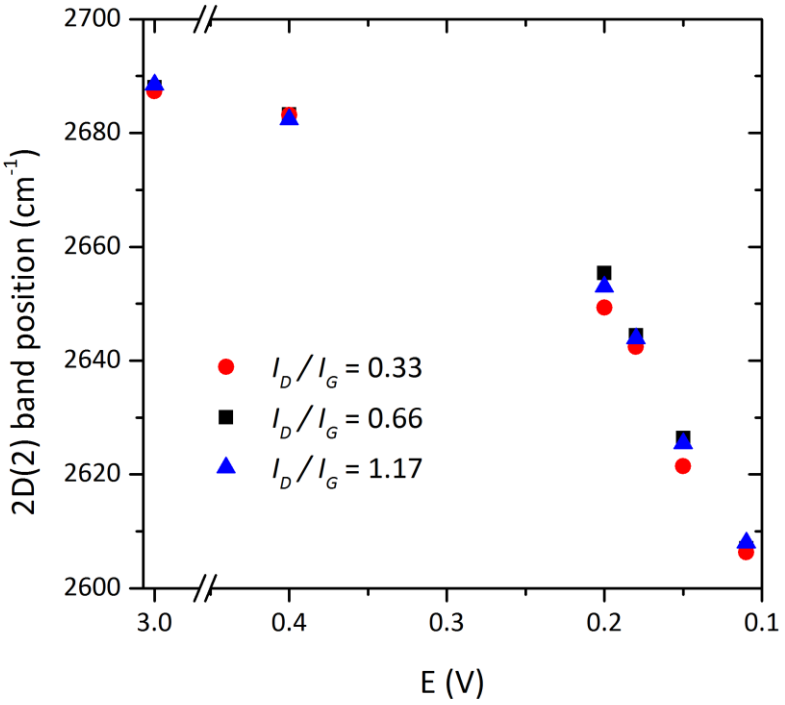

Figure 50: 2D(2) peak position for the first lithiation of modified graphite within potential range 3.0 - 0.1 V vs. Li^+/Li, for three spots with varying initial I_D/I_G ratios.

4.3. Using band positions to estimate strain and doping on interior and bounding layers

For comparison of the lithiation mechanism in graphitic materials it would be useful to estimate the C-C bond lengths and/or electronic doping of graphene sheets from *in situ* Raman spectra. The effect of bond length changes on the Raman spectra of graphene layers has been investigated by various methods.[13–16] Expansion of C-C bonds equally throughout the structure is referred to as biaxial strain (ε) and may be defined as the extension per unit length:

$$\varepsilon = \frac{\partial \mathrm{x}}{x_0} \qquad \text{Equation 4.4}$$

where ∂x is the change in length and x_0 is the original length.

The improved signal-to-noise ratio of the spectra in Figure 49 presents an opportunity for such an analysis. Recently a method to estimate the concentration of dopants and strain of graphene sheets deposited on substrates has been developed.[17–19] However, such an analysis is only valid up to ~ 1.5 x 10^{13} electrons cm^{-2} due to the non-linear shift of the G band at high levels of doping.[20] Stage 4L formation begins after ~ 20 mAh g^{-1} charge capacity,[21] corresponding to an electron concentration of ~ 3 x 10^{13} electrons cm^{-2} (see appendix for calculation). Charge carrier concentrations of ~ 4-5 x 10^{13} electrons cm^{-2} for the bounding layers in stage 4 and 3 K-GICs were calculated by density functional theory.[22] Regardless, an alternative method of strain estimation at such high levels of doping is proposed below, which is similar to the method proposed by Chacón-Torres et al.[23]

4.3.1. Model for strain estimation from 2D band position

Increased electronic doping raises the Fermi level and causes the Kohn anomaly to move from the Γ and K points as discussed in Chapter 1. This causes stiffening of the G band such that its position may be explained by a combination of bond expansion and non-adiabatic effects.[24] However, the shift of the 2D band only depends on C-C bond expansion because phonons involved in the 2D band process are far enough away from the K point that they are unaffected by movement of the Kohn anomaly.[25,26] Therefore, the 2D band position may be used to estimate the strain (and hence C-C bond length) using:

$$\varepsilon' = \frac{\omega_{2D'} - \omega_{2D^0}}{S_{2D}} = \frac{\Delta\omega_{2D}}{S_{2D}} \qquad \text{Equation 4.5}$$

Where ε' is biaxial strain, $\omega_{2D'}$ is the measured 2D band position, ω_{2D^0} is the 2D band position at zero-strain and S_{2D} is the shift in the 2D band position per % biaxial strain. Reported values for *S* are shown in Table 4.5. An average value of -164 cm^{-1} per % will be used in subsequent calculations.

Table 4.5: Literature values of G and 2D band shifts with applied biaxial strain.

Reference	**2D band shift with biaxial strain (S_{2D}) (cm^{-1} per %)**	**G band shift with biaxial strain (S_G) (cm^{-1} per %)**
Mohiuddin et al.[13]	-191	-63
Zabel et al.[14]	-140	-57
Ding et al.[16]	-160	-57
Lee et al.[17]	-	-69
Average	-164	-62

However, assignment of a zero-strain 2D band position for graphite (ω_0) is complicated by the observed shape change. As discussed, whilst the 2D band for graphite may be fitted by two peaks, stage 4L and 3L (between 0.2 V to 0.18 V) display

a single broad Lorentzian peak. Such a line-shape is indicative of carbon materials with electronic decoupling between graphene layers, as occurs in both single layer graphene (SLG) and turbostratic graphite.[27–29] However, the full width half maximum (FWHM) is significantly larger for turbostratic graphite (~ 45-60 cm^{-1}) than SLG (~ 24 cm^{-1}). In the range 0.18 V to 0.11 V the fitted 2D peak FWHM of the modified graphite is ~ 65 cm^{-1} (Table 4.4), suggesting the electronic structure is similar to turbostratic graphite. Observations of the interlayer spacing during the stage 4L to 2L range (> 3.4 Å)[30] are similar to those of turbostratic graphite (~ 3.41 Å) and may correspond to the electronic decoupling of layers.[31]

The peak position of turbostratic graphite will hence be used as a zero-strain reference position. Using 633 nm laser, the only reported 2D position of turbostratic graphite is 2652 cm^{-1} by Tan et al.[32] This position agrees with that predicted by Cançado et al.[33] However, it should be highlighted that this model may only be used for the stage 4L and 3L phases where a single peak position of the 2D band may be defined.

4.3.1.1. Application of model

Values of $\Delta\omega_{2D}$ were derived as shown in Figure 51 and used to calculate biaxial strain and C-C bond lengths between 0.18 V to 0.11 V (Table 4.6), assuming a zero-strain bond length of 1.421 Å.[34] An increase in C-C bond lengths during lithiation was observed which agrees with previous observations of continuous lattice parameter increases during this region.[30] Interestingly, at 0.11 V the calculated C-C bond length of 1.425 Å is in agreement with that found experimentally for stage 3L by Billaud and Henry.[35] Furthermore, as the increase in C-C bond length is directly linked to the concentration of electrons in the graphene layers, the observed bond expansion throughout the stage 4L to 2L phase transitions are indicative of increasing in-plane

density of Li^+ ions in the liquid (4L and 3L) phases, supporting the proposed solid solution phase transition mechanism.

Table 4.6: Shift in 2D band ($\Delta\omega_{2D}$) from 2652 cm^{-1}, calculated biaxial strain, and C-C bond length with potential. A zero-strain bond length of 1.421 Å was assumed.[34] Errors in calculated values are discussed towards the end of this Chapter.

E (V)	$\Delta\omega_{2D}$ (cm^{-1})	Calculated strain (%)	Calculated C-C bond length (Å)
0.18	-8	0.049	1.422
0.15	-26	0.16	1.423
0.11	-45	0.27	1.425

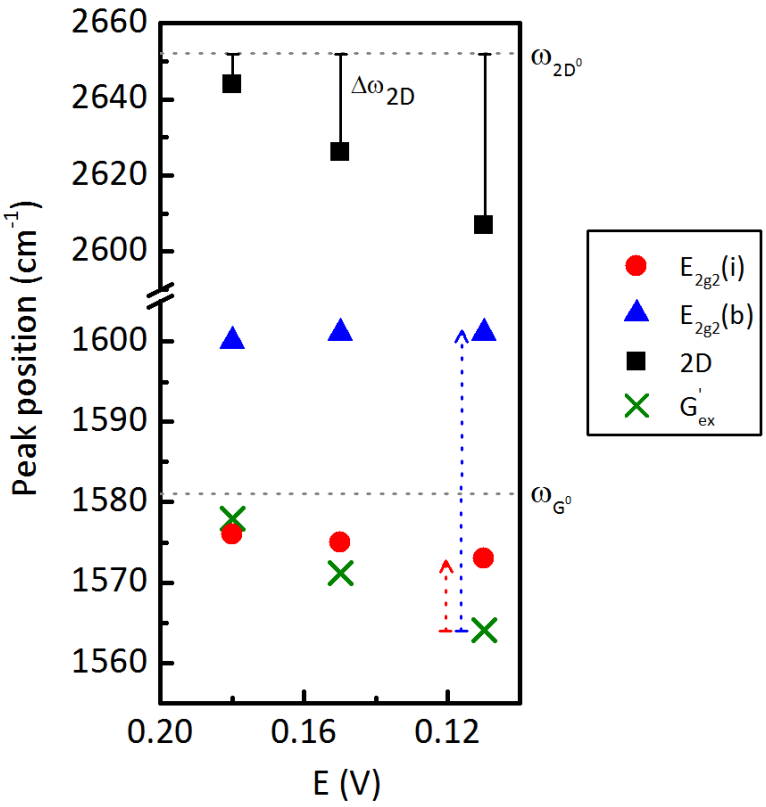

Figure 51: Peak positions of 2D band, E_{2g2}(i) and E_{2g2}(b) modes. $\omega_{2D^0}, \omega_{G^0}$ and $\omega_{G'_{ex}}$ are indicated alongside $\Delta\omega_{2D}$. Blue and red dashed arrows represent upshift of the G band explained by doping for bounding and interior layers respectively.

4.3.1.2. G band position explanation

The G band has also been observed to shift with biaxial strain (S_G) with an average value of - 62 cm^{-1} per % (Table 4.5). Therefore, an 'expected' G band position ($\omega_{G'_{ex}}$) can be defined:

$$\omega_{G'_{ex}} = \omega_{G^0} + S_G \varepsilon' \qquad \text{Equation 4.6}$$

Where ω_{G^0} is the G band position at zero-strain, and may be estimated from the open circuit potential (OCP) G band position to be 1581 cm^{-1}, in close agreement with previously reported zero-strain samples.[17,18,36] Figure 51 shows the 'expected' and measured position of the G band for both interior and bounding layers using the calculated values of biaxial strain given in Table 4.6. The difference between the measured G band position and the 'expected' position (indicated by dashed arrows in Figure 51) may be interpreted as the upshift caused by electronic doping, calculated values of which are shown in Figure 52. The small downshift of the E_{2g}(i) mode relative to the 'expected' position at low strain suggests the model is not quantitatively accurate, as electronic doping is understood to cause an upshift of the G band.[20] However, the model successfully predicts that the doping of the bounding layers is significantly larger than the interior layers in qualitative agreement with previous studies. Furthermore, as lithiation progresses there is an increase in doping of both the bounding and interior layers which may be explained by increasing in-plane density of Li^+ ions during the phase transition.

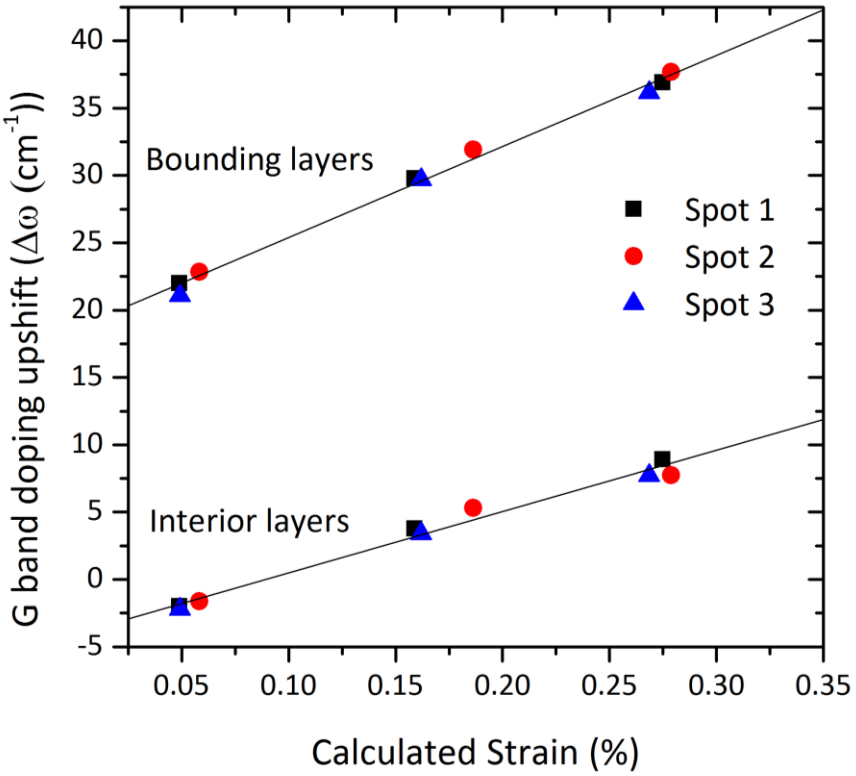

Figure 52: Calculated values for the upshift of the G band for interior and bounding layers from the expected position ($\omega_{G'_{ex}}$) of each according to the model descirbed above.

4.3.2. Discussion of errors and sensitivity analysis

The proposed model should not be considered quantitative due to the use of average values for various parameters, therefore the sensitivity of the model to the values of S_G, S_{2D} and ω_{2D^0} will be investigated.

Firstly, the sensitivity of the model to the shift of the G band (S_G) and 2D band (S_{2D}) is shown in Figure 53, by applying the model with the minimum and maximum reported values from Table 4.5. Clearly, the effect of uncertainty in the S_G and S_{2D} values is more pronounced at increased values of strain, however, in all cases there is qualitative agreement with the behaviour observed using average values.

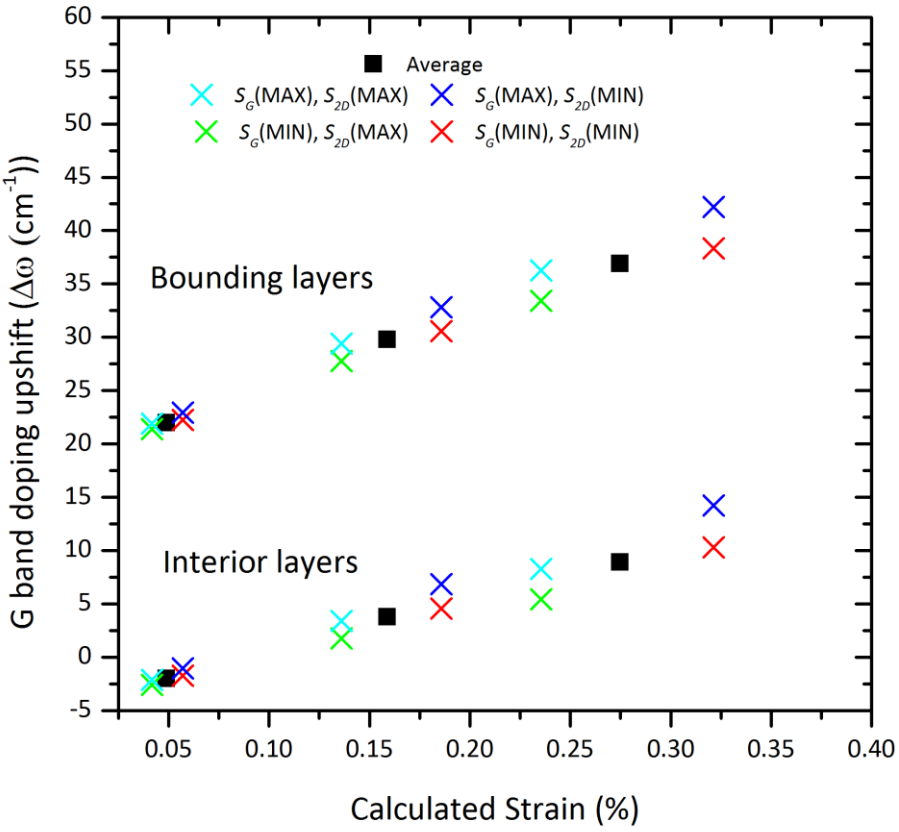

Figure 53: Sensitivity analysis of the calculated strain and G band upshift when maximum or minimum values of S_G and S_{2D} are used, where (MAX) and (MIN) indicate the use of maximum and minimum absolute values of the parameters in Table 4.5. For example, $S_G(MAX)$ indicated the use of S_G = -69 cm^{-1}.

Secondly, the sensitivity to the value of ω_{2D^0} used is analysed. It should be noted that values for the 2D band position of turbostratic graphite[31,37] which correspond to ~ 2663 cm^{-1} have been reported in studies using different wavelength lasers (after normalisation of band positions due to dispersion of 95 cm^{-1} per eV).[27] Figure 54 shows the values of strain and doping upshift predicted by the model are highly sensitive to the value of ω_{2D^0} used. Mafra et al.[37] have shown experimentally that the 2D band position of turbostratic graphite is higher than that of zero-strain graphene

layers due to an increased phonon velocity. Therefore, to increase the validity of this model, more work is required to define the value of ω_{2D^0} using a 633 nm laser. Nevertheless, a similar qualitative behaviour is observed, thus the model may be applied to compare the qualitative mechanism of intercalation into various graphitic carbons.

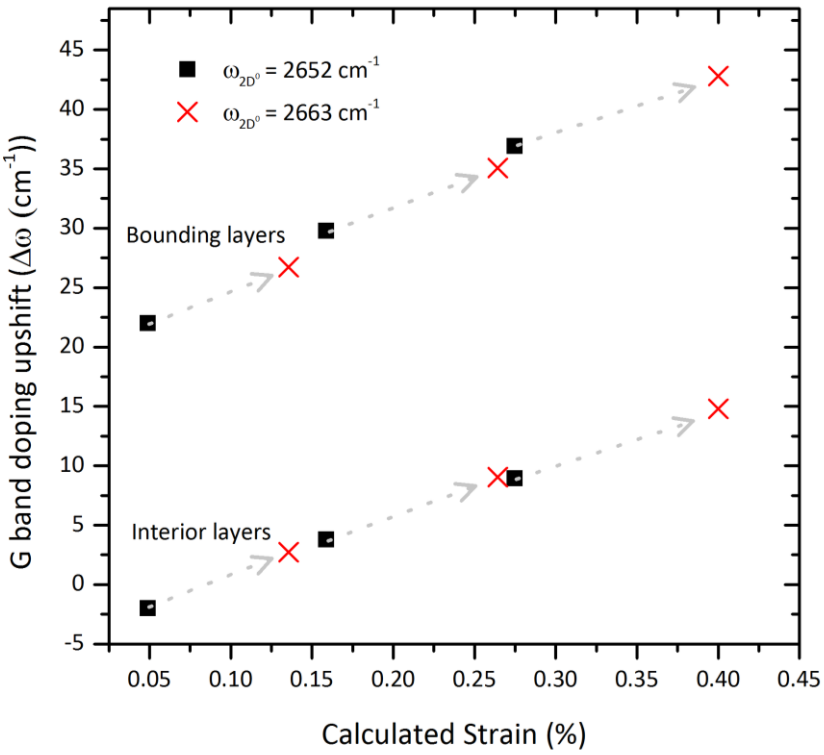

Figure 54: Sensitivity analysis of G band doping upshift and calculated strain to the value of ω_{2D^0} used. Grey dashed arrows indicate the change in values of the doping associated G band upshift upon changing the value of ω_{2D^0} from 2652 cm^{-1} to 2663 cm^{-1}.

4.4. Conclusions

Structural characterisation of a microcrystalline graphite sample, which had been modified by a cathodic electrochemical exfoliation process, revealed that significant restacking of the exfoliated material had occurred during drying. The crystallite size of the material decreased only slightly in comparison to the pristine graphite material, whilst BET measurements suggested negligible change to the surface area. However, a reduction in the rhombohedral fraction of the material was observed, suggested restacking occurred preferentially to the hexagonal stacking order. Furthermore, electrochemical charge/discharge tests showed a small increase in first cycle irreversible capacity and a reduction in lithium storage capacity, which may be linked to an increase in turbostratic disorder.

Additionally, a similar intercalation mechanism was observed by *in situ* Raman spectroscopy during lithiation of the modified graphite sample, confirming the structural similarity with the pristine graphite. Moreover, an increased signal-to-noise ratio was achieved by the use of potentiostatic conditions, which allowed clear observation of the change in 2D band shape during the stage 4L to 3L region; the observation of a single Lorentzian peak suggests electronic decoupling of the graphene layers. The red-shift of the 2D band was observed to be independent of low levels of structural disorder.

Finally, a model has been proposed to estimate the doping and strain on interior and bounding layers from the G and 2D band positions during the stage 4L to 3L region. This model supports the observations of a solid solution mechanism, and the predicted doping of bounding over interior layers. The errors associated with the choice of model parameters were observed to be substantial, thus preventing quantitative use. However,

the model may be used to qualitatively compare the mechanism of lithiation in different samples, which will be the focus of Chapter 5.

4.5. References

(1) Persson, K.; Sethuraman, V. A.; Hardwick, L. J.; Hinuma, Y.; Meng, Y. S.; van der Ven, A.; Srinivasan, V.; Kostecki, R.; Ceder, G. Lithium Diffusion in Graphitic Carbon. *J. Phys. Chem. Lett.* **2010**, *1*, 1176–1180.

(2) Sole, C.; Drewett, N. E.; Liu, F.; Abdelkader, A. M.; Kinloch, I. A.; Hardwick, L. J. The Role of Re-Aggregation on the Performance of Electrochemically Exfoliated Many-Layer Graphene for Li-Ion Batteries. *J. Electroanal. Chem.* **2015**, *753*, 35–41.

(3) Abdelkader, A. M.; Kinloch, I. A.; Dryfe, R. A. W. Continuous Electrochemical Exfoliation of Micrometer-Sized Graphene Using Synergistic Ion Intercalations and Organic Solvents. *ACS Appl. Mater. Interfaces* **2014**, *6* (3), 1632–1639.

(4) Cooper, A. J.; Wilson, N. R.; Kinloch, I. A.; Dryfe, R. A. W. Single Stage Electrochemical Exfoliation Method for the Production of Few-Layer Graphene via Intercalation of Tetraalkylammonium Cations. *Carbon* **2014**, *66*, 340–350.

(5) Buqa, H.; Würsig, A.; Goers, D.; Hardwick, L. J.; Holzapfel, M.; Novák, P.; Krumeich, F.; Spahr, M. E. Behaviour of Highly Crystalline Graphites in Lithium-Ion Cells with Propylene Carbonate Containing Electrolytes. *J. Power Sources* **2005**, *146* (1–2), 134–141.

(6) Shi, H. Structure and Lithium Intercalation Properties of Synthetic and Natural Graphite. *J. Electrochem. Soc.* **1996**, *143* (11), 3466.

(7) Zheng; Reimers; Dahn. Effect of Turbostratic Disorder in Graphitic Carbon Hosts on the Intercalation of Lithium. *Phys. Rev. B. Condens. Matter* **1995**, *51* (2), 734–741.

(8) Tuinstra, F.; Koenig, J. L. Raman Spectrum of Graphite. *J. Chem. Phys.* **1970**, *53*, 1126.

(9) Cançado, L. G.; Takai, K.; Enoki, T.; Endo, M.; Kim, Y. A.; Mizusaki, H.; Jorio, A.; Coelho, L. N.; Magalhães-Paniago, R.; Pimenta, M. A. General Equation for the Determination of the Crystallite Size L_a of Nanographite by Raman Spectroscopy. *Appl. Phys. Lett.* **2006**, *88* (16), 163106.

(10) Jorio, A.; Ferreira, E. H. M.; Moutinho, M. V. O.; Stavale, F.; Achete, C. A.; Capaz, R. B. Measuring Disorder in Graphene with the G and D Bands. *Phys. status solidi* **2010**, *247* (11–12), 2980–2982.

(11) Ferrari, A. C.; Robertson, J. Interpretation of Raman Spectra of Disordered and Amorphous Carbon. *Phys. Rev. B* **2000**, *61* (20), 14095–14107.

(12) Pietronero, L.; Strassler, S. Bond-Length Change as a Tool to Determine Charge Transfer and Electron Phonon Coupling in Graphite Intercalation Compounds. *Phys. Rev. Lett.* **1981**, *47*, 593–596.

(13) Mohiuddin, T. M. G.; Lombardo, A.; Nair, R. R.; Bonetti, A.; Savini, G.; Jalil, R.; Bonini, N.; Basko, D. M.; Galiotis, C.; Marzari, N.; et al. Uniaxial Strain in Graphene by Raman Spectroscopy : G Peak Splitting , Grüneisen Parameters , and Sample Orientation. *Phys. Rev. B* **2009**, *79*, 205433–1.

(14) Zabel, J.; Nair, R. R.; Ott, A.; Georgiou, T.; Geim, A. K.; Novoselov, K. S.; Casiraghi,

C. Raman Spectroscopy of Graphene and Bilayer under Biaxial Strain: Bubbles and Balloons. *Nano Lett.* **2012**, *12* (2), 617–621.

(15) Metzger, C.; Rémi, S.; Liu, M.; Kusminskiy, S. V.; Castro Neto, A. H.; Swan, A. K.; Goldberg, B. B. Biaxial Strain in Graphene Adhered to Shallow Depressions. *Nano Lett.* **2010**, *10* (1), 6–10.

(16) Ding, F.; Ji, H.; Chen, Y.; Herklotz, A.; Dörr, K.; Mei, Y.; Rastelli, A.; Schmidt, O. G. Stretchable Graphene: A Close Look at Fundamental Parameters through Biaxial Straining. *Nano Lett.* **2010**, *10* (9), 3453–3458.

(17) Lee, J. E.; Ahn, G.; Shim, J.; Lee, Y. S.; Ryu, S. Optical Separation of Mechanical Strain from Charge Doping in Graphene. *Nat. Commun.* **2012**, *3*, 1024.

(18) Kim, S.; Ryu, S. Thickness-Dependent Native Strain in Graphene Membranes Visualized by Raman Spectroscopy. *Carbon* **2016**, *100*, 283–290.

(19) Bepete, G.; Peicaud, A.; Drummond, C.; Anglaret, E. Raman Signatures of Single Layer Graphene Dispersed in Degassed Water, "Eau de Graphene." *J. Phys. Chem. C* **2016**, *120*, 28204–28214.

(20) Das, A.; Pisana, S.; Piscanec, S.; Chakraborty, B.; Saha, S. K.; Waghmare, U. V.; Yiang, R.; Krishnamurhthy, H. R.; Geim, A. K.; Ferrari, A. C.; et al. Electrochemically Top Gated Graphene: Monitoring Dopants by Raman Scattering. *Nat. Nanotechnol.* **2007**, *3* (4), 210–215.

(21) Dahn, J. R. Phase Diagram of Li_xC_6. *Phys. Rev. B* **1991**, *44* (17), 9170–9177.

(22) Chacón-Torres, J. C.; Wirtz, L.; Pichler, T. Manifestation of Charged and Strained Graphene Layers in the Raman Response of Graphite Intercalation Compounds. *ACS Nano* **2013**, *7* (10), 9249–9259.

(23) Lazzeri, M.; Mauri, F. Nonadiabatic Kohn Anomaly in a Doped Graphene Monolayer. *Phys. Rev. Lett.* **2006**, *97* (26), 266407.

(24) Pisana, S.; Lazzeri, M.; Casiraghi, C.; Novoselov, K. S.; Geim, A. K.; Ferrari, A. C.; Mauri, F. Breakdown of the Adiabatic Born-Oppenheimer Approximation in Graphene. *Nat. Mater.* **2007**, *6* (3), 198–201.

(25) Beams, R.; Gustavo Cançado, L.; Novotny, L. Raman Characterization of Defects and Dopants in Graphene. *J. Phys. Condens. Matter* **2015**, *27* (8), 83002.

(26) Ferrari, A. C. Raman Spectroscopy of Graphene and Graphite: Disorder, Electron-Phonon Coupling, Doping and Nonadiabatic Effects. *Solid State Commun.* **2007**, *143*, 47–57.

(27) Malard, L. M.; Pimenta, M. A.; Dresselhaus, G.; Dresselhaus, M. S. Raman Spectroscopy in Graphene. *Phys. Rep.* **2009**, *473* (5–6), 51–87.

(28) Ferrari, A. C.; Basko, D. M. Raman Spectroscopy as a Versatile Tool for Studying the Properties of Graphene. *Nat. Nanotechnol.* **2013**, *8* (4), 235–246.

(29) Cançado, L.; Reina, a.; Kong, J.; Dresselhaus, M. Geometrical Approach for the Study of G′ Band in the Raman Spectrum of Monolayer Graphene, Bilayer Graphene, and Bulk Graphite. *Phys. Rev. B* **2008**, *77* (24), 245408.

(30) Heß, M. Kinetics and Stage Transitions of Graphite for Lithium-Ion Batteries, PhD thesis. ETH / PSI, 2013.

(31) Cançado, L. G.; Takai, K.; Enoki, T.; Endo, M.; Kim, Y. a.; Mizusaki, H.; Speziali, N. L.; Jorio, a.; Pimenta, M. a. Measuring the Degree of Stacking Order in Graphite by Raman Spectroscopy. *Carbon* **2008**, *46*, 272–275.

(32) Tan, P.; Hu, C.; Dong, J.; Shen, W.; Zhang, B. Polarization Properties, High-Order Raman Spectra, and Frequency Asymmetry between Stokes and Anti-Stokes Scattering of Raman Modes in a Graphite Whisker. *Phys. Rev. B* **2001**, *64* (21), 214301.

(33) Cançado, L. G.; Pimenta, M. A.; Saito, R.; Jorio, A.; Ladeira, L. O.; Grueneis, A.; Souza-Filho, A. G.; Dresselhaus, G.; Dresselhaus, M. S.; Dresselhaus, M. S. Stokes and Anti-Stokes Double Resonance Raman Scattering in Two-Dimensional Graphite. *Phys. Rev. B - Condens. Matter Mater. Phys.* **2002**, *66* (3), 354151–354155.

(34) Nixon, D. E.; Parry, G. S. The Expansion of the Carbon-Carbon Bond Length in Potassium Graphites. *J. Phys. C Solid State Phys.* **1969**, *2* (10), 1732–1741.

(35) Billaud, D.; Henry, F. X. Structural Studies of the Stage III Lithium-Graphite Intercalation Compound. *Solid State Commun.* **2002**, *124* (8), 299–304.

(36) Berciaud, S.; Ryu, S.; Brus, L. E.; Heinz, T. F. Probing the Intrinsic Properties of Exfoliated Graphene: Raman Spectroscopy of Free-Standing Monolayers. *Nano Lett.* **2009**, *9* (1), 346–352.

(37) Mafra, D. L.; Samsonidze, G.; Malard, L. M.; Elias, D. C.; Brant, J. C.; Plentz, F.; Alves, E. S.; Pimenta, M. A. Determination of L_a and TO Phonon Dispersion Relations of Graphene near the Dirac Point by Double Resonance Raman Scattering. *Phys. Rev. B - Condens. Matter Mater. Phys.* **2007**, *76* (23).

5. *In situ* Raman spectroscopy of Li intercalation in highly crystalline graphitic flakes of varying thicknesses

5.1. Overview of chapter

This chapter describes an *in situ* Raman spectroscopy study of lithium intercalation into graphitic flakes of varying thicknesses.[1] Natural graphite flakes were mechanically exfoliated using the scotch tape method to produce low defect concentration flakes of varying dimensions. The chapter will begin with a description of how the flakes were selected and characterised. Next, optical microscopy observations during lithium intercalation are briefly discussed to better understand the Raman study. Finally, *in situ* Raman spectra of the various samples are analysed and the implications for LIB technology are discussed.

5.1.1. Mechanistic studies of lithium intercalation in few layer graphene and thin graphitic samples

As discussed in Chapter 3, the Li intercalation mechanism in bulk graphite is well studied and occurs via a series of staged compounds (4L, 3L, 2L, 2 and 1), characterised by a regular number of graphene layers separating intercalated ions.[2–4] However, the formation of stage 4L and 3L phases is clearly not feasible in few layer graphene structures of < 5 graphene layers. Furthermore, it remains unclear how the lithiation mechanism proceeds in structures of between 5 to 20 graphene layers, where the number of interlayer spaces is limited. The rate of Li diffusion has been observed to differ between the various staged GICs,[5,6] which has recently been directly linked to the improved rate capability of graphite electrodes during delithiation compared to lithiation cycles.[3] Therefore, any changes to the conventional (de)lithiation mechanism are of interest with regards to battery rate performance and an understanding of how the Li intercalation mechanism changes as the thickness of graphitic flakes decreases is desirable. Moreover, a recent study reported Li diffusion within bilayer graphene to be faster than in bulk graphite,[7] suggesting similar rate enhancements may be observed in few layer graphene samples of different thicknesses.

In that regard, the first significant mechanistic study was reported by Pollak et al.,[8] whereby Raman spectroscopy was used to show the lithiation mechanism in few layer graphene closely resembled that of bulk graphite. However, later studies have suggested there may be subtle differences in the mechanism depending on the number of graphene layers.[9,10] Raman spectroscopy has been used to study the doping and strain in few layer graphene structures during intercalation of various species.[11–13]

Therefore, it will be used here, in combination with the model developed in Chapter 4, to investigate the intercalation mechanism in graphitic flakes of varying thicknesses.

5.1.2. Flake selection and characterisation

Figure 55 shows atomic force microscopy (AFM) images, height profile and Raman spectra of three representative regions of graphite flakes investigated in this study. The measured thicknesses are 1.7 nm (Figure 55a), 3.8 nm (Figure 55b), and 20 nm (Figure 55c), corresponding to 3 graphene layers, 9 graphene layers and ~56 graphene layers respectively. These flakes represent three categories in which it is interesting to compare the Li intercalation mechanism: 1) a few layer graphene (FLG) sample where the conventional staging process of bulk graphite intercalation is not feasible, 2) a thin graphitic sample (< 10 layers) where the conventional staging process is feasible, but may be affected by the limited number of interlayer spaces and 3) an exfoliated sample with thickness comparable to bulk graphite. For further comparison a 61 nm thick flake (ca. 178 layers) and a free standing microcrystalline graphite electrode were also investigated.

The Raman spectrum of all three graphite flakes exhibit the characteristic G band (~1580 cm^{-1}) and 2D band (~2710 cm^{-1}) as expected (Figure 55d-f). Notably, whilst the 2D band for the thicker flakes may be fit by only two peaks,[14] the 3 layer sample shows a more complex line-shape as explained by Malard et al.[15] and is downshifted to ~2700 cm^{-1}. Nonetheless, the shape of the 2D band of the samples suggests a lack of rotational disorder which would produce a single, broadened 2D peak.[14] The absence of a D band at ~ 1350 cm^{-1} is attributed to the low defect density in our mechanically exfoliated natural graphite samples.

It should be highlighted that the regions shown in Figure 55 are only representative of a fraction of the total flake area following mechanical exfoliation. Flakes were specifically selected to have thicker regions (> 500 nm) at one end, to facilitate better electronic contact with the silver epoxy and Cu current collector (described in chapter 2). However, this technique means recorded current data from the *in situ* experiments are representative of the whole flake and not just the regions shown in Figure 55, effectively preventing analysis of the electrochemistry beyond the control of electrode potential.

Finally, the absolute Raman signal intensity of the 20 nm, 3.8 nm and 1.7 nm thickness flakes at OCP is shown in Figure 56, alongside the microcrystalline graphite sample for comparison. Significantly, there is a reduction in the signal to noise ratio as the thickness of the flakes decreases from 20 nm to 1.7 nm, which is caused by the reduced volume of graphitic sample in the Raman spot. This will be discussed later with reference to band position analysis of the thinnest flakes. Interestingly, the 20 nm flake shows a larger signal to noise ratio for the G band than the microcrystalline graphite, which may be explained by the increased crystallinity of the natural flake samples.

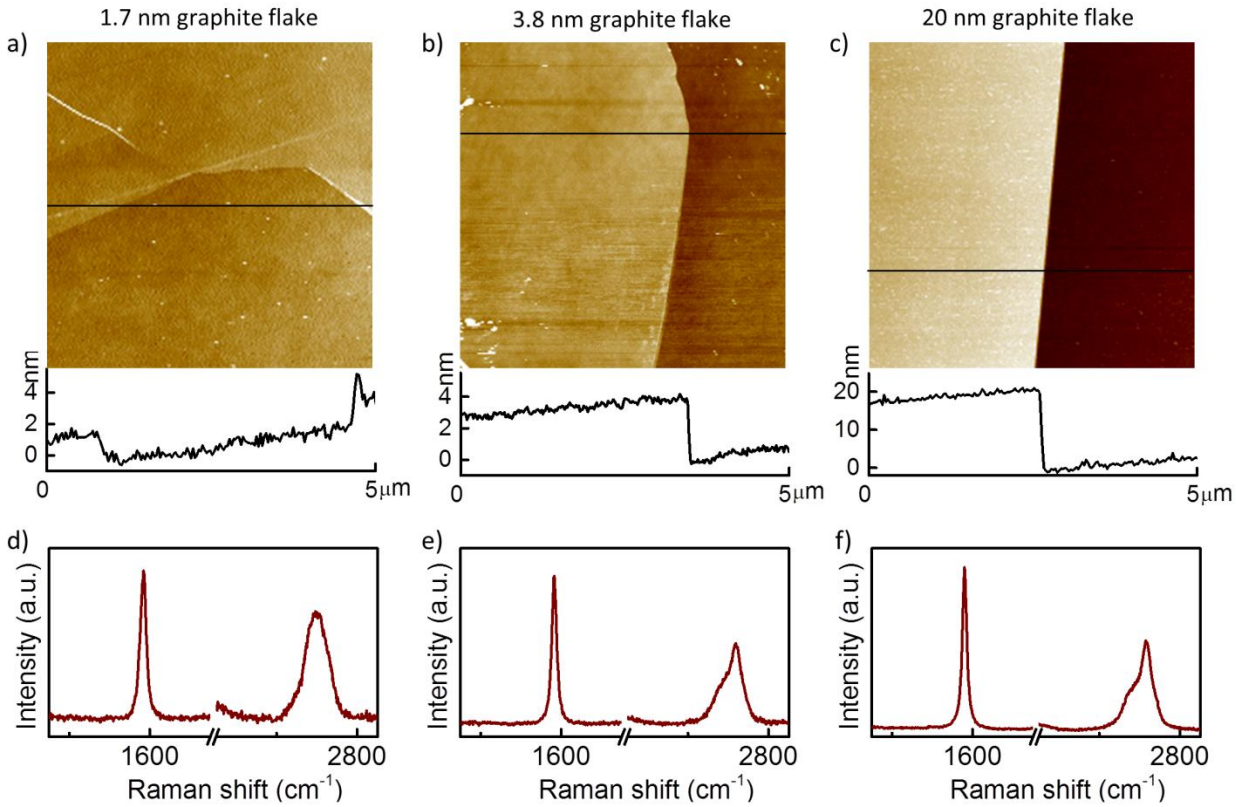

Figure 55: Characterisation of graphite flakes by AFM and Raman spectroscopy. (a-c) AFM images and height profiles of three graphite flakes with thicknesses 1.7 nm (3 graphene layers), 3.8 nm (9 graphene layers), and 20 nm (ca. 56 graphene layers). (d-f) Raman spectra of the corresponding graphite flakes. AFM images were collected by Dr. Jianli Zou.

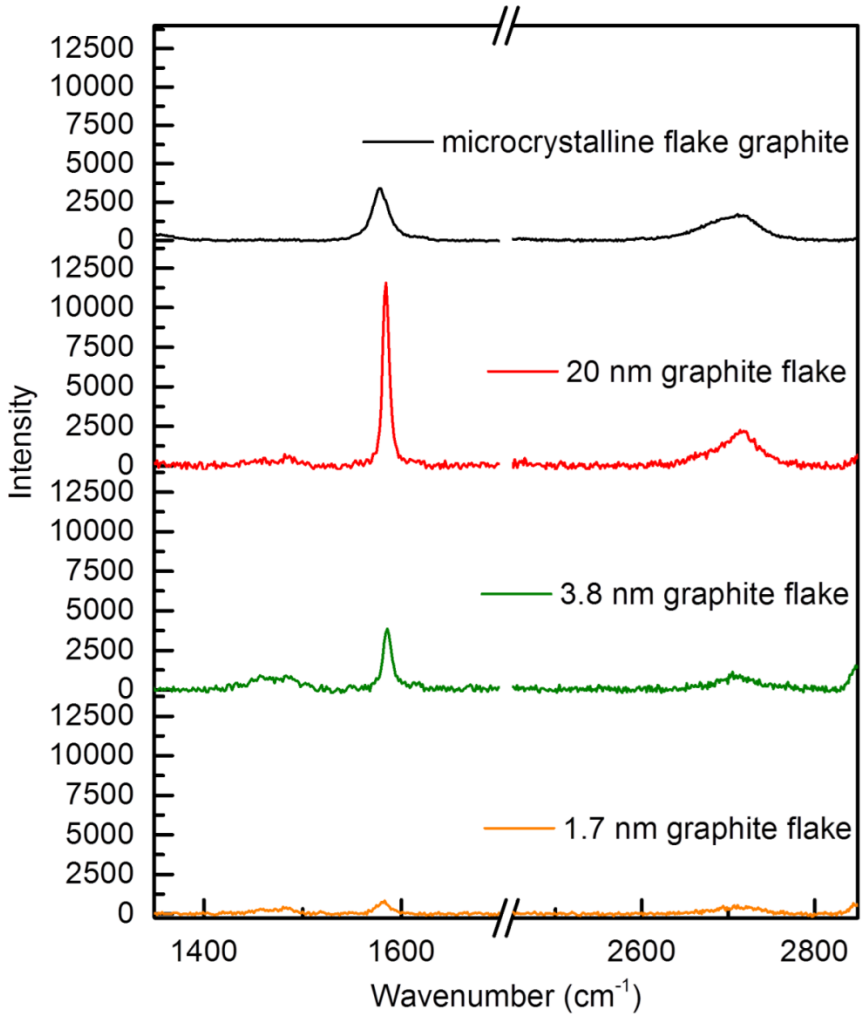

Figure 56: Raman spectra with absolute intensity of microcrystalline graphite, and graphite flakes with 20 nm, 3.8 nm and 1.7 nm thickness at OCP (2.9 V vs. Li^+/Li).

5.1.3. Observation of intercalation dynamics by optical microscopy

Lithium intercalation was induced by linear sweep voltammetry at room temperature (ca. 23 °C). The cell was discharged at 0.02 mV s^{-1} from open circuit potential (OCP) to 1.2 V (vs. Li^+/Li), then at a slower rate of 0.005 mV s^{-1} between 1.2 V to 0.005 V whilst Raman spectra were collected.

Initial experiments were performed to verify the successful electronic connection to the flakes. For example, Figure 57(a-c) shows representative time-lapse optical microscopy images from an edge of a contacted bulk graphite flake (> 50 nm thick) during lithiation. The colour changes have been previously observed during lithiation studies of single particles[16] and bulk electrodes,[17–19] and have been assigned as yellow-gold for stage 1 (LiC_6), red for stage 2 (LiC_{12}) and blue-grey for the liquid phases that appear at the beginning of lithiation (stage 4L, 3L and 2L). Due to the large lateral flake dimensions (> 1 mm) the lithiation process is limited by the diffusion of Li^+ ions,[20] and thus the optical microscope images can be used to observe the intercalation dynamics from the flake edge inwards. For example, at 0.05 V (Figure 57(b and d)) three regions with varying Raman signal can be observed along the length of the flake. Closest to the flake edge a signal characteristic of stage 2, with a broadened G band and no visible 2D band is observed; whilst around 100 nm from the flake edge a signal characteristic of the stage 4L or 3L phases is observed whereby the G band is split and the 2D band resembles a single, broad peak. At intermediate distance from the edge, the G band contains contributions from both phases suggesting they may coexist within the collected Raman spot volume. The spot closest to the edge also highlights the limitations of optical microscopy in determining the stage of the surface region: the

gold colour suggests the presence of stage 1 whilst the Raman spectra suggest stage 2. The presence of several stages along the length of the flake supports the Daumas-Hérold model of sliding intercalant domains.[21] Finally, after being held at 0.005 V for 10 hours, Figure 57(c) shows that the whole flake has completely turned to the characteristic gold colour of stage 1.

These observations validate our experimental setup and suggest the possibility of optical experiments to estimate the diffusion coefficients of Li^+ in the various stages. However, the high transparency[13] of flakes thinner than 20 nm make colour changes during lithiationdifficult to observe by optical microscopy, thus Raman spectroscopy was used as the primary characterisation tool for the remainder of the study.

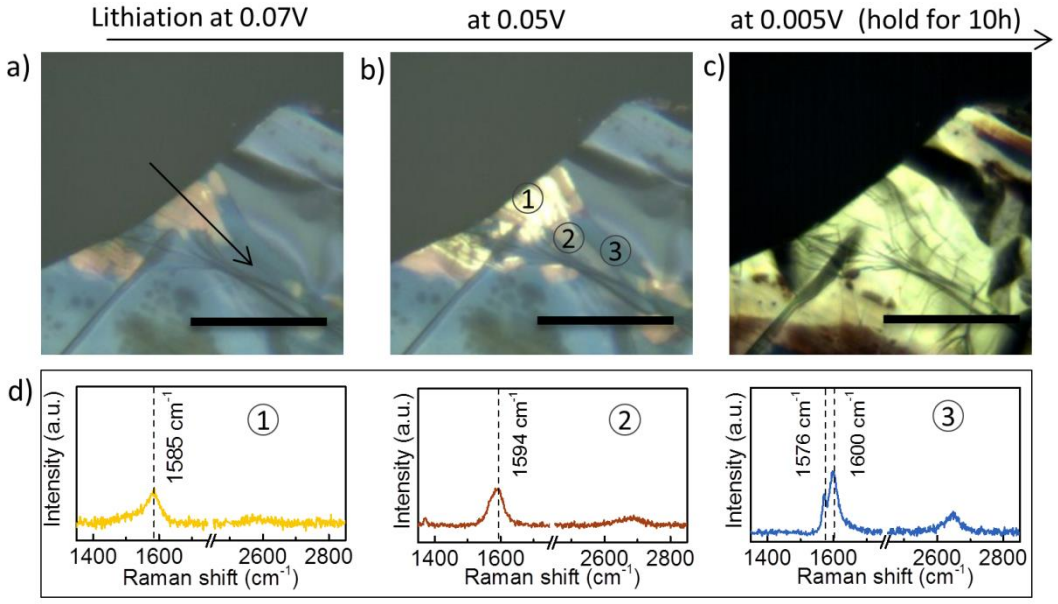

Figure 57: Intercalation dynamics during lithiation process in the bulk graphite flake. a-c) Microscopy images show the change of the colour from the graphite flake during lithiation at different voltage and d) the corresponding Raman spectra from three selected area in b) further confirm the staging process (scale bar is 100 µm).

5.2. *In situ* Raman spectra

Figure 58 shows the *in situ* Raman spectra during lithiation of 20 nm, 3.8 nm and 1.7 nm exfoliated flake samples, alongside that of a porous microcrystalline graphite electrode. The single flake Raman measurements were taken in a spot a few micrometres from the flake edge. During Li insertion for all samples, the 2D band was observed to shift to lower wavenumbers, accompanied by a decrease in intensity, as has previously been discussed.[22] The intercalation behaviour of the 20 nm and 3.8 nm thick flakes displayed similar characteristics to that of the microcrystalline graphite. An initial upshift in the G band frequency was followed by a clear splitting of the G band to E_{2g2}(i) and E_{2g2}(b) modes at around 0.22 V as previously observed.[23,24] As discussed, the splitting of the G band signifies the formation of stage 4L and 3L phases according to the nearest-layer model of Nemanich and Solin.[25]

It should be noted that the observation of G band splitting in the single flake samples are ~ 50 mV lower than those observed for the free-standing microcrystalline graphite electrode. This is likely due to increased Ohmic contact resistance in the single flake electrodes, thus an increased overpotential is required to achieve the same level of intercalation.

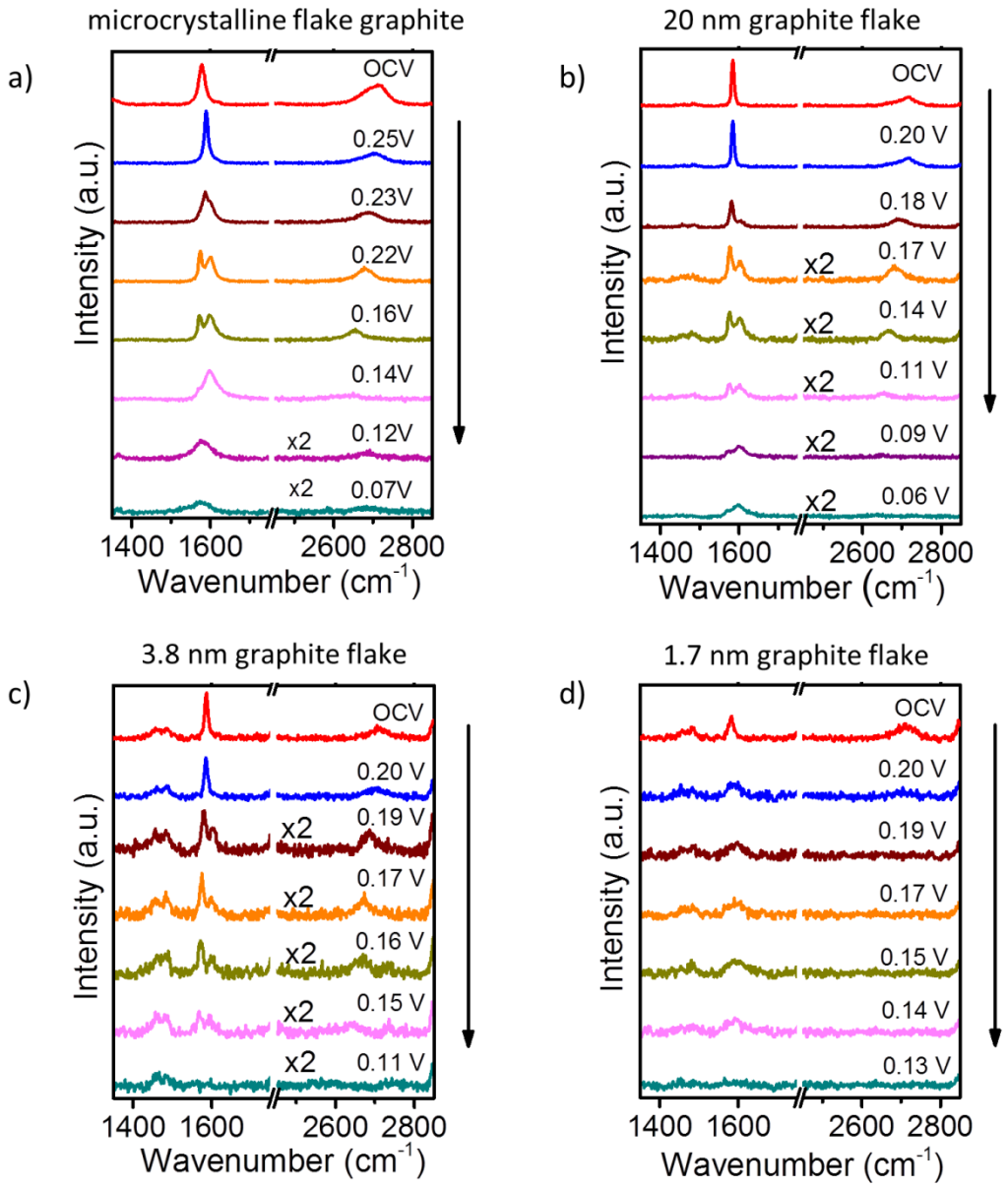

Figure 58: Raman spectra during lithiation of a) microcrystalline flake graphite with ca. 60-100 nm thickness, and graphite flakes of b) 20 nm (ca. 56 graphene layers), c) 3.8 nm (9 graphene layers) and d) 1.7 nm (3 graphene layers) thickness. OCP was ca. 2.9 V, all potentials quoted measured vs. Li^+/Li.

In contrast, the 1.7 nm (3 layer) flake showed rather different behavior whereby a definitive splitting of the G band was not observed throughout Li insertion. It should be noted that the peak broadens and is difficult to fully resolve due to the low initial signal intensity at OCP (Figure 56). Nonetheless, the absence of a split G band suggests

an alternative lithiation mechanism is followed, which agrees with the fact that stage 4L and 3L formation is not possible within trilayer graphene. Our results may be compared to a previous study whereby trilayer graphene was chemically doped by NO_2 adsorption.[26] In this case, G band splitting did occur as only the surface layers were doped, leaving the interior layers effectively non-doped. The lack of obvious splitting in Figure 58(d) therefore suggests equivalent doping of all graphene layers, implying Li^+ ions are distributed in both available interlayer spaces. Splitting of the G band would also be expected if the formation of stage 2-like structures (with either liquid or dense in-plane Li^+ ordering) were to occur during lithiation i.e. domains where one interlayer space is filled and one is empty as shown in Figure 59. For this reason our results support a mechanism of dilute stage 1 formation with increasing Li^+ density throughout lithiation.

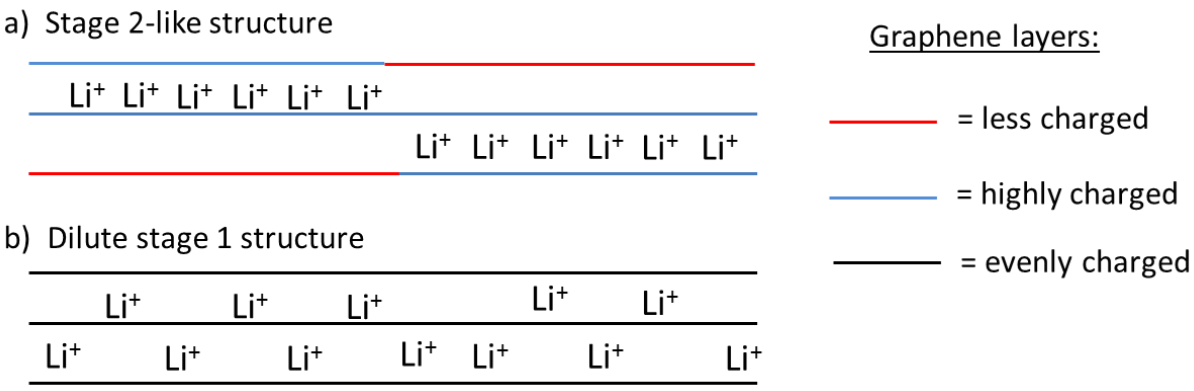

Figure 59: Possible structures during Li^+ intercalation into trilayer graphene: a) stage 2-like structure with domain formation and regions of highly and less highly charged graphene layers, b) dilute stage 1 structure with evenly charged graphene sheets.

5.2.1. G and 2D band wavenumber analysis

To gain a deeper understanding of the intercalation mechanism within the various samples the peak position of the G and 2D band versus potential was plotted. Figure 60 shows results for all but the trilayer graphene sample, and clearly illustrates the initial upshift followed by G band splitting as described above. The initial upshift in the G band can be understood as the result of dilute stage 1 formation where the electronic doping is evenly spread through the graphene sheets. The stiffening of the E_{2g2} phonon is the result of the movement of the nonadiabatic Kohn anomaly, which has been closely investigated in doping studies of graphene.[27,28] Interestingly, the microcrystalline graphite electrode showed a similar upshift to previous studies on microcrystalline samples (~ 10 cm^{-1}),[22,29] whilst all the exfoliated flake samples showed less prominent blue-shifts (~ 5 cm^{-1}). Dilute stage 1 formation has been observed to be responsible for between 4 - 7 % of the theoretical capacity of graphite in microcrystalline samples (~ 20 mAh g^{-1} vs. 372 mAh g^{-1}).[2] Therefore, the diminished G band shift in our exfoliated flake samples suggests there is less doping during this stage, and hence that the proportion of capacity involved in dilute stage 1 formation may be effected by the thickness and/or lateral dimensions of graphite particles.

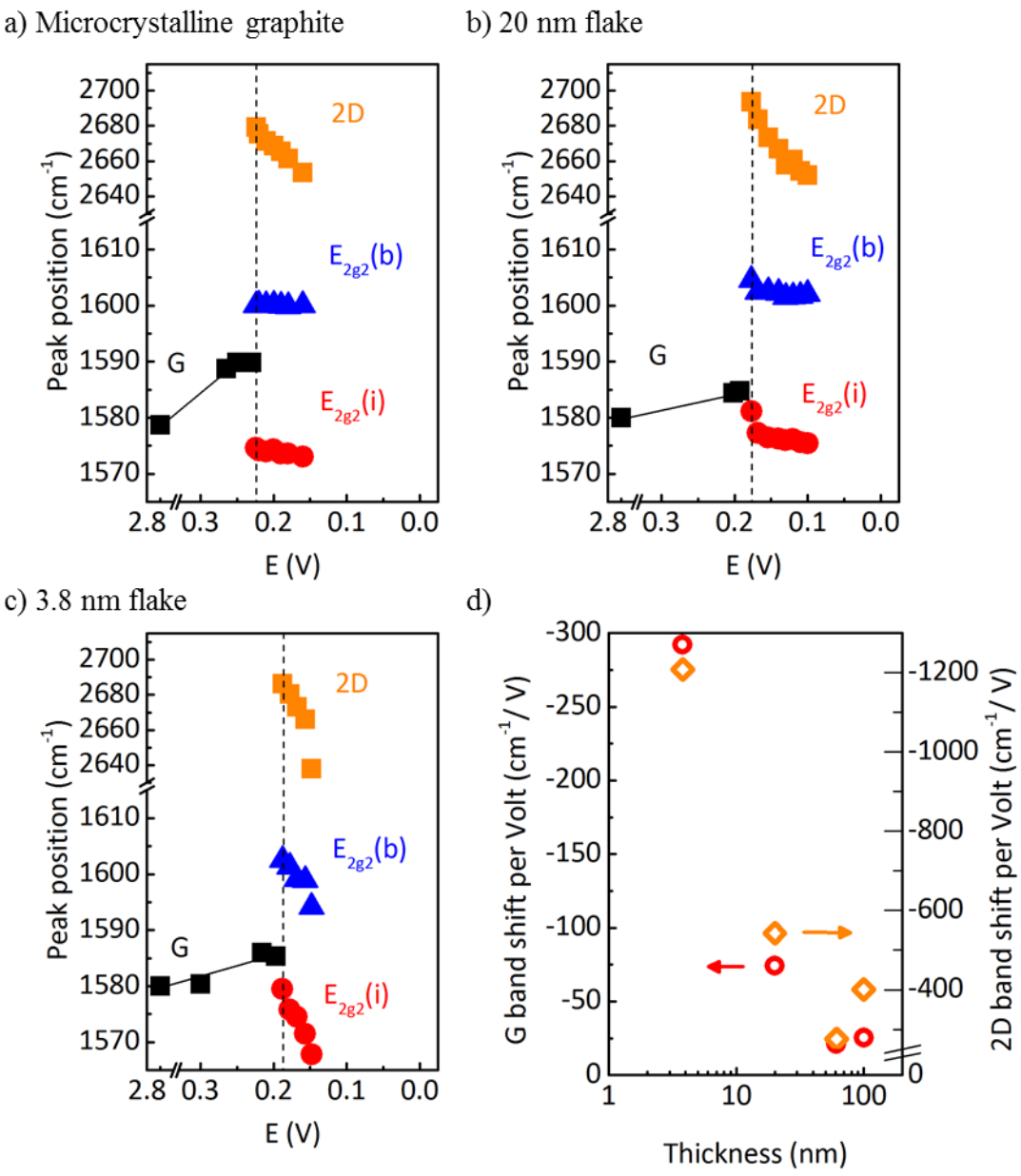

Figure 60: G and 2D band peak positions during intercalation of a) microcrystalline graphite, b) 20 nm flake and c) 3.8 nm graphite flake. The dashed line indicates the beginning of G band splitting. d) Comparison of the shift per Volt of the 2D band and G band (average of E_{2g2}(i) and E_{2g2}(b) modes) for graphite flakes of different thickness.

The G band then splits into the E_{2g2}(i) and E_{2g2}(b) modes at lower and higher wavenumbers respectively, as indicated by the dashed line in Figure 60. At this point the 2D peak has been fitted as a single Lorentzian and its position has been added to

Figure 60. Significantly, as the intercalation progressed, both the 2D band and the E_{2g2}(i) and E_{2g2}(b) modes downshifted for all samples. However, as the potential was decreased the thinnest flakes showed an increased rate of band downshift per Volt as shown in Figure 60(d). In our previous analysis,[1] we assumed the G band shift could be explained purely by the effect of biaxial strain and used the parameters of Mohiuddin et al.[30] to estimate the increase in biaxial strain for each of our samples during this phase transition. Using a value of -63 cm^{-1} per % of biaxial strain the increase in strain during the stage 4L to 3L phase transition was estimated as 0.17 % for the 9 layer sample compared to only 0.04 % for the microcrystalline graphite.

However, as the G band position is known to depend on the combination of both strain and doping effects, this assumption implies the interior and bounding layers of stage 4L and 3L compounds display a constant level of doping. The results described in Chapters 3 and 4 strongly suggest the G and 2D peak positions are representative of the increasing in-plane Li^+ density during this region, which agrees with the solid-solution mechanism of the 4L to 2L phase transitions observed by *in situ* structural studies.[2,31–33] Furthermore, in Chapter 4 an analysis method was developed to qualitatively follow this mechanism. This method will be employed here to gain deeper insight into the cause of the observed flake thickness dependence of the rate of G and 2D band softening.

5.2.1.1. Strain and doping estimation (9 layer to 61 nm flake)

As in Chapter 4 the biaxial strain at each potential has been estimated from the 2D band position using an average[30,34,35] 2D shift of -164 cm^{-1} per %, assuming the peak position of turbostratic graphite represents a zero strain sample. However, these experiments were completed using 532 nm laser wavelength where no value of the 2D band position was found in the literature for turbostratic graphite. Instead the values Tan et al.[36] and Cançado et al.[37] were adjusted by application of the measured dispersion of 95 cm^{-1} per eV,[15] giving an average value of 2690 cm^{-1}. It should be noted that this calculation introduces increased uncertainty to the estimated strain in comparison to using 633 nm laser, due to the larger range of estimated turbostratic graphite 2D band positions (ranging from 2686 cm^{-1} to 2696 cm^{-1}). However, as discussed in Chapter 4, the sensitivity of the model to this parameter does not effect the qualitative trends observed. Finally, the difference between the G band position and the calculated position after application of an (average)[30,34,35,38] -62 cm^{-1} per % biaxial strain was calculated.

Figure 61 shows the calulated upshift of the E_{2g2} modes (associated with doping) versus the derived biaxial strain for all the samples. Values for the 20 nm, 61 nm and microcrystalline graphite samples all lie along a similar trend line, suggesting similar doping of the graphene sheets per % of strain. This trend suggests in-plane Li^+ density is increasing as the voltage is decreased and that the expansion of the C-C bonds is directly related to the increasing charge on the bounding layer graphene sheets. The close agreement between results for the thicker flakes with microcrystalline graphite suggests a similar level of strain on the graphene sheets occurs during Li insertion for graphitic flakes above a certain thickness.

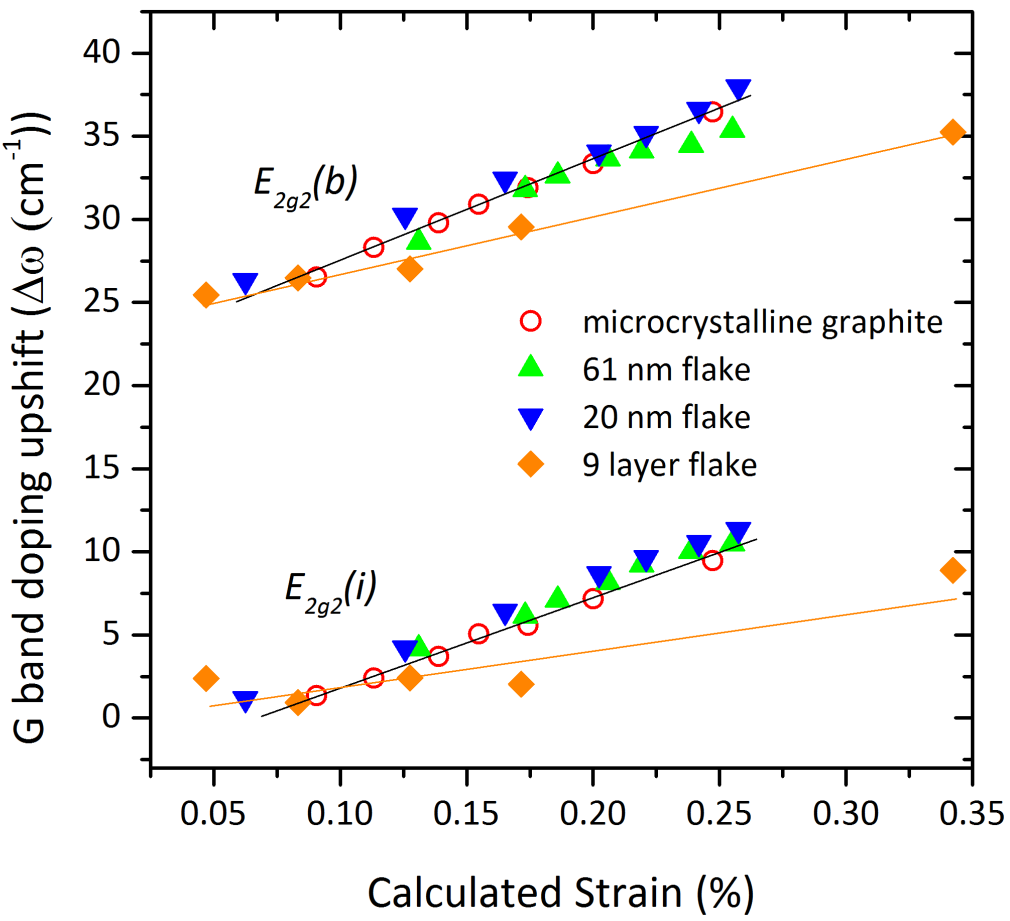

Figure 61: Upshift of G band vs. calculated strain for microcrystalline graphite and flake samples.

In contrast, frequency of the E_{2g2} modes for the 9 layer flake do not shift in agreement with the microcrystalline graphite sample. In comparison with the other samples, the Raman peak positions for the 9 layer flake shows increasing biaxial strain with a lower degree of E_{2g2} mode stiffening associated with doping. This suggests there is increased strain during intercalation that cannot be explained by the C-C bond expansion due to increased occupation of the π^* orbital. The electronic structure of 9 layer graphene should be similar to that of bulk graphite, meaning that increasing occupation of the

π^* orbital during lithiation is expected. Therefore, it is proposed that an additional source of strain is apparent.

The additional strain is caused by the reduced number of interlayer spaces in the 9 layer sample, which suggests it is relatively more difficult for the Li^+ ions to rearrange to form stage 4L and 3L structures, resulting in increased structural strain during lithiation. One way to visualise the increase in strain is by consideration of staged domains according to the Daumus-Hérold model. If the in-plane size of domains were reduced (due to a hindering of Li^+ ion rearrangement), this would result in an increased number of domain boundaries where structural distortion is concentrated, and thus an increase in the average strain measured by Raman.

Previous long term cycling studies have shown that repeated lithium intercalation/deintercalation cycles into graphite electrodes result in increased structural disorder, observable by an increased I_D/I_G ratio in the Raman spectrum.[39–41] Structural degradation exposes extra graphitic surface to the electrolyte, resulting in consumption of cycleable Li by increased SEI growth, and is a significant cause of capacity fading in LIBs. Therefore, the increased structural strain observed during intercalation of the 9 layer flake suggests that reducing the thickness of flakes in graphitic electrodes may result in accelerated structural disorder with cycling. This result agrees with the findings of Sun et al.,[42] which showed that as graphite flake dimensions decreased, the rate of capacity fading increased, suggesting that FLG materials are unsuitable for use in LIB negative electrodes due to their poor long-term cycling performance.

5.2.2. Trilayer graphene sample

Analysis of the G band position of the trilayer graphene sample provides further evidence that the G band position is a sum of doping induced upshift and strain induced downshift. The initial upshift of the G band position is again observed (Figure 62a), concurrent with dilute stage 1 formation, which continues until ~ 0.15 V. It then begins downshifting and losing intensity, until it becomes unobservable ~ 0.13 V. In Figure 62, the G band position of the trilayer graphene sample is compared to the arithmetic mean of the E_{2g2}(i) and E_{2g2}(b) mode frequencies in the 9 layer flake sample. A similar trend of initial upshift followed by downshift is observed, suggesting a comparable interplay between lithiation induced doping and strain.

However, estimation of strain from the 2D band position is not possible with the trilayer sample results because the 2D band disappears before downshifing to below the estimated zero strain position (2690 cm^{-1}). The band is no longer discernible by 0.19 V, which is a higher potential than for all other samples tested. The 2D band has been shown to rapidly lose intensity for graphene layers with high levels of doping,[26,43] and is predicted to be present only for the interior graphene layers of stage > 2 GICs.[44] Therefore, disappearance of the 2D band could be interpreted as further evidence of a continued dilute stage 1 structure, whereby each graphene layer is equivalently charged. However, given the low initial signal to noise ratio and the decrease in intensity with doping, further work is required to confirm this result.

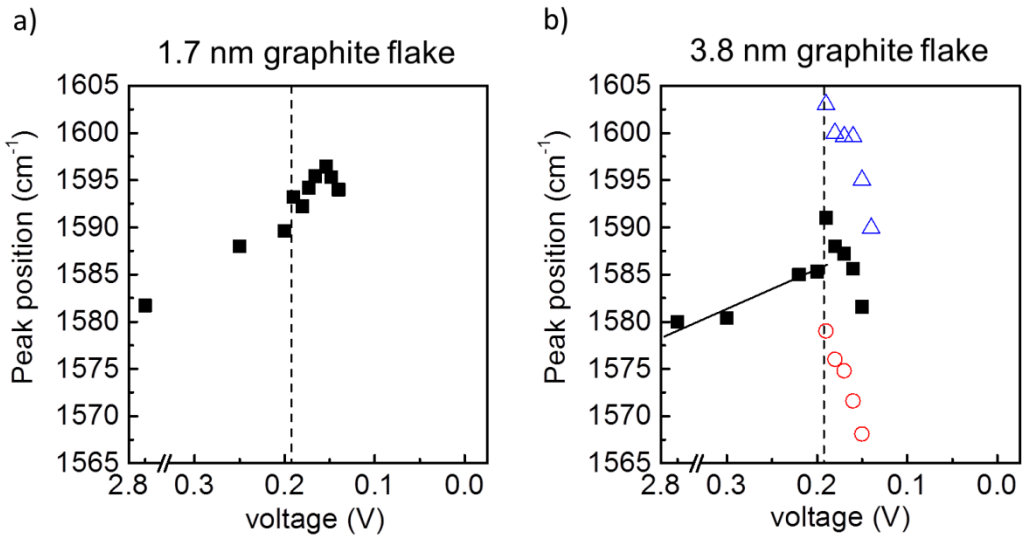

Figure 62: The comparison of a) G peak position of 1.7 nm graphite flake and b) 3.8 nm graphite flake during lithiation. The blue and red cycles in b) are the real data for E_{2g2}(i) and E_{2g2}(b) modes and the solid squares (after the dashed line) represent the arithmetic mean value of both E_{2g2} mode frequencies. The dashed line in a) indicates where the G band splits in b).

5.3. Conclusions

In summary, the lithiation mechanism of graphite flakes of 1.7 nm (trilayer graphene), 3.8 nm (9 layers), 20 nm (~ 56 layers) and 61 nm (~ 178 layers) thickness has been investigated and compared to commercial microcrystalline graphite. During the early stages of intercalation all but the trilayer graphene sample showed splitting of the G band suggesting a similar staging mechanism occurs from graphite flakes of 9 layer thickness and above. However, an accelerated red-shift of the (E_{2g2}(i)) and (E_{2g2}(b)) modes was observed for the 9 layer sample. Analysis of these peak shifts suggests the accelerated softening is caused by increased in-plane strain in the graphene sheets, beyond that which is conventionally induced by charge transfer during lithiation. Additional strain during lithiation may increase the rate of electrode degradation and associated capacity fading in lithium ion batteries, suggesting few layer graphene may be a poor choice as a long cycle life negative electrode material. Moreover, the *in situ* Raman spectra of the trilayer graphene sample suggests successful lithiation was achieved, whereby Li^+ ions occupied both available interlayer spaces without the conventional staging effects of thicker intercalation compounds.

5.4. Future work

Results from this chapter highlight the changes in fundamental lithiation mechanism that must occur as the thickness of graphitic materials approaches the limit of single layer graphene. Future studies should seek to address the following issues:

Firstly, our setup prevented analysis of the thickness dependence of lithium storage capacity alongside other electrochemical signatures of the flakes studied. Future work should attempt to count electrons whilst observing mechanistic details. This would also allow long-term cycling tests of the samples, to confirm the conclusions regarding strain and capacity fading. It should be noted that the study by Sun et al.[42] observed the reversible Li storage capacity to decrease with flakes thinner than 5 nm, however, the variation of lateral dimensions between flakes may have also contributed to this observed differences in intercalation behaviour.

Secondly, the structural information gained from *in situ* measurements in this study is significantly limited by the quality of spectra obtained at low potentials for the thinnest flakes. The quality of *in situ* Raman spectra is limited in part by the relatively low laser power that is used in order to prevent damage or laser heating effects. Besides the use of methods to enhance the Raman signal,[45,46] such as the use of shell-isolated nanoparticle-enhanced Raman spectroscopy,[47] alternative *in situ* structural characterisation techniques could be employed. However, *in situ* neutron or XRD studies require large sample volumes, whereby having similar thickness and stacking of flakes is not feasible given current exfoliation methods. *In situ* TEM with selected area electron diffraction may offer a practical route to overcome these limitations.

Finally, it should be emphasised that the configuration developed holds promise for the investigation of diffusion coefficients in bulk graphite samples. The large lateral dimensions of the natural flakes used allow direct observation of phase transformations throughout (de)lithiation, and at convenient timescales for implementing mapping techniques (such as Raman spectroscopy). Although few layer graphene flakes may not be appropriate for use in lithium ion battery anodes, the techniques developed for graphenic materials may be employed in the study of alternative energy storage materials.

5.5. References

(1) Zou, J.; Sole, C.; Drewett, N. E.; Velicky, M.; Hardwick, L. J. In Situ Study of Li Intercalation into Highly Crystalline Graphitic Flakes of Varying Thicknesses. *J. Phys. Chem. Lett.* **2016**, *7* (21), 4291–4296.

(2) Dahn, J. R. Phase Diagram of Li_xC_6. *Phys. Rev. B* **1991**, *44* (17), 9170–9177.

(3) Heß, M.; Novak, P. Shrinking Annuli Mechanism and Stage-Dependent Rate Capability of Thin-Layer Graphite Electrodes for Lithium-Ion Batteries. *Electrochim. Acta* **2013**, *106*, 149–158.

(4) Woo, K. C.; Mertwoy, H.; Fischer, J. E.; Kamitakahara, W. A.; Robinson, D. S. Experimental Phase Diagram of Lithium-Intercalated Graphite. *Phys. Rev. B* **1983**, *27* (12), 7831–7834.

(5) Levi, M. D.; Salitra, G.; Markovsky, B.; Teller, H.; Aurbach, D.; Heider, U.; Heider, L. Solid-State Electrochemical Kinetics of Li-Ion Intercalation into $Li_{1-x}CoO_2$: Simultaneous Application of Electroanalytical Techniques SSCV, PITT, and EIS. *J. Electrochem. Soc.* **1999**, *146* (4), 1279.

(6) Persson, K.; Hinuma, Y.; Meng, Y. S.; Van der Ven, A.; Ceder, G. Thermodynamic and Kinetic Properties of the Li-Graphite System from First-Principles Calculations. *Phys. Rev. B* **2010**, *82* (12), 125416.

(7) Kühne, M.; Paolucci, F.; Popovic, J.; Ostrovsky, P. M.; Maier, J.; Smet, J. H. Ultrafast Lithium Diffusion in Bilayer Graphene. **2017**.

(8) Pollak, E.; Geng, B.; Jeon, K.-J.; Lucas, I. T.; Richardson, T. J.; Wang, F.; Kostecki, R. The Interaction of Li with Single-Layer and Few-Layer Graphene. *Nano Lett.* **2010**, *10* (9), 3386–3388.

(9) Lee, E.; Persson, K. A. Li Absorption and Intercalation in Single Layer Graphene and Few Layer Graphene by First Principles. *Nano Lett.* **2012**, *12* (9), 4624–4628.

(10) Hui, J.; Burgess, M.; Zhang, J.; Rodriguez-Lopez, J. Layer Number Dependence of Li^+ Intercalation on Few-Layer Graphene and Electrochemical Imaging of Its Solid-Electrolyte Interphase Evolution. *ACS Nano* **2016**, *10* (4), 4248–4257.

(11) Parret, R.; Paillet, M.; Huntzinger, J.-R.; Nakabayashi, D.; Michel, T.; Tiberj, A.; Sauvajol, J.-L.; Zahab, A. A. In Situ Raman Probing of Graphene over a Broad Doping Range upon Rubidium Vapor Exposure. *ACS Nano* **2013**, *7* (1), 165–173.

(12) Zhao, W.; Tan, P. H.; Liu, J.; Ferrari, A. C. Intercalation of Few-Layer Graphite Flakes with $FeCl_3$: Raman Determination of Fermi Level, Layer by Layer Decoupling, and Stability. *J. Am. Chem. Soc.* **2011**, *133*, 5941–5946.

(13) Bao, W.; Wan, J.; Han, X.; Cai, X.; Zhu, H.; Kim, D.; Ma, D.; Xu, Y.; Munday, J. N.; Drew, H. D.; et al. Approaching the Limits of Transparency and Conductivity in Graphitic Materials through Lithium Intercalation. *Nat. Commun.* **2014**, *5*, 4224.

(14) Ferrari, A. C.; Basko, D. M. Raman Spectroscopy as a Versatile Tool for Studying the Properties of Graphene. *Nat. Nanotechnol.* **2013**, *8* (4), 235–246.

(15) Malard, L. M.; Pimenta, M. A.; Dresselhaus, G.; Dresselhaus, M. S. Raman Spectroscopy in Graphene. *Phys. Rep.* **2009**, *473* (5–6), 51–87.

(16) Migge, S.; Sandmann, G.; Rahner, D.; Dietz, H.; Plieth, W. Studying Lithium Intercalation into Graphite Particles via in Situ Raman Spectroscopy and Confocal Microscopy. *J. Solid State Electrochem.* **2004**, *9* (3), 132–137.

(17) Maire, P.; Evans, A.; Kaiser, H.; Scheifele, W.; Novák, P. Colorimetric Determination of Lithium Content in Electrodes of Lithium-Ion Batteries. *J. Electrochem. Soc.* **2008**, 862–865.

(18) Harris, S. J.; Timmons, A.; Baker, D. R.; Monroe, C. Direct in Situ Measurements of Li Transport in Li-Ion Battery Negative Electrodes. *Chem. Phys. Lett.* **2010**, *485*, 265–274.

(19) Maire, P.; Kaiser, H.; Scheifele, W.; Novak, P. Colorimetric Determination of Lithium-Ion Mobility in Graphite Composite Electrodes. *J. Electroanal. Chem.* **2010**, *644* (2), 127–131.

(20) Persson, K.; Sethuraman, V. A.; Hardwick, L. J.; Hinuma, Y.; Meng, Y. S.; van der Ven, A.; Srinivasan, V.; Kostecki, R.; Ceder, G. Lithium Diffusion in Graphitic Carbon. *J. Phys. Chem. Lett.* **2010**, *1*, 1176–1180.

(21) Daumas, N.; Herold, A. Untitled. *C. R. Seances Acad. Sci. Ser. C* **1969**, *268*, 373–375.

(22) Sole, C.; Drewett, N. E.; Hardwick, L. J. In Situ Raman Study of Lithium-Ion Intercalation into Microcrystalline Graphite. *Faraday Discuss.* **2014**, *172*, 223–237.

(23) Inaba, M.; Yoshida, H.; Ogumi, Z.; Abe, T.; Mizutani, Y.; Asano, M. In Situ Raman Study on Electrochemical Li Intercalation into Graphite. *J. Electrochem. Soc.* **1995**, *142* (1), 20–26.

(24) Shi, Q.; Dokko, K.; Scherson, D. A. In Situ Raman Microscopy of a Single Graphite Microflake Electrode in a Li^+-Containing Electrolyte. *J. Phys. Chem. B* **2004**, *108*, 4789–4793.

(25) Solin, S. A. *Graphite Intercalation Compounds*; Zabal, H., Solin, S. A., Eds.; Springer-Verlag: Berlin, 1990; Vol. I.

(26) Crowther, A. C.; Ghassaei, A.; Jung, N.; Brus, L. E. Strong Charge-Transfer Doping of 1 to 10 Layer Graphene by NO_2. *ACS Nano* **2012**, *6* (2), 1865–1875.

(27) Pisana, S.; Lazzeri, M.; Casiraghi, C.; Novoselov, K. S.; Geim, A. K.; Ferrari, A. C.; Mauri, F. Breakdown of the Adiabatic Born-Oppenheimer Approximation in Graphene. *Nat. Mater.* **2007**, *6* (3), 198–201.

(28) Lazzeri, M.; Mauri, F. Nonadiabatic Kohn Anomaly in a Doped Graphene Monolayer. *Phys. Rev. Lett.* **2006**, *97* (26), 266407.

(29) Shi, Q.; Dokko, K.; Scherson, D. A. In Situ Raman Microscopy of a Single Graphite Microflake Electrode in a Li^+-Containing Electrolyte. *J. Phys. Chem. B* **2004**, *108* (15), 4789–4793.

(30) Mohiuddin, T. M. G.; Lombardo, A.; Nair, R. R.; Bonetti, A.; Savini, G.; Jalil, R.; Bonini, N.; Basko, D. M.; Galiotis, C.; Marzari, N.; et al. Uniaxial Strain in Graphene

by Raman Spectroscopy : G Peak Splitting , Grüneisen Parameters , and Sample Orientation. *Phys. Rev. B* **2009**, *79*, 205433–1.

(31) Billaud, D.; Henry, F. X.; Lelaurain, M.; Willmann, P. Revisited Structures of Dense and Dilute Stage II Lithium-Graphite Intercalation Compounds. *J. Phys. Chem. Solids* **1996**, *57* (6–8), 775–781.

(32) Billaud, D.; Henry, F. X. Structural Studies of the Stage III Lithium-Graphite Intercalation Compound. *Solid State Commun.* **2002**, *124* (8), 299–304.

(33) Heß, M. Kinetics and Stage Transitions of Graphite for Lithium-Ion Batteries, PhD thesis. ETH / PSI, 2013.

(34) Zabel, J.; Nair, R. R.; Ott, A.; Georgiou, T.; Geim, A. K.; Novoselov, K. S.; Casiraghi, C. Raman Spectroscopy of Graphene and Bilayer under Biaxial Strain: Bubbles and Balloons. *Nano Lett.* **2012**, *12* (2), 617–621.

(35) Ding, F.; Ji, H.; Chen, Y.; Herklotz, A.; Dörr, K.; Mei, Y.; Rastelli, A.; Schmidt, O. G. Stretchable Graphene: A Close Look at Fundamental Parameters through Biaxial Straining. *Nano Lett.* **2010**, *10* (9), 3453–3458.

(36) Tan, P.; Hu, C.; Dong, J.; Shen, W.; Zhang, B. Polarization Properties, High-Order Raman Spectra, and Frequency Asymmetry between Stokes and Anti-Stokes Scattering of Raman Modes in a Graphite Whisker. *Phys. Rev. B* **2001**, *64* (21), 214301.

(37) Cançado, L. G.; Pimenta, M. A.; Saito, R.; Jorio, A.; Ladeira, L. O.; Grueneis, A.; Souza-Filho, A. G.; Dresselhaus, G.; Dresselhaus, M. S. Stokes and Anti-Stokes Double Resonance Raman Scattering in Two-Dimensional Graphite. *Phys. Rev. B* **2002**, *66* (3), 35415.

(38) Lee, J. E.; Ahn, G.; Shim, J.; Lee, Y. S.; Ryu, S. Optical Separation of Mechanical Strain from Charge Doping in Graphene. *Nat. Commun.* **2012**, *3*, 1024.

(39) Sethuraman, V. A.; Hardwick, L. J.; Srinivasan, V.; Kostecki, R. Surface Structural Disordering in Graphite upon Lithium Intercalation/deintercalation. *J. Power Sources* **2010**, *195* (11), 3655–3660.

(40) Kostecki, R.; McLarnon, F. Microprobe Study of the Effect of Li Intercalation on the Structure of Graphite. *J. Power Sources* **2003**, *119–121*, 550–554.

(41) Markervich, E.; Salitra, G.; Levi, M. D.; Aurbach, D. Capacity Fading of Lithiated Graphite Electrodes Studied by a Combination of Electroanalytical Methods, Raman Spectroscopy and SEM. *J. Power Sources* **2005**, *146* (1–2), 146–150.

(42) Sun, H.; Varzi, A.; Pellegrini, V.; Dinh, D. A.; Raccichini, R.; Del Rio-Castillo, A. E.; Prato, M.; Colombo, M.; Cingolani, R.; Scrosati, B.; et al. How Much Does Size Really Matter? Exploring the Limits of Graphene as Li Ion Battery Anode Material. *Solid State Commun.* **2017**, *251*, 88–93.

(43) Chen, C.; Park, C.; Boudouris, B. W.; Horng, J.; Geng, B.; Girit, C.; Zettl, A.; Crommie, M. F.; Segalman, R. A.; Louie, S. G.; et al. Controlling Inelastic Light Scattering Quantum Pathways in Graphene. *Nature* **2011**, *471* (7340), 617–620.

(44) Chacón-Torres, J. C.; Wirtz, L.; Pichler, T. Manifestation of Charged and Strained Graphene Layers in the Raman Response of Graphite Intercalation Compounds. *ACS*

Nano **2013**, *7* (10), 9249–9259.

(45) Kalbac, M.; Vales, V.; Vejpravova, J.; Fan, B.; Dresselhaus, M. S.; Liu, Z.; Kong, J.; Basko, D.; Galiotis, C.; Marzari, N.; et al. The Effect of a Thin Gold Layer on Graphene: A Raman Spectroscopy Study. *RSC Adv.* **2014**, *4* (105), 60929–60935.

(46) Wang, Y. Y.; Ni, Z. H.; Shen, Z. X.; Wang, H. M.; Wu, Y. H. Interference Enhancement of Raman Signal of Graphene. *Appl. Phys. Lett.* **2008**, *92* (4), 43121.

(47) Anema, J. R.; Li, J.-F.; Yang, Z.-L.; Ren, B.; Tian, Z.-Q. Shell-Isolated Nanoparticle-Enhanced Raman Spectroscopy: Expanding the Versatility of Surface-Enhanced Raman Scattering. *Annu. Rev. Anal. Chem.* **2011**, *4* (1), 129–150.

6. Evaluation of exfoliated graphite materials as conductive additives for high rate performance lithium ion battery composite electrodes

6.1. Overview of chapter

This chapter describes an investigation into the performance of exfoliated graphite materials as conductive additives in LIB composite electrodes. It begins with an introduction to the role of conductive additives within composite electrodes, followed by structural characterisation of the materials selected for evaluation. Results are presented from electrochemical cycling tests of both lithium titanate negative electrode and lithium cobalt oxide positive electrode systems. Finally, the challenges encountered during the investigation are discussed, and suggestions are presented to improve the outcomes of future composite electrode optimisation studies.

6.2. Composite electrodes in lithium ion batteries

In general, lithium ion batteries electrodes (LIBs) consist of porous composites which have been coated onto metallic current collectors; the purpose of which is to carry electronic current to the external circuit. These composites are conventionally composed of three material subsets with complementary functions:

- Active material (AM) particles where Li^+ ions are either stored or released as described in Chapter 1.
- Polymeric binders which provide mechanical stability by maintaining interparticle contact and adhesion to the current collector.
- Conductive additives (CA) which provide low impedance electronic pathways to AM particles throughout the electrode, thus facilitating the redox processes which occur at their surfaces. Alternatively, the same effect can be achieved by a conductive coating layer on the AM particles' surface.

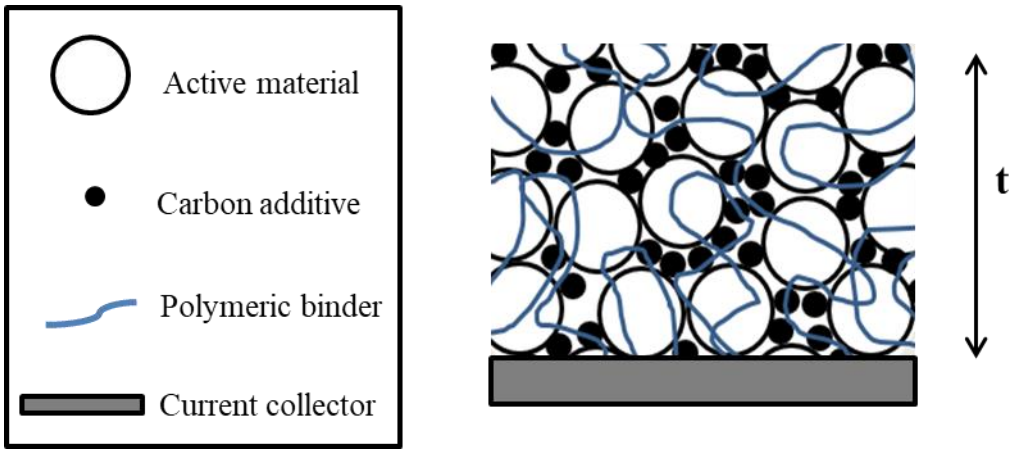

Figure 63: Schematic of composite electrode composition, **t** = electrode thickness.

The term loading will be used throughout to describe increasing active mass per area (mg cm^{-2}), which may be increased by either increasing electrode thickness or decreasing porosity.

6.2.1. Electronic Conductivity in Composite Electrodes

The variation of electronic conductivity with conductive additive content in composite electrodes has been mathematically described with some success by percolation theory.[1] In effect, percolation theory predicts that above a certain volume % of conductive additive (known as the percolation threshold) a sharp drop in specific resistivity of the electrode is observed, as shown in Figure 64.[2] At this critical volume, conductive additive particles are close enough to ensure electrical contact by either electronic tunnelling or direct contact, such that a conductive path spans the entire electrode.

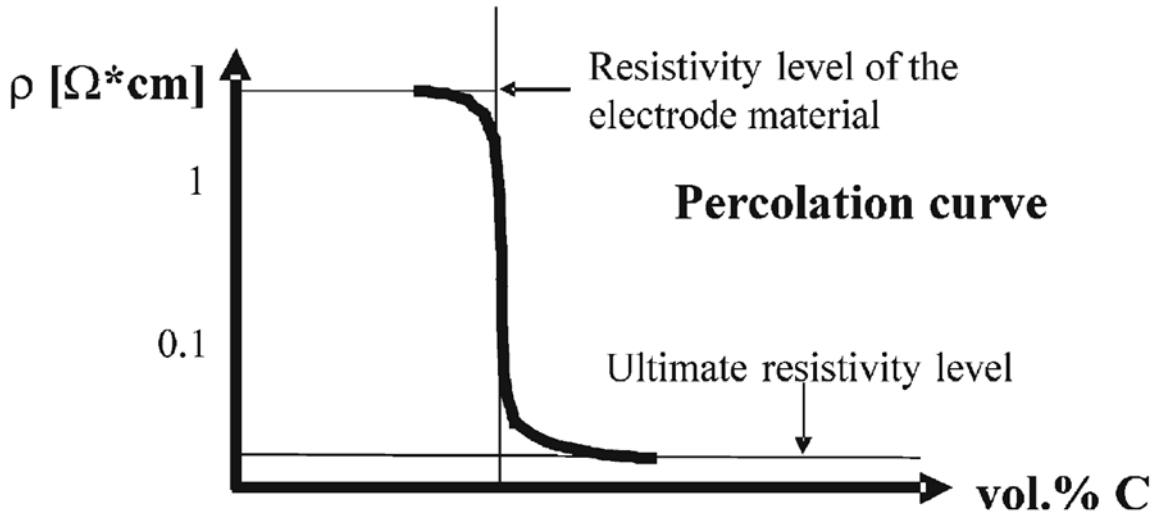

Figure 64: Schematic representation of an ideal percolation curve describing the effect of increasing conductive carbon additive volume % on electrode electronic resistivity. Adapted from Spahr.[2]

However, work by Dominko et al.[3,4] and others[5] has concluded that electrode performance is determined not only by the volume fraction of conductive additives, but also their distribution within the composite, which is generally referred to as electronic wiring. Therefore, the number of contact points between additive network

and active material plays a critical role. Furthermore, recent simulations considering binary mixtures of CA and AM suggest a strong dependence of electronic percolation and wiring on relative particle sizes as well as volume fractions of additives.[6]

Furthermore, the interaction between binder and CA is also considered to be important for electrode performance because the two components are understood to form a conductive coating layer on the surface of active material particles. This has been investigated by Battaglia and coworkers[7–9] through variation of the CA to binder ratio, suggesting that the best electrode performance does not necessarily occur with the highest electronic conductivity of either the coating layer or the overall composite. Their results suggest the optimum ratio for electrochemical performance depends strongly on mechanical properties, suggesting that the ability to maintain inter-particle contact throughout cycling is critical. In contrast, other groups ascribe an ion-blocking effect to the coating layer, whereupon increased volume fraction of binder limits electrode performance.[5,10,11]

6.2.2. Motivations for use of graphene, few layer graphene and exfoliated graphite materials as conductive additives

The development of scalable processes for the production of graphene, FLG and exfoliated graphite materials opens up the possibility of their use as additives in composite materials. Recent studies predict that the due to high aspect ratio and conductivity, well dispersed graphene sheets will display an extremely low percolation threshold in composites.[12–14] Moreover, significant enhancements to the mechanical properties of composites have been observed after the addition of graphenic materials at very low wt. %.[15] The combination of these properties suggests exfoliated graphite materials may be beneficial as conductive additives in LIB electrodes. Furthermore, a large number of studies have previously reported beneficial properties of graphenic and exfoliated graphite additives in LIB electrodes, which have been reviewed elsewhere. However, due to the lack of systematic testing procedures, weak reporting of important parameters (electrode loading, porosity, thickness) and a large variation in electrode formulation/testing methods, the bulk of this literature lacks significance for assesing additive performance, and can be misleading. This work addresses this gap by critically analysing the testing methodology for high rate performance LIB electrodes, and highlights best practice for future studies.

6.2.3. Rate limitations in composite electrodes

The development of models to quantitatively describe the rate capability of lithium ion cells generally ascribes a bulk electronic conductivity to composite electrodes.[16–18] Through analysis of these porous electrode models Doyle et al.[19] derived analytical solutions which describe three performance-limiting-phenomena, namely: solution-phase diffusion, solid-phase diffusion and cell Ohmic resistance. Significantly, since the effective electronic conductivity of commercial composite electrodes (~ 1 S cm^{-1})[16] is generally orders of magnitude larger than that of ionic charge transport in the electrolyte (~10^{-2} S cm^{-1}),[20,21] the electrode conductivity is generally disregarded with respect to high rate performance.[22] However, porous electrode theory effectively ignores interparticle interactions between active material, binder and carbon additive, thus neglecting the importance of electronic wiring effects discussed above. Therefore, empirical optimisation of high rate performance through composite electrode design is still required and will support the advancement of models to describe the effects of electrode structure on cell performance.[10]

6.3. Scope of conductive additive investigation

As highlighted above the primary role of carbon additives is to increase the electronic conductivity of composite electrodes to allow lithium insertion and removal from active material particles throughout the electrode. However, due to the interconnected nature of factors which affect composite electrode performance there are several other characteristics which are likely to be affected by modification of the electrode composition, for example:

- mechanical properties
- tortuosity of electrode microstructure
- heat dissipation during electrochemical cycling
- long term cycling performance
- cost

These factors will not be the focus of this work, although they should be investigated in similar studies. Moreover, although attempts have been made to use industrially relevant electrode formulations, this is not an exhaustive study in cell optimisation for the maximisation of energy or power metrics.

Within this Chapter the effect of exfoliated graphite additives upon the achievable capacity during high rate electrochemical cycling will be investigated; with a view to increasing power performance of industrially applicable LIB systems. Additives will be tested in comparison to a carbon black sample, as commonly used in commercial systems. In addition, a pristine graphite sample will be tested to observe any beneficial effects of exfoliation processes. A fixed 1:1 ratio of CA:binder is used throughout. Marks et al.[11] have suggested this composition maintains a relatively constant

thickness of binder on the surface of AM particles; thus preventing an increase in ion blocking and electronic isolation of particles as has been observed previously when the proportion of binder is increased relative to the CA.[5,11,23]

Furthermore, it should be highlighted that results will focus on electrochemical cycling data rather than characterisation of electrode conductivity. As will be critically discussed later, there remains a lack of consensus on the best method to measure additive dispersion, conductivity and electronic wiring in composite electrodes. Therefore, this work focuses on the practical performance of electrodes during electrochemical cycling as the most direct method to compare the effect of composition variation.

6.4. Conductive additive materials

Figure 65(a) shows the carbon black (CB) material (Super C65, TIMCAL), which was selected to be representative of a typical carbon black additive. It consists of spherical nanoparticles of 30 - 50 nm diameter, which are known to form conductive chains of aggregates throughout composites.[24,25] This arrangement permits electronic percolation at low volume % and helps to form many contact points with active material particles.

Figure 65(b) shows the microcrystalline graphite sample (SFG6, TIMCAL, TIMREX®), the structure of which has been discussed in previous chapters. Briefly, it shows average lateral flake dimensions of ~ 6 µm and out-of-plane crystallite dimensions > 100 nm.[26]

Figure 65(c, d) shows a liquid exfoliate graphene (LEG) material (Elicarb® Premium Grade Graphene Powder, Thomas Swan Advanced Materials). The suppliers report average lateral flake dimensions ~ 1 µm and average flake thickness of between 5 - 7 graphene layers.[27]

Figure 65(e, f) shows a material produced by collaborators at the University of Manchester according to the electrochemical exfoliation process developed by Abdeljader et al.[28,29] (described in Chapter 2). This sample will be referred to as cathodic electrochemically exfoliated graphene (cEEG). The presence of few layer graphene sheets was confirmed by TEM (Figure 65(e)), although the results of Chapter 4 suggest significant restacking may have occurred prior to testing. A distribution of lateral flake dimensions in the range (100 nm to 1 µm) can be observed by SEM (Figure 65(f)).

Figure 65(g, h) shows a material produced by collaborators at the University of Manchester according to the oxidative electrochemical exfoliation process of Parvez et al.[30] This material will be referred to as anodic electrochemically exfoliated graphene (aEEG). TEM images suggest the presence of few layer graphene (Figure 65(g). SEM images show a large distribution of lateral flake dimensions (Figure 65(h)); the majority of which by wt. % are in the 3 - 10 μm range, however, smaller flakes (< 1 μm) are also observed.

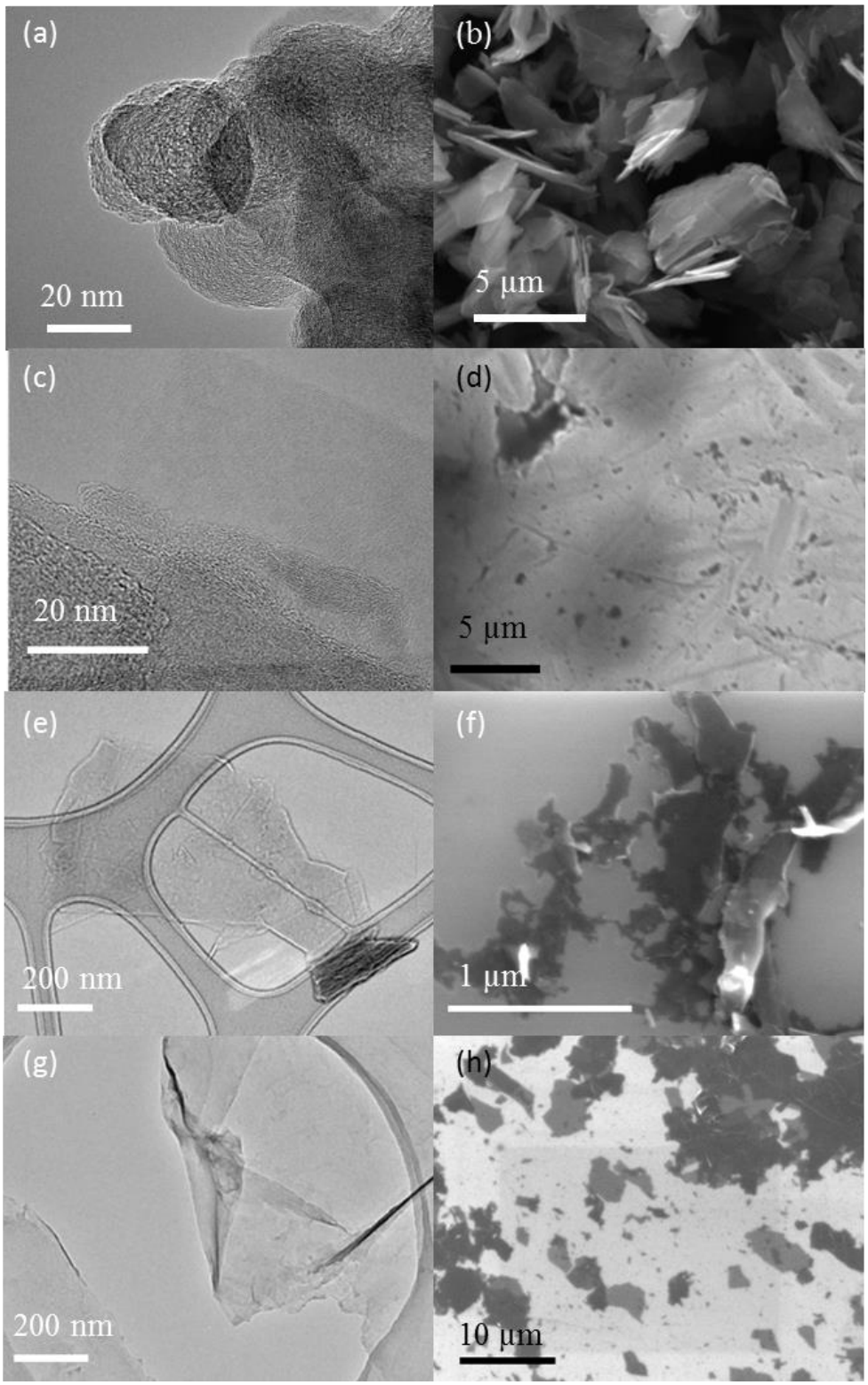

Figure 65: TEM and SEM images of (a) carbon black, (b) microcrystalline graphite (c, d) LEG, (e, f) cathodic EEG and (g, h) anodic EEG. TEM images collected by Dr Laura Cabo Fernandez (a, c) and Dr Jianyun Cao (e, g). SEM images (f) and (h) were collected by Jianyun Cao.

Figure 66 shows Raman spectra of the conductive additive materials. All spectra show the characteristic D, G and 2D bands of disordered graphitic materials. The level of disorder increases moving from the microcrystalline graphite to LEG, cEEG and aEEG as indicated by an increasing I_D/I_G ratio (Table 6.1). This is explained by a reduction in the average size of crystallites and/or an increasing frequency of defects.[31,32]

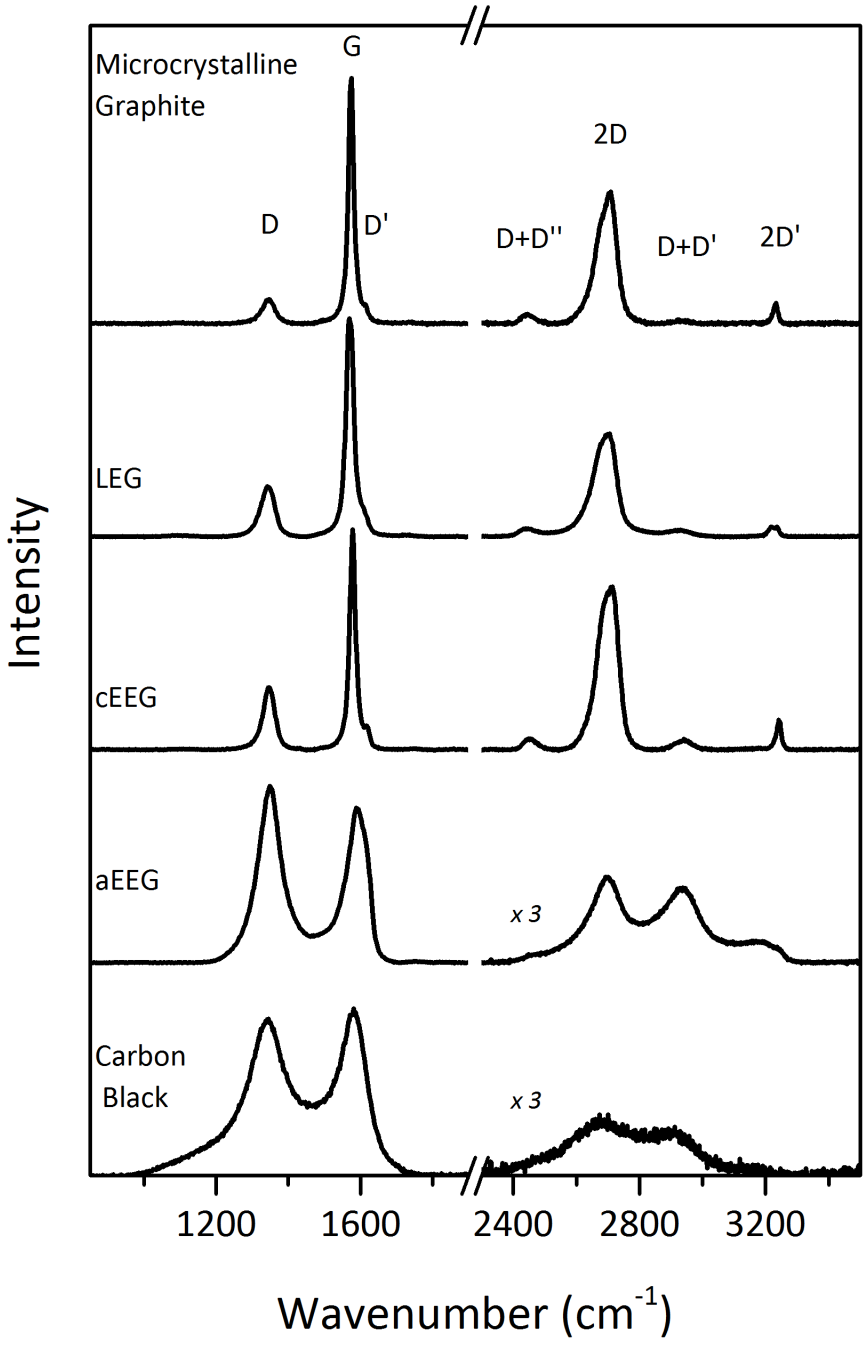

Figure 66: Raman Spectroscopy data of conductive additives, 532nm laser.

Furthermore, the 2D band for microcrystalline graphite, LEG and cEEG shows a doublet shape, indicating the presence of more than 4 stacked graphene layers.[33] In contrast, the level of disorder in the aEEG material is similar to that of carbon black, as indicated by a large I_D/I_G ratio, as well as a similar bandshape in the overtone region (2400 – 3200 cm^{-1}). In particular, the loss of the doublet 2D band-shape, suggests a loss in three dimensional ordering of graphene sheets.[31,33] This suggests the disorder induced by the anodic electrochemical exfoliation process, prevents the restacking of sheets as occurred for the cathodic process, discussed in Chapter 4.

Table 6.1: I_D/I_G ratio, 2D band positions and FWHM (of constituent peaks) for the conductive additives investigated.

Material	I_D/I_G **ratio**	**2D(1)**		**2D(2)**	
		ω (cm^{-1})	**FWHM (cm^{-1})**	**ω (cm^{-1})**	**FWHM (cm^{-1})**
Microcrystalline Graphite	0.11	2677	69	2711	43
LEG	0.24	2677	77	2711	42
cEEG	0.29	2684	64	2719	42
aEEG	1.1	-	-	2696	156
Carbon Black	1.0	-	-	2679	282

6.5. Lithium Titanate as a model negative electrode system

Lithium titanate, $Li_4Ti_5O_{12}$, was selected as a model system to investigate the performance of the selected carbon materials as conductive additives in LIB negative electrodes. The reversible intercalation of Li^+ ions proceeds via a two-phase reaction:[34]

$$Li_4Ti_5O_{12} + 3Li^+ + 3e^- \leftrightarrow Li_7Ti_5O_{12} \qquad \text{Equation 6.1}$$

The two phase reaction gives a plateau around 1.55 V vs. Li^+/Li at low rates as shown in Figure 67 producing a theoretical capacity of 175 mAh g^{-1}. The insertion reaction is highly reversible as indicated by the small hysteresis between charge and discharge plateaus.

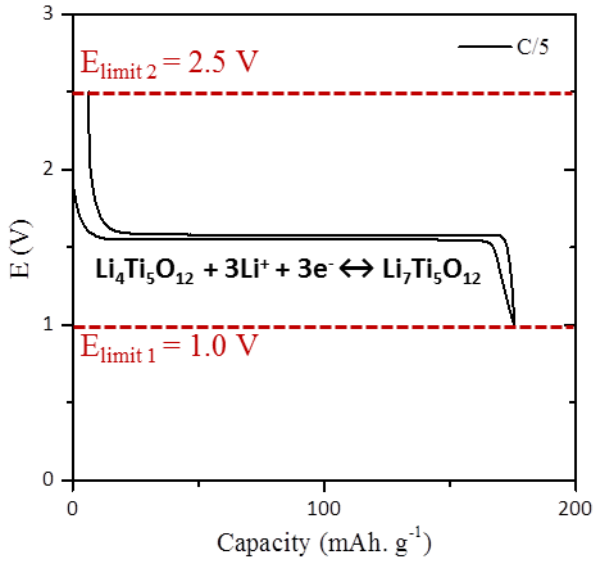

Figure 67: Representative voltage profile (vs. Li^+/Li) for the first charge/discharge cycle of $Li_4Ti_5O_{12}$ at C/5 rate. $E_{limit\ 1}$ and $E_{limit\ 2}$ show cut-off voltages.

$Li_4Ti_5O_{12}$ has received particular attention as an anode material due to its impressive high rate performance, safety and cyclability.[35,36] The impressive cycling characteristics have been attributed to the nearly zero volume change between lithiated phases[37,38] which prevents mechanical degradation of electrodes during cycling. This makes $Li_4Ti_5O_{12}$ electrodes appropriate for applications with high current rates - enabling conductive additive evaluation without the complexity arising from rapid capacity fading during cycling. In addition, the intercalation potential is above where Li intercalation into graphitic carbons[39,40] and electrolyte reduction reactions readily occur,[41] thus avoiding significant complication of the analysis by competing electrochemical processes. However, it should be noted that evidence for the formation of a surface layer at the $Li_4Ti_5O_{12}$ particle surface have been reported.[42,43] Furthermore, commercial utilisation of $Li_4Ti_5O_{12}$ electrodes has been limited due to problems associated with gas formation during cycling,[44] low energy metrics and cost.[45]

Figure 68(a) shows SEM images of the selected $Li_4Ti_5O_{12}$ powder (HOMBITEC LTO5), with average particle size of around 250 nm as reported by Carvalho et al.[46] PXRD data is shown in Figure 68(b) and shows the cubic $Fd\bar{3}m$ structure. Reported electronic conductivity of lithium titanate spinel falls in the range 10^{-6} –10^{-13} S cm^{-1}.[47] This low conductivity suggests the addition of significant volume fractions of conductive additives is required to achieve electronic percolation.

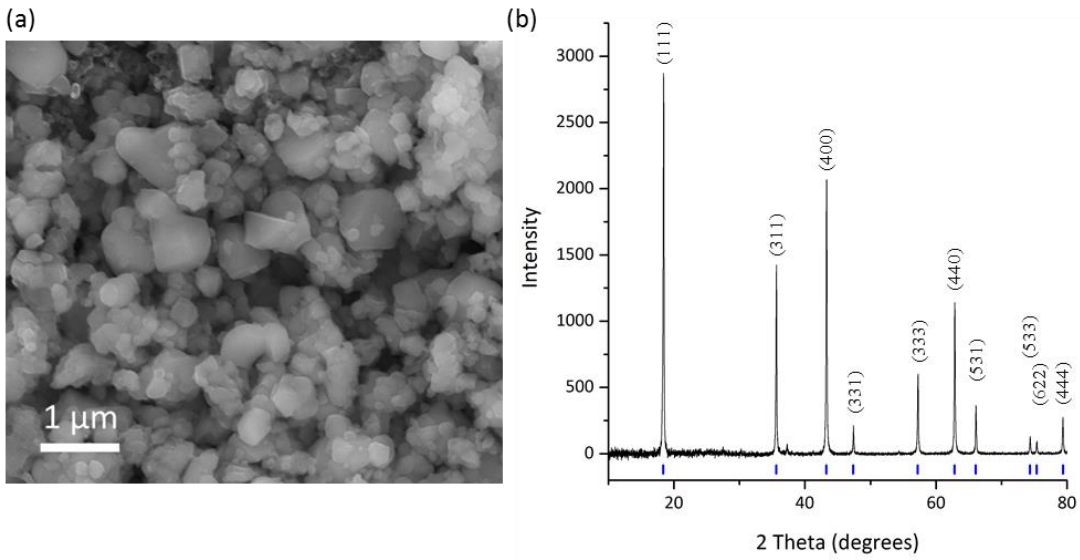

Figure 68: (a) Scanning electron microscopy image and (b) PXRD pattern of $Li_4Ti_5O_{12}$.

6.5.1. Effect of electrode loading and thickness

Initial tests were performed with carbon black (CB), however, it was found challenging to produce electrodes with similar thickness, loading and porosity at the lab scale. Adjusting the additive ratio strongly affected the volume of NMP required to effectively disperse and cast electrodes. This caused different additive compositions to dry at different thicknesses compared to the wet casting, which makes it challenging to prepare electrodes of varying composition with similar thickness and loading. Therefore in order to facilitate comparison of additives it was important to investigate how significant the effect of thickness and loading were on rate performance. Electrodes with weight fractions of 96:2:2 ($Li_4Ti_5O_{12}$:CB:binder) were prepared and calendered to a porosity of ~ 30 % as described in Chapter 2. A symmetric cycling procedure was used whereby cells were discharged to 1.0 V then charged to 2.5 V at the current rates shown in Table 6.2.

Table 6.2: Galvanostatic current and approximate C rate for lithiation/delithiation cycles of $Li_4Ti_5O_{12}$ electrodes

Cycle Number	1	2 - 6	7 - 11	12 - 16	17 - 21	22 - 26	27 - 31
Current Rate /mA g^{-1}	35	87.5	175	350	875	1750	35
C Rate	C/5	C/2	C	2C	5C	10C	C/5

Figure 69(a) shows how the specific capacity (on delithiation) of the electrodes decreases with increased C rate for all loadings. However, the effect of increased C rate is far more significant for the electrodes with higher loading. For example the 30 µm electrodes decrease from ~ 170 mAh g^{-1} at C/5 to ~ 130 mAh g^{-1} at 10C, whilst the 60 µm electrodes decreases rapidly from ~ 170 mAh g^{-1} to ~ 25 mAh g^{-1}. Moreover, whilst comparison of rate performance based on C rate is widespread in the literature

it should be highlighted that it is an unfair metric for comparing electrodes of different active mass loading. For example at the 10C rate the current density for the 30 µm electrode is ~ 11.1 mA cm^{-2} whilst for the 60 µm electrode is ~ 23.4 mA cm^{-2}. As discussed in Chapter 1 (Equation 1.12 and Equation 1.14), the current density relates directly to electrolyte and electronic Ohmic resistance, in addition to the build-up of concentration gradients (Equation 1.15) and associated concentration overpotential. Therefore, when cycled at identical C rates, cells with increased electrode loading reach the cut-off voltage at shorter discharge times due to increased cell overpotentials, and hence achieve lower delithiation capacities.

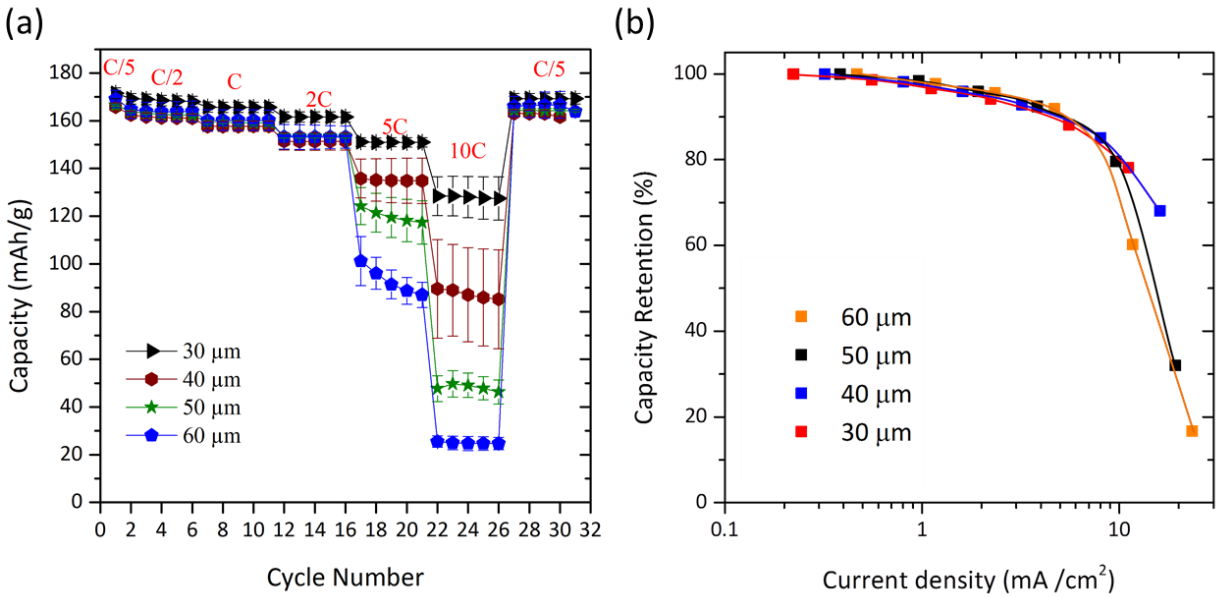

Figure 69: Effect of thickness on (a) Specific capacity vs. C rate and (b) % capacity retention vs. current density, for $Li_4Ti_5O_{12}$ electrodes with 96:2:2 ($Li_4Ti_5O_{12}$:CB:binder) composition by wt. %. (a) Data is average of 3 – 4 cells. (b) Capacity retention has been calculated assuming 100 % capacity on the first delithiation cycle (C/5). Curves were drawn manually for visualisation purposes.

A more useful comparison is shown in Figure 69(b), where capacity retention (defined as a percentage of the first delithiation cycle capacity) is plotted versus current density, for the best performing electrodes. Below ~ 7 mA cm^{-2}, as current density increases there is a similar drop in capacity retention for all loadings. It has been observed that at low current densities capacity retention is governed solely by solid-state diffusion limitations and both electrolyte and electronic transport limitations may be neglected.[48,49] Therefore, capacity retention is limited by the same intrinsic property of the $Li_4Ti_5O_{12}$ active material and is loading independent in this range. However, as the current density increases above 7 mA cm^{-2}, a divergence in performance is observed, whereby the capacity retention of thicker electrodes (increased loading) decreases faster than those of thinner electrodes (decreased loading). At high current densities electrolyte transport limitations are likely to become significant.[16,19,22,48] However, the glass fibre separators used for these measurements have a combined thickness of > 200 µm, which suggests that an additional 10 µm of the electrode thickness may not contribute significantly to the observed electrolyte transport limitation. Therefore, it is suggested that the reduction in rate performance with increased electrode thickness (and loading) can be linked to an increase in Ohmic resistance from electronic transport through the electrode.

6.5.2. Effect of increased carbon black and binder content

Figure 70 shows the effect of increasing the CB and binder wt. % on the rate performance, with fixed thickness (40 µm) and porosity ~ 30 %. Surprisingly, the increase in additive content appears to result in a reduction in rate performance. However, as both of the electrodes with increased additive content also displayed larger porosities, this the reduction in rate performance may also be also linked to increasing porosity. This emphasises the importance in keeping porosity constant between electrodes in order to compare the effect of composition variation fairly.

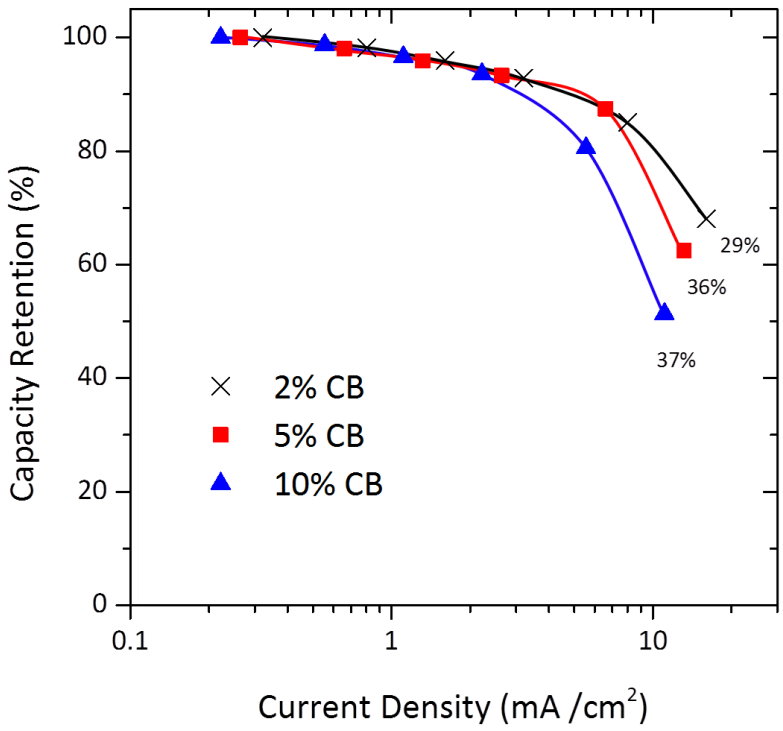

Figure 70: Effect of increasing carbon black and binder content in $Li_4Ti_5O_{12}$ electrodes (40 µm), the calculated porosity of electrodes is indicated.

Furthermore, there appeared to be a reduction in mechanical properties of the casts with larger additive content; for example, no casts above 40 µm in thickness (after calendering to ~ 30 % porosity) could be produced with the 5 wt. % CB and binder

composition, due to cracking and mechanical failure. Later it will be shown that a similar composition works well with the micron sized $LiCoO_2$ active material. This suggests mechanical failure of these electrodes is linked to the small particle size of the $Li_4Ti_5O_{12}$ active material, suggesting an increased binder fraction is required to produce thick electrodes with $\geq$ 5 wt. % CB. However, increasing the binder content may also impede Li^+ transport to the active material surface as previously observed.[5,10,11]Moreover, as discussed, previous work has shown the mechanical properties of composite electrodes to be significant to the rate performance due to the importance of interparticle contact. This suggests variation of mechanical properties between electrodes may be significant to the rate performance observed in this system.[23]

6.5.3. Effect of conductive additive variation

Different additives were tested in a 1:1 ratio with CB at this 2 wt. % total conductive additive composition, i.e. 96:1:1:2 wt. % ($Li_4Ti_5O_{12}$:X:CB:binder) where X = the conductive additive. All casts were calendered to 50 µm except for the aEEG cast which was 60 µm thick. The porosity was set around 30 % for all casts. Figure 71 shows that the electrodes containing graphenic additives exhibit no enhancement in rate performance. Electrodes containing LEG exhibited very similar performance to the CB electrodes. Meanwhile, electrodes with aEEG additive exhibited a decreased performance at high current density; however, this electrode was the thickest and had the highest porosity. The reduction in capacity retention was more significant than that observed for the 60 µm cast with 2 wt. % CB shown in Figure 69(b), therefore this suggested that the porosity was again playing a significant role in the rate performance.

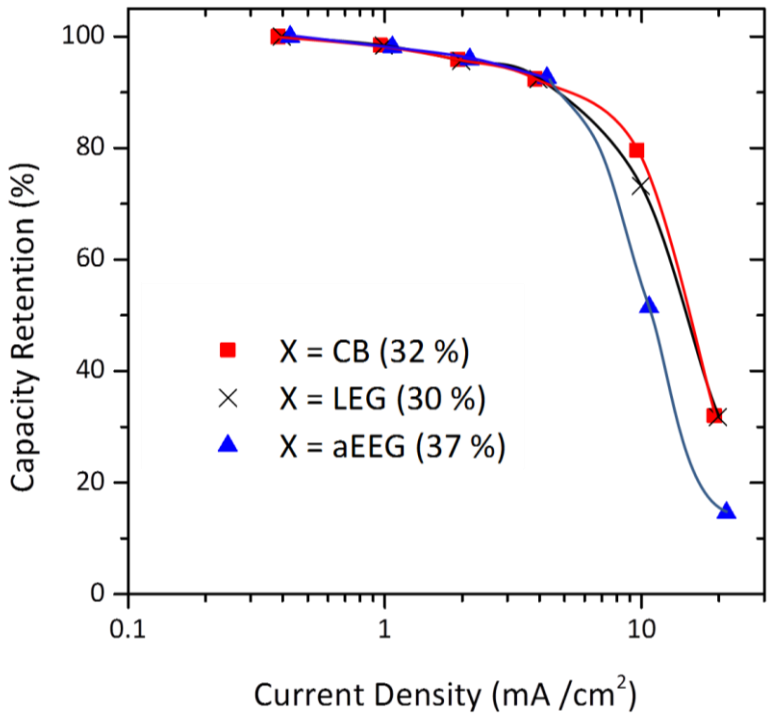

Figure 71: Capacity retention of $Li_4Ti_5O_{12}$ electrodes with composition 96:1:1:2 ($Li_4Ti_5O_{12}$:X:CB:binder) by wt. %, where X is indicated in the graph.

6.5.4. Effect of porosity in casts with fixed composition and thickness

To investigate the effect of porosity more closely, casts were produced using the optimised composition (96:2:2 wt. % ($Li_4Ti_5O_{12}$:CB:binder)), with varying porosity and 50 µm thickness. A different electrochemical cycling procedure (based on the 'rate test' procedure described below) was used for these experiments, details of which are given in the appendix. Figure 72 clearly shows that as the porosity is decreased the rate performance improves. In contrast, previous electrode optimisation studies have shown that increasing the porosity improved the rate performance, by reducing the effective resistance of electrolyte transport.[50–52] Therefore, this finding suggests the limiting factor for capacity retention at high current density is Ohmic resistance to electron transport rather than electrolyte transport limitations.

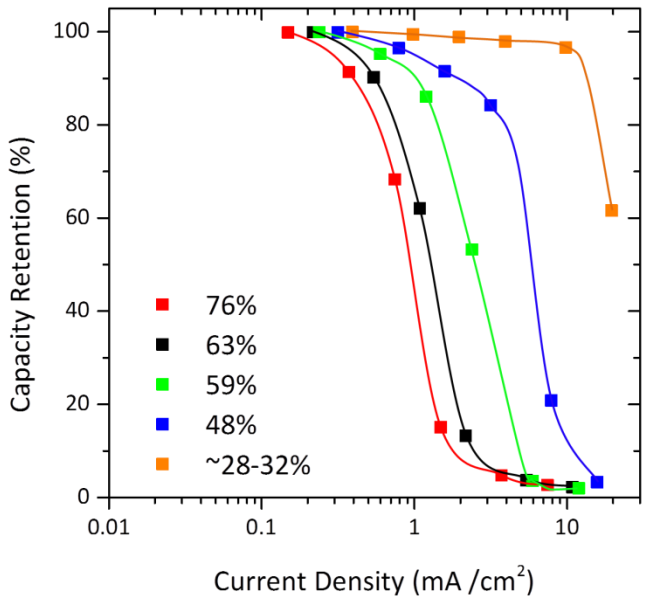

Figure 72: Effect of porosity on rate performance of $Li_4Ti_5O_{12}$ electrodes (50 µm, 96:2:2 ($Li_4Ti_5O_{12}$:CB:binder) by wt. %) using accelerated 'rate test' procedure, discussed later.

6.5.5. Discussion - explaining electrode optimisation results for the $Li_4Ti_5O_{12}$ system

The rate performance of the studied $Li_4Ti_5O_{12}$ electrodes appears to be optimised at low additive content and with low porosity. Previous studies have observed a rapid increase in electronic conductivity (σ) of $Li_4Ti_5O_{12}$ during lithiation whereby σ increased from $< 10^{-7}$ S cm^{-1} in $Li_4Ti_5O_{12}$, to ~ 2.5 S cm^{-1} in $Li_7Ti_5O_{12}$.[47] This explains why Kim et al.[53] have been able to achieve close to the theoretical capacity using $Li_4Ti_5O_{12}$ electrodes of similar thickness to this study, without any carbon additives. Similar results were also reported by Wang et al.[54] The mechanism of electronic percolation during lithiation is illustrated in Figure 73. At high potentials (> 1.5 V vs. Li^+/Li) particles in the electrode are present as $Li_4Ti_5O_{12}$ with low conductivity. Lithiation begins at particles close to the current collector where charge transfer may occur; the lithiated surface of these particles is then able to carry electrons to particles further from the current collector, eventually allowing full lithiation of the electrode.

Kim et al.[53] also highlighted a strong sensitivity to electrode porosity, whereby large capacities were only achieved at low porosity, when interparticle contact was optimised. Thus, a similar mechanism is proposed to explain the results of the present study. The substitution of conductive additives causes no significant changes in performance because electronic transport is occurring primarily through the lithiated surfaces of $Li_4Ti_5O_{12}$ particles. Therefore, another system is required to observe the influence of conductive additive materials.

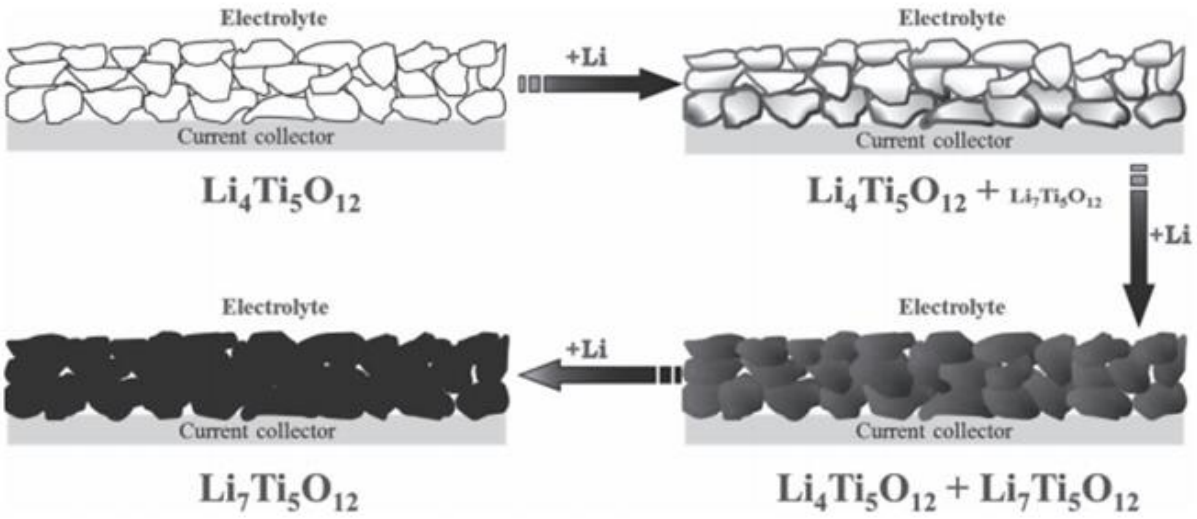

Figure 73: Explanatory diagram showing how lithiation may occur in a carbon free $Li_4Ti_5O_{12}$ electrode by initial lithiation of particle surfaces adjacent to the current collector (adapted from [53]).

6.6. Lithium Cobalt Oxide as a model positive electrode system

Lithium cobalt oxide ($LiCoO_2$) was selected as a suitable positive electrode material due to its widespread use and in-depth literature. $LiCoO_2$ is able to reversibly (de)intercalate lithium according to the reaction:

$$LiCoO_2 \leftrightarrow Li_xCoO_2 + (1\text{-}x)Li^+ + (1\text{-}x)e^-$$

as first demonstrated in 1980 by Goodenough and coworkers.[55] The structural changes during deintercalation have been well studied by *in situ* XRD.[56,57] Morcrette et al.[57] observed a two-phase region occurring between x = 0.99 - 0.73 composition range (in Li_xCoO_2), which is responsible for the first plateau around 3.93 V. A single phase range then exists between x = 0.73 - 0.55, followed by two further phase transformations at 4.05 V and 4.18 V. Figure 74 shows the potential vs. capacity for the first cycle charge-discharge cycle with a cut-off voltage of 4.2 V, corresponding to x around 0.45[58] and giving a capacity of 140 - 150 mAh g^{-1}.

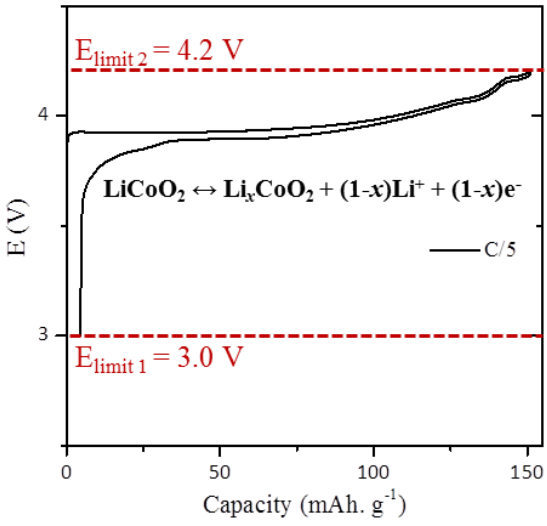

Figure 74: Representative voltage profile (vs. Li^+/Li) of $LiCoO_2$ first charge/discharge cycle at C/5 rate. $E_{limit\ 1}$ and $E_{limit\ 2}$ show cut-off voltages.

Figure 75 shows SEM images of the $LiCoO_2$ particles used in the present study, exhibiting primary particles of ellipsoidal shapes, with diameters between 3 - 10 µm. $LiCoO_2$ is in the rhombohedral system (space group $R\bar{3}M$) with the layered α-$NaFeO_2$ type structure, as confirmed by the PXRD pattern shown in Figure 76.[58]

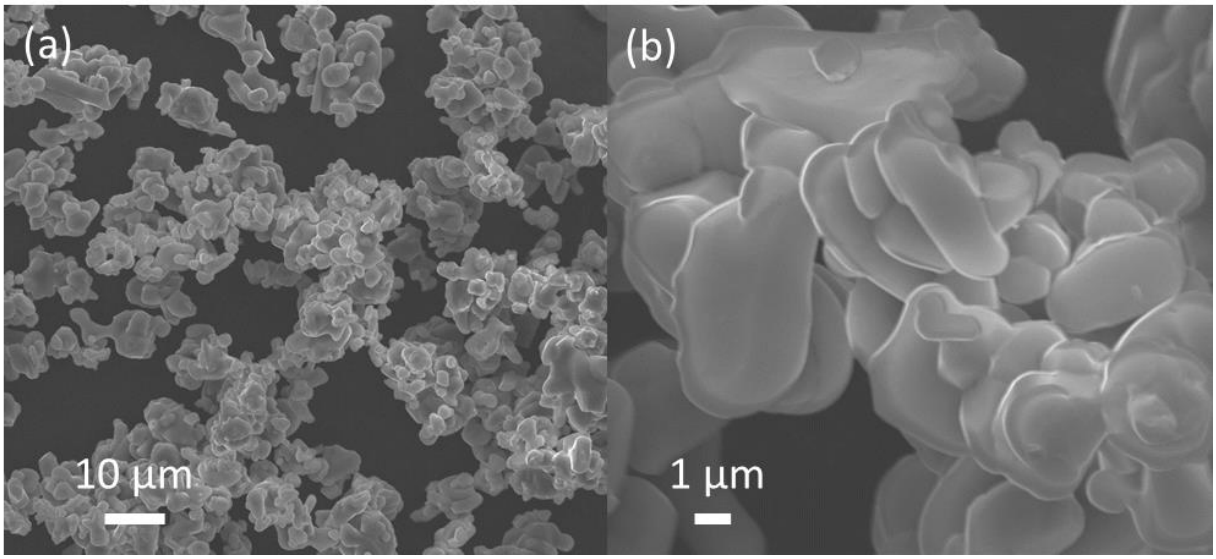

Figure 75: SEM images of $LiCoO_2$ powder

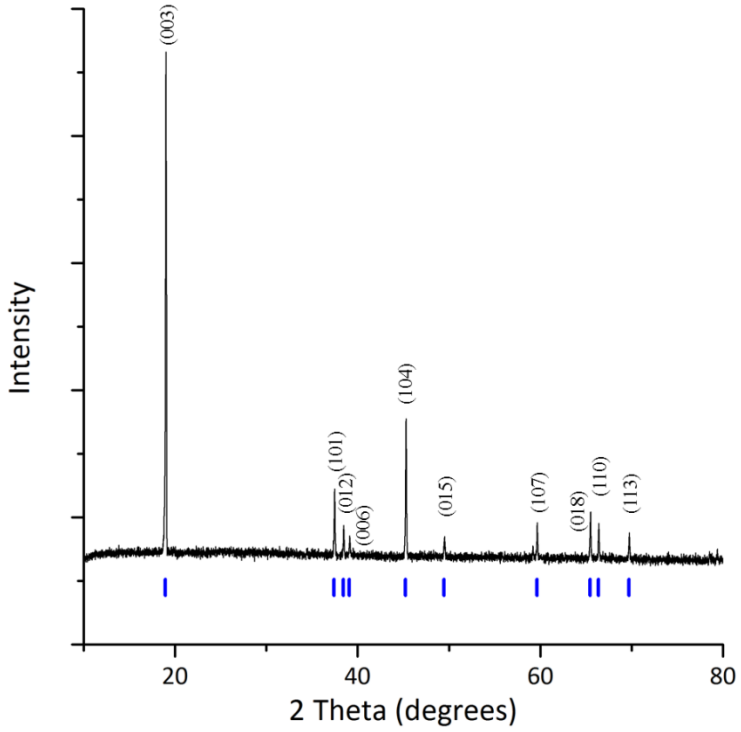

Figure 76: PXRD pattern for $LiCoO_2$

In contrast to $Li_4Ti_5O_{12}$, studies of $LiCoO_2$ sintered pellets have shown that the conductivity increases as lithium is removed.[58,59] Ménétrier et al.[58] have reported a transition from semiconducting to metallic behaviour between Li_1CoO_2 and $Li_{0.7}CoO_2$ with a respective increase in conductivity from ~ 7 x 10^{-3} S cm^{-1} to ~ 5 x 10^{1} S cm^{-1} (at ~ 273K). This explains why successful electrochemical cycling of porous, sintered electrodes has been achieved without the addition of carbon additives.[60] However, such sintered electrodes are likely to have high tortuosity and hence be strongly limited by electrolyte transport at high current rates. Furthermore, attempts to cycle carbon-free $LiCoO_2$ electrodes composed of micron sized particles and binder (similar to that achieved with $Li_4Ti_5O_{12}$) failed to reach full capacity and suffered from rapid capacity fading.[53] Poor performance was explained by the anisotropic volume change of ~ 2 % during the first phase transition of delithiation,[57] which causes loss of interparticle contact and electronic percolation in electrodes without sufficient conductive additives.[53]

6.6.1. Effect of additive content and loading

Initially, tests to optimise composition and investigate electrode loading effects were performed with CB. The performance of a 96:2:2 ($LiCoO_2$:CB:binder) composition was compared to a 90:5:5 composition (by wt. %). A symmetric cycling procedure was used whereby cells were charged to 4.2 V then discharged to 3.0 V at the current rates shown in Table 6.3.

Table 6.3: Galvanostatic current and approximate C rate for delithiation and lithiation cycles of $LiCoO_2$ electrodes.

Cycle number	1	2 - 6	7 - 11	12 - 16	17 - 21	22 - 26	27 - 31
Current rate /mA g^{-1}	27.5	68.75	137.5	275	687.5	1375	27.5
C Rate	C/5	C/2	C	2C	5C	10C	C/5

When increasing electrode loading, a similar trend to the $Li_4Ti_5O_{12}$ system was expected, whereby at low current densities there is no difference in capacity retention between cells, whilst at higher current densities the performance deviates as the cells with lowest loading perform best. However, as shown in Figure 77(a), the 96:2:2 composition did not show the expected decrease in rate performance with increased loading. Furthermore, electrodes prepared from the same cast showed a large discrepancy in rate performance making analysis challenging. Upon closer inspection, it was again observed that electrodes with lower porosity showed improved rate performance to those with higher porosity; suggesting a similar mechanism of electronic percolation through surfaces of active material particles. The variation in porosity of electrodes from the same cast occurs due to inhomogeneity in the casting procedure, which is challenging to avoid on the lab-scale.

In contrast, the 90:5:5 composition (Figure 77(b)) showed improved reproducibility of performance and similar behaviour at all loadings. The improved reproducibility implies porosity variations have less significance, suggesting an alternative conduction mechanism may be prevalent. Furthermore, the similarity in rate performance across loadings suggests that electrolyte transport limitations may be the limiting factor, as expected at high current densities.[16,19,22,48] As discussed, due to the large separator thickness (> 200 µm), the small increments of ~ 10 µm thickness between cells causes negligible changes to the electrolyte transport limitation, hence all electrodes show similar rate performance.

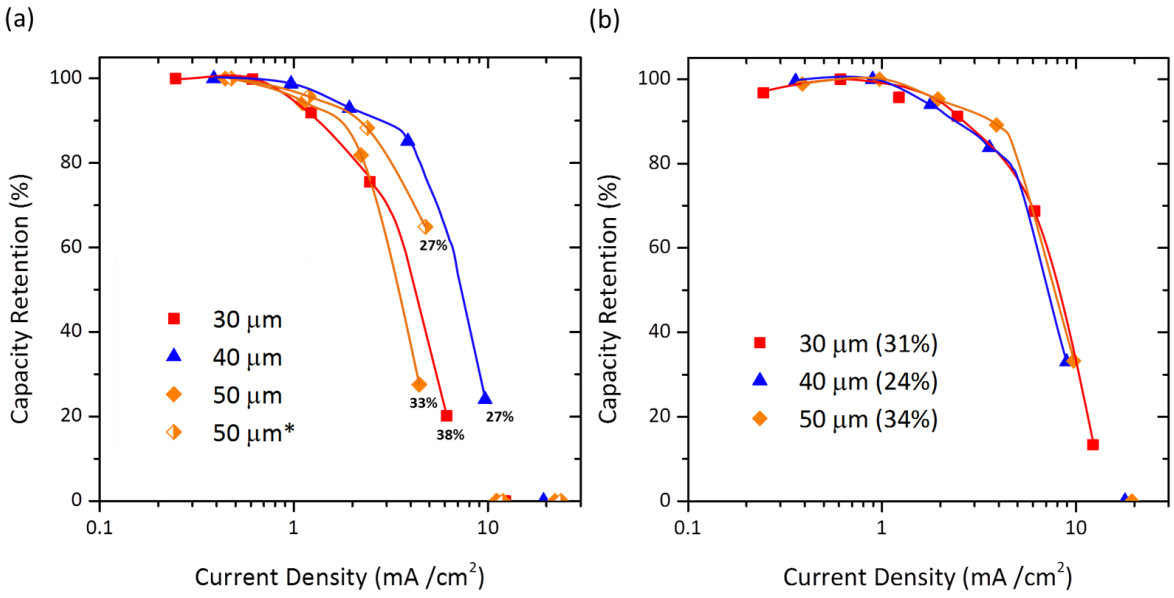

Figure 77: Capacity retention data for symmetric cycling of electrodes with of various loadings with composition by wt. % ($LiCoO_2$:CB:binder) of (a) 96:2:2 and (b) 90:5:5. Labelled percentage values on graphs indicate calculated porosity. 50 µm* represents a second electrode from the same cast.

6.6.2. Effect of porosity

The effect of porosity was investigated to confirm the suggested electrolyte transport limitation observed in the 90:5:5 ($LiCoO_2$:CB:binder) composition tests. The rate performance of electrodes (thickness of ~ 50 µm) with varying porosity is shown in Figure 78. The electrode with lowest porosity (21 %) showed significantly worse rate performance than all other cells. At low porosities the effective tortuosity of electrolyte transport paths through the electrode is increased thus increasing the resistance to electrolyte transport,[52] thus this suggests electrolyte transport is limiting in these cells.

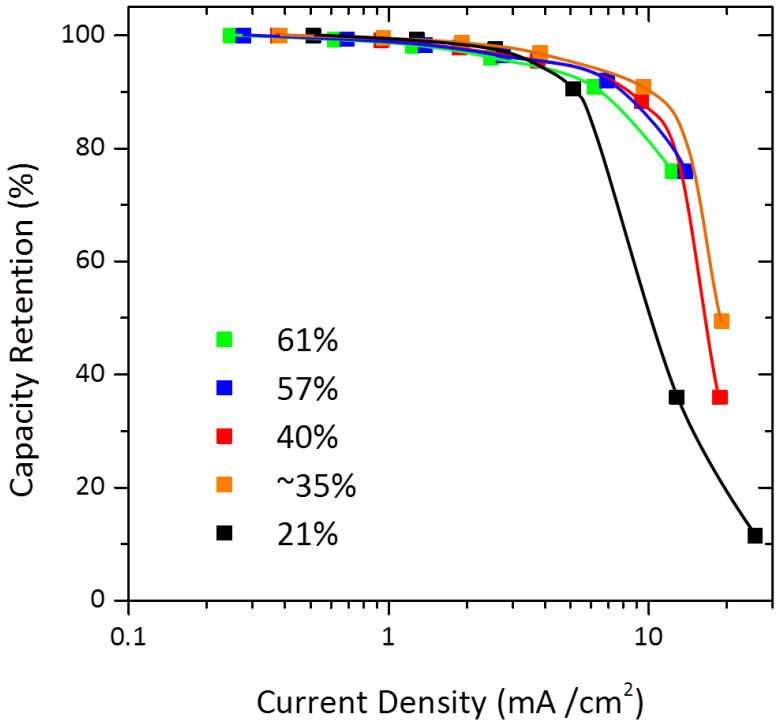

Figure 78: Effect of porosity on rate performance of $LiCoO_2$ electrodes of 90:5:5 by wt. % ($LiCoO_2$:CB:binder) using two glass fibre separators and rate test procedure (see below).

Moreover, the rate performance of electrodes with porosities > 30 % is similar; especially in comparison to the drastic effect of increasing porosity in the $Li_4Ti_5O_{12}$

system discussed above. This suggests low impedance paths for electronic percolation exist, even in electrodes with high porosities, indicating interparticle contact between active material particles is not as significant to the conduction mechanism. This behaviour coincides with an increased wt. % of CB, thus it may be concluded that electronic conduction is occurring primarily through the conductive additive network. Therefore, this composition was deemed suitable for the comparison of conductive additives.

6.6.3. Optimisation of testing procedure

To facilitate the observation of changes in the rate performance due to the conductive additive, the limitations due to other experimental factors were analysed using electrodes with the optimised composition of 90:5:5 ($LiCoO_2$:CB:binder) (porosity ~ 35 %, thickness ~ 50 µm). Firstly, an alternative electrochemical testing procedure,[61] labelled throughout as 'rate test', was compared to the symmetric cycling procedure used above. The 'rate test' procedure is based upon the method developed by Doyle et al.[61,62] The method involves initial symmetric cycling to stabilise the cell performance, followed by a constant current – constant voltage (CCCV) type step, where the cell is either lithiated (negative electrode material) or delithiated (positive electrode material) by a galvanostatic step followed by a potentiostatic step; in order to achieve maximum utilisation of available capacity. Finally, the cells are either delithiated or lithiated at progressively slower rates, with a 5 minutes rest period at OCV separating each current rate. The capacity retention at each current rate is estimated by assuming the cumulative charge of all the delithiation (negative electrode material) or lithiation (positive electrode material) steps (excluding the symmetric cycles) corresponds to 100 % discharge capacity. The cumulative capacity at each rate has been shown to be similar to the conventionally measured capacity at each discharge rate (starting from a fully charged electrode).[61] The 'rate test' procedure used to test $LiCoO_2$ cells is summarised into 5 steps in Table 6.4.

Table 6.4: Rate test procedure for $LiCoO_2$ electrodes

Step	**Description**
1	Symmetric galvanostatic cycling between 4.2 V – 3.0 V at C/5 for 1 cycle
2	Symmetric galvanostatic cycling between 4.2 V – 3.0 V for 2 cycles at C/2
3	Charge at C/5 until 4.2 V
4	Hold at 4.2 V until current drops below C/20 (< 6.875 mA g^{-1})
5	Charge at 10C, 5C, 2C, C, C/2, C/5, C/20 down to 3.0 V cut-off, with 5 minute OCV period in between charges.

During the symmetric cyling procedure the rate of charge and discharge cycles is increased equally, in comparison to the 'rate test' described above. Therefore, at high C rates the $LiCoO_2$ electrode is not fully delithiated prior to the lithiation step, which limits the discharge capacity achievable. Figure 79 shows the discharge capacity at high rates is increased by using the 'rate test' procedure. The 'rate test' procedure also represents a faster alternative to asymmetric methods, often used in the literature,[50,63] where each charge step is performed at low rate.

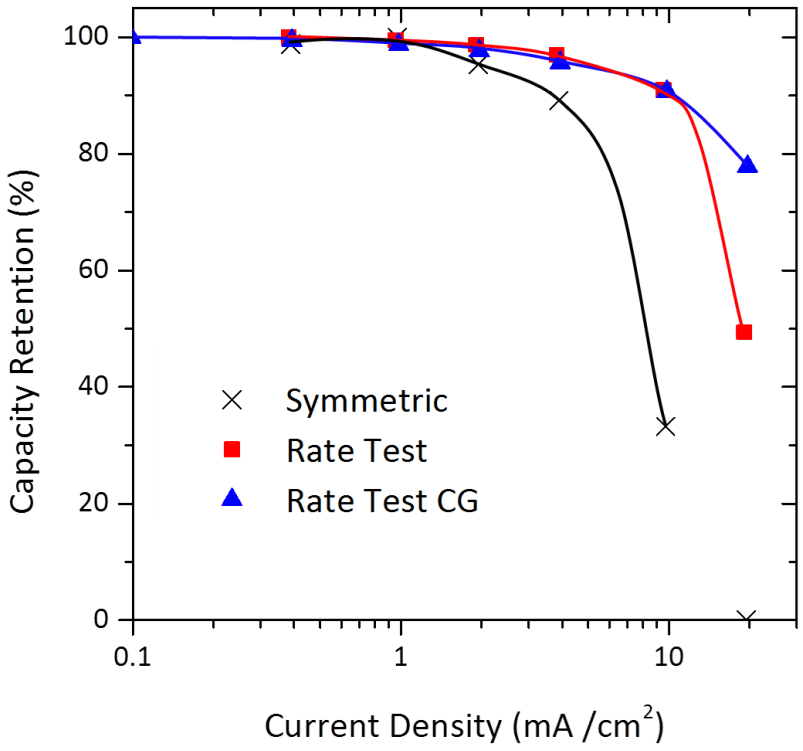

Figure 79: Comparison of symmetric cycling and 'rate test' methods for 90:5:5 (LiCoO2:CB:binder) electrodes, using two glass fibre separators, and 'rate test CG' with one Celguard 2500 separator.

The procedure was further optimised by replacement of the two glass fibre separators (combined thickness > 200 µm) with one Celguard 2500 polyolefin separator (thickness = 25 µm). Figure 79 shows that the capacity retention increased significantly at the highest current density (~ 19 mA cm^{-2}), from ~ 49 % to ~ 78 %. This confirmed that electrolyte transport limitations play a key role at high current densities. Interestingly, at the second highest rate (~ 10 mA cm^{-2}) there was no variation in capacity retention, which indicates the distance for electrolyte transport only limits capacity above this current density.

6.6.5. Effect of Carbon Additive

The optimised testing procedure (‘rate test’ with Celguard separator) was used to compare the various conductive additives at composition 90:5:5 ($LiCoO_2$:X:binder), where X = the tested carbon additive. Figure 80(a) shows data for the first charge/discharge cycle. The cells with LEG and graphite additives showed increased resistance, observable by the increased voltage hysteresis between charge and discharge, and thus reached the cut-off voltage before delivering full capacity (~ 150 mAh g^{-1}). Furthermore, a spike in voltage is observable during the initial delithiation of these cells, suggesting the pristine electrode is not conductive and an activation process occurs during the initial delithiation process; presumably linked to the formation of conductive $Li_{0.7}CoO_2$ at the surface of $LiCoO_2$ particles. These results suggest that 5 wt. % is below the critical volume fraction required for electronic percolation of LEG and graphite additives, and furthermore the electronic wiring is insufficient to achieve full capacity.

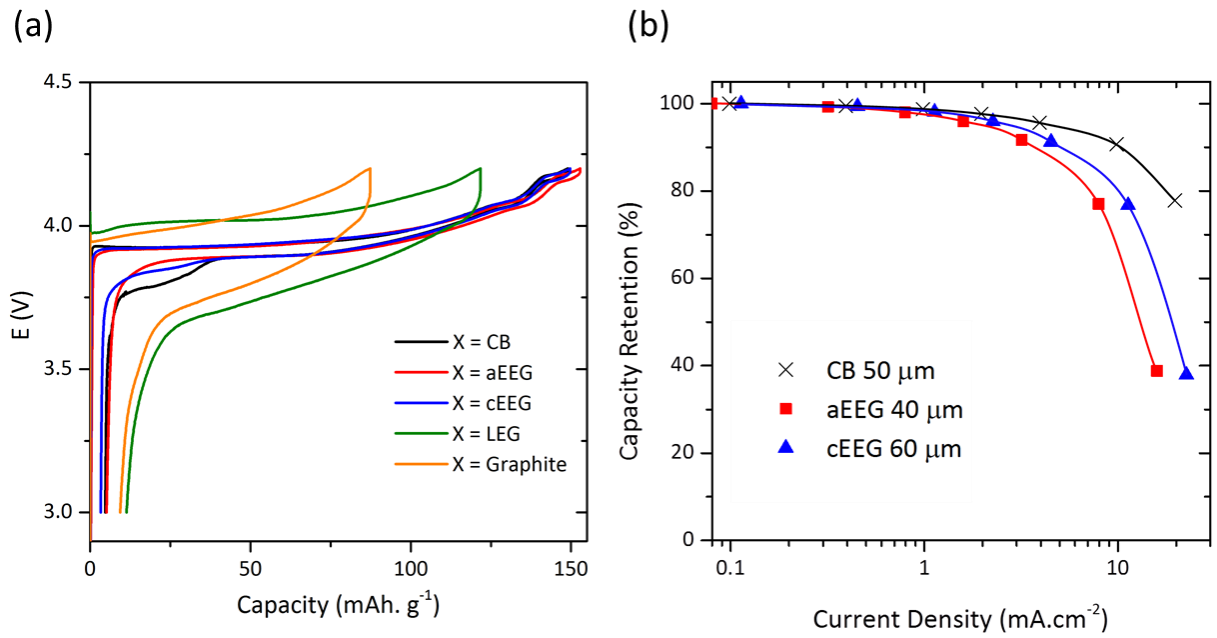

Figure 80(a): First galvanostatic charge/discharge cycle at C/5 for electrodes with composition 90:5:5 (LiCoO2:X:binder) where X is given above, (b) Rate test data for X = carbon black, aEEG and cEEG where measured electrode thickness is given in graph and calculated porosities are 34%, 33% and 37% respectively. One Celguard separator was used in all tests.

In contrast, the voltage hysteresis of cells with electrochemically exfoliated graphenes (cEEG and aEEG) exhibit a similar cell resistance to CB (Figure 80(a)). These cells all achieved full capacity, demonstrating they are able to form an effective conductive network and make sufficient contact with the active material particles. However, Figure 80(b) shows that at higher rates the performance of cEEG and aEEG containing electrodes is worse than with CB. Differences in the performance of these electrodes begin at current densities above ~ 1 mA cm^{-2}, whilst electrolyte transport limitations are only expected to become significant above ~ 10 mA cm^{-2} (Figure 79). Thus it is concluded that increased electronic Ohmic resistance limits the performance of the EEG containing electrodes relative to those with CB. However, the effect of increasing

tortuosity for electrolyte transport (particularly for electrodes with the larger aEEG flakes) should not be discounted, and should be investigated in future studies.

Previous studies have suggested that the use of mixtures of carbon additives with different shapes and aspect ratios is advantageous for creating percolating networks.[64,65] 50 µm thick electrodes were prepared with composition by wt. % 90:2.5:2.5:5 ($LiCoO_2$:CB:X:binder), to observe whether the addition of CB nanoparticles to promote contact with AM particles throughout the electrode improved the rate performance. All cells reached full capacity (~ 150 mAh g^{-1}) during the slow rate first cycle, as could be expected given this had been already achieved with only 2 wt. % CB (Figure 77).

At the highest current density tested (19 - 20 mA cm^{-2}) no significant variation in the performance of the electrodes was observed except for with the cEEG containing cell. On closer analysis it was revealed this cell may have been over calendered as the calculated porosity was ~ 25 %. Such a low porosity may have led to electrolyte transport limitations causing the poor rate performance as observed earlier in Figure 78. Excluding this result, all the carbon additives performed better as a hybrid mixture with the carbon black, and comparable performance to the 5 wt. % CB electrode at high rate was demonstrated. However, no significant advantage of using these additives was observed. Furthermore, the trend of all data sets above 10 mA cm^{-2}, suggests similar capacity limitations will be encountered at higher current densities.

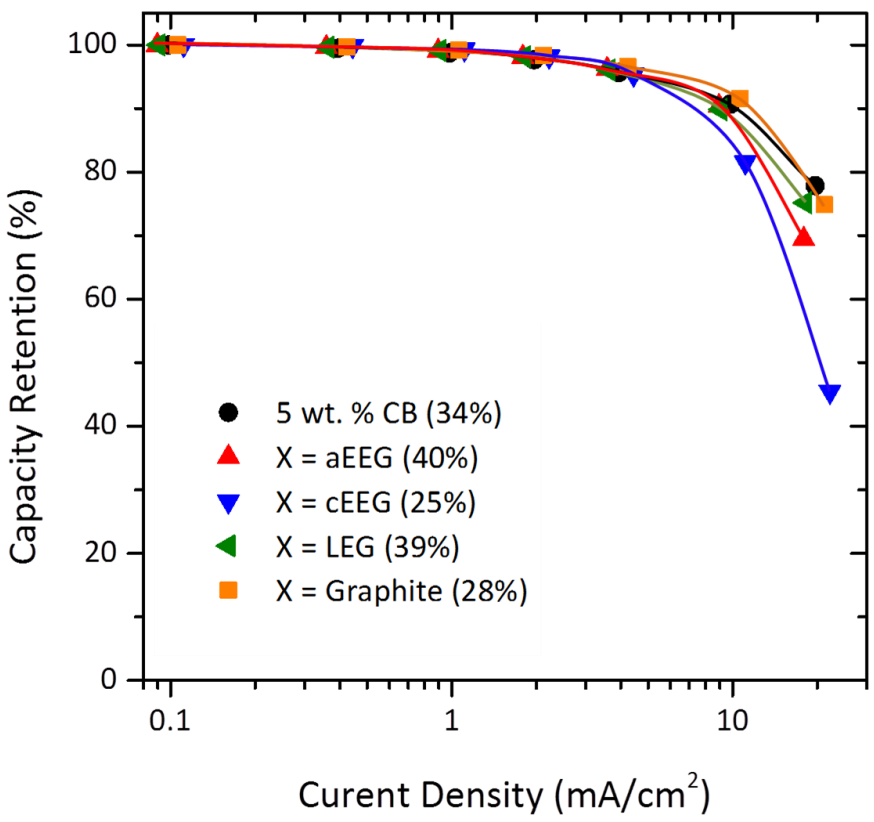

Figure 81: Rate test data for electrodes with composition 90:2.5:2.5:5 ($LiCoO_2$:X:binder) where X is given in graph. The results for 5 wt. % CB are plotted for comparison and calculated porosities are given in brackets.

6.7. Conclusions

Exfoliated graphite additives showed no significant benefit to the rate performance of either $Li_4Ti_5O_{12}$ or $LiCoO_2$ electrodes. In the $Li_4Ti_5O_{12}$ system rate performance was more sensitive to porosity than to carbon additive content or type of additive. Electrodes with low porosity and additive content exhibited the best rate performance, which indicated that electronic conduction was occurring primarily through the active material where contacts could be maintained throughout cycling due to the practically zero volume change between lithiated phases. In comparison, the $LiCoO_2$ electrodes showed less sensitivity to porosity with 5 wt. % carbon black compared to 2 wt. %, suggesting electronic conduction occurred through a percolating network of carbon black particles in the former. However, the graphite and liquid exfoliated graphene samples were unable to form a percolating network at the 5 wt. % composition. Meanwhile, the electrochemically exfoliated graphenes did manage to form a sufficient network to achieve full capacity at low rates, but were inferior to the carbon black additive at higher current densities. In electrodes with a binary mixture of 2.5 wt. % additive and 2.5 wt. % carbon black, similar performance at low and high rates was observed compared to 5 wt. % carbon black.

Furthermore, the improvements in testing procedure developed during the work should be highlighted; firstly, the applied ‘rate test’ procedure allows a faster comparison of electrode rate performance compared to symmetric cycling methods; secondly, the separator thickness was found to be highly significant to half cell rate performance and should be minimised whenever possible. Finally, the effects of electrode loading, thickness and porosity must be carefully controlled in future work.

6.8. Discussion of research challenges and suggestions for future electrode optimisation studies

Significant challenges were encountered during additive testing which if addressed would facilitate progress in future lab-scale composite electrode optimisation studies, and lead to improved research outcomes.

Firstly, although electrode casting techniques used herein aimed to emulate industrial practice, the slurry formulation process involved the addition of significantly increased NMP solvent wt. % whilst and less intensive dispersion than in more industrially led work.[66,67] For example, in this work slurries were formulated with around 1 – 2 g (NMP) per g solids, in contrast to the work of Peterson et al.[66] where values ~ 0.5 – 0.7 g (NMP) per g solids were reported. The slurry formulation and drying process effects how carbon additive, binder and active material particles are dispersed throughout the electrode,[66–69] suggesting results could vary if industry techniques were followed. Also, the NMP volume was varied depending on the slurry composition which led to difficulty in achieving constant loading, porosity and thickness of electrodes with different compositions; adding an additional layer of complexity to additive comparison. Furthermore, other groups[23] have highlighted the detrimental effect on electrochemical performance of atmospheric moisture during slurry formulation and electrode casting, suggesting conditions comparable to a dry room environment may be required to achieve state of the art performance. Further work should aim to close the gap between industrial and lab-scale testing to ensure meaningful results are achievable given practical and financial limitations.

Secondly, methods for characterisation of composite electrodes require renewed focus to advance the fundamental understanding of the role of composition on performance. Direct electronic conductivity measurements on as-prepared or calendered electrodes are hindered by the current collector, which introduces significant contact resistance or thickness dependent variation, depending on the measurement orientation. This has often been avoided through the use of four point probe style measurements on free standing[68] or delaminated electrodes,[23,66,70] alongside dry impedance measurements on compressed pellets[5] or powders.[25] However, whether these measurements provide true values for electrodes' properties within cells is unclear. The recent development of a 'micro-four-line-probe', with the ability to measure film conductivity without current collector delamination should be beneficial in this regard, but requires complex setup and was not accessible for this study.[71] Furthermore, enhanced techniques to investigate additive and binder dispersion within electrode structures beyond the limits of 2D microscopy techniques and Raman mapping measurements would be advantageous. The characterisation of 3D microstructures (e.g. by X-Ray tomography) and nanoscale resolution electrical/mechanical mapping,[72] alongside improved modelling of the electrochemical impact of electrode microstructure is likely to bring enhanced understanding for electronic wiring and ion transport optimisation.[10,73]

Thirdly, more stringent electrochemical testing should be required in order to claim improved rate performance in LIB literature. For example, the comparison of capacity retention by C rate is widespread in the literature, yet as observed above, this is only a fair comparison for electrodes with very similar loading. Instead, testing electrodes at the same current density is a fairer comparison to ensure differences in loading are taken into account. To avoid limitations that arise from the Li metal electrode, the use of full cell configuration could be employed or ideally a three electrode setup. This

would allow *in situ* measurements, particularly of electrochemical impedance spectroscopy, which would enable better understanding of changes in the conduction mechanism at different stages of lithiation. To conduct these measurements at high rates would require a setup with a thin separator and carefully designed positioning of the reference electrode to avoid the confusion of artefacts during results analysis.[74] Recently, such cells have been commercially developed by EL-Cell with a ring-shaped reference electrode geometry although no analysis of their use has thus far been reported.[75] Additionally, the use of pulse power tests[76] should be considered, as this is a likely application of high power LIB cells.

Regarding the use of graphenic materials as conductive additives, a more productive approach may be to compare their percolation threshold with conventional carbon additives in composites. As discussed, previous reports suggest they may display extremely low percolation thresholds[12–14,77] (similar to those observed in carbon nanotubes[78] and carbon fibres[79]). This would allow production of electrodes with lower additive wt. % hence increasing energy metrics. Furthermore, effects of the conductive additive are likely to be clearer in systems where electronic conductivity is a rate limiting factor, for example $LiFePO_4$ (intrinsic conductivity ~ 10^{-9} S cm^{-1})[80] which has shown significant improvements with carbon coating.[81]

Moreover, the production, characterisation, storage and dispersion of graphene materials needs further development. A larger wt. % of thicker graphitic material (due to restacking or low yield exfoliation processes) will reduce the effectiveness of electronic wiring and increase the percolation threshold dramatically. However, it remains challenging to accurately quantify the degree of restacking within an electrode composite, whilst techniques capable of this characterisation are lacking. Such

techniques would be required to optimise the dispersion of exfoliated graphite additives. In this context a thorough review by Raccichini et al.[82] concluded that electrochemical properties are likely to be enhanced by non-conventional electrode preparation (i.e. “one-pot synthesis, decoration and/or anchoring”) compared to mechanical mixing, although the complication this would cause to industrial processing is likely to be prohibitive. Moreover, the effect on ionic transport properties and cell energy density of exploiting such non-conventional electrode architectures has not been fully assessed.

6.9. References

(1) Stauffer, D.; Aharony, A. *Introduction To Percolation Theory*; Taylor & Francis e-Library, 2010.

(2) Spahr, M. E. Carbon-Conductive Additives for Lithium-Ion Batteries. In *Lithium-Ion Batteries: Science and Technologies*; Yoshio, M., Brodd, Ralph J. Kozawa, A., Eds.; Springer Science + Business Media, 2009; pp 117–154.

(3) Dominko, R.; Gaberšček, M.; Drofenik, J.; Bele, M.; Jamnik, J. Influence of Carbon Black Distribution on Performance of Oxide Cathodes for Li Ion Batteries. *Electrochim. Acta* **2003**, *48* (24), 3709–3716.

(4) Dominko, R.; Gaberscek, M.; Drofenik, J.; Bele, M.; Pejovnik, S.; Jamnik, J. The Role of Carbon Black Distribution in Cathodes for Li Ion Batteries. *J. Power Sources* **2003**, *119*, 770–773.

(5) Guy, D.; Lestriez, B.; Bouchet, R.; Guyomard, D. Critical Role of Polymeric Binders on the Electronic Transport Properties of Composites Electrode. *J. Electrochem. Soc.* **2006**, *153* (4), A679.

(6) Cerbelaud, M.; Lestriez, B.; Videcoq, A.; Ferrando, R.; Guyomard, D. Understanding the Structure of Electrodes in Li-Ion Batteries: A Numerical Study. *J. Electrochem. Soc.* **2015**, *162* (8), A1485–A1492.

(7) Zheng, H.; Yang, R.; Liu, G.; Song, X.; Battaglia, V. S. Cooperation between Active Material, Polymeric Binder and Conductive Carbon Additive in Lithium Ion Battery Cathode. *J. Phys. Chem. C* **2012**, *116* (7), 4875–4882.

(8) Liu, G.; Zheng, H.; Kim, S.; Deng, Y.; Minor, A. M.; Song, X.; Battaglia, V. S. Effects of Various Conductive Additive and Polymeric Binder Contents on the Performance of a Lithium-Ion Composite Cathode. *J. Electrochem. Soc.* **2008**, *155* (12), A887.

(9) Chen, Y.-H.; Wang, C.-W.; Liu, G.; Song, X.-Y.; Battaglia, V. S.; Sastry, a. M. Selection of Conductive Additives in Li-Ion Battery Cathodes. *J. Electrochem. Soc.* **2007**, *154*, A978.

(10) Mistry, A.; Robles, D. J.; Stein IV, M.; Mukherjee, P. Analysis of Long Range Interaction in Lithium-Ion Battery Electrodes. *J. Electrochem. Energy Convers. Storage* **2016**, *13*, 031006–0310013.

(11) Marks, T.; Trussler, S.; Smith, A. J.; Xiong, D.; Dahn, J. R. A Guide to Li-Ion Coin-Cell Electrode Making for Academic Researchers. *J. Electrochem. Soc.* **2011**, *158* (1), A51.

(12) Jan, R.; Habib, A.; Abbasi, H. Y. High Aspect Ratio Graphene Nanosheets Cause a Very Low Percolation Threshold for Polymer Nanocomposites. *Int. Sci. Congr. Exhib. APMAS2015* **2016**, *129*.

(13) Zhang, B.; Yu, Y.; Liu, Y.; Huang, Z.-D.; He, Y.; Kim, J.-K.; Colombo, L.; Ruoff, R. S.; Zhang, B.; Yang, Q. H.; et al. Percolation Threshold of Graphene Nanosheets as Conductive Additives in $Li_4Ti_5O_{12}$ Anodes of Li-Ion Batteries. *Nanoscale* **2013**, *5* (5), 2100.

(14) Stankovich, S.; Dikin, D. A.; Dommett, G. H. B.; Kohlhaas, K. M.; Zimney, E. J.; Stach, E. A.; Piner, R. D.; Nguyen, S. T.; Ruoff, R. S. Graphene-Based Composite Materials. *Nature* **2006**, *442* (7100), 282–286.

(15) Papageorgiou, D. G.; Kinloch, I. A.; Young, R. J. Mechanical Properties of Graphene and Graphene-Based Nanocomposites. *Prog. Mater. Sci.* **2017**, *90*, 75–127.

(16) Fuller, T. F. Simulation and Optimization of the Dual Lithium Ion Insertion Cell. *J. Electrochem. Soc.* **1994**, *141* (1), 1.

(17) Doyle, M. Comparison of Modeling Predictions with Experimental Data from Plastic Lithium Ion Cells. *J. Electrochem. Soc.* **1996**, *143* (6), 1890.

(18) Arora, P.; Doyle, M.; Gozdz, A. S.; White, R. E.; Newman, J. Comparison between Computer Simulations and Experimental Data for High-Rate Discharges of Plastic Lithium-Ion Batteries. *J. Power Sources* **2000**, *88* (2), 219–231.

(19) Doyle, M.; Newman, J. Analysis of Capacity–rate Data for Lithium Batteries Using Simplified Models of the Discharge Process. *J. Appl. Electrochem.* **1997**, *27* (7), 846–856.

(20) Gabano, J. P. *Lithium Batteries*; Academic Press: London, 1983.

(21) Linden, D.; Reddy, T. B. *Handbook of Batteries*; McGraw-Hill: New York, 2002.

(22) Jiang, F.; Peng, P.; Wang, C. Y.; Liu, L.; Wang, Y. Elucidating the Performance Limitations of Lithium-Ion Batteries due to Species and Charge Transport through Five Characteristic Parameters. *Sci. Rep.* **2016**, *6* (1), 32639.

(23) Zheng, H.; Yang, R.; Liu, G.; Song, X.; Battaglia, V. S. Cooperation between Active Material, Polymeric Binder and Conductive Carbon Additive in Lithium Ion Battery Cathode. *J. Phys. Chem. C* **2012**, *116* (7), 4875–4882.

(24) Yoshio, M. (Masaki); Brodd, R. J.; Kozawa, A. *Lithium-Ion Batteries : Science and Technologies*; Springer, 2009.

(25) Spahr, M. E.; Goers, D.; Leone, A.; Stallone, S.; Grivei, E. Development of Carbon Conductive Additives for Advanced Lithium Ion Batteries. *J. Power Sources* **2011**, *196* (7), 3404–3413.

(26) TIMCAL TIMREX® SFG6 Primary Synthetic Graphite (material property data sheet) http://www.matweb.com/search/datasheet.aspx?matguid=7ccdb40c6318412eb847b97a27876491&ckck=1 (accessed Sep 18, 2017).

(27) Thomas Swan Advanced Materials. Elicarb ® Premium Grade Graphene Powder and Elicarb ® Premium Grade Graphene Dispersion (AQ) http://www.thomas-swan.co.uk/sites/pdf/TSwan_Graphene_Datasheet_Berlin_WEB.PDF (accessed Sep 23, 2017).

(28) Abdelkader, A. M.; Kinloch, I. A.; Dryfe, R. A. W. Continuous Electrochemical Exfoliation of Micrometer-Sized Graphene Using Synergistic Ion Intercalations and Organic Solvents. *ACS Appl. Mater. Interfaces* **2014**, *6* (3), 1632–1639.

(29) Sole, C.; Drewett, N. E.; Liu, F.; Abdelkader, A. M.; Kinloch, I. A.; Hardwick, L. J. The Role of Re-Aggregation on the Performance of Electrochemically Exfoliated

Many-Layer Graphene for Li-Ion Batteries. *J. Electroanal. Chem.* **2015**, *753*, 35–41.

(30) Parvez, K.; Li, R.; Puniredd, S. R.; Hernandez, Y.; Hinkel, F.; Wang, S.; Feng, X.; Müllen, K. Electrochemically Exfoliated Graphene as Solution-Processable, Highly Conductive Electrodes for Organic Electronics. *ACS Nano* **2013**, *7* (4), 3598–3606.

(31) Ferrari, A. C.; Robertson, J. Interpretation of Raman Spectra of Disordered and Amorphous Carbon. *Phys. Rev. B* **2000**, *61* (20), 14095–14107.

(32) Beams, R.; Gustavo Cançado, L.; Novotny, L. Raman Characterization of Defects and Dopants in Graphene. *J. Phys. Condens. Matter* **2015**, *27* (8), 83002.

(33) Ferrari, A. C.; Basko, D. M. Raman Spectroscopy as a Versatile Tool for Studying the Properties of Graphene. *Nat. Nanotechnol.* **2013**, *8* (4), 235–246.

(34) Scharner, S. Evidence of Two-Phase Formation upon Lithium Insertion into the $Li_{1.33}Ti_{1.67}O_4$ Spinel. *J. Electrochem. Soc.* **1999**, *146* (3), 857.

(35) Jung, H.-G.; Jang, M. W.; Hassoun, J.; Sun, Y.-K.; Scrosati, B. A High-Rate Long-Life $Li_4Ti_5O_{12}$/$Li[Ni_{0.45}Co_{0.1}Mn_{1.45}]O_4$ Lithium-Ion Battery. *Nat. Commun.* **2011**, *2*, 516.

(36) Amine, K.; Belharouak, I.; Chen, Z.; Tran, T.; Yumoto, H.; Ota, N.; Myung, S. T.; Sun, Y. K. Nanostructured Anode Material for High-Power Battery System in Electric Vehicles. *Adv. Mater.* **2010**, *22*, 3052–3057.

(37) Jung, H.-G.; Myung, S.-T.; Yoon, C. S.; Son, S.-B.; Oh, K. H.; Amine, K.; Scrosati, B.; Sun, Y.-K. Microscale Spherical Carbon-Coated $Li_4Ti_5O_{12}$ as Ultra High Power Anode Material for Lithium Batteries. *Energy Environ. Sci.* **2011**, *4*, 1345.

(38) Haetge, J.; Hartmann, P.; Brezesinski, K.; Janek, J.; Brezesinski, T. Ordered Large-Pore Mesoporous $Li_4Ti_5O_{12}$ Spinel Thin Film Electrodes with Nanocrystalline Framework for High Rate Rechargeable Lithium Batteries: Relationships among Charge Storage, Electrical Conductivity, and Nanoscale St. *Chem. Mater.* **2011**, *23*, 4384–4393.

(39) Dahn, J. R.; Zheng, T.; Liu, Y.; Xue, J. S. Mechanisms for Lithium Insertion in Carbonaceous Materials. *Science* **1995**, *270*, 590–593.

(40) Winter, M.; Besenhard, J. O.; Spahr, M. E.; Novák, P. Insertion Electrode Materials for Rechargeable Lithium Batteries. *Adv. Mater.* **1998**, *10* (10), 725–763.

(41) Aurbach, D. Review of Selected Electrode–solution Interactions Which Determine the Performance of Li and Li Ion Batteries. *J. Power Sources* **2000**, *89* (2), 206–218.

(42) Nordh, T.; Younesi, R.; Brandell, D.; Edström, K. Depth Profiling the Solid Electrolyte Interphase on Lithium Titanate ($Li_4Ti_5O_{12}$) Using Synchrotron-Based Photoelectron Spectroscopy. *J. Power Sources* **2015**, *294*, 173–179.

(43) He, Y.-B.; Liu, M.; Huang, Z.-D.; Zhang, B.; Yu, Y.; Li, B.; Kang, F.; Kim, J.-K. Effect of Solid Electrolyte Interface (SEI) Film on Cyclic Performance of $Li_4Ti_5O_{12}$ Anodes for Li Ion Batteries. *J. Power Sources* **2013**, *239*, 269–276.

(44) Han, C.; He, Y.-B.; Liu, M.; Li, B.; Yang, Q.-H.; Wong, C.-P.; Kang, F. A Review of Gassing Behavior in $Li_4Ti_5O_{12}$-Based Lithium Ion Batteries. *J. Mater. Chem. A* **2017**, *5*.

(45) Yuan, T.; Tan, Z.; Ma, C.; Yang, J.; Ma, Z.-F.; Zheng, S. Challenges of Spinel $Li_4Ti_5O_{12}$ Lithium-Ion Battery Industrial Applications. *Adv. Energy Mater.* **2017**, *7* (12), 1601625.

(46) Carvalho, D.; Loeffler, N.; Kim, G.-T.; Marinaro, M.; Wohlfahrt-Mehrens, M.; Passerini, S. Study of Water-Based Lithium Titanate Electrode Processing: The Role of pH and Binder Molecular Structure. *Polymers (Basel).* **2016**, *8* (8), 276.

(47) Young, D.; Ransil, A.; Amin, R.; Li, Z.; Chiang, Y.-M. Electronic Conductivity in the $Li_{4/3}Ti_{5/3}O_4$ - $Li_{7/3}Ti_{5/3}O_4$ System and Variation with State-of-Charge as a Li Battery Anode. *Adv. Energy Mater.* **2013**, *3* (9), 1125–1129.

(48) Delacourt, C.; Ati, M.; Tarascon, J. M. Measurement of Lithium Diffusion Coefficient in LiyFeSO4F. *J. Electrochem. Soc.* **2011**, *158* (6), A741.

(49) Santhanagopalan, S.; Guo, Q.; Ramadass, P.; White, R. E. Review of Models for Predicting the Cycling Performance of Lithium Ion Batteries. *J. Power Sources* **2006**, *156*, 620–628.

(50) Buqa, H.; Goers, D.; Holzapfel, M.; Spahr, M. E.; Novák, P. High Rate Capability of Graphite Negative Electrodes for Lithium-Ion Batteries. *J. Electrochem. Soc.* **2005**, *152* (2), A474–A481.

(51) Yu, S.; Kim, S.; Kim, T. Y.; Nam, J. H.; Cho, W. Il. Model Prediction and Experiments for the Electrode Design Optimization Model Prediction and Experiments for the Electrode Design Optimization of $LiFePO_4$ /Graphite Electrodes in High Capacity Lithium-Ion Batteries. *Bull. Korean Chem. Soc* **2013**, *34* (1).

(52) Ebner, M.; Chung, D.-W.; Edwin García, R.; Wood, V.; Ebner, M.; Wood, V.; Chung, D.; García, R. E. Tortuosity Anisotropy in Lithium-Ion Battery Electrodes. *Adv. Energy Mater* **2013**.

(53) Kim, C.; Norberg, N. S.; Alexander, C. T.; Kostecki, R.; Cabana, J. Mechanism of Phase Propagation during Lithiation in Carbon-Free $Li_4Ti_5O_{12}$ Battery Electrodes. *Adv. Funct. Mater.* **2013**, *23*, 1214–1222.

(54) Wang, J.; Zhao, H.; Li, Z.; Wen, Y.; Xia, Q.; Zhang, Y.; Yushin, G. Revealing Rate Limitations in Nanocrystalline $Li_4Ti_5O_{12}$ Anodes for High-Power Lithium Ion Batteries. *Adv. Mater. Interfaces* **2016**, *3* (13), 1600003.

(55) Mizushima, K.; Jones, P. C.; Wiseman, P. J.; Goodenough, J. B. LixCoO2 (0<x<-1): A New Cathode Material for Batteries of High Energy Density. *Mater. Res. Bull.* **1980**, *15* (6), 783–789.

(56) Reimers, J. N.; Dahn, J. R. Electrochemical and In Situ X-Ray Diffraction Studies of Lithium Intercalation in Li_xCoO_2. *J. Electrochem. Soc.* **1992**, *139* (8), 2091.

(57) Morcrette, M.; Chabre, Y.; Vaughan, G.; Amatucci, G.; Leriche, J.-B.; Patoux, S.; Masquelier, C.; Tarascon, J.-M. In Situ X-Ray Diffraction Techniques as a Powerful Tool to Study Battery Electrode Materials. *Electrochim. Acta* **2002**, *47* (19), 3137–3149.

(58) Ménétrier, M.; Saadoune, I.; Levasseur, S.; Delmas, C.; Trichet, L.; Mehauté, A. Le; Greenbaum, S. G. The Insulator-Metal Transition upon Lithium Deintercalation from $LiCoO_2$: Electronic Properties and 7Li NMR Study. *J. Mater. Chem.* **1999**, *9* (5), 1135–

1140.

(59) Molenda, J.; Stoklosa, A.; Bak, T. Modification in the Electronic Structure of Cobalt Bronze Li_xCoO_2 and the Resulting Electrochemical Properties. *Solid State Ionics* **1989**, *36* (1–2), 53–58.

(60) Lai, W.; Erdonmez, C. K.; Marinis, T. F.; Bjune, C. K.; Dudney, N. J.; Xu, F.; Wartena, R.; Chiang, Y.-M. Ultrahigh-Energy-Density Microbatteries Enabled by New Electrode Architecture and Micropackaging Design. *Adv. Mater.* **2010**, *22* (20), E139–E144.

(61) Doyle, M.; Newman, J.; Reimers, J. A Quick Method of Measuring the Capacity versus Discharge Rate for a Dual Lithium-Ion Insertion Cell Undergoing Cycling. *J. Power Sources* **1994**, *52* (2), 211–216.

(62) Ding, Y.; Zanardelli, S. G.; Zwally, J. M. Technique for Rapid Battery Capacity Testing. 20130307481 A1, 2013.

(63) Li, Z.; Ban, C.; Chernova, N. A.; Wu, Z.; Upreti, S.; Dillon, A.; Whittingham, M. S. Towards Understanding the Rate Capability of Layered Transition Metal Oxides $LiNi_yMn_yCo_{1-2y}O_2$. *J. Power Sources* **2014**, *268*, 106–112.

(64) Cheon, S. E.; Kwon, C. W.; Kim, D. B.; Hong, S. J.; Kim, H. T.; Kim, S. W. Effect of Binary Conductive Agents in LiCoO2 Cathode on Performances of Lithium Ion Polymer Battery. *Electrochim. Acta* **2000**, *46* (4), 599–605.

(65) Wang, H.; Umeno, T.; Mizuma, K.; Yoshio, M. Highly Conductive Bridges between Graphite Spheres to Improve the Cycle Performance of a Graphite Anode in Lithium-Ion Batteries. *J. Power Sources* **2008**, *175* (2), 886–890.

(66) Peterson, S. W.; Wheeler, D. R. Direct Measurements of Effective Electronic Transport in Porous Li-Ion Electrodes. *J. Electrochem. Soc.* **2014**, *161* (14), A2175–A2181.

(67) Kraytsberg, A.; Ein-Eli, Y. Conveying Advanced Li-Ion Battery Materials into Practice The Impact of Electrode Slurry Preparation Skills. *Adv. Energy Mater.* **2016**, *6* (21), 1600655.

(68) Nguyen, B. P. N.; Mariage, N.; Fredon, R.; Kelder, E. M.; Lestriez, B. Manufacturing of $LiNi_{0.5}Mn_{1.5}O_4$ Positive Composite Electrodes with Industry-Relevant Surface Capacities for Lithium Ion-Cells. *J. Electrochem. Soc.* **2015**, *162* (8), A1451–A1459.

(69) Forouzan, M. M.; Chao, C.-W.; Bustamante, D.; Mazzeo, B. A.; Wheeler, D. R. Experiment and Simulation of the Fabrication Process of Lithium-Ion Battery Cathodes for Determining Microstructure and Mechanical Properties. *J. Power Sources* **2016**, *312*, 172–183.

(70) Yan, B.; Lim, C.; Yin, L.; Zhu, L. Three Dimensional Simulation of Galvanostatic Discharge of $LiCoO_2$ Cathode Based on X-Ray Nano-CT Images. *J. Electrochem. Soc.* **2012**, *159* (10), A1604–A1614.

(71) Lanterman, B. J.; Riet, A. A.; Gates, N. S.; Flygare, J. D.; Cutler, A. D.; Vogel, J. E.; Wheeler, D. R.; Mazzeo, B. A. Micro-Four-Line Probe to Measure Electronic Conductivity and Contact Resistance of Thin-Film Battery Electrodes. *J. Electrochem. Soc.* **2015**, *162* (10), A2145–A2151.

(72) Prastani, C.; Vetushka, A.; Hývl, M.; Fejfar, A.; Nanu, M.; Nanu, D.; Schropp, R. E. I.; Rath, J. K. Conductivity Measurement of Individual SnS Nanoparticles by Peak Force AFM. In *MRS Online Proceedings Library*; 2013; Vol. 1557.

(73) Stephenson, D. E.; Walker, B. C.; Skelton, C. B.; Gorzkowski, E. P.; Rowenhorst, D. J.; Wheeler, D. R. Modeling 3D Microstructure and Ion Transport in Porous Li-Ion Battery Electrodes. **2011**.

(74) Costard, J.; Ender, M.; Weiss, M.; Ivers-Tiffée, E. Three-Electrode Setups for Lithium-Ion Batteries. *J. Electrochem. Soc.* **2017**, *164* (2), A80–A87.

(75) EL-CELL GmbH. Electrochemical test cells | EL-CELL https://el-cell.com/products/test-cells (accessed Jun 2, 2017).

(76) Idaho National Engineering & Environmental Laboratory. *Battery Test Manual for Plug-In Hybrid Electric Vehicles*; Idaho Falls, ID, USA, 2010.

(77) Vo, N. H.; Dao, T. D.; Jeong, H. M. Electrically Conductive Graphene/Poly(methyl Methacrylate) Composites with Ultra-Low Percolation Threshold by Electrostatic Self-Assembly in Aqueous Medium. *Macromol. Chem. Phys.* **2015**, *216* (7), 770–782.

(78) Ounaies, Z.; Park, C.; Wise, K. E.; Siochi, E. J.; Harrison, J. S. Electrical Properties of Single Wall Carbon Nanotube Reinforced Polyimide Composites. *Compos. Sci. Technol.* **2003**, *63* (11), 1637–1646.

(79) Guoping, W.; Qingtang, Z.; Zuolong, Y.; MeiZheng, Q. The Effect of Different Kinds of Nano-Carbon Conductive Additives in Lithium Ion Batteries on the Resistance and Electrochemical Behavior of the $LiCoO_2$ Composite Cathodes. *Solid State Ionics* **2008**, *179* (7), 263–268.

(80) Safari, M.; Delacourt, C. Mathematical Modeling of Lithium Iron Phosphate Electrode: Galvanostatic Charge/Discharge and Path Dependence. *J. Electrochem. Soc.* **2011**, *158* (2), A63.

(81) Ravet, N.; Chouinard, Y.; Magnan, J. F.; Besner, S.; Gauthier, M.; Armand, M. Electroactivity of Natural and Synthetic Triphylite. *J. Power Sources* **2001**, *97–98*, 503–507.

(82) Raccichini, R.; Varzi, A.; Wei, D.; Passerini, S. Critical Insight into the Relentless Progression Toward Graphene and Graphene-Containing Materials for Lithium-Ion Battery Anodes. *Adv. Mater.* **2017**, *29* (11), 1603421.

7. Conclusions

In Chapter 3, *in situ* Raman spectroscopy was used to study the mechanism of electrochemical Li intercalation into microcrystalline graphite in a typical LIB electrolyte. The behaviour of the G band showed the characteristic splitting and wavenumber shifts indicative of the formation of the expected staged graphite intercalation compounds. Furthermore, observation of a large red-shift in the 2D band position during lithiation was explained by the expansion of C-C bond lengths. The continual shift of 2D band position during the stage 4L to 3L phase transition thus supported previous reports of a solid solution mechanism.

In Chapter 4, the effects of an electrochemical exfoliation process and subsequent re-agglomeration on the Li insertion behaviour of the microcrystalline graphite sample were investigated. Structural characterisation revealed that upon drying significant restacking of graphene sheets had occurred, producing graphitic particles with only minor deviations in stacking order compared to the pristine material. Moreover, electrochemical cycling experiments revealed the modified sample showed an increase in first cycle irreversibility and reduction in total reversible capacity. In effect, this suggested the process was not advantageous to the performance of graphite materials in LIB negative electrodes. Finally, *in situ* Raman spectroscopy was used to confirm the similarity in Li intercalation mechanism. The improved signal-to-noise ratio of these spectra allowed a model to be developed for the estimation of strain and doping of graphene layers from the G and 2D band positions during the stage 4L to 3L regions of lithiation.

In Chapter 5, mechanical exfoliation of highly crystalline, natural graphite flakes was employed to produce flakes with large areas of clearly defined thickness. This avoided the restacking problem and facilitated investigation of changes to the Li intercalation mechanism as a function of flake thickness, by *in situ* Raman spectroscopy. A similar intercalation mechanism was observed during intercalation of flakes with thicknesses of 9 graphene layers, ~ 56 layers and ~ 178 layers. However, application of the model developed in Chapter 4 suggested an increase in lithiation induced in-plane, biaxial strain for the thinnest flake. Increased strain may be linked to accelerated electrode degradation and capacity fading, suggesting few layer graphene materials (< 10 layers) may be inferior to bulk graphite as insertion electrode materials for long cycle-life applications. Furthermore, lithiation of a trilayer graphene sample was observed, whereby Li^+ ions occupied both available interlayer spaces and demonstrated an alternative lithiation mechanism compared to the conventional staging process; suggesting the dynamics of intercalation must vary for extremely thin graphitic structures.

In Chapter 6, the potential application of exfoliated graphite materials as conductive additives in LIB composite electrodes was investigated. Initially, additives were compared in the $Li_4Ti_5O_{12}$ system, however; by analysis of porosity, thickness and additive content effects; it was concluded that electronic conduction occurred primarily through the active material surfaces, preventing meaningful evaluation of additive performance. In contrast, performance of the $LiCoO_2$ system was shown to be highly sensitive to variation of the conductive additive used, with reproducible electronic percolation/wiring only achieved with the carbon black additive or the electrochemically exfoliated graphene additives (at 5 wt. %). In contrast, microcrystalline graphite and liquid exfoliated graphene materials tested at the same

wt. % displayed inferior performance. However, at high rates the performance of electrodes with only the electrochemically exfoliated graphenes was inferior to those with carbon black, or any of the additives in combination with carbon black in a 1:1 ratio (5 wt. % total additive).

8. Outlook for the application of few layer graphene and exfoliated graphite materials in lithium ion batteries

This work investigated the application of few layer graphene and exfoliated graphite materials in lithium ion batteries: both as the negative electrode active material and as a conductive additive within both positive and negative composite electrodes. Regarding the prospects for use as an alternative negative electrode insertion material, no advantages were observed to suggest these materials should remain under strong consideration for commercial applications in the future. Whilst previous studies have reported large irreversible capacities and voltage hysteresis which are detrimental to cell energy metrics, mechanistic *in situ* Raman studies herein suggest an increase in structural strain during the intercalation of few layered graphene samples, which may explain the accelerated capacity fading observed during long-term cycling.

Furthermore, regarding the prospects for increased rate performance through the nano-sizing of graphite particle thickness, it remains unlikely that any improvements in solid state diffusion kinetics can be converted to enhancements in practical battery performance. Increased lithium diffusion rates have been reported in bilayer graphene,[1] which suggests the observation herein, of an alternative lithiation mechanism in trilayer graphene could be indicative of a similarly interesting phenomenon. However, although diffusion coefficients in few layer graphene samples should be investigated from a fundamental perspective, it has been observed in Chapter 6 that composite electrode rate performance is often limited by electrolyte transport rather than by the intrinsic active material properties. A more productive approach may

be to design composite graphite electrodes with reduced tortuosity of electrolyte pathways, such as in the work by Billaud et al.,[2] where magnetic alignment of graphite particles was used to produce electrodes with high loading and increased rate capability. Moreover, the restacking behaviour observed in Chapter 4 must be prevented in order to maintain few layer graphene structures within composite electrodes, which appears to be incompatible with current methods of industrial electrode preparation.

Finally, regarding the prospects for application as conductive additives, the studies in Chapter 5 suggest that significant improvements in rate capability of lithium ion batteries are not likely to be achieved by simple substitution of conventional additives with exfoliated graphite materials. However, as discussed, this work has not closely investigated the minimum percolation threshold of these additives, which could be significantly lower for few layer graphene materials, leading to improvements in energy metrics of composite electrodes. Furthermore, the use of high aspect ratio additives may be advantageous for other reasons (e.g. mechanical properties, localised heat dissipation, etc.), as discussed in Chapter 6. Further studies are required to confirm the practical advantages of use of these materials as additives, although commercialisation will depend on an economic assessment of whether additional costs are worthwhile for the desired energy storage application.

8.1. References

(1) Kühne, M.; Paolucci, F.; Popovic, J.; Ostrovsky, P. M.; Maier, J.; Smet, J. H. Ultrafast Lithium Diffusion in Bilayer Graphene. *Nat. Nanotechnol.* **2017**, *12*, 895–901.

(2) Billaud, J.; Bouville, F.; Magrini, T.; Villevieille, C.; Studart, A. R. Magnetically Aligned Graphite Electrodes for High-Rate Performance Li-Ion Batteries. *Nat. Energy* **2016**, *1* (8), 16097.

9. Appendix

9.1. Charge carrier concentration at the start of stage 4L formation

Summary:

The charge concentration (electrons cm^{-2}) at the start of stage 4L formation (or the end of dilute stage 1 formation) corresponds to ~ 20 mAh g^{-1}.

$$\frac{e^-}{cm^2} = \frac{e^-}{g} \times \frac{g}{cm^2} \qquad \text{Equation 9.1}$$

$$= \frac{e^-}{g} \times \frac{Mass}{Area} \qquad \text{Equation 9.2}$$

Mass and area calculation:

For dilute stage 1, C-C bond ~ 1.424 Å.

Mass of carbon atom = 1.994 x 10^{-23} g

Unit cell contains 2 carbon atoms, therefore:

$$Mass = 2 \times 1.994 \times 10^{-23}\ g \qquad \text{Equation 9.3}$$

$$Area = \frac{3\sqrt{3}}{2}(1.424 \times 10^{-8}\ cm)^2 \qquad \text{Equation 9.4}$$

Therefore,

$$\frac{Mass}{Area} = 7.57 \times 10^{-8} g\ cm^{-2} \qquad \text{Equation 9.5}$$

Conversion of mAh g^{-1} to electrons g^{-1}:

1 Ah = 3600 C

1mAh = 3.6 Coulombs

Charge on 1 e^{-1} = -1.6 x 10^{-19} C

No. of electrons in in 1 C = 6.25 x 10^{18} e^{-}

Therefore,

$$\frac{e^-}{g} = 20 \times 3.6 \times 6.25 \times 10^{18} = 4.5 \times 10^{20}$$ Equation 9.6

Finally;

$$\frac{e^-}{cm^2} = \frac{e^-}{g} \times \frac{g}{cm^2}$$ Equation 9.7

$$Charge\ carrier\ concentration = 3.41 \times 10^{13}\ \frac{e^-}{cm^2}$$ Equation 9.8

9.2. Rate test procedure for lithium titanate electrodes

Table 9.1: Rate test procedure for lithium titanate electrodes, where 1C = 175 mA g^{-1}.

Step number	**Description**
1	Symmetric galvanostatic cycling between 1.0 V – 2.5 V at C/5 for 1 cycle
2	Symmetric galvanostatic cycling between 1.0 V – 2.5 V for 2 cycles at C/2
3	Discharge at C/5 until 1.0 V
4	Hold at 1.0V until current drops below C/20 (< 8.75 mA g^{-1})
5	Charge at 10C, 5C, 2C, C, C/2, C/5, C/20 up to 2.5 V cut-off, with 5 minute OCV period in between charges.

Summary of Research Papers and Conference Presentations

Christopher G. Sole
E-mail: cgsole@hotmail.co.uk

Education

09/2013 – 05/2017 PhD in Chemistry, Stephenson Institute for Renewable Energy, University of Liverpool (UK)

Thesis title**:**

Application of few layer graphene and exfoliated graphite materials in lithium ion batteries Supervisor: Prof. Laurence J. Hardwick

Projects:

- Mechanistic analysis of Li intercalation in graphitic carbons of varying layer number and few layer graphene by *in situ* Raman spectroscopy.
- Evaluation of the performance of exfoliated graphite materials as conductive additives for high rate-performance lithium ion battery composite electrodes.

Conferences, Presentations and Courses Attended

- Pre-sessional Live Lecture Series, English Language Centre - Science and Engineering group, University of Liverpool, 10th August 2016. Oral presentation entitled: "Saving the world, batteries included: Electrochemical energy storage technologies of the past, present and future"
- SIRBATT Workshop "Controlling Lithium Battery Interfaces", Orlando, Florida 27th May, 2016, USA. Oral presentation entitled "**In situ observation of Li intercalation into graphitic flakes of varying layer number." (Chapters 3, 4 and 5)**
- Symposium of the U.K. Northwest Electrochemical Society Student Chapter, University of Manchester 10th Feb 2016, **1st place poster prize** awarded for presentation entitled "**In situ Raman study of lithium-ion intercalation into microcrystalline graphite**." **(Chapters 3 and 4)**
- Energy Innovation Centre Battery School, October 2015, WMG, University of Warwick,
- Graphene week 2015, University of Manchester, 22nd-26th June 2015, Poster presentation "**In situ Raman study of lithium-ion intercalation into**

graphite and electrochemically exfoliated few layer graphene." **(Chapters 3 and 4)**

- Attendance and comments contributed to Faraday Discussion 172 - Carbon in Electrochemistry, University of Sheffield, 28th to 30th July 2014.
- Electrochem North West 2014, University of Liverpool 23rd June 2014, Poster presentation "**In situ Raman study of lithium-ion intercalation into microcrystalline graphite**." **(Chapter 3)**

Publications

1. ***In situ*** **Raman study of lithium-ion intercalation into microcrystalline graphite,** C. Sole, N. E. Drewett & L. J. Hardwick, *Faraday Discussions.*, 172 (2014) 223-237
   (Chapter 3)

2. **The role of re-aggregation on the performance of electrochemically exfoliated many-layer graphene for Li-ion batteries,** C. Sole, N. E. Drewett, F. Liu, A. Abdelkader, I. Kinloch, L. J. Hardwick, *Journal of Electroanalytical Chemistry,* 753 (2015) 35-41
   (Chapter 4)

3. ***In situ*** **study of Li intercalation into highly crystalline graphitic flakes of varying thicknesses,** J. Zou, C. Sole, N. E. Drewett, M Velický & L. J. Hardwick, *Journal of Physical Chemistry Letters*, 7 (2016) 4291-4296
   (Chapter 5)